General Disclaimer

One or more of the Following Statements may affect this Document

- This document has been reproduced from the best copy furnished by the organizational source. It is being released in the interest of making available as much information as possible.

- This document may contain data, which exceeds the sheet parameters. It was furnished in this condition by the organizational source and is the best copy available.

- This document may contain tone-on-tone or color graphs, charts and/or pictures, which have been reproduced in black and white.

- This document is paginated as submitted by the original source.

- Portions of this document are not fully legible due to the historical nature of some of the material. However, it is the best reproduction available from the original submission.

Produced by the NASA Center for Aerospace Information (CASI)

UNIVERSITY OF ILLINOIS
URBANA

AERONOMY REPORT NO. 67

AN INVESTIGATION OF THE SOLAR ZENITH ANGLE VARIATION OF D-REGION IONIZATION

(NASA-CR-143217) AN INVESTIGATION OF THE SOLAR ZENITH ANGLE VARIATION OF D-REGION IONIZATION (Illinois Univ.) 290 p HC $8.75 CSCL 04A
N75-28597
Unclas
G3/46 31113

by
P. A. J. Ratnasiri
C. F. Sechrist, Jr.

RECEIVED
NASA STI FACILITY
INPUT BRANCH
AUG 1975

April 1, 1975

Library of Congress ISSN 0568-0581

Aeronomy Laboratory
Department of Electrical Engineering
University of Illinois
Urbana, Illinois

Supported by
National Science Foundation
Grant GA 36911X

NSF-GA-

ABSTRACT

A review of the *D*-region ionization measurements and its solar zenith angle variation reveals that a unified model of the *D* region, incorporating both the netural chemistry and the ion chemistry, is required for a proper understanding of this region of the ionosphere. Model calculations are carried out with a view to interpreting the solar zenith angle variation of *D*-region ionization as measured on July 24, 1968 at Wallops Island. All input data are taken corresponding to this day.

The model developed for the neutral chemistry includes the transport terms relating to molecular and eddy diffusion. It describes the diurnal behavior of the minor neutral constituents formed in an oxygen-hydrogen-nitrogen atmosphere, in the height interval between 30 and 120 km. Computations carried out for two cases of the eddy diffusion coefficient models indicate that the constituents which are important for the *D*-region positive-ion chemistry do not show a significant variation with zenith angle for values up to 75° over the *D*-region heights.

In the ion chemistry model, ion-pair production rates are calculated for solar X-rays between 1 Å and 100 Å, EUV radiations from 100 Å up to the Lyman-α line, precipitating electrons and galactic cosmic rays. Two cases of O_2^+ production rates due to different fluxes of precipitating electrons and X-rays below 3 Å have been considered. The model describes the solar zenith angle variation of the positive-ion composition, negative-ion composition and the electron densities up to 75° zenith angle, in the height interval between 60 and 100 km.

A comparison of the computed electron-density profiles with the rocket measured profiles reveals that good overall agreement is obtained when the neutral chemistry model associated with the low eddy diffusion coefficient values is used. The computed solar zenith angle variation, however, is only a fraction of the measured variation. This discrepancy is probably due to short-term variations in the mesopause temperatures and X-ray fluxes below 3 Å.

TABLE OF CONTENTS

Page

ABSTRACT ii

TABLE OF CONTENTS iv

LIST OF TABLES vii

LIST OF FIGURES viii

1. INTRODUCTION 1

1.1 *The Ionospheric* D *Region* 1

1.2 *Methods for* D-*Region Investigations* 4

1.2.1 *Ground-based experiments* 5

1.2.2 *Rocket experiments* 8

1.3 *Evidence for Diurnal Variation* 13

1.4 *Some Outstanding Problems of the* D *Region* 17

1.5 *Objectives and the Outline* 24

2. PHOTOCHEMISTRY OF NEUTRAL SPECIES 26

2.1 *Neutral Atmosphere* 26

2.2 *Photodissociation Coefficients* 28

2.2.1 *Solar radiation in the 1000-4000 Å region* 33

2.2.2 *Absorption cross-sections* 34

2.2.3 *Solar variation of photodissociation coefficients* . 42

2.3 *Reactions of Oxygen Constituents* 46

2.4 *Oxygen-Hydrogen Reactions* 49

2.5 *Nitrogen Reactions* 55

2.6 *Carbon Reactions* 63

3. MODEL CALCULATION OF NEUTRAL SPECIES DISTRIBUTION 68

3.1 *Transport Processes in the Upper Atmosphere* 68

Page

3.1.1 *Eddy-diffusion coefficients* 69

3.1.2 *Molecular diffusion coefficients* 73

3.2 *Solution of Continuity Equation with Transport Term* . . . 75

3.3 *Boundary Conditions* 82

3.3.1 *Boundary conditions for lower atmosphere produced constituents* 82

3.3.2 *Boundary conditions for upper atmosphere produced constituents* 85

3.4 *Calculation of the Initial Values* 87

3.5 *Constant Zenith Angle Calculations* 98

3.5.1 *Oxygen and oxygen-hydrogen constituents* 98

3.5.2 *Nitrogen and oxygen-nitrogen constituents* 104

3.6 *Diurnal Variation of Neutral Species* 107

3.6.1 *Oxygen constituents* 109

3.6.2 *Oxygen-hydrogen constituents* 119

3.6.3 *Nitrogen and oxygen-nitrogen constituents* 129

4. ION-PAIR PRODUCTION RATES 138

4.1 *Solar EUV Radiations* 139

4.1.1 NO *ionization* 139

4.1.2 $O_2(^1\Delta_g)$ *ionization* 143

4.1.3 O_2 *ionization* 144

4.2 *Solar X-Rays* 148

4.2.1 *X-rays below 10 Å* 150

4.2.2 *30 - 100 Å X-rays* 161

4.3 *High-Energetic Particles* 163

4.3.1 *Precipitating electrons* 163

Page

4.3.2 *Galactic cosmic rays* 167

4.4 *Discussion* 170

5. *D*-REGION ION CHEMISTRY 176

5.1 *Measurement of Charged Species Distribution* 176

5.1.1 *Positive-ion composition* 176

5.1.2 *Negative-ion measurements* 180

5.1.3 *Electron-density measurements* 181

5.2 *Ionic-Reaction Schemes* 183

5.2.1 *Positive-ion reactions* 183

5.2.2 *Negative ion reactions* 188

5.3 *Reaction Rate Constants* 197

6. ION COMPOSITION AND ELECTRON-DENSITY PROFILES 207

6.1 *Ion-Composition Model* 207

6.1.1 *Continuity equations* 208

6.1.2 *Methods of composition* 212

6.2 *Positive-Ion Composition* 214

6.2.1 *Molecular-ion concentrations* 214

6.2.2 *Cluster-ion concentrations* 220

6.3 *Negative-Ion Composition* 224

6.4 *Electron Density* 231

6.4.1 *Comparison with measured profiles* 231

6.4.2 *Solar zenith angle variation* 239

7. SUMMARY AND CONCLUSIONS 244

APPENDIX I. NUMERICAL SOLUTION OF PARTIAL DIFFERENTIAL EQUATIONS . 249

REFERENCES 253

LIST OF TABLES

Table		Page
2.1	Neutral atmosphere composition at ground level	27
2.2	Photodissociation reactions	44
2.3	Oxygen reactions	48
2.4	Oxygen-hydrogen reactions	54
2.5	O-N and O-N-H reactions	62
2.6	C-O-H reactions	66
4.1	Ionization potential and threshold wavelengths of ionization for atmospheric gases	140
5.1	Positive-ion reactions	189
5.2	Negative-ion reactions	194
5.3	Recombination coefficients	202
5.4	Photodetachment rates	206

LIST OF FIGURES

Figure		Page
1.1	Structure of the day-time electron-density profile of the earth's ionosphere	2
1.2	Diurnal variation of 'phase height' of reflection for L.F. radio waves propagated to the distance marked [*Belrose*, 1963]	14
1.3	Rocket measured *D* region electron-density profiles at solar zenith angles 90°, 84°, 18°, and 60° on July 24, 1968 [*Mechtly and Smith*, 1970]	18
1.4	Rocket measured daytime positive-ion composition in the *D* region [*Narcisi and Bailey*, 1965]	20
2.1	The temperature and density profiles of the neutral atmosphere over Wallops Island on July 24, 1968. Values up to 90 km are based on rocket measurements by *Smith et al.* [1970] and above 90 km, on empirical formulas given by *Jacchia* [1971]	29
2.2	The penetration depths of solar radiation incident normally on the atmosphere. 63% of the incident energy in a given wavelength interval is lost above the altitude shown	31
2.3	The solar spectrum between 1000 and 4000 Å, based on the measurements by *Detwiler et al.* [1961], *Parkinson and Reeves* [1969] and *Tousey* [1963]	35
2.4	Absorption cross sections of neutral constituents having relatively high dissociation energies	37

Figure Page

2.5 Absorption cross sections of neutral constituents having relatively low dissociation energies 40

2.6 Photodissociation coefficients of neutral constituents having high dissociation energies, for solar zenith angles 18° and 60° 43

2.7 Photodissociation coefficients of neutral constituents having low dissociation energies, for solar zenith angles 18° and 60° 45

3.1 Eddy diffusion coefficient models used in this study. Molecular diffusion coefficient for oxygen is shown for comparison 74

3.2 The height distributions of oxygen constituents at noon obtained as initial values 92

3.3 The height distributions of hydrogen and oxygen-hydrogen constituents at noon, obtained as initial values 93

3.4 The height distributions of nitrogen and oxygen-nitrogen constituents at noon, obtained as initial values 96

3.5 The height distributions of carbon constituents at noon, obtained as initial values 97

3.6 The height distributions of oxygen constituents at noon, calculated using the transport model corresponding to a constant zenith angle and high eddy diffusion coefficient profile 99

3.7 The height distributions of hydrogen and oxygen-hydrogen constituents at noon, calculated using the transport model

Figure Page

corresponding to a constant zenith angle and high eddy diffusion coefficient profile 103

3.8 The height distributions of nitrogen and oxygen-nitrogen constituents at noon, calculated using the transport model corresponding to a constant zenith angle and high eddy diffusion coefficient profile 106

3.9 The height distribution of oxygen constituents at noon, calculated using the diurnal model with high eddy diffusion coefficient profile 110

3.10 The height distribution of oxygen constituents at noon, calculated using the diurnal model with low eddy diffusion coefficient profile 111

3.11 The height distributions of $O(^3P)$ at noon, 60° zenith angles and pre-dawn, calculated using the diurnal model with high eddy diffusion coefficient profile 112

3.12 The height distributions of $O(^3P)$ at noon, 60° zenith angles and pre-dawn, calculated using the diurnal model with low eddy diffusion coefficient profile 113

3.13 The height distributions of $O_2(^1\Delta_g)$ at noon, 60° zenith angles and pre-dawn, calculated using the diurnal model with high eddy diffusion coefficient profile 115

3.14 The height distributions of $O_2(^1\Delta_g)$ at noon, 60° zenith angles and pre-dawn, calculated using the diurnal model with low eddy diffusion coefficient profile 116

3.15 The height distributions of hydrogen and oxygen-hydrogen constituents at noon, calculated using the diurnal model with high eddy diffusion coefficient profile 120

Figure Page

3.16 The height distributions of hydrogen and oxygen-hydrogen constituents at noon, calculated using the diurnal model with low eddy diffusion coefficient profile 121

3.17 The height distributions of H at noon, 60° zenith angles and pre-dawn, calculated using the diurnal model with high eddy diffusion coefficient profile 124

3.18 The height distributions of H at noon, 60° zenith angles and pre-dawn, calculated using the diurnal model with low eddy diffusion coefficient profile 125

3.19 The height distributions of OH at noon, 60° zenith angles and pre-dawn, calculated using the diurnal model with low eddy diffusion coefficient profile 127

3.20 The height distributions of HO_2 at noon, 60° zenith angles and pre-dawn, calculated using the diurnal model with low eddy diffusion coefficient profile 128

3.21 The height distributions of nitrogen and oxygen-nitrogen constituents at noon, calculated using the diurnal model with high eddy diffusion coefficient profile 131

3.22 The height distributions of nitrogen and oxygen-nitrogen constituents at noon, calculated using the diurnal model with low eddy diffusion coefficient profile 132

3.23 The height distributions of NO at noon, 60° zenith angles, and pre-dawn, calculated using the diurnal model with low eddy diffusion coefficient profile 136

4.1 The ion-pair production rates due to Lyman-α (1216 Å) ionization of NO at zenith angles 18° (noon) and 60° . . . 142

Figure Page

4.2 The ion-pair production rates due to EUV (1027-1118 Å) ionization of $O_2(^1\Delta_g)$ at zenith angles 18° (noon) and 60° 145

4.3 The ion-pair production rates due to Lyman-β (1027 Å) and C III (977 Å) ionization of O_2 at zenith angles 18° (noon) and 60° 147

4.4 The absorption cross sections of oxygen and nitrogen at X-ray wavelengths (1-100 Å) 149

4.5 The spectral distributions of X-rays below 10 Å corresponding to different flux values in the 1-8 Å and 0.5-3 Å bands. The broken curve shows the spectrum measured by *Pounds* [1970] 155

4.6 X-ray fluxes in the bands 0.5-3 Å, 1-8 Å, and 8-20 Å as measured on July 24, 1968 with instruments on board SOLRAD 9 satellite (courtesy NOAA Environmental Data Service). 158

4.7 The ion-pair production rates due to X-rays below 10 Å at zenith angles 18° (noon) and 60°, calculated for the two 1-10 Å spectra shown in Figure 4.5 (curves 1 and 2) . . .160

4.8 The ion-pair production rates due to X-rays in the bands 30-44 Å and 40-100 Å, calculated for zenith angles 18° (noon) and 60° 164

4.9 The ion-pair production rates due to galactic cosmic rays, and precipitating electrons having energies greater than 40 keV (N(> 40 keV) = 300), and hardness indices of 2, 3, and 4 168

Figure		Page
4.10	The ion-pair production rates in the *D* region due to major ionization sources at daytime (χ = 18°)	171
4.11	The variation of the *D*-region ion-pair production function with the solar zenith angle, shown with contributions from two different precipitating electron spectra	173
5.1	More important positive-ion reaction paths in the *D* region	192
5.2	More important negative-ion reaction paths in the *D* region	198
6.1	The height distributions of positive-ion species. These results correspond to low eddy diffusion and summer noon (χ = 60°) conditions	215
6.2	The height distributions of positive-ion species. These results correspond to low eddy diffusion and summer morning (χ = 60°) conditions	216
6.3	The height distributions of positive-ion species. These results correspond to low eddy diffusion and summer evening (χ = 60°) conditions	217
6.4	The computed height distributions of negative-ion species. These results correspond to low-eddy diffusion and summer noon (χ = 18°) conditions	225
6.5	The computed height distributions of positive-ion species. These results correspond to low eddy diffusion and summer morning (χ = 60°) conditions	226

Figure		Page
6.6	The computed height distributions of negative-ion species. These results correspond to low eddy diffusion and summer evening (χ = 60°) conditions	227
6.7	The computed electron-density profiles corresponding to 18° and 60° solar zenith angles. The measured profiles are also shown for comparison	232
6.8	The solar zenith angle variation of the computed electron densities, shown for heights 75, 80 and 85 km	240
6.9	The effective recombination coefficient of the electrons, obtained from the electron densities computed at 18° and 60°	242

1. INTRODUCTION

1.1 *The Ionospheric* D *Region*

Solar and other extra-terrestrial radiations incident on the upper atmosphere of a planet ionize its neutral molecules producing pairs of free electrons and positive ions. The region where such free electrons occur in significant amounts is known as the ionosphere. The single parameter that characterizes the ionosphere is the electron density, which is a function of the height, latitude and time of the day, among other factors.

The propagation of a high frequency radio wave through the ionosphere is influenced by the free electrons present in it. These free electrons give rise to a complex refractive index for the propagating radio wave, resulting in its deviation from the original path, and also causing its attenuation. It was in fact, the experiments conducted to study the long-distance propagation of radio waves in the 1920's that led to the discovery of the Earth's ionosphere.

In these early experiments, different layers of the ionosphere which cause reflection of radio waves of different frequency bands were identified and were designated *D*, *E*, and *F*. Later studies on the ionospheric structure revealed that these layers could be identified with different regions, similarly designated, where the electron-density profile exhibits a plateau or a peak, as illustrated in Figure 1.1. It is sometimes possible to identify more than one layer within the same region, depending on the time of the day. For example, during the sunrise period a *C* layer, having a distinct peak develops in the lower part of the *D* region. During nighttime, the *F* region exhibits two distinct peaks known as the *F*1 and *F*2 layers.

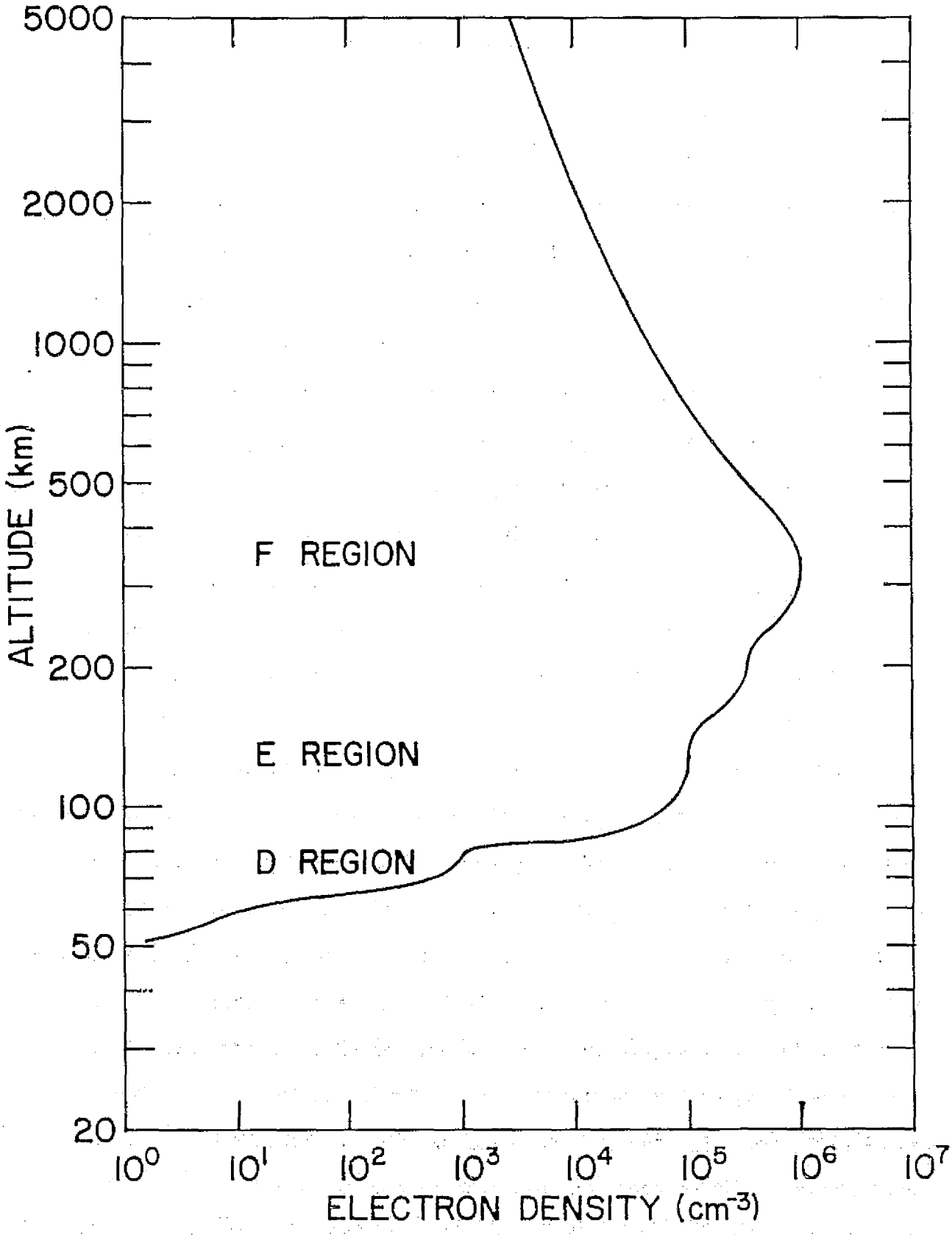

Figure 1.1 Structure of the day-time electron-density profile of the earth's ionosphere.

The present investigation is concerned with the *D* region, or the region below about 90 km of the ionosphere. This region exhibits several distinct features not found in the other regions of the ionosphere. The main reason for this distinction is the fact that the neutral atmosphere over this region has sufficiently high density so as to cause strong coupling between itself and the *D* region. The features referred to above are: (1) high absorption of radio waves, (2) complexity of the ion chemistry and (3) the occurrence of negative ions.

The absorption of radio waves in the ionosphere at a given height depends on the product of the electron density and the collision frequency between the electrons and the neutral particles. The collision frequency is directly proportional to the atmospheric pressure, and hence decreases with the height. The electron density, on the other hand, generally increases with height, at least in the *D* and *E* regions. The product of these two quantities, therefore, reaches a maximum, which happens to occur at *D*-region heights. Thus, the absorption of high frequency radio waves propagating in the ionosphere takes place mostly in the *D* region. The reception of radio signals from long-distance transmitters is limited by this ionospheric absorption. Therefore, a knowledge of the behavior of the *D* region is important for the proper operation of high-frequency radio networks.

The second feature mentioned above is really a consequence of the neutral chemistry of the region. The composition of the major constituents of the atmosphere up to the top of the *D* region is similar to that near the ground. In addition, a variety of active minor neutral constituents is produced in this part of the atmosphere as a result of the photodissociation of the major constituents as well as others that are transported from the ground.

The primary ionization process produces electron-ion pairs. The positive ion will either undergo dissociative recombination with the electron, or react with other neutral species in a charge transfer process to yield a large number of new positive ions. Some of these positive ions can undergo three-body reactions producing complex cluster ions. These reactions become important only when the third-body density is high; the necessary density being found at *D*-region heights and below. The *D*-region positive-ion chemistry is, therefore, much more complex than that of the higher regions.

Finally, the high efficiency of the three-body reactions at these heights is also revealed in the formation of the negative ions. These are formed when a free electron gets attached to a neutral molecule through a three-body reaction. These ions also undergo a series of charge transfer and attachment reactions producing a variety of negative molecular and complex cluster ions. In the *D* region during daytime, negative ions become important below about 75 km, the negative-ion and electron concentrations becoming equal around 70 km. At heights below, the negative-ion chemistry controls the electron concentration. At nighttime, negative ions dominate most of the *D*-region heights.

1.2 *Methods for* D-*Region Investigations*

The methods available for investigating *D*-region ionospheric processes fall into two main categories: ground-based and rocket-borne. Until about a decade ago, when the rocket techniques were developed, studies on the ionosphere were totally dependent on ground-based radio sounding experiments. The ground-based methods can also be classified into two groups; the conventional methods which provide only an integrated picture of the *D* region, and the more recent methods which directly provide the electron-density values as a function of the height. The rocket-borne experiments

measure the electron densities as well as the positive-ion densities *in situ*, and are considered to give the most reliable picture of the *D* region at present. In this section, a brief review of these methods will be given.

1.2.1 *Ground-based experiments.* In these experiments, a radio wave is employed as a tool for probing the ionosphere. The propagation of a radio wave in the ionosphere is governed by its refractive index, which is a function of both the electron density and the wave frequency. When the electron density increases with height, the refractive index continues to decrease, causing the wave normal to deviate more and more from its original path. When the refractive index becomes zero, which happens when the plasma frequency of the medium is equal to the wave frequency, the wave begins to return to the ground.

According to the simple ray theory of propagation, the frequency of a vertically incident wave that is reflected from a point having an electron density, N cm^{-3}, is given by

$$f = 8.98\sqrt{N} \quad \text{kHz}. \tag{1.1}$$

For a wave incident at an angle θ, this is multiplied by sec θ. The maximum frequency that gets reflected from a peak or a plateau in the electron-density profile is called the critical frequency of the corresponding layer. The electron density at the top of the *D* region is about 10^4 electrons cm^{-3}, and hence the maximum frequency that is reflected from the *D* region is of the order of 1 MHz, when incident vertically on the ionosphere.

Low frequency and very low frequency propagation experiments were among the early experiments carried out to investigate the *D* region. Frequencies in the range 15-100 kHz are reflected from the low and middle portions of the daytime *D* region. Signals from transmitters generally used for navigational purposes were monitored at various distances, ranging from 100's to 1000's of kilometers. The amplitude of the skywave as well as its phase relative to the phase of the ground wave was recorded. From these recordings, the diurnal behavior of the region near the reflecting level, and also effects such as the sunrise and sunset phenomena were studied.

In the vertical incidence absorption measurements, the signals from a pulse transmitter, after reflection from the ionosphere, are received in a receiver located near the transmitter. Usually, frequencies ranging from about 1.8 to about 6 MHz are used. The received echoes are displayed on a cathode ray tube, and the amplitude and the delay are recorded. At nighttime when the *D*-region ionization vanishes and the absorption is low, multiple echoes are observed. The amplitude of these yield the calibration constant of the system, or the unattenuated amplitude of the signal. Hence, the absorption during daytime is determined by deducting the observed amplitude from this calibration constant. The time delay gives the virtual height of the reflecting layer.

Generally, the lowest frequencies, i.e., those between 1.8-2.0 MHz return from heights in the range 95-100 km, well above the *D* region. However, most of the absorption takes place at *D*-region heights, between about 80 and 90 km, as mentioned before. Any changes in the observed absorption could, therefore, be attributed to changes in the electron-density values at these heights. However, the absorption, being an

integrated effect, cannot yield information about the fine structure of the *D* region.

The experiments developed more recently to study particularly the *D* region are: (1) Partial-Reflection Method, and (2) Cross-Modulation Method. A third method, developed for studying the upper ionosphere and applied recently for lower ionosphere studies, is the Incoherent-Scatter Method.

In the partial-reflection method, weak signals reflected from irregularities in the electron-density profile at *D*-region heights are recorded in both the ordinary and extraordinary modes [*Gardner and Pawsey*, 1953]. From the ratio of these amplitudes, the electron-density values are derived over the height range 65-80 km. In view of the very low intensity of these echoes, high-power transmitters and low-noise receiving sites have to be used. The finite pulse width, the errors in reading the echo amplitudes, and the long sampling periods are some of the factors that limit the accuracy of the electron densities derived from this method. *Coyne and Belrose* [1973] estimated the accuracy in the absolute values of the electron densities at any height to be about 50%, while the accuracy of any changes was estimated to be within ± 20%.

The cross modulation of two radio waves in the ionosphere was long known, and was commonly referred to as the Luxembourg Effect. This method, first applied to ionospheric studies by *Fejer* [1955], essentially consists of measuring the difference between the absorption of two downcoming waves, one passing through the normal ionospheric region, and the other passing through a heated or disturbed region. The heating or the disturbing of the ionosphere is done by a high-power transmitter whose signal is directed

to meet the downcoming radio wave at a required height. The high power beam raises the electron temperature of the plasma, which in turn, modifies the collision frequency. The resulting change in absorption, which is of the order of 1-2%, is measured. From these data, both the electron density as well as the collision frequency could be determined as a function of the height [*Thrane et al.*, 1968; *Lee and Ferraro*, 1969].

Incoherent-scatter facilities have been in existence for a number of years to study the ionospheric *E* and *F* regions. In view of the variety of information this method provides, it has proved to be a powerful tool for investigating the middle and upper regions of the ionosphere [*Bowles*, 1958]. In the original systems, the presence of interferring ground clutter signals has made it impracticable to obtain useful signals from the lower ionosphere, particularly below about 150 km. Recently, *Armistead et al.* [1972] have shown that, with certain system modifications, it is possible to bring down the heights of measurement to about 80 km. However, this technique has not been perfected yet to provide *D*-region profiles with sufficient accuracies. At present, results could be considered reliable down to about 90 km only.

1.2.2 *Rocket experiments*. *In situ* measurements of ionospheric parameters by rocket experiments have been widely used in recent years. Of these, the experiments designed for *D*-region studies can be divided into two groups: (1) radio propagation experiments and (2) ion-probe experiments. In radio experiments, the generalized magnetoionic theory is employed to deduce the electron densities, while in ion-probe experiments, the total probe current gives the electron densities.

The radio experiment essentially consists of sending two signals, one in the ordinary mode and the other in the extraordinary mode, on the same

frequency from ground-based transmitters, and receiving them on a rocket-borne receiver. The two signals are recorded separately and telemetered to the ground [*Mechtly et al.*, 1967]. The Faraday rotation or the rotation of plane of polarization of the wave containing both the ordinary and the extraordinary modes is also measured and telemetered to the ground. From the two independent signals, the differential absorption is measured. By combining these two measurements, the collision frequency is determined. This value, in turn, is used with either of the two measurements to yield electron densities. The Faraday rotation method gives reliable electron densities at the upper portion of the *D* region, while the differential absorption gives reliable results in the lower half of the *D* region. Both methods give overlapping electron densities in the central part. In view of the approximations made in the formulations, iterative techniques are employed to arrive at the final results. Recently, the accuracy and the height resolution of the measurements have been improved by employing two independent propagation experiments operating on two different frequencies [*Mechtly*, 1974].

Propagation experiments by themselves do not yield high resolution data to reveal the fine structure of the electron-density profiles. Usually, in the measurement of absorption below 90 km, large fluctuations occur in the telemetered data. The differential absorption is therefore determined by employing a sampling technique, and averaging over a selected range of points. This results in poor height resolution in the final electron densities.

Ion probes which respond to the electron or ion concentrations in the immediate neighborhood of the probe are widely used in rocket experiments.

This method has the advantage over the propagation experiments in that it reveals the fine structure of the electron-density profiles, but certain types lack the capability of yielding absolute values of electron concentrations. Though several types of *in situ* probes are available for ionospheric investigations [*Sayers*, 1970], only the following used specifically for *D* region studies will be discussed here: (1) Langmuir probe, (2) Gerdien condenser, and (3) electrostatic probe.

The Langmuir probe technique was developed for ionospheric studies by *Smith* [1964]. This consists of a metallic electrode mounted axially on the nose tip of a rocket. The probe is biased at a fixed potential relative to the rocket body and it collects either the positive or the negative ions depending on the polarity of the bias potential. The probe current is directly proportional to the concentration of the ions or electrons collected, the constant of proportionality being a function of the probe shape and size. In view of the uncertainties involved in determining this parameter, direct measurement of the ion or electron concentration by this method is not possible. Therefore, it is customary to convert the collector current into electron concentrations with the help of radio propagation experiments or ionosonde data. The most reliable *D*-region electron densities have been obtained by calibrating the Langmuir probe current profiles with the electron densities deduced from differential absorption and Faraday rotation experiments described previously.

The Gerdian condenser has been generally used to measure the positive-ion concentrations. In the upper part of the *D* region where the abundance of negative ions is negligible, the electron density could be obtained from this measurement. This is essentially a pair of two concentric

metallic cylinders located axially at the nose tip of the rocket. The passage of the rocket through the plasma maintains a flow of ionized air through the two cylinders. An electric field applied across the annular region between the two cylinders causes a flow of electric current through the condenser. When the applied electric field exceeds a certain value, this current reaches saturation. At this saturation mode, the current collected is equal to the product of the charge density of the plasma, aperture area, electronic charge, and the effective velocity of ion flow into the condenser. The velocity is deduced from the rocket speed and its inclination to the trajectory. Thus, from the current measurements, charge density can be determined directly. At *D*-region heights where the mean free path of the particles is small compared to the dimensions of the condenser, reflection of particles take place at supersonic speeds. At altitudes above 70 km, this effect can cause errors up to about 25% [*Kane*, 1972], which can become serious at lower altitudes. Further, at altitudes above about 85 km, vehicle potential can cause errors up to a factor of two in the measurement of positive-ion densities. Thus, the Gerdien condenser is best suited for measurements in the middle part of the *D* region.

Sagalyn and Smiddy [1964] developed a technique for measuring independently the positive and negative charge densities of a plasma. Their instrument consists of two spherical electrostatic probes, one for the collection of positively-charged particles, and the other for the collection of negatively-charged particles, enclosed in outer spherical grids. The collector is maintained at a fixed bias voltage relative to the outer grid, which is maintained at the vehicle potential for the positive-ion probe, and at a slightly positive value for the negative-ion probe. Under normal operation, the fixed bias voltage collects all the charged particles

entering the outer grid, and the resulting current flow is measured. To evaluate the corrections due to vehicle potentials, the outer grid voltage is swept linearly and the resultant currents are measured. From a knowledge of the dimensions of the probes and pre-determined parameters, the total ion densities are evaluated in terms of the collector currents.

In addition to the above probes which measure the total ion or electron densities, mass spectrometers are also flown in rockets to measure the distribution of different ionic species in the ionosphere. With the development of this technique, a complete new picture of the *D* region has emerged. The presence of complex cluster ions in the lower part of the *D* region was first detected by *Narcisi and Bailey* [1965] who flew a quadrupole mass spectrometer in a rocket.

This instrument has four rods mounted axially at the four corners of a square. The ions are drawn in through an aperture at one end, while the ion detector is located at the opposite end. Suitable RF and DC potentials are applied across these rods which make it possible for an ion of only a certain charge-to-mass ratio to reach the ion detector. Sweeping of the RF voltage results in the collection of ions of different charge-to-mass ratios sequentially. In order to make the trajectory time smaller than the collision period, the spectrometer chamber is evacuated continuously and maintained at liquid nitrogen temperatures. The collector currents are proportional to the respective ion densities. The absolute values are obtained by conducting an independent experiment which measures the total ion density, using a different method such as the electrostatic probes described before. Inaccuracies in reading the current peaks, drifts in the DC amplifier could result in overall errors up to about 50%.

1.3 *Evidence for Diurnal Variation*

Both the LF and VLF recordings and the absorption measurements provided the first evidence of the strong solar control of the *D* region. [*Bracewell et al.*, 1951; *Appleton and Piggott*, 1954]. Figure 1.2 illustrates a typical recording of the phase variations obtained more recently by *Belrose* [1963]. The phase variations could be attributed to variations in the apparent height of reflection. For a fixed path and frequency, the apparent height corresponds to a level having a given electron density. Hence, these curves in effect show the displacement of the electron-density profile near the level of reflection. For the shorter path, which corresponds to a higher level of reflection, the variation between sunrise and sunset is rather smooth. For the longer path, the variation is abrupt near the sunrise and sunset, and in between, there is no significant variation. These results indicate that the upper portion of the *D* region has a strong solar control, while the lower region has virtually no solar control during the daytime hours.

In summer, the daytime variations over short paths are so regular and constant, that the observed variations can be represented by the expression

$$h_\chi = h_o + A \log_e (\sec \chi), \tag{1.2}$$

where h_χ and h_o are the apparent heights when the solar zenith angle is χ and o, respectively, and A is a constant for the day. A closer look at the results show that the curves are not quite symmetrical about the local noon. This becomes apparent when h values are plotted against $\log_e$ (sec χ). The straight lines passing through the morning values do not fall

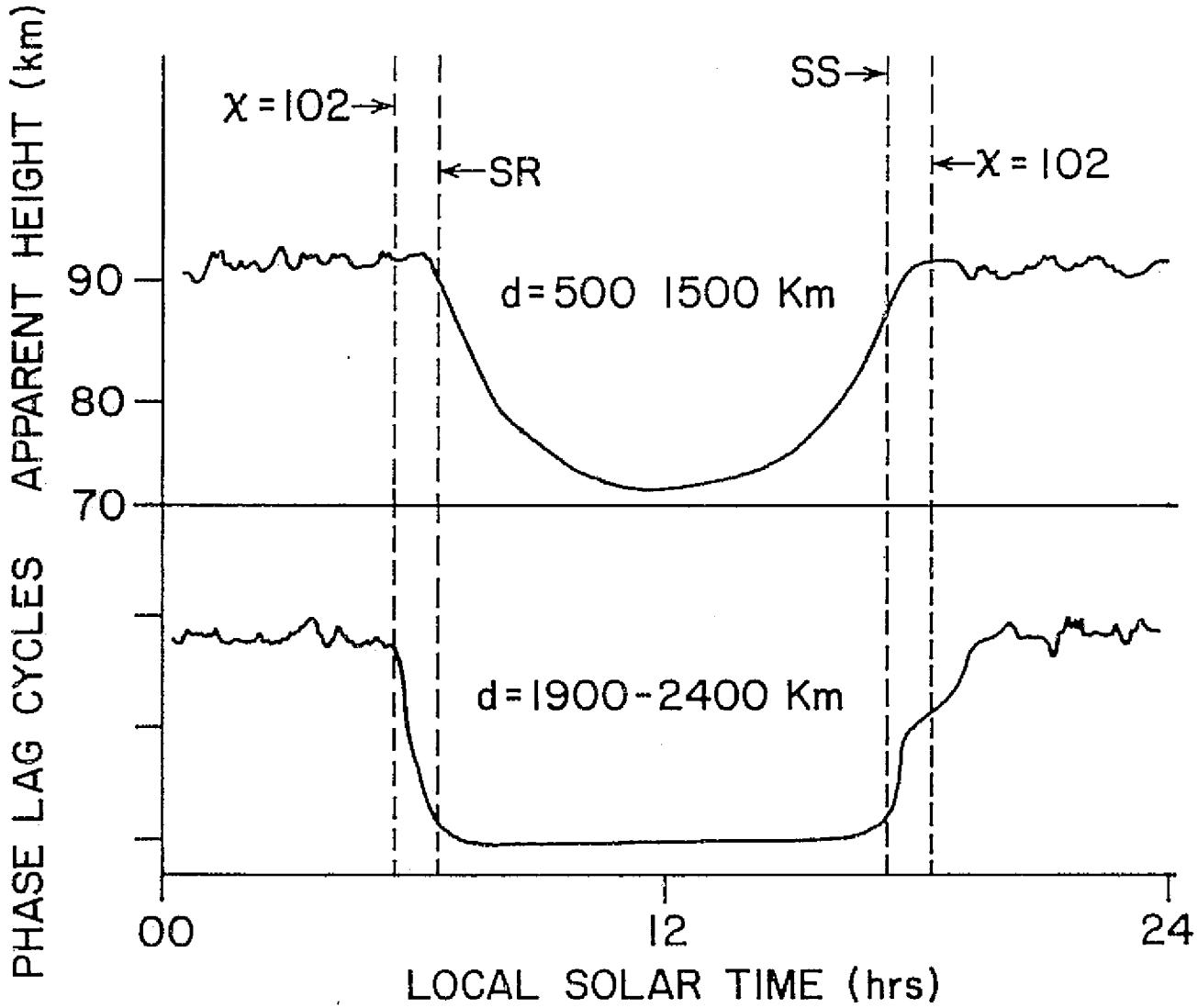

Figure 1.2 Diurnal variation of 'phase height' of reflection for L.F. radio waves propagated to the distance marked [*Belrose*, 1963].

on the straight line connecting the afternoon values. There is a delay of about 20-30 minutes in the appearance of the minimum points in these curves.

Vertical-incidence absorption measurements have been carried out in the past over long periods of time, both at mid-latitudes and low latitudes [*Appleton and Piggott*, 1954; *Gnanalingam*, 1974]. These measurements show that the absorption varies linearly with the sunspot number, has a diurnal variation, seasonal variation, and also a day-to-day variation. The diurnal variation of absorption is usually expressed in the form

$$L = L_o \cos^n \chi, \tag{1.3}$$

where L and L_o are the absorption values at solar zenith angles χ and o, respectively; and n is a constant. The simple ray theory predicts that the index n for the diurnal variation of the total nondeviative absorption for waves traveling in a Chapman layer is 1.5. However, observations show that n takes the value 0.75 for mid-latitude stations [*Beynon and Davies*, 1955]. Using the method of oblique incidence absorption, *Schwentek* [1966] also found that $n = 0.75$ on most of the quiet days. On the other hand, *Gnanalingam* [1974] found that, for a low latitude station, n takes the values 0.8 and 0.9 for the equinoctial months at solar maximum and solar minimum, respectively. These results have important implications on the diurnal behavior of the D-region ionization.

The plots of absorption against $\log_e (\cos \chi)$ also exhibit the diurnal asymmetry. The morning points lie on a straight line having a smaller gradient than that joining the afternoon points. This asymmetry is again of the order of 20-30 minutes.

Coyne and Belrose [1972] used the partial-reflection system to measure both the diurnal and seasonal variations of the electron densities between 65 and 81 km. They found a strong solar variability in these measurements, at least up to a solar zenith angle of about 75°. Here again, the variation was found to have a slight asymmetry about local noon.

Using both the partial-reflection and cross-modulation techniques, *Thrane et al.* [1968] measured the diurnal variation of the electron densities between 65 and 85 km at a mid-latitude station during quiet solar conditions. *Thrane* [1969] attempted to interpret these measurements using a *D*-region model where the electron losses are due to a recombination process, for which the production rate q is proportional to N^2.

For a Chapman-type ionosphere, consisting of a single ionizable constituent ionized by monochromatic radiation, which is attenuated by a single absorbing gas, the rate of production q is related to χ according to

$$\log_e q(z,\chi) = A - B(z) \sec \chi, \tag{1.4}$$

where A is a constant, and

$B(z)$ is a function of the height z only.

From the measured values of N, the production rates were deduced using known electron loss rates. The $\log_e q$ values were then plotted against $\sec \chi$ for different heights. It was observed that the gradients of these plots were much steeper than the values of $B(z)$ calculated for the corresponding heights. According to Thrane, this discrepancy could be explained if the ionizable constituent or the electron loss rate has a

solar zenith angle variation, or if the dominant ionization is not produced by a single gas.

Haug and Thrane [1970] have re-examined these measurements in the light of a new *D*-region model suggested by *Haug and Landmark* [1970]. In this model, electron losses take place through an attachment-like process. Consequently, the production rate q is proportional to N under quasi-equilibrium conditions. Haug and Thrane compared the plots of log N versus sec χ made on the basis of this theory, with the experimental plots, and found that the discrepancy is smaller with this model than with that used by Thrane. In view of the uncertainties involved in the measurements, as well as in the other parameters used, this small discrepancy does not appear to be significant.

The diurnal study of the ionosphere by rocket experiments is a difficult task due to the high costs and various operational problems. Hence rocket experiments are not generally employed to study diurnal variations of the ionosphere. Nevertheless, *Mechtly and Smith* [1970] were successful in making four sets of reliable measurements of the electron-density profiles at four zenith angles on the same day (Figure 1.3). The extent of the solar control of the *D*-region ionization becomes evident from this set of measurements.

The two large angle profiles were measured during the sunrise hours. The $\chi = 18°$ profile corresponds to the noon. To study the variability of the *D*-region ionization during the daytime, only the two profiles at $\chi = 18°$ and $60°$ are of interest.

1.4 *Some Outstanding Problems of the* D *Region*

Much progress in our understanding of the *D* region has been made during the past few years, though some problems still remain unsolved. The

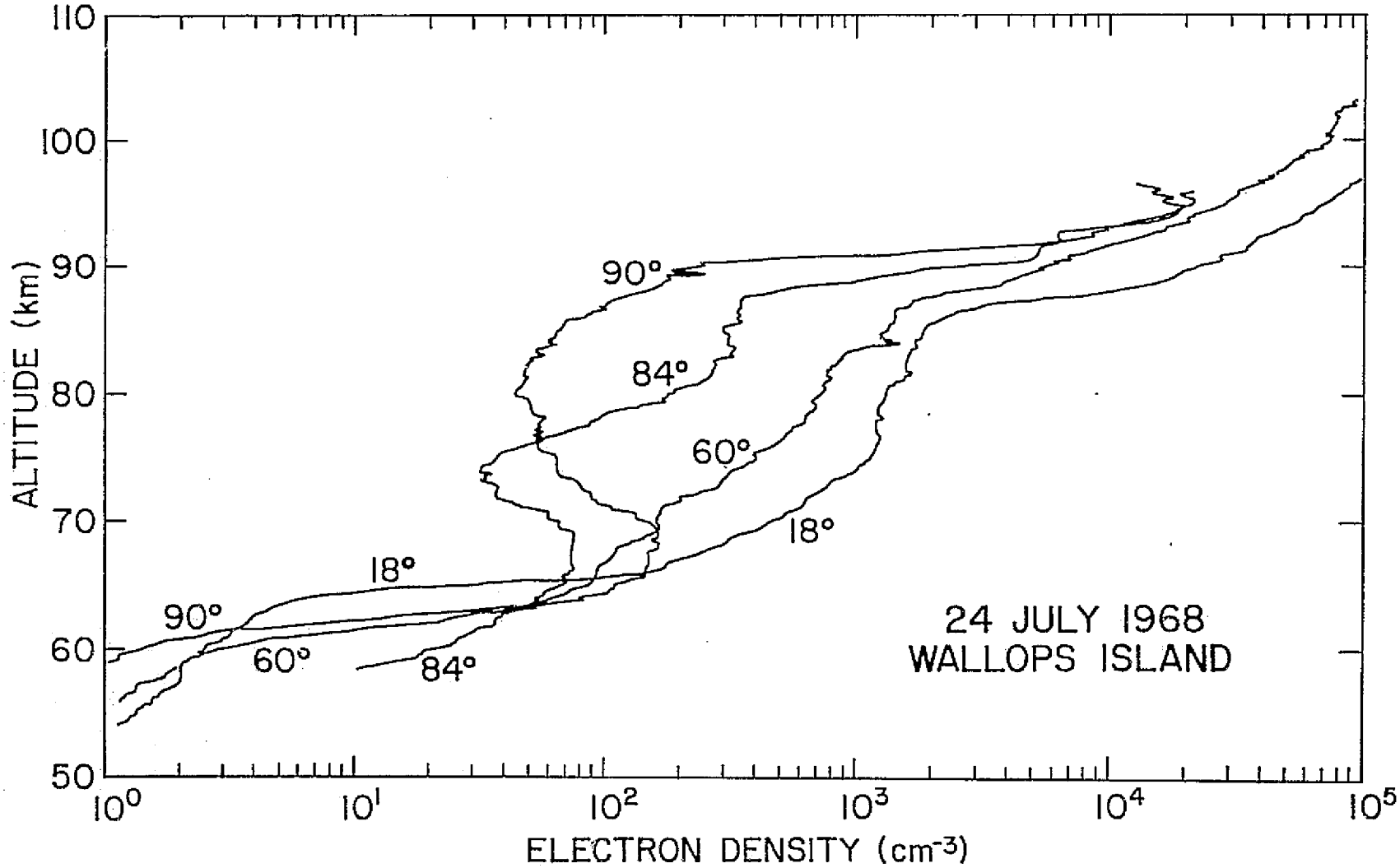

Figure 1.3 Rocket measured *D* region electron-density profiles at solar zenith angles 90°, 84°, 18°, and 60° on July 24, 1968 [*Mechtly and Smith*, 1970].

present status of the *D* region has been the subject of two recent reviews by *Sechrist* [1972] and *Thomas* [1974]. Some salient features of the *D* region, its production and loss processes will be given here in order to identify some of these outstanding problems.

A large number of *D*-region electron-density profiles have been measured during the daytime at Wallops Island (latitude = 40°N) using rocket-borne propagation and Langmuir-probe experiments [*Mechtly et al.*, 1972a]. All of these profiles were measured at the same zenith angle, viz 60°, and during different seasons and solar conditions. Yet, almost all of them exhibit some consistent characteristic features.

Between about 82 and 88 km, the electron density increases very rapidly with altitude. In most cases, this increase is more than an order of magnitude and takes place within a height interval of about 2 km. Above 90 km, the increase is rather gradual, varying between 10^4 and 10^5 electrons cm^{-3} in the height range 90-105 km. A second ledge appears around 60 km. This is more prominent in the active-sun profiles. In the quiet-sun profiles, this ledge is absent, but they show a marked plateau region between 60 and 80 km, where the increase in the electron density is very slow.

These features of the electron-density profiles are closely associated with some features present in the ion distributions. Direct measurements of the *D*-region positive-ion composition obtained from rocket-borne mass-spectroscopic experiments reveal (Figure 1.4) that heavy cluster ions of the type $H^+ \cdot (H_2O)_n$, (n = 1, 2, ...) become dominant below about 82-85 km level, and that molecular ions NO^+ and O_2^+ dominate the altitudes above [*Narcisi and Bailey*, 1965; *Goldberg and Aikin*, 1971; *Krankowsky et al.*,

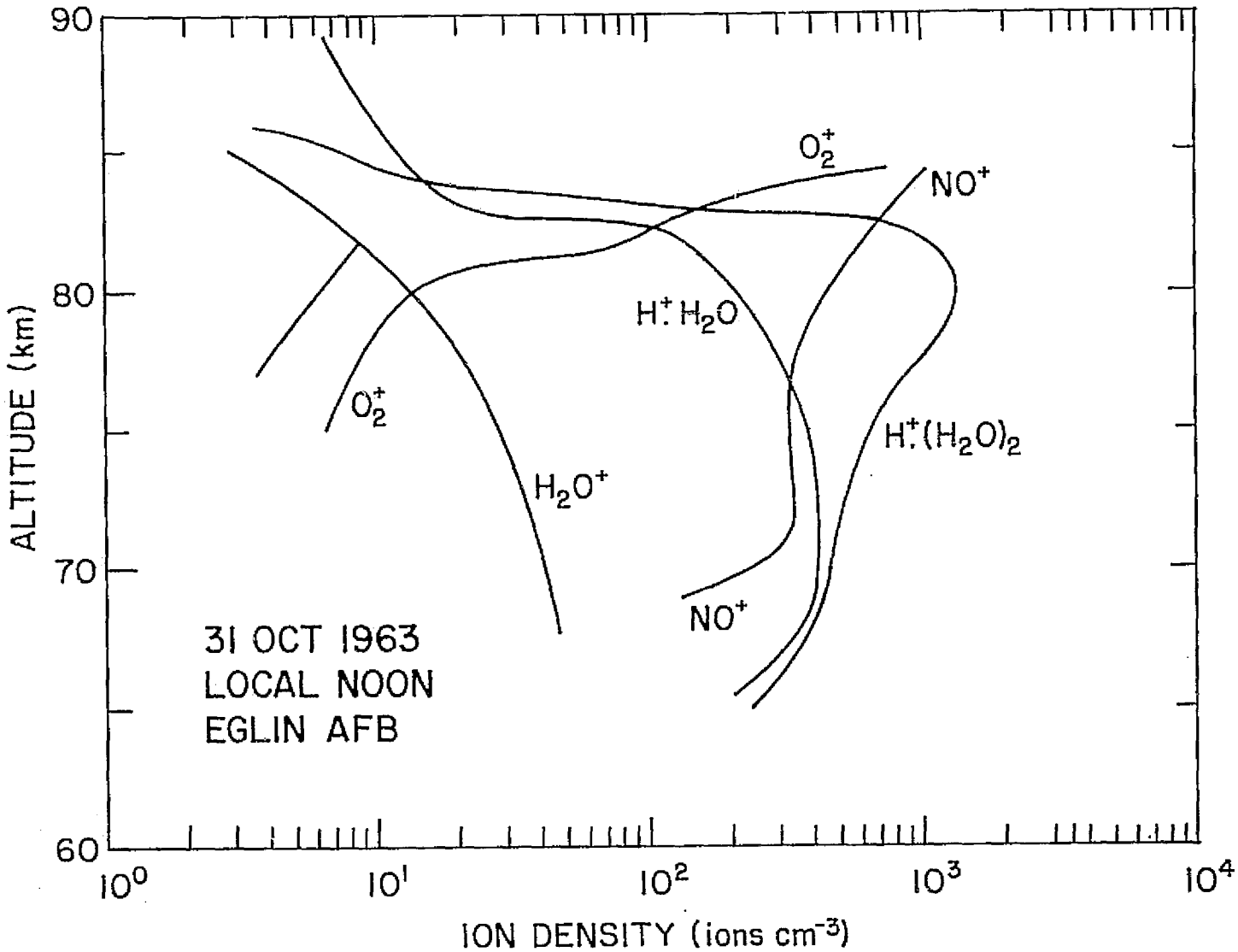

Figure 1.4 Rocket measured daytime positive-ion composition in the *D* region [*Narcisi and Bailey*, 1965].

1972]. This sudden drop in the hydrated cluster ion concentration and the sudden increase in the electron density at the same height range has been interpreted as due to hydrated cluster ions having a higher recombination coefficient than that of the molecular ions [*Sechrist*, 1970]. Though laboratory measurements of the recombination coefficients of both the molecular ions and the cluster ions are available, uncertainties in the distributions of such minor constituents as H_2O, O, NO, H, etc. which are important in the reaction schemes yielding these cluster ions, have made it difficult to interpret the observations quantitatively. Attempts by several workers to reproduce theoretically the sudden disappearance of the cluster ions and the sharp ledge in the electron densities near 82-85 km have so far failed [*Reid*, 1970; *Goldberg and Aikin*, 1971; *Hunt*, 1971a].

More than the sharp drop of the cluster ions, the prediction of the actual type of the dominant cluster ion present in the *D* region by itself has remained an outstanding problem [*Reid*, 1971]. The known values of NO and the ionization rates would yield water clusters of NO^+ around 80 km, rather than those of the type $H^+ \cdot (H_2O)_n$ which have been observed to dominate these altitudes. Attempts to solve this problem have not been successful so far, due to the lack of proper knowledge of either the rate constants involved or the concentrations of the minor neutral species, or due to both.

The other problem is concerned with the NO^+ production rates in the *D* region. The strong solar Lyman-α line at 1216 Å ionizes the neutral NO present in the mesosphere producing NO^+. Direct measurements of NO concentration show that it varies between 1.5×10^7 and 1×10^8 cm^{-3} in the *D* region with a minimum near 85 km [*Meira*, 1971]. Near 80 km, or immediately

below the ledge in the electron-density profile, the major source of electron production is this ionization of NO. Through various ion-molecular reactions, NO^+ produced will yield a variety of cluster ions including the water clusters that are dominant at these altitudes. Under quasi-equilibrium conditions, the final electron density values will be determined by the rate of recombination of these dominant ions and the electrons.

The ion-pair production rates have been calculated using known values of fluxes, ionization cross sections. The rocket-measured electron densities are then used to calculate the effective recombination coefficient, defined as

$$\alpha_{eff} = q/N^2 \tag{1.5}$$

Calculations show that near 80 km, α_{eff} has to be greater than 1×10^{-5} cm^3 sec^{-1} in order to balance the production and loss rates [*Donahue*, 1972]. Recent estimates by *Mechtly et al.* [1972b] using rocket observations of the changes in the electron-density profiles during eclipses give values about 5×10^{-5} cm^3 sec^{-1} for heights immediately below the ledge in the electron-density profiles. However, the laboratory measurements of *Leu et al.* [1973] give values about 3×10^{-6} cm^3 sec^{-1}, almost an order of magnitude less than the values deduced from ionospheric observations for the recombination coefficient of $H^+ \cdot (H_2O)_2$, which is the dominant ion near 80 km.

This suggests that either the production rates used are too high, or the actual dominant ion below the ledge is something other than $H^+ \cdot (H_2O)_2$.

According to *Donahue* [1972], a low production rate can be realized if a reduced ionization rate is used for NO above 75 km. On the other hand, the presence of a heavy cluster ion having a larger recombination coefficient than that of $H^+ \cdot (H_2O)_2$ could be accepted if it is assumed that these heavy clusters get fragmented during the process of rocket measurements, resulting in the recording of a lower mass number than the mass number of the ion actually present in the ambient *D* region.

Another problem that has drawn relatively little attention is the production rates of O_2^+ between 70 and 90 km. Above 90 km, X-rays between 30 and 100 Å ionizing both O_2 and N_2, and the Lyman-β radiation ionizing O_2, produce O_2^+. Below 70 km, galactic cosmic rays ionizing both O_2 and N_2 produce the necessary O_2^+. In between, there are several sources producing O_2^+, all of them being minor sources compared to NO ionization. X-rays between 2 and 10 Å ionizing both N_2 and O_2, solar EUV radiation ionizing $O_2(^1\Delta_g)$ and precipitating electrons with initial energies greater than 40 keV, all produce O_2^+. Near equatorial latitudes, the precipitating electrons are not considered important. The theoretical calculations of *Goldberg and Aikin* [1971] show O_2^+ concentrations rapidly falling off below 82 km, while their measurements show O_2^+ which remains almost constant between 75 and 82 km. This indicates that either the precipitating electrons are important near the equatorial latitudes where the measurements are taken, or some other source of O_2^+ is present in this height range. Comparing the O_2^+ production rates due to EUV photoionization of $O_2(^1\Delta_g)$ with the results of *Narcisi and Bailey* [1965], *Huffman et al.* [1971] have also come to a similar conclusion. *Norton and Reid* [1972] have examined the possibility of such an additional source of

O_2^+, without success. A source of O_2^+ below the ledge can also solve, at least partly, the problem of the formation of the water-cluster ions.

It will be possible to identify the origin of the O_2^+ ionizing source if a diurnal study of the O_2^+ distribution could be made. A source such as precipitating electrons has no diurnal variation, whereas one with solar origin will show a diurnal variation, at least over the height range where the optical depth for the ionizing radiation is comparable to or larger than unity.

Thus, a realistic model of the *D* region should be able to explain:

1) the sharp ledge in the electron-density profile,
2) the formation of the dominant water-cluster ions,
3) the balance of production and loss rates, and
4) the O_2^+ concentrations between 70 and 90 km.

1.5 *Objectives and the Outline*

The observation of the variation of ionization with the solar angle will give information as to the height at which sources of different origins, such as Lyman-α and precipitating electrons become important. Such a deduction is straightforward, however, only if the incident radiation alone is a function of the solar zenith angle. Departures from this behavior will show that others, such as the concentration of ionizable constituents and those responsible for the electron losses could also vary with the zenith angle. Thus, an understanding of the phenomena occurring in the *D* region requires an understanding of the behavior of the neutral constituents at different solar zenith angles, and also of the variations in the ionizing radiations. In this report, an attempt will be made to construct a unified diurnal model of the neutral atmosphere between 30 and

120 km, and the *D* region. The neutral atmosphere will contain the major constituents such as N_2 and O_2, as well as the minor constituents that are either transported from the ground, or produced through photodissociation and photoionization. The final objective is to compare the calculated electron-density profiles with those measured by rocket experiments at $\chi = 18°$ and $60°$ on July 24, 1968 at Wallops Island [*Mechtly and Smith*, 1970]. Therefore, the input data taken for this study will correspond to this date and location. The emphasis will be for the region where the negative ions are not important.

In Chapter 2, the photochemistry of the minor neutral constituents, including their photodissociation rates and the production-loss mechanisms of different groups of constituents are discussed. The calculation of the initial values using the steady-state transport and photochemical equations for use in the time-dependent transport model are presented in Chapter 3. The solar zenith angle variation of the minor neutral constituent concentrations is also investigated in this chapter. The ion-pair production rates responsible for daytime *D*-region ionization are calculated in Chapter 4. In Chapter 5, the production and the loss processes, as well as the measurements of the composition of both the positive and negative ions are discussed. The results of the model calculations describing the solar zenith angle variation of the positive-ion composition, negative-ion composition, and the electron densities are given in Chapter 6. Chapter 7 presents the summary and the conclusions.

2. PHOTOCHEMISTRY OF NEUTRAL SPECIES

The ionosphere is formed as a result of the ionization of neutral molecules present in the upper atmosphere, by solar and other radiations. Therefore, a study of the ionosphere should necessarily include the study of the behavior of the neutral constituents. If one begins with a simple model of the atmosphere having only the two major constituents, molecular oxygen and nitrogen and subject them to the effects of solar radiation, the development of it into its present form can be followed up through different stages.

This chapter begins with a discussion of the neutral atmosphere model used in the present study. The calculation of the photodissociation coefficients of various constituents will be next given, followed up by a discussion of the photochemical production and loss processes of different groups of constituents.

2.1 *Neutral Atmosphere*

From direct measurements of the density of air it has been established that the neutral atmosphere composition remains unchanged from the ground level up to a height of about 100 km. Below this level the atmosphere is considered to be well mixed maintaining constant mixing ratios for those constituents that are not chemically active. At higher altitudes, the distribution of each constituent is governed by diffusive equilibrium.

The ground level composition adopted here is taken from the model of *Jacchia* [1971], and is given in Table 2.1.

According to Jacchia's model, molecular oxygen begins to photodissociate at 90 km and form atomic oxygen. The mean molecular weight is defined by a sixth order polynomial, from which the distribution

Table 2.1

Neutral atmosphere composition at ground level.

Constituent	Mixing Ratio
Nitrogen	0.[illegible]110
Oxygen	0.20955
Argon	0.0093432
Helium	0.0000061

of the individual species is calculated. The hydrostatic equations using the scale heights corresponding to each constituent are used to calculate the number densities above 100 km.

The temperature appears as an independent parameter in Jacchia's model. Up to 90 km, the temperature profile is constructed from three sets of direct measurements carried out on July 24, 1968 at Wallops Island [*Smith et al.*, 1970]. The temperatures above 90 km are determined by empirical formulas whose coefficients depend on the 10.7 cm solar flux, latitude, longitude and the time of day. For the purpose of this study, a 10.7 cm flux of 150 units (10^{-22} W m^{-2} Hz^{-1}) and local noon (χ = 17.8°) corresponding to Wallops Island geographic coordinates were used. The density and temperature profiles thus obtained are shown in Figure 2.1.

The calculation of the distribution of minor neutral constituents involves the simultaneous solution of several continuity equations which are in the form of parabolic type partial differential equations. The solution of such equations call for the imposing of boundary conditions. For many constituents these boundary conditions are not well known, and in some cases, suitable values have to be determined by initial trial calculations. The departure of the solution from the exact situation due to the use of incorrect boundary values will be largest near the boundaries. Therefore, in order to minimize such errors within *D*-region heights, the boundaries are extended up to 120 km at the top, and down to 30 km at the bottom.

2.2 *Photodissociation Coefficients*

The amount of radiation energy absorbed by a single molecule of a constituent (denoted *i*) at a given altitude over a wavelength interval $\Delta\lambda$ at

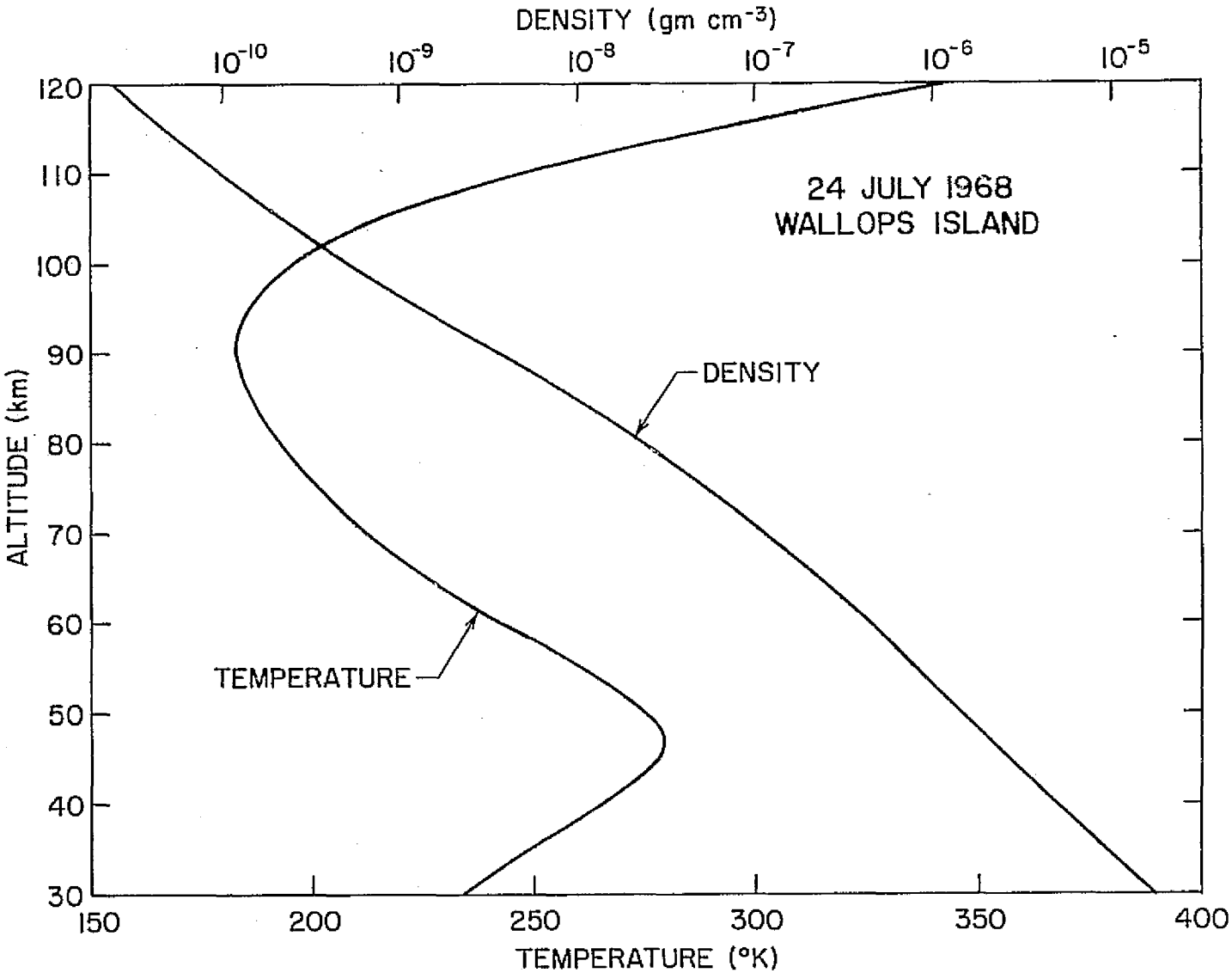

Figure 2.1 The temperature and density profiles of the neutral atmosphere over Wallops Island on July 24, 1968. Values up to 90 km are based on rocket measurements by *Smith et al.* [1970] and above 90 km, on empirical formulas given by *Jacchia* [1971].

a wavelength λ is given by

$$\delta J_i(z,\lambda) = I(\lambda,\Delta\lambda,z)\ \sigma_i(\lambda), \tag{2.1}$$

where $I(\lambda,\Delta\lambda,z)$ is the intensity of solar radiation at the altitude z and wavelength λ taken over the wavelength interval $\Delta\lambda$, and $\sigma_i(\lambda)$ is the absorption cross section of the ith constituent at the wavelength λ.

The intensity of solar radiation remaining at a given height depends on the amount absorbed by the column of air above that height measured along the ray path, and is given by

$$I(\lambda,\Delta\lambda,z) = I_o(\lambda,\Delta\lambda)\ \exp(-\tau(\chi,z)) \tag{2.2}$$

where $I_o(\lambda,\Delta\lambda)$ is the solar radiation flux integrated over the wavelength interval $\Delta\lambda$ incident on top of the atmosphere, and $\tau(\chi,z)$ is the optical depth factor.

The ability of the solar radiation to penetrate the atmosphere for different wavelengths is expressed in terms of the unit optical depth, defined as the altitude where the optical depth factor is unity. It follows from equation (2.2) that at this altitude, the fractional attenuation of the incident radiation is equal to $1/e$. Figure 2.2 illustrates the penetration depths for radiation incident normally on the atmosphere, as a function of the wavelength up to 3200 Å. It is seen from this curve that wavelengths above 1000 Å could reach heights below 120 km. Between 1800 and 2000 Å, there is a sharp drop in the optical depth, from a height of 80 km to 40 km. This wavelength interval corresponds to the Schumann-Runge bands in the O_2 absorption spectrum. Beyond 2000 Å up to about

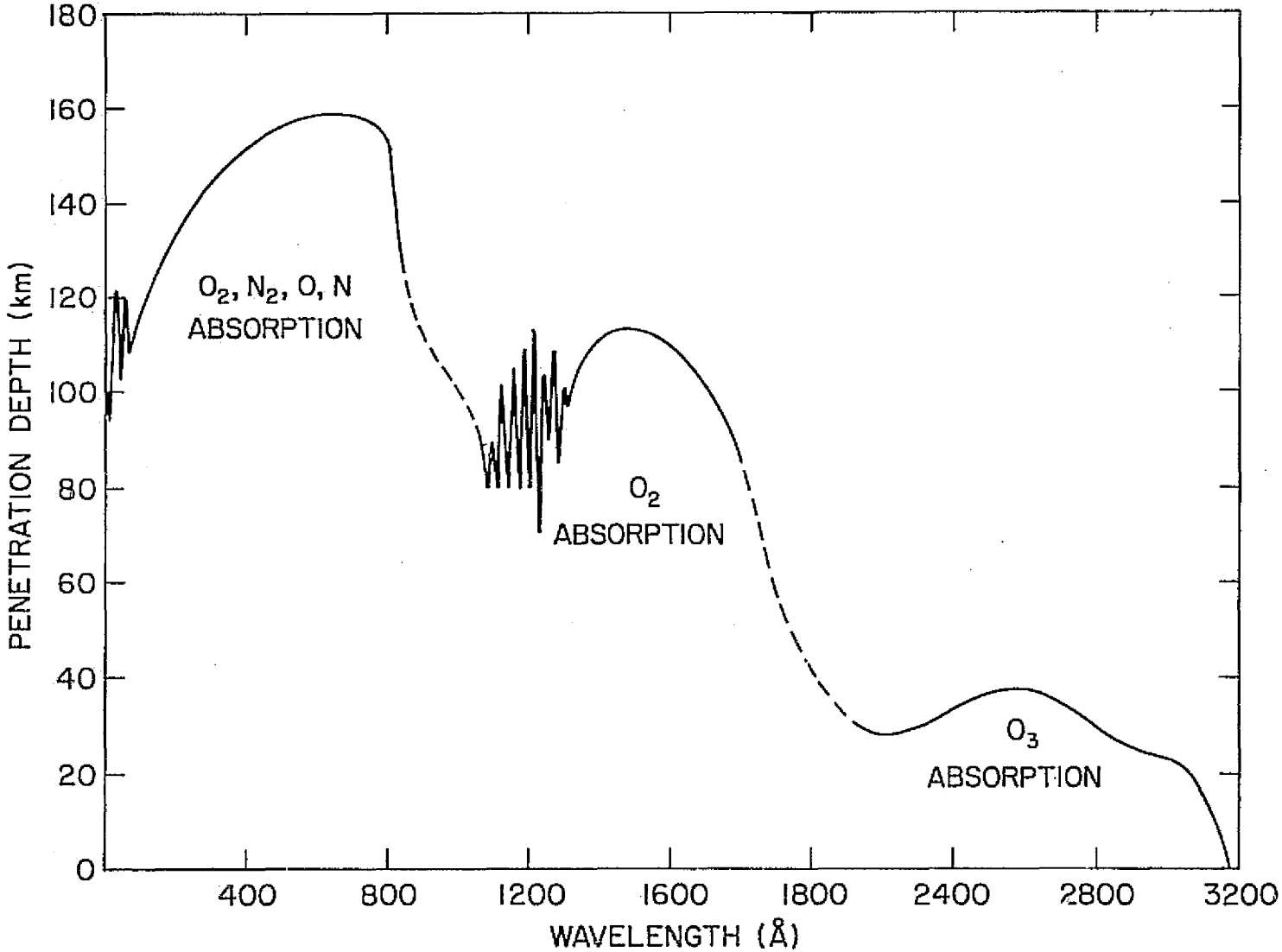

Figure 2.2 The penetration depths of solar radiation incident normally on the atmosphere. 63% of the incident energy in a given wavelength interval is lost above the altitude shown.

3000 Å, the penetration depth lies more or less constant in the 30-40 km interval. By comparing this curve with the absorption spectra of oxygen and ozone, it becomes apparent that the penetration of wavelengths below about 2000 Å is controlled by absorption due to oxygen, while ozone absorption controls the penetration of longer wavelengths.

In determining the optical depth factor, it is therefore necessary to consider only the absorption by oxygen and ozone. It is calculated using the formula

$$\tau(\chi,z) = \left\{\sigma_{O_2}(\lambda) \int_z^\infty [O_2]dz + \sigma_{O_3}(\lambda)\int_z^\infty [O_3]dz\right\}\sec\chi \tag{2.3}$$

where $[O_2]$ is the number density of oxygen, and

$[O_3]$ is the number density of ozone.

The photodissociation coefficient, J_i is obtained by summing up the energy absorbed over the entire spectrum effective in dissociating the given constituent, and is given by

$$J_i(\chi,z) = \sum_\lambda I_o(\lambda,\Delta\lambda)\ \sigma_i(\lambda)\ \exp(-\tau(\chi,z)) \tag{2.4}$$

The height dependence of J_i is determined solely by the optical depth factor. For small values of τ, it is almost independent of the height. In calculating the optical depth factor for wavelengths where absorption by ozone is important, it is necessary to assume initially the height distribution of this gas. The adopted distribution, which is based on direct observations, is given by

$$[O_3] = 10^{16-z/10} \tag{2.5}$$

for heights above 30 km.

2.2.1 *Solar radiation in the 1000-4000 Å region.* The ranges of wavelength that are of interest in photodissociation studies of the neutral constituents lies between 1000 and 4000 Å. This is mainly a continuous spectrum, being of thermal origin, except for the lines that appear towards the 1000 Å end. Of these, the more intense lines are the Lyman-β at 1025.7 Å and Lyman-α at 1215.7 Å. However, for the purpose of calculating the photodissociation rates, only the latter is of importance. This line has been under investigation over several years, and it has been observed that it is a fairly stable line, with the intensity variation at most of the order of 1.5 between the solar maximum and minimum [*Weeks*, 1967]. The intensity of this line has also been measured using satellite-borne instruments in the recent past. *Timothy and Timothy* [1970] have measured the intensity variations of both the Hydrogen I Lyman-α (1215.7 Å) and Helium 2 Lyman-α (304 Å) lines from 1967 to 1969. The intensity of 1215.7 Å lines measured on July 24, 1968, the day that is of interest here, is 3.7×10^{11} photons cm^{-2} sec^{-1}. The average for the whole period is 3.6×10^{11} photons cm^{-2} sec^{-1}. This value, however, is slightly higher than 3×10^{11} photons cm^{-2} sec^{-1}, the value reported by *Vidal-Madjar et al.* [1973] as the average for the years 1969 and 1970, monitored on board the OSO 5.

The flux values used in the region 1027-1310 Å are those recommended by *Hinteregger* [1970] for medium solar activity. This region includes a few *Si* and O lines and a continuum which contains about 1/5 the total energy (excluding the Lyman-α line) in the band.

The fluxes between 1300 and 2000 Å used in aeronomical calculations in the past were taken from the observations of *Detwiler et al.* [1961]. Recent measurements of the spectrum between 1400 and 1875 Å using photoelectric instruments, carried out on 1968 September 24 (10.7 cm flux =

143 units) by *Parkinson and Reeves* [1969], however, give values much less, about 1/3 to 1/5 of those reported by Detwiler et al. Considering the reliability of the experimental technique employed by Parkinson and Reeves, *Hinteregger* [1970] suggests that the values quoted by Detwiler et al. for the above range of wavelengths should be scaled down by a factor of 3. In the present calculations, therefore, this correction was applied over most of this region. Towards the two ends, this factor was made to reduce gradually down to unity in order to join smoothly with the rest of the spectrum.

The region between 2000 and 4000 Å was measured by *Tousey* [1963] as early as 1960, the intensities measured being averages over 50 Å intervals from 2000 to 2600 Å, and over 100 Å intervals from 2600 to 4000 Å. More recent measurements of *Bonnet* [1968] generally agree with Tousey's measurements. Slight disagreement over small wavelength intervals could be attributed to averaging effects by the measuring instruments. The spectral distribution expressed in photons cm^{-2} sec^{-1} $Å^{-1}$ over the entire region 1000-4000 Å, adopted in the present calculations, is shown in Figure 2.3.

2.2.2 *Absorption cross sections.* The absorption cross section of a constituent, which is a function of the wavelength, gives a measure of the radiation absorbed by the constituent resulting in its dissociation. In general, the absorption of energy need not necessarily give rise to dissociation; instead the molecule which absorbs the energy could be raised to a higher excitation level. However, in the present work, it is assumed that the absorption of energy by a molecule results only in its dissociation.

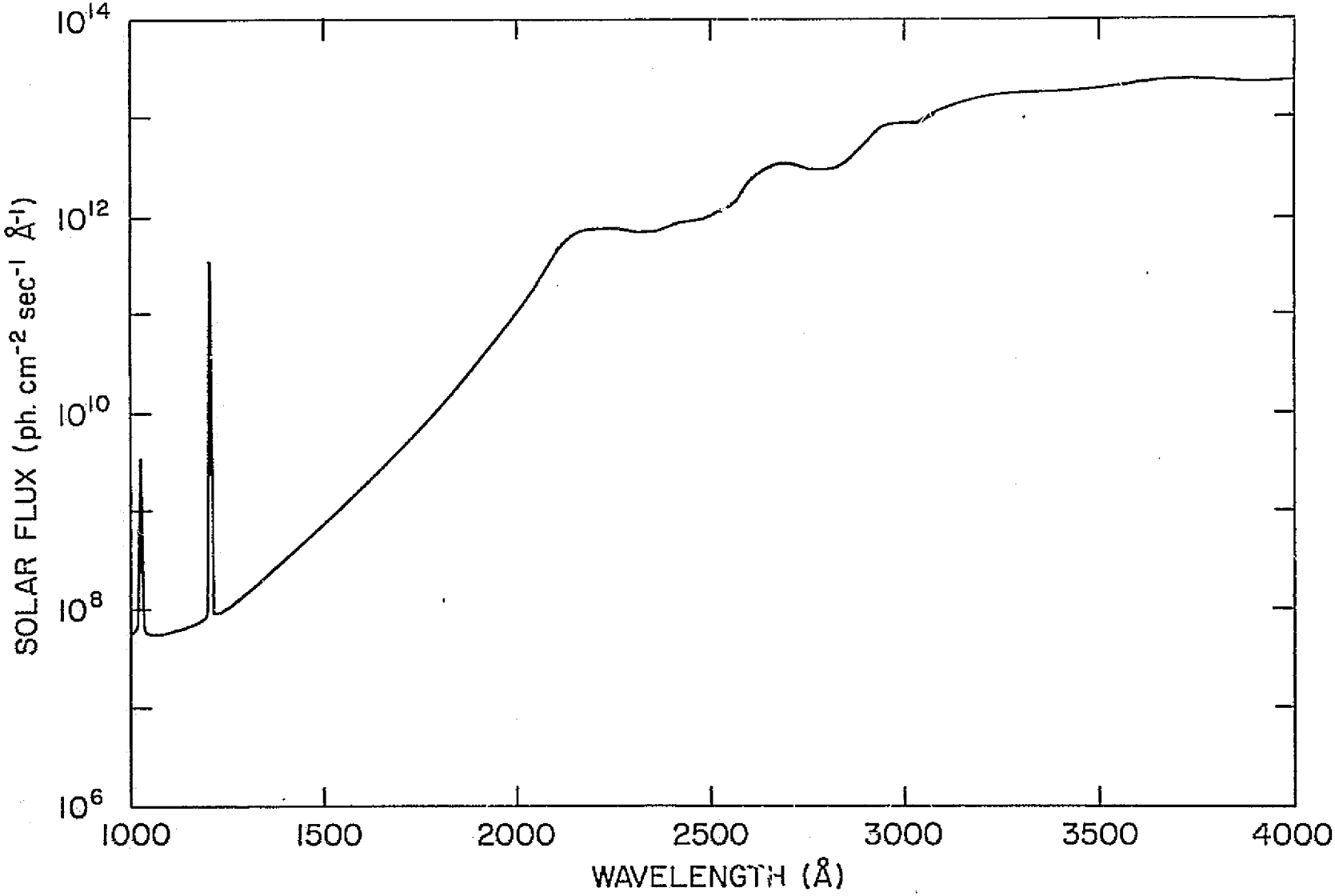

Figure 2.3 The solar spectrum between 1000 and 4000 Å, based on the measurements by *Detwiler et al.* [1961], *Parkinson and Reeves* [1969] and *Tousey* [1963].

As mentioned previously, wavelengths below 2000 Å are absorbed mainly by oxygen while wavelengths above are absorbed by ozone. Hence, the absorption cross sections of these two constituents control the photodissociation coefficients of all constituents, and their values adopted in this study are illustrated in Figure 2.4. Of the wavelengths below 1300 Å, only the window at the Lyman-α wavelength is of importance. The presence of this atmospheric window allows the strong Lyman-α radiation to reach *D*-region heights resulting in the photoionization of NO, which is the major source of *D*-region ionization. This line is also important in the photodissociation of constituents such as H_2O and CH_4 which have large absorption cross sections around this wavelength. High resolution measurements of the absorption cross section of O_2 at the bottom of the window were carried out by *Ogawa* [1968]. He finds that the minimum of the transmission window, having a value 0.945×10^{-20} cm^2, lies at 1216.0 Å, while the value at the center of Lyman-α line is 1.05×10^{-20} cm^2. There fore, a value of 1.00×10^{-20} cm^2 is taken as the mean absorption cross section of oxygen at the Lyman-α line.

The cross sections for wavelengths in the Schumann-Runge continuum (1950-1750 Å) and up to 1900 Å were measured by *Watanabe et al.* [1953]. This region shows a peak between 1400 and 1500 Å, and a sharp continuous drop up to about 1750 Å. Beyond this wavelength, up to about 2000 Å, the spectrum consists of a large number of rotational bands (Schumann-Runge bands). The maxima of the rotational lines in each of the vibrational bands lying in the region 1760-1900 Å have been measured by *Ackerman et al.* [1969]. The continuum (Herzberg continuum) in the 1850-2600 Å interval, underlying the Schumann-Runge bands, has been measured by

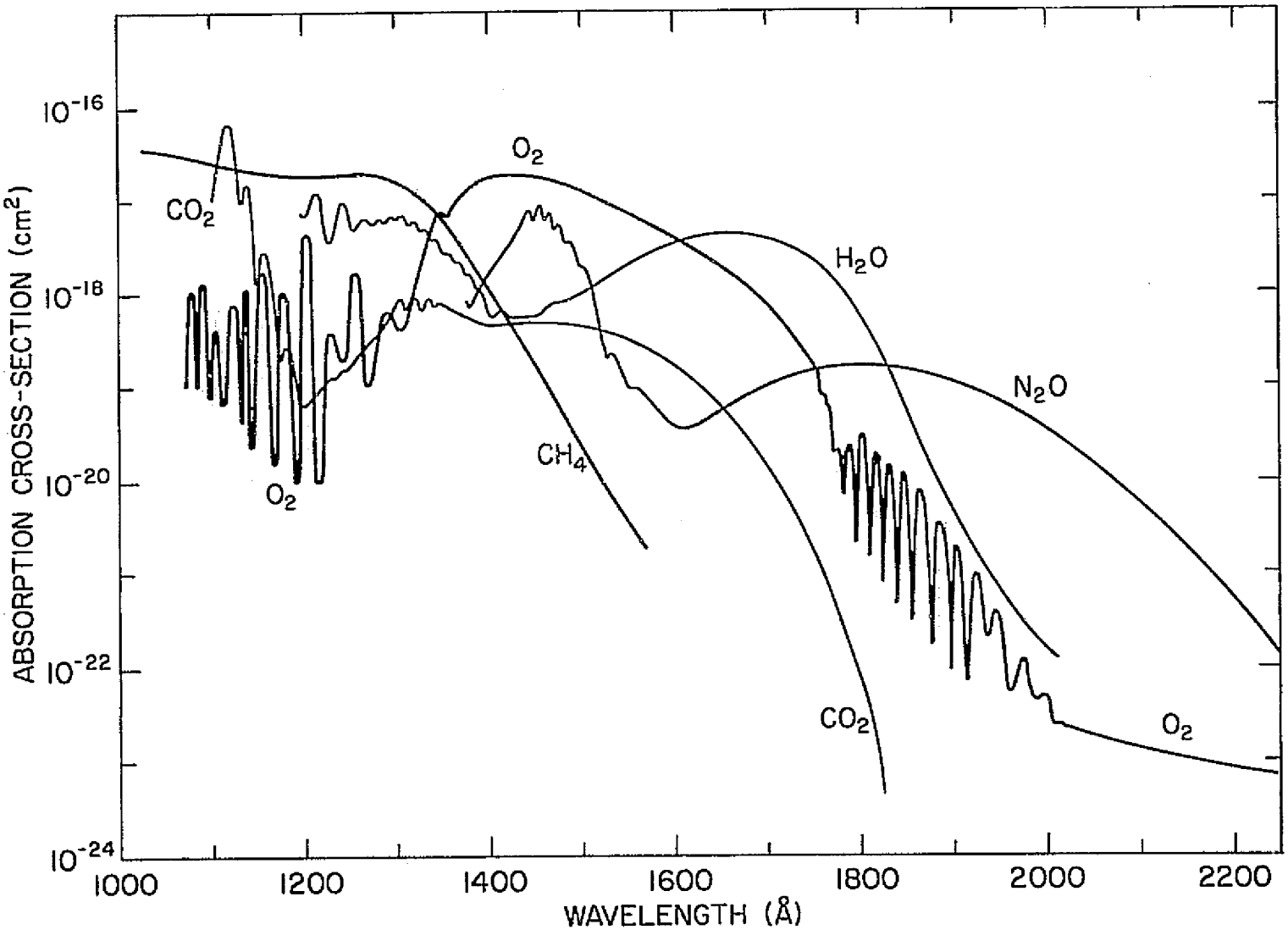

Figure 2.4 Absorption cross sections of neutral constituents having relatively high dissociation energies.

Ogawa [1971], and it is found that this continuum lies more than 100 times below the peak values reported by Ackerman et al. In spite of these measurements, a proper knowledge regarding the detailed structure of these bands is still lacking, and this has caused much uncertainty is estimating the extent of penetration of solar radiation down to lower mesospheric heights. Even if such measurements are available, the calculation of the contributions due to radiation penetrating through each of these windows would be a difficult exercise in view of their fine structure.

To get over this problem, *Hudson et al.* [1969] measured the transmission factor for radiation of different wavelength bands passing through a column of oxygen. These results can be conveniently used to calculate the photodissociation rates in the corresponding wavelength bands. Molecular oxygen actually undergoes predissociation at these wavelengths, and the photodissociation coefficients of O_2 include the contributions from this effect.

The absorption cross section of many of the constituents, with the exception of O_3, NO_2, HO_2, H_2O_2 and HNO_3 fall off below 2000 Å. For these constituents the photodissociation coefficients are controlled solely by O_2 absorption, and their values vanish off before reaching lower heights. Since the solar fluxes below 2000 Å are much less than those in the higher wavelengths, the photodissociation coefficients of these constituents generally have small values even at zero optical depths.

For the constituents mentioned above, however, the large flux above 2000 Å, and the smaller attenuation due to ozone absorption result in higher photodissociation coefficients. Further, they maintain almost constant values down to about 50-40 km, where they begin to get attenuated

due to the presence of the ozone layer. In fact, the second term in equation (2.3) is important only for these constituents.

The ozone absorption spectrum is illustrated in Figure 2.5. Values between 1100 and 2000 Å are taken from *Tanaka et al.* [1953], and for the region above 2000 Å, values are taken from *Inn and Tanaka* [1959]. The ozone spectrum exhibits a peak in the Hartley continuum near 2600 Å. Above 3000 Å, the cross section decreases with the wavelength allowing the wavelengths in near ultraviolet and visible regions to reach the ground.

The photodissociation of H_2O is most important in the chemistry of O-H constituents, and also in estimating the residual H_2O in the mesosphere. The cross sections used for H_2O are taken from *Watanabe and Zelikoff* [1953] and *Thompson et al.* [1963]. In the SR continuum, this curve reaches a peak near 1650 Å, and drops off rapidly beyond about 1800 Å. Since large values of σ_{H_2O} occur in the region of SR bands, any errors in estimating the penetration depth of the solar radiation at these wavelengths could cause a certain amount of uncertainty in the corresponding photodissociation coefficients. *Anderson* [1971a] calculated the photodissociation coefficients of H_2O using the transmission factors determined by *Hudson et al.* [1969]. The values obtained by him are about a factor of 10 higher than the values given by conventional data for similar solar zenith angles at 60 km. In the present work, the cross-section curve over the SR bands was modified to give H_2O dissociation rates close to those obtained by Anderson.

Of the other O-H constituents, both HO_2 and H_2O_2 can get photodissociated producing OH molecules. Due to non-availability of absorption data for HO_2, it has been customary in the past to assume the same values for HO_2 cross sections as those measured for H_2O_2. However, recent measurements of the absorption cross sections of HO_2 by *Paukert and Johnston*

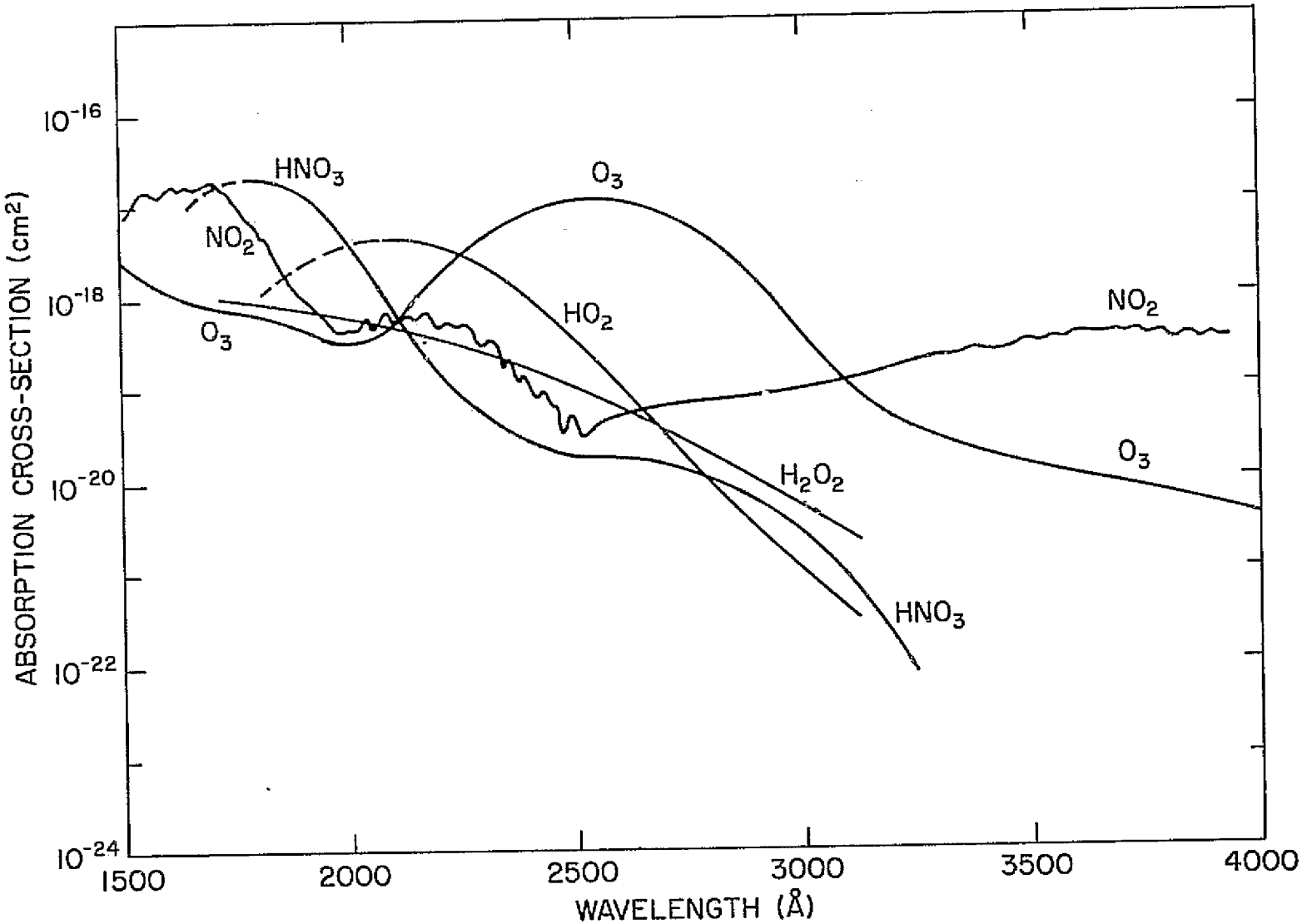

Figure 2.5 Absorption cross sections of neutral constituents having relatively low dissociation energies.

[1972] have enabled independent calculation of the photodissociation rates for this constituent. These new data give photodissociation rates about six times higher than those of H_2O_2 at zero optical depth. The data used for H_2O_2 are those quoted by Paukert and Johnston.

Cross sections used for NO_2 are taken from the work of *Nakayama et al.* [1959] for wavelengths between 1080 and 2700 Å, while the values of *Hall and Blacet* [1952] are used for higher wavelengths. In the case of N_2O, absorption cross sections measured over the region 1080-2100 Å by *Zelikoff et al.* [1953], and values quoted by *Bates and Hays* [1967] for higher wavelengths are adopted. The absorption spectrum of NO_2 maintains a high value even above 2000 Å, while the N_2O spectrum falls off rapidly after reaching its peak near 1800 Å. Consequently, the photodissociation rates of NO_2 are generally much higher than those of N_2O. Cross sections used for HNO_3 are taken from the recent work of *Johnston and Graham* [1973].

Recently *Strobel* [1971b] suggested that $\delta(0,0)$, $\delta(1,0)$ and $\delta(1,0)$ bands, among others, could produce predissociation of NO in the mesosphere. The dissociation coefficients due to these three bands are also included in the present work, assuming an average value for the absorption cross section of O_2 at the corresponding wavelengths.

For CO_2, cross sections measured by *Nakata et al.* [1965] and *Thompson et al.* [1963], and for CH_4, values reported by *Okabe and Becker* [1963] are adopted. In both of these, cross section profiles are important at wavelengths below 1800 Å only, and hence, their photodissociation rates are respectively small.

The complete set of absorption cross sections used in the present work are shown in Figures 2.4 and 2.5.

2.2.3 *Solar variation of photodissociation coefficients.* The entire photochemistry of the upper atmosphere rests on the photodissociation of its constituents. The rates of production, as well as the loss of certain constituents are solely governed by their photodissociation processes. The diurnal behavior of these constituents could, therefore, be expected to have a strong dependence on the solar variation of the respective photodissociation coefficients.

In certain constituents such as O_2 and O_3, different regions of the spectrum yield different species. These have different chemical properties, and therefore, to evaluate their yields separately the photodissociation coefficients over these different spectral regions have been determined separately. The complete list of the photodissociative reactions is given in Table 2.2. The calculated coefficients for both $\chi = 18°$ and $60°$ are illustrated in Figures 2.6 and 2.7.

For heights where the optical depth factor is small, the photodissociation coefficients are independent of both the height and the solar zenith angle. Towards the end of the penetration depth, the dissociation curves tail off as the exponential term in equation (2.1) takes large values. It is only at these heights that the effect of solar zenith angle and the O_2 column density become prominent on the photodissociation values. As the zenith angle increases from 18° to 60°, the tail in the dissociation curves can get lifted by about 4-5 km, while the values decrease by more than an order of magnitude. However, the role played by the dissociation coefficients become less important as their values drop off. Thus, it is really a limited height interval over which the solar variation begins to show up in the chemistry of the constituents.

Exceptions to this behavior are the O_2 and H_2O dissociation coefficients. These two curves are composed of contributions made by different

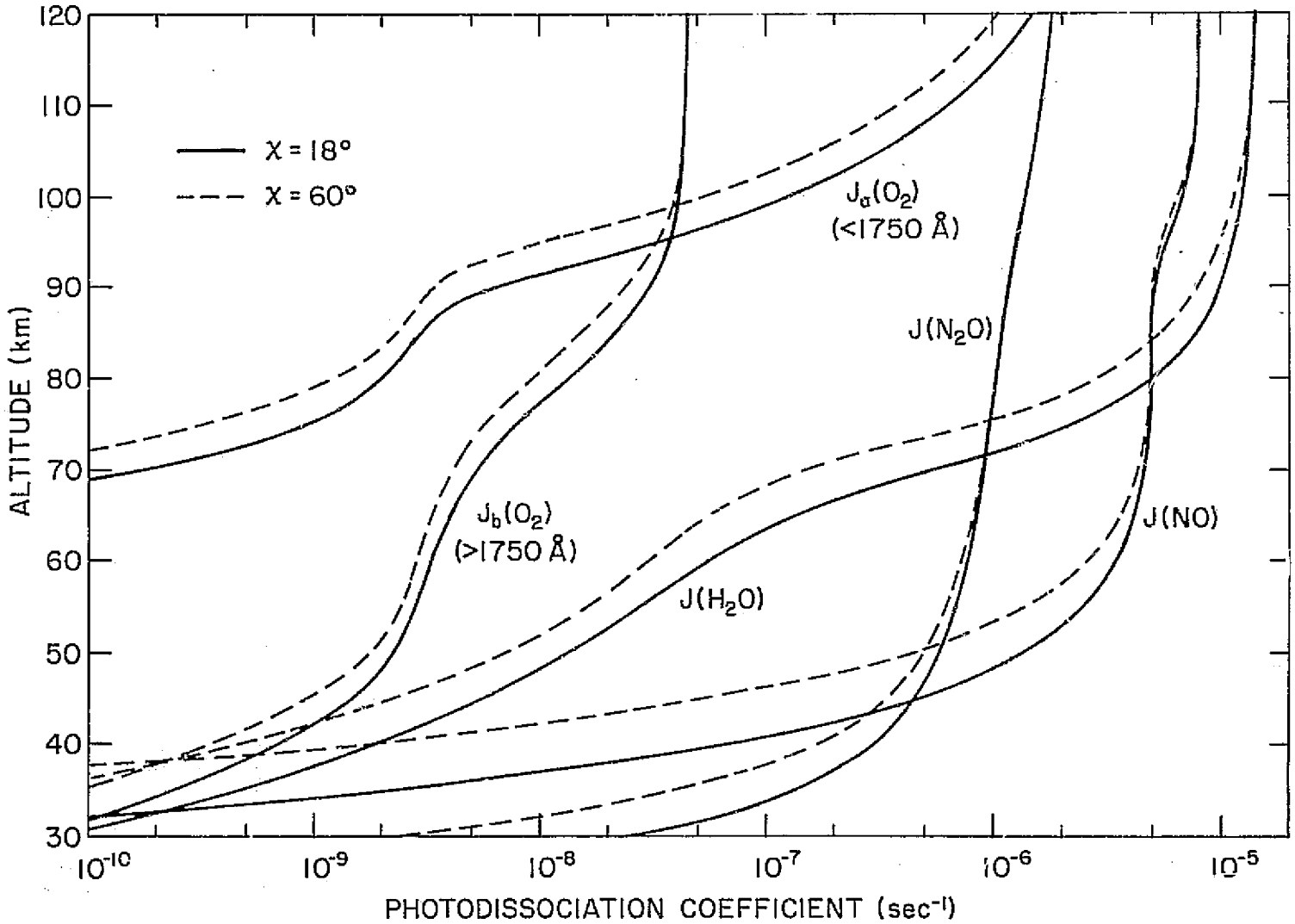

Figure 2.6 Photodissociation coefficients of neutral constituents having high dissociation energies, for solar zenith angles 18° and 60°.

Table 2.2

Photodissociation reactions.

J_{1a}	$O_2 + h\nu \rightarrow O(^1D) + O(^3P)$	$\lambda < 1750$ Å
J_{1b}	$O_2 + h\nu \rightarrow O(^3P) + O(^3P)$	1750 Å $< \lambda <$ 2400 Å
J_{3a}	$O_3 + h\nu \rightarrow O_2(^1\Delta_g) + O(^1D)$	$\lambda < 2660$ Å
J_{3b}	$O_3 + h\nu \rightarrow O_2(^1\Delta_g) + O(^1D)$	2600 Å $< \lambda <$ 3100 Å
J_{3c}	$O_3 + h\nu \rightarrow O_2 + O(^3P)$	3100 Å $< \lambda$
J_4	$NO_2 + h\nu \rightarrow NO + O$	$\lambda < 3975$ Å
J_5	$N_2O + h\nu \rightarrow N_2 + O(^1D)$	$\lambda < 3370$ Å
J_6	$NO + h\nu \rightarrow N + O$	
J_7	$H_2O + h\nu \rightarrow OH + H$	$\lambda < 2350$ Å
J_8	$HO_2 + h\nu \rightarrow OH + O$	
J_9	$H_2O_2 + h\nu \rightarrow OH + OH$	
J_{10}	$HNO_3 + h\nu \rightarrow OH + NO_2$	
J_{11}	$CO_2 + h\nu \rightarrow CO + O(^1D)$	$\lambda < 1700$ Å
J_{12}	$CH_4 + h\nu \rightarrow CH_2 + H_2$	

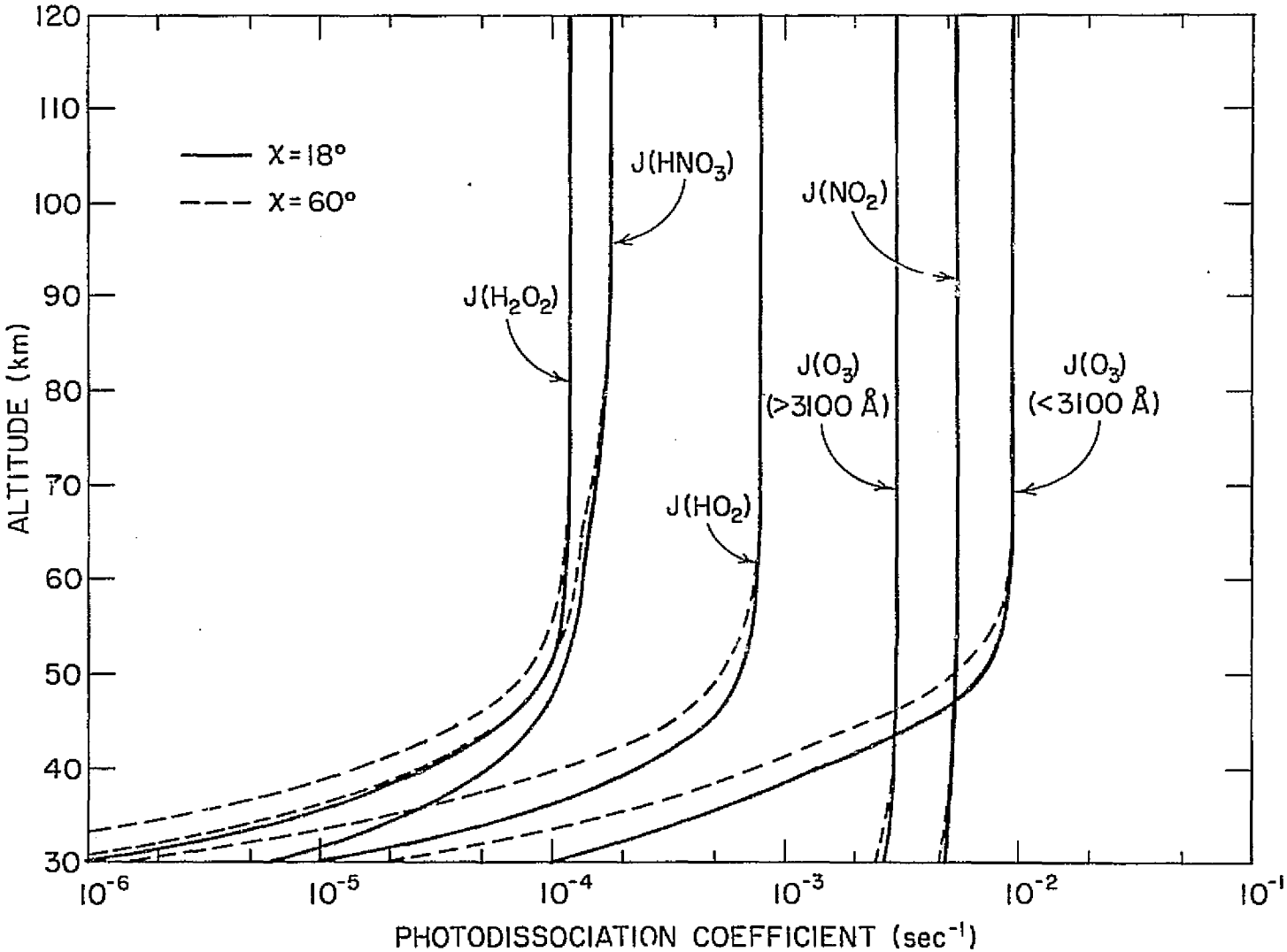

Figure 2.7 Photodissociation coefficients of neutral constituents having low dissociation energies, for solar zenith angles 18° and 60°.

regions of the respective spectra. Each component has a different penetration depth and when one takes the sum, the height over which the solar variation occurs is extended.

It should be noted that any variation of the O_2 column density can cause the dissociation coefficients to vary in a manner similar to that caused by the zenith angle variation. Hence, in the time-dependent calculations, the dissociation coefficient at time t was computed by taking O_2 column densities evaluated at the previous time step, $(t-\Delta t)$. At zenith angles greater than 75°, the sec χ term in equation (2.2) was replaced by the Chapman function, $Ch(\chi)$.

2.3 *Reactions of Oxygen Constituents*

The problem of the production of atomic oxygen in the upper atmosphere has been the topic of several investigators [*Nicolet and Mange*, 1954; *Colegrove et al.* 1965; *Shimazaki*, 1967]. The production of the atomic oxygen species, as well as ozone, is a consequence of the photodissociation of O_2. The energy absorbed in the Schumann-Runge continuum results in the formation of one atom in the ground state $O(^3P)$, and the other in the metastable state $O(^1D)$, out of one molecule of oxygen. Wavelengths above 1750 Å, produce both atoms in the ground state. The shorter wavelengths do not penetrate to lower heights, and therefore, the direct production of the metastable species from O_2 is restricted to higher altitudes, generally above 80 km. The metastable atoms thus formed undergo quenching reactions with N_2 and O_2 making them to attain ground-state energies, according to

$$O(^1D) + N_2 \rightarrow O(^3P) + N_2$$

$$O(^1D) + O_2 \rightarrow O(^3P) + O_2$$

The oxygen atoms recombine with each other and with O_2 in the presence of a third body to give metastable $O_2(^1\Delta_g)$ and O_3, respectively, according to

$$O + O + M \rightarrow O_2(^1\Delta_g) + M,$$

$$O + O_2 + M \rightarrow O_3 + M$$

The metastable $O_2(^1\Delta_g)$ gets converted to ground level O_2 in the quenching reactions,

$$O_2(^1\Delta_g) + N_2 \rightarrow O_2 + N_2,$$

$$O_2(^1\Delta_g) + O_2 \rightarrow O_2 + O_2,$$

and also through the spontaneous emission

$$O_2(^1\Delta_g) \rightarrow O_2 + h\nu.$$

Ozone, through photodissociation, yields both ground-state and excited-state molecular and atomic oxygen (Table 2.2). As the photodissociation coefficients of O_3 extend to lower heights, these processes become the major sources of the atomic species and $O_2(^1\Delta_g)$ in the lower mesosphere and the stratosphere.

The list of the reactions used in the present calculations is given in Table 2.3, along with the adopted rate constants. Many of these reactions have been reviewed by *Schiff* [1969, 1972]. In reactions involving atomic oxygen, quantitative measurements are generally difficult to make because of the errors that creep in due to wall effects. Most of the measurements of the rate constant of Reaction 1 have been made at high temperatures where the temperature dependence is found to be T^{-1}. However,

Table 2.3

Oxygen reactions.

Reaction No.	Reaction	Rate Constant $cm^n\ sec^{-1*}$
R_1	$O + O + M \rightarrow O_2(^1\Delta_g) + M$	$^+3.0(-33)\ (T/300)^{-2.9}$ *Campbell and Thrush* [1967]
R_2	$O + O_2 + M \rightarrow O_3 + M$	$6.57(-35)\ \exp(1.01/RT)$ *Huie et al.* [1972]
R_3	$O + O_3 \rightarrow O_2 + O_2\ (^1\Delta_g)$	$1.05(-11)\ \exp(-4.31/RT)$ *McCrumb and Kaufman* [1972]
R_4	$O_2(^1\Delta_g) + N_2 \rightarrow O_2 + N_2$	4.0(-19) *Zipf* [1969]
R_5	$O_2(^1\Delta_g) + O_2 \rightarrow O_2 + O_2$	$2.22(-18)\ (T/300)^{0.78}$ *Findlay and Snelling* [1971]
R_6	$O_2(^1\Delta_g) \rightarrow O_2 + h\nu$	2.6(-4) *Badger et al.* [1965]
R_7	$O(^1D) + O_2 \rightarrow O + O_2$	5.5(-11) *Schiff* [1972]
R_8	$O(^1D) + N_2 \rightarrow O + N_2$	5.0(-11) *Schiff* [1972]
R_9	$O(^1D) + O_2 \rightarrow O + O_2(^1\Delta_g)$	1.0(-12) *Vallance-Jones and Gattinger* [1963]
R_{10}	$O(^1D) + O_3 \rightarrow O_2 + O_2$	3.0(-10) *Schiff* [1969]

*n = 3 for binary reactions, and 6 for 3-body reactions

+Read a(-n) as a x 10^{-n}

at temperatures below 350 K, the temperature dependence was found to be nearly T^{-3}. At *D*-region heights, therefore, this reaction is relatively unimportant. In his latest review, *Schiff* [1972] has recommended the value 1.2 (-35) exp(2.1/RT) for the rate constant of Reaction 2 (Table 2.3). In this work, however, a more recent measurement [*Huie et al.*, 1972] has been adopted. This reaction is different from many other 3-body reactions in that it has a negative activation energy. It also happens to be the main source of O_3 in the upper atmosphere, and therefore plays an important role in aeronomical studies.

The binary reaction between $O(^3P)$ and O_3 (Reaction 3; Table 2.3) begins to dominate as a loss process for O_3, when losses due to direct photodissociation are absent. The value for its rate constant is taken from the recent work of *McCrumb and Kaufman* [1972]. This value agrees well with the results of *Krazenski et al.* [1971] within experimental errors. It is, however, smaller by nearly a factor of 2 than the values deduced by previous workers [*Schiff*, 1969]. The rest of the reactions given in Table 2.3 are all concerned with the excited species, $O_2(^1\Delta_g)$ and $O(^1D)$ which are produced in the photodissociation of O_2 and O_3, and also through Reactions 1 and 3. Their loss mechanism is mainly through quenching by N_2 and O_2, and the corresponding rates have been adopted from the reviews of *Zipf* [1969] and *Schiff* [1972].

2.4 *Oxygen-Hydrogen Reactions*

Bates and Nicolet [1950] first introduced the oxygen-hydrogen reactions into the upper atmosphere photochemical models. In their work, the presence of various O-H products in the mesosphere was hypothesized in order to explain the OH airglow emissions observed to originate in the mesosphere. However, many of the parameters that went into the calculation

of the distribution of the species were not known at that time. Hence their results were rather of a qualitative nature. A more detailed calculation of the behavior of the O-H products and their influence on the ozone distribution was carried out by *Hunt* [1966]. He also included non-equilibrium conditions in his calculations. *Hesstvedt* [1968] extended these studies by introducing the effects of vertical eddy transport on the distribution of the minor neutral species at mesospheric and lower thermospheric heights. More recent studies of this subject which include the solution of a system of time-dependent continuity equations having transport terms were carried out by *Shimazaki and Laird* [1970], *Hunt* [1971b] and *Thomas and Bowman* [1972].

The basic process responsible for the production of O-H constituents in the upper atmosphere is the photodissociation and oxidation of water vapor which is assumed to be constantly transported into the stratosphere from the troposphere. The exact mechanism of this transport through the tropopause is not well understood. It is expected that the tropopause with temperatures below the freezing point would act as a barrier for any transport of water vapor through it. The water vapor that is carried to the stratosphere and above is subject to photochemical loss processes; its dissociation by solar radiation, and oxidation by $O(^1D)$, according to

$$H_2O + h\nu \rightarrow H + OH$$

$$H_2O + O(^1D) \rightarrow OH + OH.$$

In the stratosphere where the photodissociation coefficients are small, the main loss process is the oxidation reaction.

The by-products of the H_2O dissociation and oxidation reactions, *viz.* OH and H are highly chemically active species. In the presence of ozone

and atomic oxygen, these constituents participate in catalytic reactions, giving rise to other O-H products such as HO_2 and H_2O_2, and also to molecular hydrogen, H_2. The two reactions

$$O(^3P) + OH \rightarrow H + O_2$$

$$H + O_3 \rightarrow OH + O_2$$

both of which have high rate constants greater than 10^{-11} cm^3 sec^{-1} [*Kaufman*, 1969], however, do not yield any new constituents. They merely interchange OH and H while converting $O(^3P)$ and O_3 into molecular oxygen. Nevertheless, they are important as loss processes for $O(^3P)$ and O_3.

The main sources of HO_2 are the reactions

$$O(^3P) + OH + M \rightarrow HO_2 + M,$$

$$H + O_3 \rightarrow HO_2 + O(^3P).$$

Many workers in the past have also included the reaction

$$OH + O_3 \rightarrow HO_2 + O_2$$

as a possible source of HO_2. However, *Schiff* [1972] has cautioned against using this reaction as no direct evidence for its occurrence with the ground-state OH is available. The HO_2 thus formed undergoes fast reactions with $O(^3P)$ and H destroying it to produce OH according to

$$HO_2 + O(^3P) \rightarrow OH + O_2$$

$$HO_2 + H \rightarrow OH + OH,$$

respectively. Another reaction that has been postulated as converting HO_2 back to OH is

$$HO_2 + O_3 \rightarrow OH + 2O_2$$

According to *Schiff* [1972], this again has to be dismissed as no direct evidence is available for its occurrence. It is seen now that the production and loss of both OH and HO_2 are closely linked with the chemistry of $O(^3P)$ and O_3.

Reactions between two HO_2 molecules result in the production of a single H_2O_2 molecule, according to

$$HO_2 + HO_2 \rightarrow H_2O_2 + O_2$$

while the loss of H_2O_2 is governed by its reactions with $O(^3P)$ and OH:

$$H_2O_2 + O(^3P) \rightarrow OH + HO_2$$

$$H_2O_2 + OH \rightarrow H_2O + HO_2$$

While breaking up H_2O_2, these reactions reproduce OH, HO_2 and also H_2O.

The molecular hydrogen, H_2 is produced as a result of the reduction of OH, HO_2 and H_2O_2 by atomic hydrogen, according to

$$H + OH \rightarrow H_2 + O,$$

$$H + HO_2 \rightarrow H_2 + O_2,$$

$$H + H_2O_2 \rightarrow H_2 + HO_2.$$

Several reactions that take place between these newly formed O-H constituents result in the reformation of H_2O, the original source of all the O-H constituents. Some of these reactions are

$$OH + OH \rightarrow H_2O + O,$$

$$OH + HO_2 \rightarrow H_2O + O_2,$$

$$OH + H_2O_2 \rightarrow H_2O + HO_2.$$

In addition to the above reactions, a large number of other reactions involving the hydrogen species take place at relatively slow rates. These reactions, however, can become important at certain heights and hours of the day when the concentrations of the constituents in the above-mentioned reactions drop to insignificant values. Such instances occur during the night time when both the $O(^3P)$ and H concentrations below about 60 km decrease by several orders of magnitude from the values occurring in the daytime.

The complete list of reactions involving O-H species, along with their rate constants is given in Table 2.4. Many of these reactions and the available data on the rate constants has been reviewed by *Kaufman* [1964, 1969], and *Schofield* [1967]. For some of the fast reactions including HO_2 (Reactions 21, 23, 24, and 25) only the lower limits of the rate constants have been estimated in these reviews, and these have been used by all investigators in the past. For two of these reactions (Reactions 21 and 24), improved estimates have been made recently by *Hochanadel et al.* [1972], and these have been adopted in this study. For the other two reactions, lower limits given by *Kaufman* [1964] have been used. However, for the production of OH, as well as for the loss of H and HO_2, the role played by these reactions is of minor importance. Hence any errors in these rate constants are not expected to influence the results of the present computations to any great extent.

Table 2.4

Oxygen-hydrogen reactions.

Reaction No.	Reaction	Rate Constant $cm^n\ sec^{-1}$*
R_{11}	$H + O_2 + M \rightarrow HO_2 + M$	+3.0(-32) $(273/T)^{1.3}$ *Schofield* [1967]
R_{12}	$H + H + M \rightarrow H_2 + M$	1.2(-32) $(273/T)^{0.7}$ *Kaufman* [1969]
R_{13}	$H + O_3 \rightarrow OH + O_2$	2.6(-11) *Kaufman* [1969]
R_{14}	$H_2 + O \rightarrow OH + H$	7.0(-11) exp(-10.2/RT) *Kaufman* [1969]
R_{15}	$H_2 + O(^1D) \rightarrow OH + H$	7.5(-11) *de More* [1967]
R_{16}	$H_2O + O(^1D) \rightarrow OH + OH$	3.5(-10) *Schiff* [1972]
R_{17}	$OH + O \rightarrow H + O_2$	5.0(-11) *Kaufman* [1969]
R_{18}	$OH + O_3 \rightarrow HO_2 + O_2$	See Text
R_{19}	$OH + OH \rightarrow H_2O + O$	2.7(-12) *Hochanadel et al.* [1972]
R_{20}	$OH + H + M \rightarrow H_2O + M$	2.5(-31) *Kaufman* [1964]
R_{21}	$HO_2 + O \rightarrow OH + O_2$	6.6(-11) *Hochanadel et al.* [1972]
R_{22}	$HO_2 + O_3 \rightarrow OH + 2\ O_2$	See Text
R_{23}	$HO_2 + OH \rightarrow H_2O + O_2$	2.0(-10) *Hochanadel et al.* [1972]
R_{24}	$HO_2 + H \rightarrow H_2 + O_2$	$\geq$ 3.0(-12) *Schofield* [1967]
R_{25}	$HO_2 + H \rightarrow OH + OH$	1.0(-11) *Schofield* [1967]
R_{26}	$HO_2 + HO_2 \rightarrow H_2O_2 + O_2$	6.0(-12) *Hochanadel et al.* [1972] *Paukert and Johnston* [1972]
R_{27}	$H_2 + OH \rightarrow H_2O + H$	6.3(-11) exp(-5.49/RT) *Kaufman* [1969]
R_{28}	$H_2O_2 + O \rightarrow OH + HO_2$	1.0(-15) *Foner and Hudson* [1962]
R_{29}	$H_2O_2 + H \rightarrow H_2 + HO_2$	1.2(-11) exp(-4.2/RT) *Kijewski and Troe* [1971]
R_{30}	$H_2O_2 + OH \rightarrow H_2O + HO_2$	4.0(-13) *Foner and Hudson* [1962]

*n = 3 for binary reactions, and 6 for 3-body reactions

+Read a(-n) as a x 10^{-n}

The rate constant for Reaction 26 (Table 2.4) has been estimated recently by *Hochanadel et al.* [1972]. The value quoted is the average of the two measured values. The reaction between OH and O_3 (Reaction 18) has been observed to take place only when the OH is in the vibrationally excited state, and the rate constants have been measured for the states $\nu = 2$ to $\nu = 9$ [*Coltharp et al.*, 1971]. This reaction becomes the major source of HO_2 at nighttime when both $O(^3P)$ and H vanish at night below 80 km. Therefore, even a small value assumed for its rate constant can make a significant contribution towards the production of HO_2. Though such a value can be assigned to this reaction by extrapolating the measured values down to $\nu = 0$, this reaction has been left out from the calculations in view of the absence of direct evidence for its occurrence. For similar reasons, Reaction 22 (Table 2.4) has also been left out of the present calculations.

2.5 *Nitrogen Reactions*

The photochemistry of N-O reactions has been pursued in the past in view of the importance of NO in the formation of the *D* region [*Nicolet*, 1965; *Norton and Barth*, 1970; *Strobel et al.*, 1970; *Strobel*, 1971a, 1971b]. Nicolet, and also Norton and Barth, in their calculations included only the photochemical continuity equations. Identifying the weakness of these photochemical models, *Shimazaki and Laird* [1970], and *Strobel et al.* [1970] introduced diffusive transport terms into the continuity equations. Schimazaki and Laird's calculations are restricted to the chemistry of the neutral species only, while the work of Strobel et al. and Strobel is restricted only to the thermosphere and the mesosphere, respectively.

The chemically inert nature of N_2 make the photochemistry of N-O reactions somewhat different to that of O-H reactions. The absorption of ultraviolet radiation by N_2 is very little. Its atomic species, the ground-state $N(^4S)$ and the excited $N(^2D)$ are produced from N_2 through ionization by high energy EUV radiation and X-rays. Therefore, the photochemistry of these constituents should also include the ionic species, N_2^+, NO^+, and O_2^+. Most of the EUV radiation and X-rays do not penetrate below about 90 km, and hence the production of these atomic species and the subsequent formation of NO is restricted to altitudes above this level.

The ionization rates used in the calculation of production of ionic species N_2^+, O^+, O_2^+, and NO^+ will be discussed in detail in Chapter 4. The important reactions which produce the neutral atomic nitrogen species from the above ions are:

$$O^+ + N_2 \rightarrow NO^+ + N(^4S),$$

$$N_2^+ + O \rightarrow NO^+ + N(^4S),\ N(^2D),$$

$$NO^+ + e \rightarrow O + N(^4S),\ N(^2D),$$

$$N_2^+ + e \rightarrow N(^4S) + N(^4S).$$

In the reaction of N_2^+ with O and the recombination of NO^+, the formation of the excited state $N(^2D)$ is energetically possible. The yield of $N(^2D)$ from these two reactions has important consequences in the production of NO. The conversion of $N(^4S)$ to NO is effected through the reactions:

$$N(^4S) + O_2 \rightarrow NO + O,$$

$$N(^4S) + O_3 \rightarrow NO + O_2,$$

$$N(^4S) + O_2(^1\Delta_g) \rightarrow NO + O,$$

$$N(^4S) + O + M \rightarrow NO + M.$$

However, the largest contribution in the thermosphere comes from the reaction

$$N(^2D) + O_2 \rightarrow NO + O,$$

which has a rate constant of 6×10^{-12} cm^3 sec^{-1} [*Lin and Kaufman*, 1971], compared to 5×10^{-17} cm^3 sec^{-1} for the reaction between $N(^4S)$ and O_2. The problem here is that the exact yield of $N(^2D)$ in the above reactions is still not known accurately. *Strobel* [1971b] showed that a percentage branching ratio of 100 for the $N_2^+ + O$ reaction, and 75 for the NO^+ recombination reaction could give results in agreement with the observations of *Meira* [1971]. Strobel in his work has also included the production of $N(^2D)$ through the impact of fast electrons with N_2. However, the contribution of this process below 120 km is not very important, and hence it was neglected in this study. The predissociation of N_2 has also been suggested as a possible source of atomic nitrogen in the lower thermosphere. According to *Hudson and Carter* [1969], however, its yield of atomic nitrogen is small compared to other sources, and therefore, this process has not been included here.

While NO is produced from N in the thermosphere, reactions between the two also form major mutual loss processes for the two constituents:

$$NO + N \rightarrow N_2 + O.$$

Therefore, the abundance of NO in the lower thermosphere is strongly coupled to that of N.

In the lower regions the oxidation of N_2O by $O(^1D)$ can produce NO molecules as well as nitrogen molecules according to

$$N_2O + O(^1D) \rightarrow N_2 + O_2,$$
$$\rightarrow NO + NO.$$

Nicolet and Peetermans [1972] in their recent study of the stratospheric N_2O have assumed equal branching ratios for this reaction. The photodissociation of N_2O, having a dissociation energy of 38.5 kcal, is capable of producing N_2, $O(^1D)$, $O(^1S)$, $N(^2D)$ and NO, according to

$$N_2O + h\nu \rightarrow N_2 + O(^1D), \qquad \lambda < 3400 \text{ Å}$$
$$\rightarrow N_2 + O(^1S), \qquad \lambda < 2100 \text{ Å}$$
$$\rightarrow NO + N(^4S), \qquad \lambda < 2515 \text{ Å}$$
$$\rightarrow NO + N(^2D). \qquad \lambda < 1695 \text{ Å}$$

However, photolysis studies of N_2O carried out at wavelengths 1849, 2139, and 2288 Å show that the excited oxygen atom produced is exclusively the $O(^1D)$ state, and that the yield of NO and N makes only a negligible contribution towards the photolysis of N_2O [*Preston and Barr*, 1971]. Since the major contributions to the photodissociation of N_2O come from wavelengths larger than 2100 Å, the N_2O photodissociation is assumed to produce only N_2 and $O(^1D)$.

The main loss process for NO is due to its reactions with O and O_3, which convert NO into NO_2:

$$O + NO + M \rightarrow NO_2 + M,$$
$$NO + O_3 \rightarrow NO_2 + O_2,$$
$$NO + O \rightarrow NO_2 + h\nu.$$

However, NO is reformed through the reaction of NO_2 with atomic oxygen:

$$NO_2 + O \rightarrow NO + O_2.$$

The photodissociation of NO_2, which has a coefficient as high as 5×10^{-3} sec^{-1} during the daytime, also reproduces NO:

$$NO_2 + h\nu \rightarrow NO + O$$

The chemistry of NO and NO_2 are, therefore, strongly coupled to each other through O and O_3, somewhat similar to the situation with HO_2 and OH. During the daytime, NO_2 is lost rapidly through these reactions and photochemical equilibrium is attained. For NO, however, the loss processes indicated above are not so rapid, having the lifetime against chemical losses of the order of a day in the mesosphere. Though the pre-dissociation of NO as suggested by *Strobel* [1971b] is a major sink for NO in the mesosphere, it is not sufficiently fast enough to make the lifetime of NO short. It is therefore necessary to include diffusive transport in the continuity equations for NO. For the purpose of calculating the initial values in the next chapter, however, only the photochemistry has been used.

The reactions between nitrogen species and hydrogen species have been thought as the final sinks for the odd nitrogen species produced in

the thermosphere and the mesosphere. It is believed that species such as HNO_2 and HNO_3 produced in the stratosphere diffuse downwards and finally get washed down with rain water [*Schiff*, 1972]. The presence of HNO_3 above the tropopause has already been detected by *Murcray et al.* [1969] and *Harries* [1973] using spectroscopic techniques, and found mixing ratios to be about 3×10^{-3} ppm. *Crutzen* [1971] who studied the production of O_3 in a O-H-N atmosphere found that the data available at that time for the relevant reaction rates could not explain the observed concentrations of HNO_3.

The production of HNO_2 and HNO_3 takes place according to the 3-body reactions

$$OH + NO + M \rightarrow HNO_2 + M,$$

$$OH + NO_2 + M \rightarrow HNO_3 + M$$

The HNO_3 formed gets destroyed through the oxidation reaction

$$HNO_3 + O(^3P) \rightarrow OH + NO_3,$$

and by photodissociation, both of which occur only during the daytime in the stratosphere.

The reaction between H and NO_2 is a possible means of converting NO_2 into NO:

$$H + NO_2 \rightarrow NO + OH.$$

However, at heights where NO_2 concentrations are large, H concentrations are much smaller than $O(^3P)$ concentrations, so that it cannot compete with the reaction between NO_2 and $O(^3P)$ in the conversion of NO_2 and NO.

Strobel [1972b] has also included the reaction

$$N(^4S) + OH \rightarrow NO + H$$

in his study of the *D*-region nitric oxide abundance. As a means of converting $N(^4S)$ into NO, this reaction has to compete with the reaction

$$N(^4S) + O_3 \rightarrow NO + O_2,$$

which has a rate constant of about 7×10^{-13} cm^3 sec^{-1}. Since the concentration of OH is much less than that of O_3 at all heights, the reaction between $N(^4S)$ and OH will be of no importance, unless its rate constant is several orders higher than that of the reaction with O_3. This reaction is therefore not included in the present study.

The complete list of the neutral reactions between O-N species and O-N-H species considered in this study are listed in Table 2.5. Some of these O-N reactions and their rate constants have been discussed by *Schiff* [1969] in his review of reactions involving oxygen and nitrogen. Unlike the case of the O-H species, many of these reactions are relatively slow, and the only fast reaction here involving ground-state species is the Reaction 39. The reaction between N and NO_2 may also be considered fast. This reaction produces N_2 and O, and to a lesser extent NO (Reactions 42 and 43).

The more recent data adopted here are the rate constants of Reaction 37 (Table 2.5) measured by *Slanger and Black* [1970], Reaction 34 measured by *Lin and Kaufman* [1971], Reaction 41 measured by *Davis et al.* [1973], and the oxidation reaction of N_2O (Reactions 44 and 45) measured by *Scott et al.* [1971]. Among the N-O-H reactions, the rate constants of Reactions 46 and 47 are those measured recently by *Westenberg and*

Table 2.5

O-N and O-N-H reactions.

Reaction No.	Reaction	Rate Constant $cm^n\ sec^{-1}$*
R_{31}	$N + O_2 \rightarrow NO + O$	+6.5(-12) exp(-7.0/RT) *Schiff* [1969]
R_{32}	$N + O_2(^1\Delta_g) \rightarrow NO + O$	2.8(-15) *Clark and Wayne* [1969]
R_{33}	$N + O_3 \rightarrow NO + O_2$	3.4(-11) exp(-2.4/RT) *Phillips and Schiff* [1962]
R_{34}	$N(^2D) + O_2 \rightarrow NO + O$	6.0(-12) *Lin and Kaufman* [1971]
R_{35}	$N(^2D) + O \rightarrow N + O$	2.0(-13) *Weill* [1969]
R_{36}	$NO + O \rightarrow NO_2 + h\nu$	6.4(-17) *Fontijin et al.* [1964]
R_{37}	$NO + O + M \rightarrow NO_2 + M$	6.8(-32) *Slanger and Black* [1970]
R_{38}	$NO + O_3 \rightarrow NO_2 + O_2$	9.5(-13) exp(-2.46/RT) *Schiff* [1969]
R_{39}	$NO + N \rightarrow N_2 + O$	2.2(-11) *Phillips and Schiff* [1962]
R_{40}	$NO + NO + O_2 \rightarrow NO_2 + NO_2$	1.0(-33) *Schiff* [1969]
R_{41}	$NO_2 + O \rightarrow NO + O_2$	9:12(-12) *Davis et al.* [1973]
R_{42}	$NO_2 + N \rightarrow N_2O + O$	7.3(-12) *Phillips and Schiff* [1965]
R_{43}	$NO_2 + N \rightarrow NO + NO$	6.0(-12) *Phillips and Schiff* [1965]
R_{44}	$N_2O + O(^1D) \rightarrow N_2 + O_2$	1.0(-10) *Scott et al.* [1971]
R_{45}	$N_2O + O(^1D) \rightarrow NO + NO$	1.0(-10) *Scott et al.* [1971]
R_{46}	$OH + NO + M \rightarrow HNO_2 + M$	$9.2(-31)(T/300)^{-4.0}$ *Westenberg and de Haas* [1972]
R_{47}	$OH + NO_2 + M \rightarrow HNO_3 + M$	$1.6(-30)(T/300)^{-2.8}$ *Westenberg and de Haas* [1972]
R_{48}	$HNO_3 + O \rightarrow OH + NO_3$	$\leq$ 2.0(-14) *Morris and Niki* [1971]
R_{49}	$H + NO_2 \rightarrow NO + OH$	1.2(-9) exp(-1.93/RT) *Schofield* [1967]
R_{50}	$OH + N(^4S) \rightarrow NO + H$	See Text

*n = 3 for binary reactions and 6 for 3-body reactions

+Read a(-n) as a x 10^{-n}

de Haas [1972]. The value for the HNO_3 oxidation reaction is only an upper limit. These values differ widely from those used by *Crutzen* [1971] in his calculations of HNO_3 concentrations.

2.6 *Carbon Reactions*

The chemistry of carbon species has not drawn much attention in the past as compared to the chemistry of other species, in photochemical model calculations of the terrestrial atmosphere. The importance of including the C-O-H chemistry in the studies of the other minor neutral constituents was highlighted by *Strobel* [1972a] who suggested that CO could act as a sink for OH above 80 km. Further, CH_4 is believed to yield H_2O through oxidation processes increasing the mixing ratio of H_2O in the upper stratosphere [*Nicolet*, 1970]. Both of these constituents, OH and H_2O play important roles in the ion chemistry of the *D* region. Hence it is important to investigate the effects of the chemistry of C-O-H species on the distribution of OH and H_2O in the mesosphere.

The sources of C-O-H species in the upper atmosphere are the photodissociation and oxidation of CO_2 and CH_4. *Hays and Olivero* [1970] studied the production of CO due to photodissociation of CO_2 only, while *Wofsy et al.* [1972] investigated the production of CO due to photodissociation and oxidation of CH_4 in the troposphere and stratosphere, and its effect on the distribution of O-H species.

CO_2 is relatively inert and it does not play any significant role in the chemistry of neutral constituents. However, it gets photodissociated by solar radiation below about 2000 Å yielding CO and atomic oxygen. These products recombine to form CO_2 in a 3-body reaction

$$CO + O + M \rightarrow CO_2 + M$$

While this reaction converts CO into CO_2 efficiently at higher altitudes, the reaction

$$CO + OH \rightarrow CO_2 + H$$

becomes important in this oxidation process at lower altitudes. However, as a sink for OH, this reaction becomes more important at higher altitudes where the concentration of CO is expected to be large. According to *Hays and Olivero* [1970], the CO profile obtained by considering only the photodissociation of CO_2 has a peak of about 30 ppm between 100 and 120 km, the exact height depending on the eddy diffusion values and the rate constant of the recombination reaction used in the calculations.

It is known that CH_4 is present in the lower stratosphere in concentrations slightly above 1 ppm around 24 km [*Bainbridge and Heidt*, 1966; *Kyle et al.*, 1969]. In the stratosphere, CH_4 is subject mainly to oxidation losses. Reactions with both O and OH result in the removal of one H atom from CH_4 yielding CH_3. The removed H atom forms an OH molecule with O, and a H_2O molecule with OH, according to

$$CH_4 + O \rightarrow CH_3 + OH,$$

$$CH_4 + OH \rightarrow CH_3 + H_2O.$$

The CH_3 formed gets converted to CH_2O by its reactions with O and O_2,

$$CH_3 + O(^3P) \rightarrow CH_2O + H$$

$$CH_3 + O_2 \rightarrow CH_2O + OH.$$

Here, the by-products are H and OH, respectively. Next, $O(^3P)$ and OH

oxidize CH_2O to produce HCO through the reactions

$$CH_2O + O(^3P) \rightarrow HCO + OH$$

$$CH_2O + OH \rightarrow HCO + H_2O,$$

yielding OH and H_2O. In the final step, HCO is converted to CO according to

$$HCO + O(^3P) \rightarrow CO + OH$$

$$HCO + O_2 \rightarrow CO + HO_2.$$

It is therefore seen that the four H atoms in the CH_4 are removed by O and OH, forming in the process OH and H_2O, respectively.

Table 2.6 shows the complete set of reactions used in the calculations. The rate constant for Reaction 51 was in dispute for several years, mainly in view of the uncertainty in its activation energy. The latest values for this rate constant were obtained by *Slanger et al.* [1972], who found that it has a positive temperature dependence, with CO as the third body. In this work, the value obtained at 296 K with N_2 as the third body was employed along with the temperature dependence obtained with CO.

Established rate constants for the reactions with CO and CH_4 (Reactions 52-55) have been adopted here. For the rest of the C-H-O species, most of the rate constants are not so well known. The value for Reaction 56 is only a lower limit, while that of Reaction 57 is an approximate figure. The values for Reactions 59 and 62 are lower limits. The rate constant for Reaction 61 is only an estimate.

Table 2.6

C-O-H reactions.

Reaction No.	Reaction	Rate Constant $cm^n\ sec^{-1}$*
R_{51}	$CO + O(^3P) + M \rightarrow CO_2 + M$	+3.8(-33) exp(-4.34/RT) *Slanger et al.* [1972]
R_{52}	$CO + OH \rightarrow CO_2 + H$	9.0(-13) exp(-1.0/RT) *Kaufman* [1969]
R_{53}	$CH_4 + O(^3P) \rightarrow CH_3 + OH$	3.5(-11) exp(-8.1/RT) *Herron* [1969]
R_{54}	$CH_4 + O(^1D) \rightarrow CH_3 + OH$	2.0(-11) *de More and Raper* [1967]
R_{55}	$CH_4 + OH \rightarrow CH_3 + H_2O$	1.2(-10) exp(-5.91/RT) *Schofield* [1967]
R_{56}	$CH_3 + O(^3P) \rightarrow CH_2O + H$	3(-11) *Niki et al.* [1968]
R_{57}	$CH_3 + O_2 \rightarrow CH_2O + OH$	5(-14) *Christie* [1958]
R_{58}	$CH_3 + O_2 + M \rightarrow CH_3O_2 + M$	1.6(-31) *Hoare and Walsh* [1957]
R_{59}	$CH_2O + OH \rightarrow HCO + H_2O$	6.7(-12) *Herron and Penzhorn* [1969]
R_{60}	$CH_2O + O(^3P) \rightarrow HCO + OH$	1.5(-13) *Herron and Penzhorn* [1969]
R_{61}	$CHO + O_2 \rightarrow CO + HO_2$	1(-15) *Hoare and Pearson* [1964]
R_{62}	$CHO + O(^3P) \rightarrow CO + OH$	1(-10) *Herron* [1969]

*n = 3 for binary reactions and 6 for 3-body reactions

+Read a(-n) as a x 10^{-n}

In view of the uncertainties in the rate constants of these reactions, the height profiles of these intermediate species cannot be considered as accurate. However, the loss rates of CH_4 as well as the production and loss rates of CO can be evaluated with less uncertainty as more reliable values for the rate constants of these processes become available.

3. MODEL CALCULATION OF NEUTRAL SPECIES DISTRIBUTION

Most of the minor neutral constituents discussed in the last chapter are produced as a result of the photodissociation and oxidation processes of the major constituents O_2, N_2, CO_2 and those transported from the troposphere to higher levels through various transport mechanisms. In this chapter, a time-dependent transport model will be developed to investigate the distribution and the diurnal behavior of these minor neutral constituents in the height interval 30-120 km.

It is necessary first to set up a model for the transport processes which are responsible for carrying the constituents such as H_2O, N_2O and CH_4 from the troposphere into the stratosphere and above. This is discussed in the following section. The method of solution of the continuity equations which are in the form of second-order partial differential equations is discussed next. It is then possible to calculate the set of initial values required as input parameters for the solution of the time-dependent continuity equations. These equations are next solved for the case of a constant solar zenith angle which corresponds to noon conditions. From the results of these calculations it is possible to eliminate those constituents that need to be further investigated for their diurnal behavior. Finally the solar zenith angle variation is incorporated to simulate the diurnal behavior. These calculations are continued over several simulated days until 24-hour reproducibility is reached.

3.1 *Transport Processes in the Upper Atmosphere*

Several types of motions are responsible for the transport of minor constituents in the upper atmosphere. These include macroscopic motions such as mean motions, wave motions, and winds as well as transport mechanisms

such as turbulence and molecular diffusion. Of these motions, only those which cause vertical transport of minor constituents are considered in the present study.

Mean motions are associated with the large-scale general circulation of the atmosphere. The vertical components of these circulations constitute the mean-vertical motions. Thermodynamic considerations show that mean-downward motion results in the heating of the atmosphere while the upward motions cause cooling. The constraints on the atmosphere heat budget show that such mean-vertical motions cannot have velocities more than a few centimeters per second. According to *Gudiksen et al.* [1968], however, the mean-meridional circulation is found to play only a minor role in the transport processes at stratospheric heights. At higher altitudes its effect is considered to be further reduced. Hence, this motion has not been included in this study. Zonal and other prevailing winds, being associated with horizontal motions, are also excluded.

Transport effects caused by such irregular motions as wave motions, tides, and turbulence are all described under a single mechanism, *viz.* eddy diffusion, in terms of a lumped parameter called eddy diffusion coefficient. This quantity is analogous to the molecular diffusion coefficient, except that the former deals with the diffusion of 'eddies', while the latter deals with the diffusion of molecules.

3.1.1 *Eddy diffusion coefficients.* Transport by eddy diffusion is considered to be taking place through the exchange of 'eddies' having scale lengths ranging from several meters to several kilometers. These eddies are formed by such phenomena as wind shears, internal gravity waves, tides, and in the case of large-scale eddies, by planetary waves.

[*Sheppard*, 1959; *Hines*, 1963; *Hodges*, 1969; *Geisler and Dickinson*, 1968]. The main outcome of such exchange processes is local mixing.

The behavior of air parcels under eddy diffusion has been evident in experiments conducted to study the dynamics of the upper atmosphere. In these experiments chemiluminous vapor trails are released from rockets and their rate of growth is observed visually or photographed from the ground. Such observations have shown that the trails initially grow under molecular diffusion and later disperse into erratic shapes under eddy diffusion below a certain level. Above this level, the growth is controlled only by molecular diffusion at all times [*Blamont and de Jager*, 1961; *Zimmerman and Champion*, 1963; *Justus*, 1969]. This transition level where the turbulence ceases allowing molecular diffusion to dominate is generally known as the turbopause. *Blamont and de Jager* [1961] found that this turbopause level appeared distinctly on each occasion the observations were made, with its value lying between 102 and 110 km. According to *Zimmerman and Champion* [1963] the transverse growth of the turbulent clouds observed in the height range 60-100 km showed two sequential time dependencies; an initial growth due to molecular diffusion with $r \propto t^{1/2}$ and a subsequent growth due to eddy diffusion with $r \propto t$, where r is the Gaussian half-width of the clouds and t is the time lapse. The diameter of these clouds generally indicates the order of magnitude of the scale length of the eddies.

Lettau [1951] expressed the eddy diffusion coefficient, D_e, as

$$D_e = \lambda_D \zeta_D \quad , \tag{3.1}$$

where λ_D is a length fixing the scale of turbulent displacements (mixing length), and ζ_D is a velocity fixing the speed of turbulent motions. Using this definition, *Zimmerman and Champion* [1963] calculated the value of D_e which was found to be between 2×10^6 and 1.5×10^7 cm^2 sec^{-1} at 75 km and between 1.5×10^7 and 10^8 at 100 km. More recent studies by *Keneshea and Zimmerman* [1970] show D_e having values between 2×10^6 and 8×10^6 cm^2 sec^{-1} around 100 km.

The observation of the vapor trails from ground level below can detect only the horizontal spread of the turbulent clouds, and as such the values obtained are in respect of the horizontal component of the eddy diffusion coefficient. In the lower thermosphere where the negative lapse rate of the temperature tends to inhibit any vertical movements, one cannot expect the turbulence to be isotropic. However, *Keneshea and Zimmerman* [1970], considering the scale lengths of turbulent sources near 100 km, assumed the vertical component of the eddy diffusion coefficient to be equal to the measured horizontal component.

In another method, it is possible to estimate D_e by studying the heat budget of the lower thermosphere and the mesosphere. Here, the diffusion coefficient for thermal conductivity of the atmosphere is calculated, and from the equality between this parameter and the eddy diffusion coefficient, the latter is estimated [*Johnson and Gottlieb*, 1971; *Olivero*, 1970]. This method really gives upper limits for the eddy diffusion coefficients, and shows that the D_e values decrease from about 3×10^6 cm^2 sec^{-1} near 100 km to about 10^5 cm^2 sec^{-1} near 60 km.

In the stratosphere, the negative lapse rate of the temperature makes the atmosphere stable against vertical convections. This in turn, lowers

the value of vertical eddy diffusion coefficient. The effective values for this quantity in the stratosphere have been determined by studying the distribution of the radioactive debris from upper atmosphere nuclear explosions. *Karol* [1966] has deduced from aircraft measurements of radon daughters RaD and RaF, values in the range (0.2-2.0) x 10^4 cm^2 sec^{-1} for the vertical eddy diffusion coefficient in the lower stratosphere between 35°N and 34°N latitudes. In a different method, *Reed and German* [1965] attempted to explain the large-scale mixing processes using published heat flux data, and arrived at values lying between 1 x 10^3 and 5 x 10^3 cm^2 sec^{-1} for the vertical component of the lower stratosphere eddy diffusion coefficient for the months of July and September.

Using a different approach, *Shimazaki* [1971] determined effective eddy diffusion coefficients which yield solutions to model calculations that would agree with the observed composition structure in the lower thermosphere. He found that a D_e profile having a peak value of 1 x 10^7 cm^2 sec^{-1} in the height range 95-105 km, and a peak half-width of about 8 km explains most of the rocket-obersved composition height variations. However, in view of the uncertainties in other variables such as solar flux, reaction rate constants, etc., it is difficult to arrive at unambiguous results from such model calculations.

From the results of previous workers [*Keneshea and Zimmerman*, 1970; *Shimazaki and Laird*, 1970] it is known that values of eddy diffusion coefficient play a crucial role in determining the height profiles of minor neutral species. Hence, in this work, two models for D_e height profiles have been adopted, with the values fixed on the basis of the above discussions. In both cases, D_e is kept constant at 10^4 cm^2 sec^{-1} below

40 km. Between 40 and 80 km, its values are given by (Figure 3.1).

$$D_e = 10^{(a-b\Delta z)} \quad , \tag{3.2}$$

where a and b are constants, and $\Delta z = (z-80)$ km. The values of a and b are selected such that at 80 km, $D_e = 2 \times 10^6$ cm^2 sec^{-1} in the 'high' model, and $D_e = 4 \times 10^5$ cm^2 sec^{-1} in the 'low' model. Above 80 km, D_e is described by the following expression so that it peaks at 105 km.

$$D_e = 10^{a + b(\Delta z)^2 + c(\Delta z)^3} \quad , \tag{3.3}$$

where a, b, and c are constants, and $\Delta z = (z-105)$ km. The 'high' model has a peak value of 1×10^7 cm^2 sec^{-1} and the 'low' model a peak value of 5×10^6 cm^2 sec^{-1}, both at 105 km. The above expression shows D_e to drop rapidly near 110 km, so that molecular diffusion takes over above these heights.

3.1.2 *Molecular diffusion coefficients.* From the kinetic theory of gases, the molecular diffusion coefficient, D_m can be derived as

$$D_m = \frac{3}{8[X]d} \left\{\frac{kT}{2 \quad m^*}\right\}^{1/2} \quad , \tag{3.4}$$

where $[X]$ is the total number density, d is the mean molecular diameter, m^* is the reduced mass of the molecules and k is the Boltzmann's constant. In the upper atmosphere, the molecular diffusion coefficients of constituent gases is calculated for the motion of the gas molecules in the medium of an N_2-atmosphere. Hence, for a constituent other than oxygen, $[X]$ is

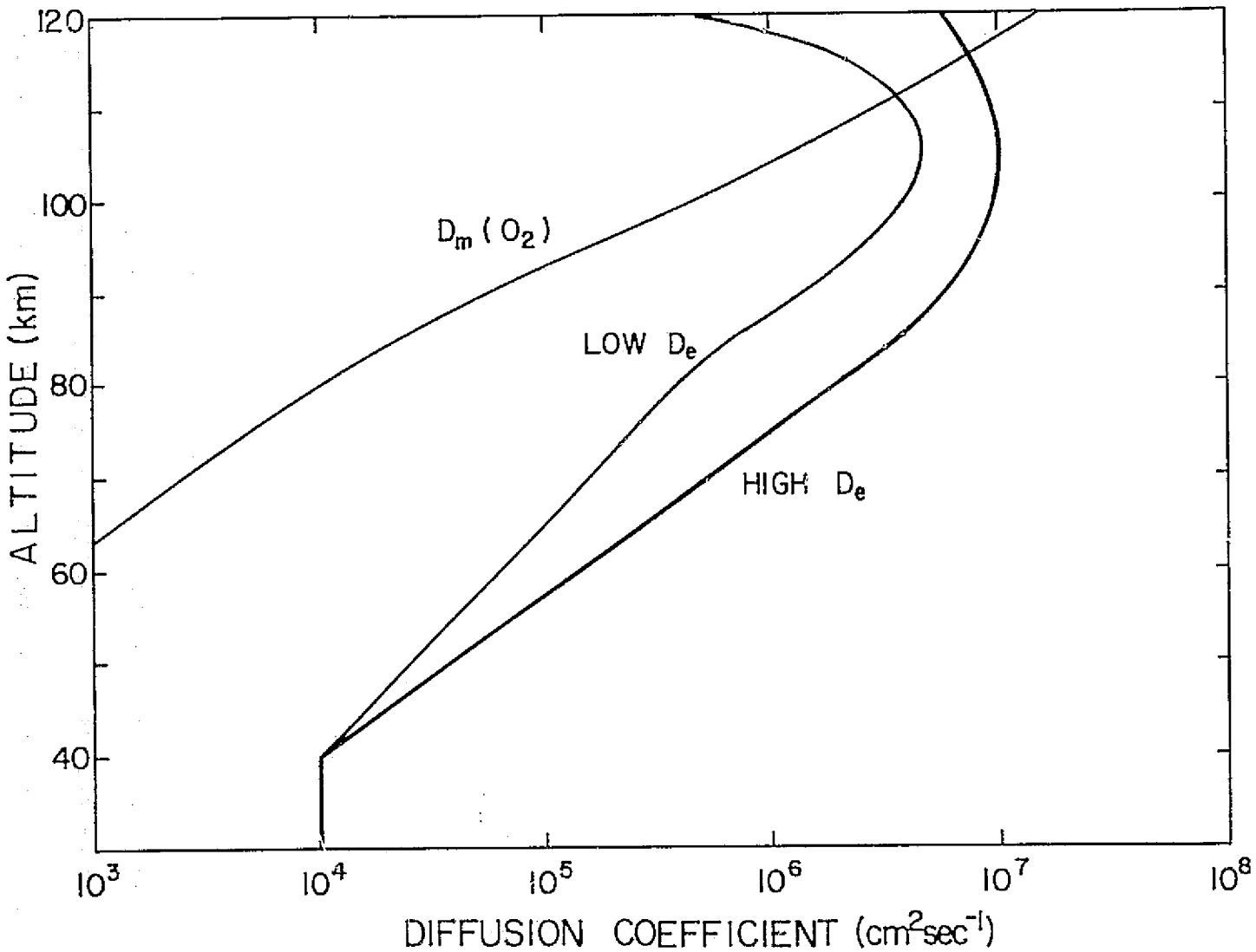

Figure 3.1 Eddy diffusion coefficient models used in this study. Molecular diffusion coefficient for oxygen is shown for comparison.

essentially equal to $[N_2]$. This quantity decreases exponentially in the atmosphere, and up to about 100 km, the variation of T does not exceed a factor of 1.5. Therefore, in this height interval, D_m increases exponentially with the same scale height as that of the density variation. About 100 km, the increase is further enhanced due to the increase in T which takes place in the thermosphere until it reaches a constant value.

The values of D_m for atmospheric gases at standard temperature and pressure lies between 0.14 and 0.21 $cm^2\ sec^{-1}$, except for hydrogen and atomic oxygen whose values are 0.67 and 0.47 $cm^2\ sec^{-1}$, respectively, [*Lettau*, 1951]. The variation of D_m for oxygen with altitude is illustrated in Figure 3.1. It is seen that D_m is much less than D_e below about 110 km. Above 110 km, molecular diffusion dominates over eddy diffusion.

Direct observations of the spread of rocket released vapor trails have established the existence of a transition level separating the molecular diffusion and eddy diffusion regions, as mentioned before.

The observation of the spread of vapor trails above the turbopause yields the molecular diffusion coefficients. Values obtained by *Golomb and MacLeod* [1966] and other workers are in general agreement with the values calculated from equation (3.4).

3.2 *Solution of Continuity Equation with Transport Term*

Diffusion results in the loss of a constituent within a given volume. The rate of loss of its concentration is given by the divergence of its flux caused by diffusion. Since the transport effects are considered only in the vertical direction, this can be simply written as

$$\left.\frac{\partial [X]}{\partial t}\right|_{\text{dif}} = -\frac{\partial \phi}{\partial z} \tag{3.5}$$

where $[X]$ is the concentration of the constituent X, and ϕ is the vertical flux.

The continuity equation with this transport term then appears as

$$\frac{\partial [X]}{\partial t} = Q - P[X] - \frac{\partial \phi}{\partial z} \tag{3.6}$$

where Q is the production rate per unit volume and P is the loss coefficient. The loss due to recombination of two like particles is neglected here.

It is seen from equation (3.6) that the diffusion term is important only if the chemical loss rate is smaller than the loss rate due to diffusion. These rates are described in terms of respective time constants, which are given by (neglecting molecular diffusion)

$$\tau(\text{chem}) = 1/P \tag{3.7}$$

$$\tau(\text{dif}) = H_a^2/D_e \quad , \tag{3.8}$$

where H_a is the scale height of the mixed atmosphere. With the D_e profiles used, the time constant against eddy diffusion in the mesosphere is of the order of a day. Therefore, for constituents having fast chemical loss rates, it is not necessary to include the transport term in their continuity equation. For such cases the continuity equation is simply

$$\frac{\partial [X]}{\partial t} = Q - P[X] \quad . \tag{3.9}$$

For constituents having chemical time constants more than about a day, the transport term is included. The total flux due to diffusion is given by

$$\phi = \phi_m + \phi_e \quad , \tag{3.10}$$

where ϕ_m and ϕ_e are the flux contributions due to molecular diffusion and eddy diffusion, respectively. The molecular diffusion flux is expressed in the form [*Chapman and Cowling*, 1952]

$$\phi_m = - D_m \left\{ \frac{\partial [X]}{\partial z} + (1+\alpha) \frac{[X]}{T} \frac{\partial T}{\partial z} + \frac{[X]}{H_i} \right\} \quad , \tag{3.11}$$

where α is the thermal diffusion factor and H_i is the scale height of the constituent X_i. In the same manner, *Colegrove et al.* [1965] expressed the eddy diffusion flux as

$$\phi_e = - D_e \left\{ \frac{\partial [X]}{\partial z} + \frac{[X]}{T} \frac{\partial T}{\partial z} + \frac{[X]}{H_a} \right\} \quad , \tag{3.12}$$

where H_a is the scale height of the mixed atmosphere.

Combining equations (3.11) and (3.12) one gets

$$\phi = - \left\{ A(z) \frac{\partial [X]}{\partial z} + B(z) [X] \right\} \quad , \tag{3.13}$$

where

$$A(z) = D_m + D_e \tag{3.14}$$

$$B(z) = \left\{D_e + (1+\alpha)D_m\right\} \frac{1}{T}\frac{\partial T}{\partial z} + \frac{D_e}{H_a} + \frac{D_m}{H_i} \quad . \tag{3.15}$$

Substituting equation (3.13) in the continuity equation for the ith constituent (equation (3.6)),

$$\frac{\partial [X]_i}{\partial t} = a \frac{\partial^2 [X]_i}{\partial^2 z} + b \frac{\partial [X]_i}{\partial z} + c[X]_i + d \tag{3.16}$$

where

$$b = \frac{\partial A}{\partial z} + B \tag{3.17}$$

$$c \quad \frac{\partial B}{\partial z} - P \tag{3.18}$$

If the distributions of all the constituents are known at time $t-\Delta t$, it is possible to evaluate the loss term P and the production term Q, and in turn, the parameters c and d appearing in equation (3.16) written for time t. Strictly, the values of P and Q deduced at time t should be used to evaluate these parameters. This, however, is not possible, unless one does an iterative calculation for each time step. Nevertheless, if the variation of the distributions between successive time steps is small, the use of P and Q corresponding to time step $(t-\Delta t)$ is not expected to introduce any serious errors in the solution for $[X]_i$ at time t. From trial calculations, this assumption was found to be valid, except at sunrise. Since the emphasis of this work is to study the variations occurring at daytime, this approximation was used and any deviations occurring at sunrise were not considered important.

The concentrations of the constituents at height z and time t are therefore given by a system of non-linear equations, comprising a set of second-order partial-differential equations (equation (3.16)) and a set of single-order ordinary differential equations (equation (3.9)). In view of the above mentioned assumption it is possible to solve these equations taken individually.

In order to solve these non-linear equations, one has to resort to numerical techniques. It is customary in these methods to replace the differentials with difference quantities; and to solve the resulting algebraic equations. In converting the differential equation to a difference equation, the space between the two boundaries z_0 and z_N is divided into N intervals with spacing Δz, so that

$$z = z_0 + n\Delta z \ , \qquad n = 0, 1, 2, \ldots N \quad . \tag{3.19}$$

Similarly, the time lapsed from an initial time $t = 0$ is expressed as

$$t = m\Delta t, \qquad m = 0, 1, 2, \ldots \tag{3.20}$$

The concentration of a given constituent whose distribution is governed by equation (3.16) can then be written as (see Appendix II for details of converting the differential equation to its difference form)

$$\alpha_n \, y_{n+1}^m + \beta_n^{m-1} \, y_n^m + \gamma_n \, y_{n-1}^m = \delta_n^{m-1} \quad , \tag{3.21}$$

where

$$y_n^m = [X]_i \ (z,t)$$

and the coefficients α_n, β_n, and γ_n are functions of a, b, Δz, and Δt. β_n^{m-1}, in addition, includes terms containing $[X]_j(z,t-\Delta t)$ $j \neq i$, while δ_n^{m-1} contains these terms as well as $[X]_i(z,t-\Delta t)$. For simplicity omitting the prefix m and suffix n from the coefficients in equation (3.21), one gets

$$\alpha \ y_{n+1} + \beta \ y_n + \gamma \ y_{n-1} = \delta \tag{3.22}$$

For N intervals, one can write (N-2) such equations containing N unknowns. The two boundary conditions provide the two additional equations required for the solution of this set of simultaneous equations. The values of $[X]_i$ at $t = 0$ also have to be specified as initial conditions.

This system of equations can be expressed in the form

$$[A] \ [Y] = [B] \tag{3.23}$$

where $[A]$ is a tridiagonal matrix of order (N-2) and $[B]$ is a column matrix. The most direct method of solving this system of equations is to invert $[A]$ and express $[Y]$ in the form

$$[Y] = [A]^{-1} \ [B] \tag{3.24}$$

The finite-difference scheme is only an approximate method and it is expected that the solution obtained by this method is also an approximation to the exact solution of the differential equation. If the solution is stable, it will converge to the exact solution as $\Delta z \rightarrow o$. However, in the computer solution of these equations, the accumulation of round-off errors results in the solution diverging more from the exact solution as the number of steps is increased by making Δz smaller. This problem was overcome by adopting a more efficient method than the above one, developed mainly for the solution of a system of equations whose coefficients form a tridiagonal matrix [*Richtmyer*, 1957]. The details of this method are found in Appendix II.

The boundary conditions required for the solution of the above set of equations are obtained from known physical quantities at the two boundaries. These can be either the number density or the flux across the boundary. With the number density, one specifies either y_0 or y_N, while with the flux as a boundary condition, one specifies the gradient of y_n at the boundary.

In order to get the necessary information regarding the number densities or the flux at the boundaries, one has to depend on direct measurements of these quantities or estimates of them by other indirect means. In the next section, sources of such information and the values adopted as boundary conditions are discussed.

The transformation of the ordinary differential equation (equation (3.9)) into its difference form yields

$$[X]_i(z,t) = \frac{Q(z,t)\Delta t - [X]_i\ (z,t-\Delta t)}{1 + P(z,t)\Delta t} \tag{3.25}$$

The use of this implicit form in the conversion from differential to difference equation results in better stability [*Shimazaki*, 1967], and does not impose restrictions on the choice of the height and time increments.

From trial calculations it was found that height increments of 1 km were most convenient with regard to resolution and computer time. Time increments during the daytime were selected corresponding to $\chi = 10°$ up to $\chi = 70°$ and thereafter $\chi = 5°$ up to $\chi = 100°$. During nighttime one-hour time increments were used.

3.3 *Boundary Conditions*

The boundary conditions required for the solution of the continuity equations having the transport terms appear either as a number density or a flux across the boundary. The constituents for which transport effects are important can be divided into two groups. Those originating in the troposphere and transported upwards into the stratosphere, such as H_2O, N_2O, CO_2, and CH_4 fall into one group. The constituents in the other group, such as O, NO, CO, H and H_2 are produced in the lower thermosphere and upper mesosphere and are transported either downwards or upwards. The boundary conditions that are applicable for these two groups are therefore quite distinct.

3.3.1 *Boundary conditions for lower atmosphere produced constituents.* In the stratosphere and mesosphere, these constituents are subject to losses due to either oxidation or photodissociation. Hence an upward flux across the lower boundary is required to maintain their concentrations at these high altitudes. The most suitable boundary condition for them is to specify this upward flux. Values of this quantity,

however, cannot be measured directly and can only be estimated from measurements of their number densities at the lower boundary. Such measurements have been carried out in the lower stratosphere using either air-borne or balloon-borne instruments, and these have been employed in specifying the lower boundary conditions for the above constituents.

Though H_2O is one of the important minor constituents in the upper atmosphere its concentration above the tropopause in only little known. Early measurements carried out using frost-point hygrometers have shown wide disparity in the mixing ratios obtained above the tropopause, with the values varying from a few parts per million to about 40-50 ppm [*Gutnick*, 1961]. More recent measurements carried out using improved techniques, however, have shown consistently lower mixing ratios, in the range 2-3 ppm between 100 and 40 mb levels or 16 and 22 km [*Mastenbrook*, 1968, 1971]. In view of the precautions taken in these measurements to minimize errors due to any contaminations and also, because of the consistency in the measurements which have been taken over a period of six years, the lower values are preferred to the high values reported previously. Water vapor concentrations deduced from solar spectra recordings using air-borne instruments have also shown mixing ratios in the range 2.4 - 2.6 ppm at 18 km in the mid-latitudes [*McKinnon and Morewood*, 1970]. The measurement carried out near the stratopause by *Scholz et al.* [1970], however has shown a high mixing ratio, about 6 ppm. This increase in the water vapor concentration above the lower stratosphere values has given rise to much speculation regarding production of water vapor through other means such as oxidation of methane, as mentioned before. For the purpose of fixing the boundary value, however, a mixing ratio of 3 ppm at 30 km has been adopted. From trial calculations it was found that an

upward flux of 1×10^9 cm^{-2} sec^{-1} with an eddy-diffusion coefficient of 10^4 cm^2 sec^{-1} at 30 km gives rise to this mixing ratio.

For nitrous oxide, which is the most abundant nitrogen compound in the lower atmosphere next to N_2, direct measurements are available only up to about 24 km. These measurements carried out by *Schutz et al.* [1970] show mixing ratios about 0.1 ppm near 24 km. Some recent spectral observations have shown that the mixing ratio reduces from a tropospheric value of 0.27 ppm to a value 0.21 ppm taken 3 km above the tropopause [*Harries*, 1973]. Theoretical calculations of *Bates and Hays* [1967] show that the mixing ratio at 30 km could lie in the range 0.02-0.15 ppm for stratospheric eddy diffusion coefficients between 10^3 and 10^4 cm^2 sec^{-1}, corresponding to a tropospheric mixing ratio of 0.25 ppm. On the basis of these data, a mixing ratio of 0.1 ppm has been adopted at 30 km, which corresponds to an upward flux of 1×10^7 cm^{-2} sec^{-1} at this altitude.

In the case of CO_2, the loss rate due to photodissociation is rather small, and hence it maintains a constant mixing ratio up to the mesopause level [*Hays and Olivero*, 1970]. The mixing ratio in the troposphere has been found to be in the range 310-320 ppm [*Seiler and Junge*, 1970] and a similar value has been detected near the stratopause [*Scholz et al.*, 1970]. To be compatible with a mixing ratio of 3.14×10^{-4} ppm, a flux value of 6.4×10^{11} cm^{-2} sec^{-1} has been assumed as the boundary condition at 30 km.

Methane is a trace constituent of high abundance in the troposphere. According to measurements of *Bainbridge and Heidt* [1966], it has a constant mixing ratio of 1.6 ppm in the troposphere while around 24 km its mixing ratio drops to about 1.0 - 1.3 ppm. *Kyle et al.* [1969] found

C-2

that the total content of methane above 30 km is about 1/5 that above the tropopause. *McConnell et al.* [1971] calculated the vertical distribution of CH_4 below 20 km using eddy diffusion coefficients determined from trace studies, and arrived at a mixing ratio of 0.9 ppm and a flux of 1×10^9 cm^{-2} sec^{-1} at 20 km. Their results show that the flux drops by about an order of magnitude between 10 and 20 km. Assuming the same loss rate holds between 20 and 30 km, the same flux value, 1×10^8 cm^{-2} sec^{-1} was adopted as the lower boundary value for CH_4, and from trial calculations, this was found to yield a mixing ratio of 0.15 ppm at 30 km.

In specifying the upper boundary conditions for these constituents H_2O, N_2O, CO_2, and CH_4, as well as for O_2, one can make use of the fact that all of these constituents are subject to photodissociation and are lost above the upper boundary. Upward flux across the upper boundary replenishes this loss. Near this altitude level the dissociation rates are independent of the height as their optical depths are nearly zero. In the case of O_2, however, the level of zero optical depth is near 160 km. Though its dissociation rate has a small variation between 120 and 160 km, for the purpose of calculating the upward flux its value has been assumed to be constant. Assuming each of these constituents has a distribution under its own scale height above 120 km, the flux can be determined from

$$\phi_i(z_N) = [X]_i \ (z_N) \ J_i(z_N) \ H_i(z_N) \tag{3.26}$$

where $J_i(z_N)$ and $H_i(z_N)$ are the dissociation rates and the scale heights of the constituents evaluated at 120 km.

3.3.2 *Boundary conditions for upper atmosphere produced constituents.* The constituents in the second group all move downwards

after being produced in the thermosphere, except in the case of H and H_2. In the case of O and CO, the downward flux across the upper boundary is determined by the rate at which O_2 and CO_2 are carried upwards. The time average of the downward flux of O and CO has to be equal to that of the upward flux of O_2 and CO_2, respectively, in order to conserve the total amounts of these species. Strictly speaking, this equality may not hold if one takes the instantaneous values of the fluxes. However, for the sake of simplicity the boundary values for these two species have been calculated with this assumption, and are given by

$$\phi_O(z_N) = -2\phi_{O_2}(z_N) \quad , \tag{3.27}$$

$$\phi_{CO}(z_N) = -\phi_{CO_2}(z_N) \quad . \tag{3.28}$$

The estimation of the downward flux of NO at 120 km is more complex, and one has to go into the details of ion chemistry in the *E* and *F* regions to evaluate this quantity. *Strobel* [1971a] has studied this problem and found that the NO concentration at 120 km is about 1×10^8 cm^{-3} and that it has no diurnal variation below this height. This concentration is also in agreement with the measurements of *Meira* [1971]. Since no estimate of the flux value at 120 km is given, a number density of 1×10^8 cm^{-3} is used as the upper boundary value for NO.

Atomic hydrogen, being light in weight escapes from the earth's atmosphere, and gives rise to the geocorona surrounding the earth. From measurements of the intensity of the geocorona radiation, and also from measurements of the absorption of the solar Ly-α line by geocoronal

atomic hydrogen the abundance of this species in the thermosphere and above can be deduced. In these calculations it is customary to use a distribution profile such as the Kockarts-Nicolet model which takes into account the upward escaping flux, and normalize the concentration at the base of the thermosphere to fit the observations. The atomic hydrogen concentrations so determined near 100 km fall in the range (2.5 -) x 10^7 cm^{-3} [*Meier and Prinz*, 1970; *Meier and Mange*, 1970; *Vidal-Madjar et al.*, 1973]. Based on these values, a number density of 1 x 10^7 cm^{-3} was adopted as the upper boundary condition for *H*.

Molecular hydrogen is produced mostly in the mesosphere through various chemical reactions, and it is possible to have both an upward flux above the mesosphere as well as a downward flux below the mesosphere. However, at the upper boundary level no evidence is available to estimate flux. Hence, it has been assumed that this flux is zero at the upper boundary. Since H_2 is rather inactive in the ion chemistry of the *D* region, any errors in the H_2 profile caused by improper upper boundary value is not of much significance.

At the lower boundary, the above constituents which have their source in the upper altitudes are subject to chemical reactions having short time constants. A zero flux at the lower boundary is therefore a reasonably valid assumption for use in this study.

3.4 *Calculation of the Initial Values*

In the solution of equations (3.22) and (3.25) for the number density of the constituents at time t, a knowledge of these values at time $(t-\Delta t)$ was required. Therefore, these initial values have to be calculated first, before one can solve the above time dependent equations. This was done by employing a steady-state semi-transport model.

First, the distribution of the pure oxygen constituents, $O(^3P)$, $O(^1D)$, and O_3 are obtained using the Chapman's reaction scheme. Next, the height distribution of the constituents belonging to the first group mentioned in the last section, *viz.* H_2O, N_2O, CO_2, and CH_4 are calculated using steady-state continuity equations which included transport terms and loss terms due to photodissociation and oxidation subject to the boundary conditions mentioned in the last section. Finally, the height distributions of the rest of the constituents are obtained assuming photochemical equilibrium corresponding to noon conditions.

By writing the continuity equations and assuming photochemical equilibrium, the following expressions for the oxygen species are readily obtained:

$$[O(^3P)] = \left\{\frac{J_1\ J_3\ [O_2]}{(R_1 J_3 + R_2 R_3 [O_2])\ [M]}\right\}^{1/2} , \tag{3.29}$$

$$[O(^1D)] = \frac{(R_2[O(^3P)]\ [M] + J_{1a})\ [O_2]}{R_8[N_2] + (R_7+R_9)\ [O_2]} , \tag{3.30}$$

$$[O_3] = \frac{R_2[O_2][M]\ [O(^3P)]}{J_3} , \tag{3.31}$$

where

$$J_1 = J_a + J_b ,$$

$$J_3 = J_{3a} + J_{3b} + J_{3c} .$$

The production of $O(^3P)$ vanishes at nighttime, but its loss processes are maintained throughout the day by collisional reactions. Hence, at lower heights where the collisional rates are large due to the high density of the atmosphere, its concentration at night will vanish. At higher altitudes, where the collisional losses are small, the loss rates are controlled by diffusive processes having lifetimes of a few days. Therefore, the $O(^3P)$ concentrations are maintained at these heights even at nighttime. The excited-state, $O(^1D)$, abundance, on the other hand, vanishes at all heights during the night. In the case of O_3, its production is proportional to the square of the neutral particle density while its loss rate, mainly due to photodissociation, remains almost constant at all heights during the day and vanishes during the night. Therefore, O_3 is expected to have higher values at nighttime than at daytime.

The photochemical loss term used in calculating the $O(^3P)$ concentrations as given in equation (3.32), yields unrealistically high values above about 90 km. It is known from the work of previous investigators [*Shimazaki and Laird*, 1970; *Keneshea and Zimmerman*, 1970] that the $O(^3P)$ profile has a peak around 90 km with the distribution above this peak given approximately by the diffusive equilibrium conditions. Hence $O(^3P)$ values above 95 km were adjusted to have an exponential drop with the scale height factor determined by its own molecular weight.

In calculating the height distribution of the O-H constituents, it is convenient to start with an H_2O profile that has already been transported into the high altitudes subject to photodissociation and oxidation. In this preliminary calculation, the recycling of H_2O through reactions between constituents such as HO_2 and OH was neglected. Also steady-

state conditions were employed. Therefore, the continuity equation for H_2O was written independent of the concentrations of other species, and the profile thus obtained depends only on the upward flux and the eddy diffusion coefficient used.

The photodissociation products of H_2O, *viz.* OH, HO_2, and H_2O_2 have short time constants against chemical losses and under steady conditions their production rates become equal to their photochemical loss rates. This is not so in the case of H and H_2. However, to obtain the initial distributions, photochemical equilibrium was assumed for these two species as well. The production and loss terms for the odd hydrogen constituents, H, OH, and HO_2 are written using the reaction scheme given in Table 2.4. These three continuity equations when added together yield the expression

$$R_{24}\ [H][HO_2] + R_{23}[HO_2][OH] = J_7[H_2O.] \tag{3.32}$$

Next, taking the major terms in the equations for OH and HO_2,

$$[OH] = \frac{R_{21}[HO_2][O] + R_{13}[H][O_3]}{R_{17}[O]} \tag{3.33}$$

$$[HO_2] = \frac{R_{11}[H][O_2][M]}{R_{21}[O]} \tag{3.34}$$

Substituting these equations in equation (3.32) yield

$$[H] = \left\{\frac{J_7[H_2O]}{A(R_{24} + B\ R_{23})}\right\}^{1/2} , \tag{3.35}$$

where

$$A = k_{11}[O_2][M]/k_{21}[O], \qquad \text{and}$$

$$B = (k_{11}[O_2][M] + k_{13}[O_3])/k_{17}[O] \quad .$$

It is now possible to include the effects of the Reactions 11 and 13 into the expressions for $O(^3P)$ and O_3 obtained before. The corrected expressions which include the H concentrations are

$$[O(^3P)] = \left\{\frac{J_1 J_3[O_2] - (k_{11}[O_2][M] + k_{13}[O_3])[H]}{(k_1 J_3 + k_2 k_3[O_2])[M]}\right\}^{1/2} \tag{3.36}$$

and

$$[O_3] = \frac{k_2[O_2][M][O(^3P)]}{J_3 + k_{13}[H]} \tag{3.37}$$

In actual computation a quadratic equation, obtained after eliminating $[O_3]$ in equation (3.36) using equation (3.37) was solved. The final values were obtained after iterating the whole set of equations until convergence was reached. Since the effects of [H] terms on $[O(^3P)]$ is rather small and the two sets of equations are loosely coupled, convergence was reached rapidly. The results of these calculations are shown in Figure 3.7 and 3.8.

The initial values for the concentrations of the nitrogen species other than N_2O have also been obtained using only photochemical equations, though it is not really valid for certain constituents such as NO. The N_2O profile was calculated using the steady-state transport equation with the boundary conditions given in the last section. Before calculating the distribution of the rest of the neutral species, it is

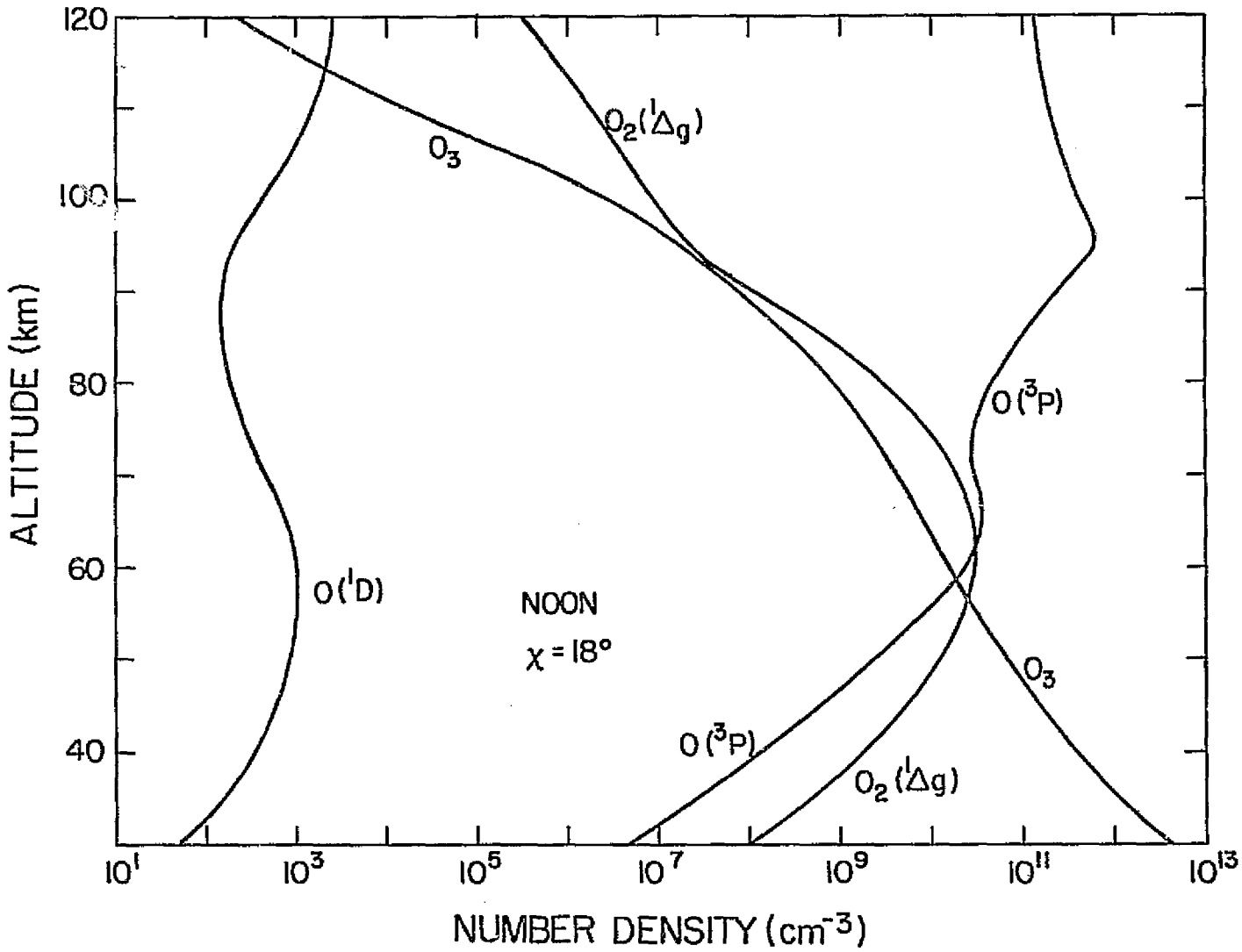

Figure 3.2 The height distributions of oxygen constituents at noon obtained as initial values.

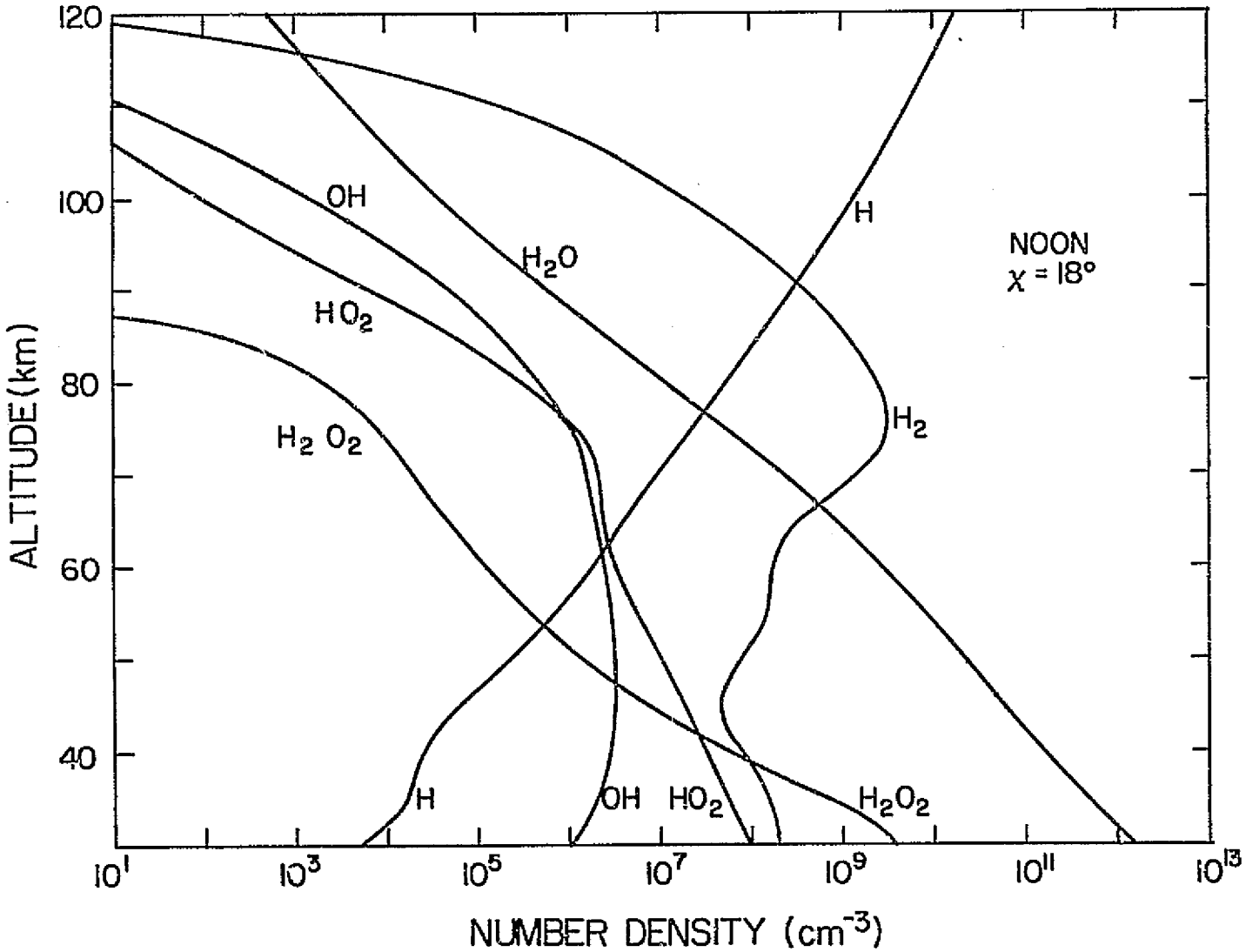

Figure 3.3 The height distributions of hydrogen and oxygen-hydrogen constituents at noon, obtained as initial values.

necessary to calculate the distribution of the charged species which appear in the continuity equation for $N(^4S)$ and $N(^2D)$. For this purpose, an electron-density profile given by

$$[e] = 10^{(z-50)/10} \quad , \; z < 100 \text{ km}$$

and (3.38)

$$[e] = 10^5 \qquad 100 \leq z \leq 120 \text{ km}$$

was assumed. The region of the electron-density profile which is important for the production of $N(^2D)$, the principal source of NO, lies above the ledge where the cluster ions are absent. Hence, the distribution of the positive ions could be expressed in a straight forward manner in terms of the assumed electron densities. The calculation of the ion-pair production functions required for this purpose will be given in detail in the next chapter along with the relevant reaction rates.

The quasi-equilibrium photochemical continuity equations for N, $N(^2D)$, NO, and NO^+ can be combined to yield the equation

$$[N][NO] + a[NO] = b \tag{3.39}$$

where

$$a = (R_{36}[O] + R_{37}[O][M] + R_{38}[O_3])/2\, R_{39}$$

$$b = (R_{45}[N_2O][O(^1D)] + R_{101}[O^+][N_2] + R_{103}[N_2^+][O] + N_2[N_2^+][e])/R_{39}$$

Eliminating [N] in the above equation using the expression for [N] obtained from the photochemical continuity equation one gets a quadratic equation in [NO], the solution of which gives the required initial values.

The $[NO_2]$ and $[N(^2D)]$ profiles are next calculated using the photochemical equations,

$$[NO_2] = \frac{((R_{36}+R_{37}[M])[O] + R_{38}[O_3])\ [NO]}{J_4 + R_{41}[O]} \tag{3.40}$$

$$[N(^2D)] = \frac{\gamma_1\ R_{103}[N_2^+][O] + \gamma_2\ \alpha_{NO}[NO^+][e]}{R_{34}[O_2] + R_{35}[O]} \tag{3.41}$$

where γ_1 and γ_2 are the branching ratios of the reactions $N_2^+ + O$ and $NO^+ + e$, which yield $N(^2D)$.

The resulting profiles of the O-N species are illustrated in Figure 3.4.

The initial distributions of CO_2 and CH_4 are first determined employing the steady-state transport equations having loss terms due to photodissociation and/or oxidation, subject to the boundary conditions given in Section 3.3. The behavior of CO is somewhat similar to that of $O(^3P)$ above the mesopause. Its chemical loss term has a long time constant in this region and, therefore, the profiles calculated using photochemical equations alone would yield unrealistically high values. Hence, the height distribution of this constituent was also obtained by solving the steady-state transport equation. The profiles of $[CH_4]$ and [CO] thus obtained are shown in Figure 3.5.

In addition to CO, the CH_4 and CO_2 dissociation and oxidation yield minor compounds such as CH_2O, CH_3, and HCO. Of these only CH_2O reaches any significant level, and this is shown in Figure 3.5 along with the profiles of $[CH_4]$ and [CO].

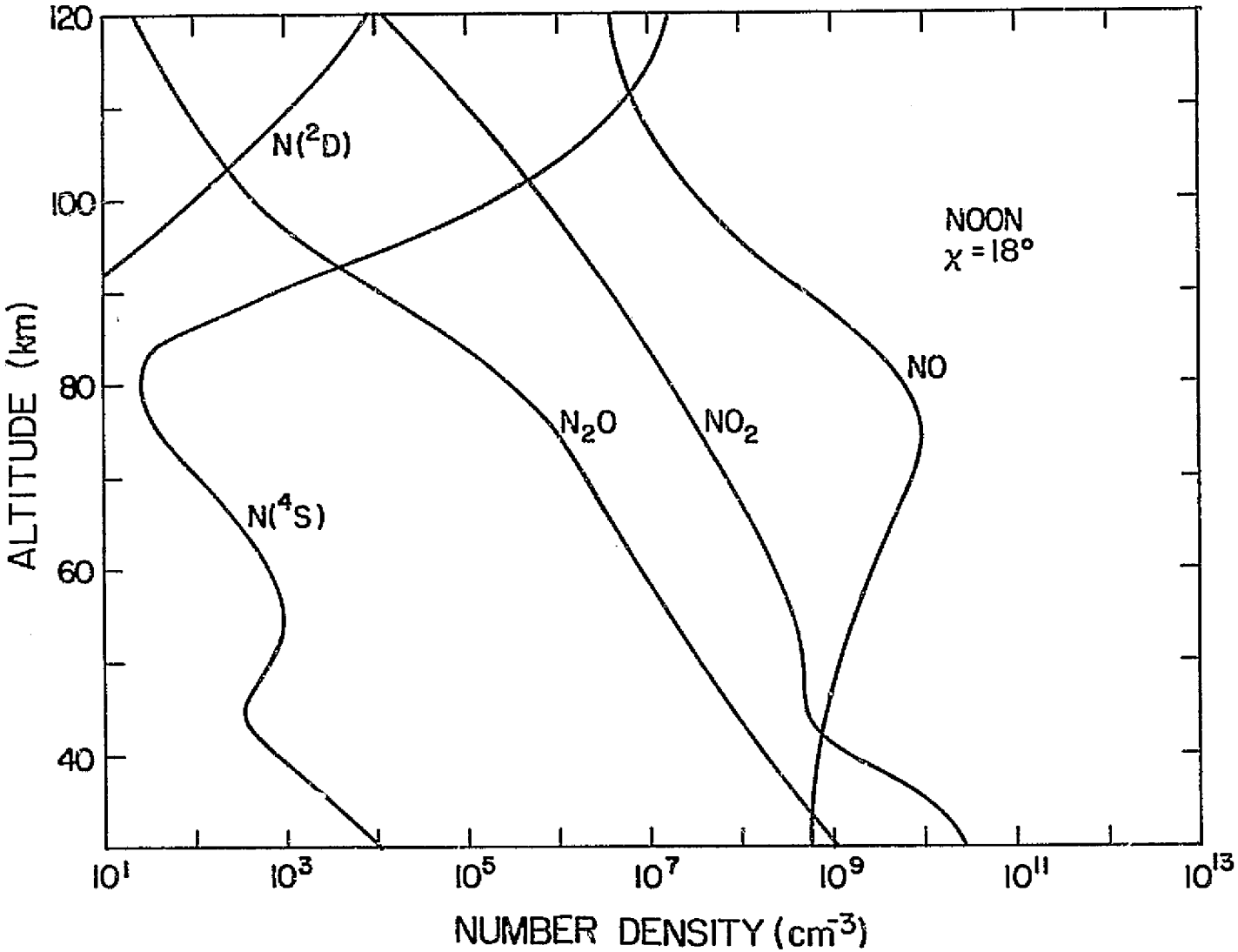

Figure 3.4 The height distributions of nitrogen and oxygen-hydrogen constituents at noon, obtained as initial values.

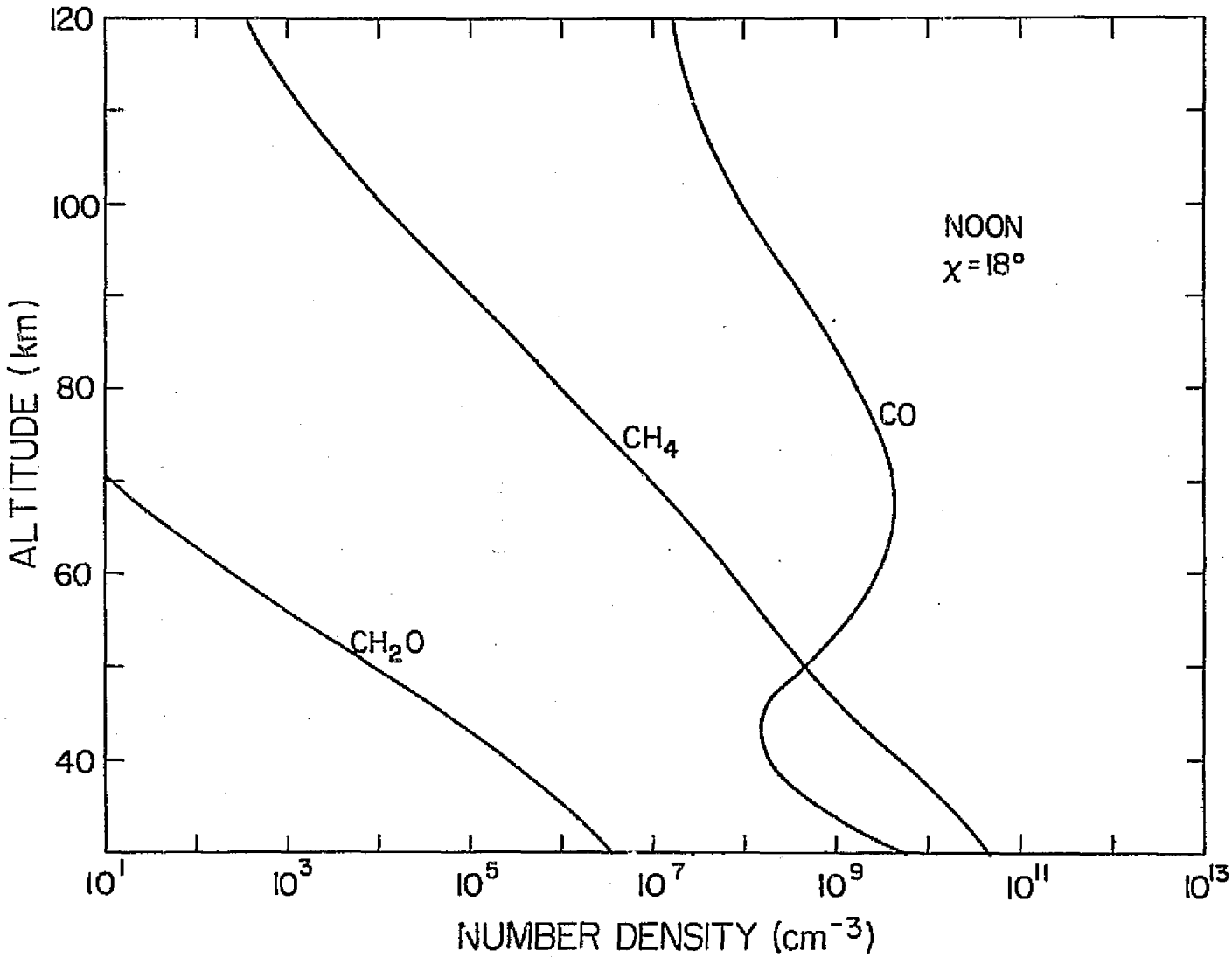

Figure 3.5 The height distributions of carbon constituents at noon, obtained as initial values.

The calculated amounts of these two constituents, CH_4 and CO were found to have negligible effect on the distribution of the O-H species, OH, in particular [*Ratnasiri and Sechrist*, 1971]. Hence, these constituents are not incorporated in the diurnal model calculations.

3.5 *Constant Zenith Angle Calculations*

The height distributions of the minor neutral constituents obtained as initial values in the last section do not represent any real situation. The calculation of more realistic values involves the simulation of the diurnal variation of the incident solar flux, and repeating the calculations over several diurnal cycles. In this study, however, an intermediate set of calculations has also been made in order to investigate the effects of transport mechanisms on the distribution of the long-lived constituents. This is done by keeping the solar zenith angle constant at 18° corresponding to noon conditions. Only the high D_e values have been used in these calculations which are continued with time increments of one-half hour until convergence in the distribution of most of the constituents is reached.

3.5.1 *Oxygen and oxygen-hydrogen constituents.* The height distributions of the oxygen species, $O(^3P)$, $O(^1D)$, $O_2(^1\Delta_g)$ and O_3 calculated using the transport model with the solar zenith angle fixed at noon, are shown in Figure 3.6. Comparing these with the corresponding distributions obtained as initial values using the photochemical model, it is seen that significant differences between the two sets of results appear mostly above about 55 km.

With the eddy diffusion coefficients adopted, the time constants against eddy diffusion in the stratosphere are found to be of the order of several months. As such, for any constituent having a small chemical

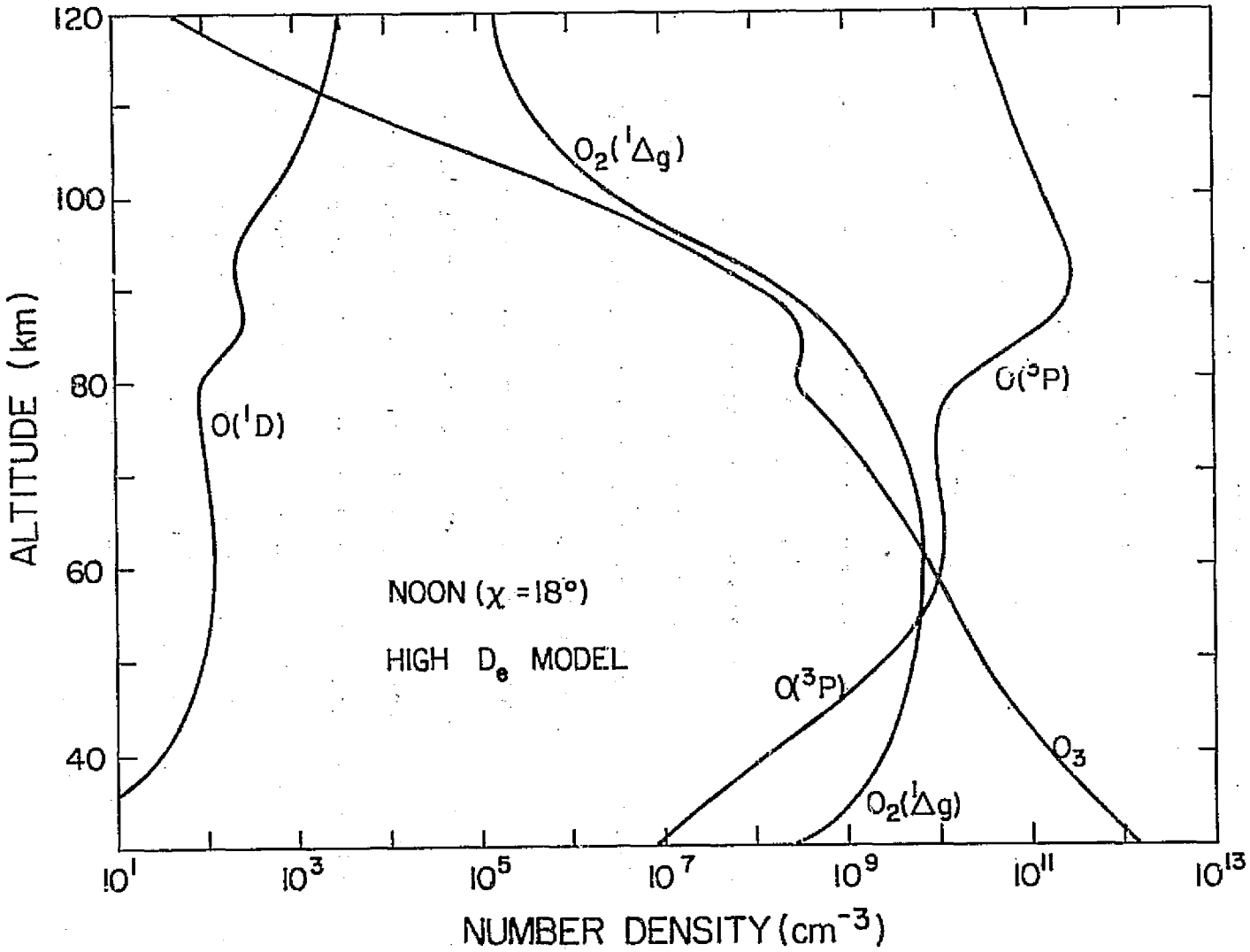

Figure 3.6 The height distributions of oxygen constituents at noon, calculated using the transport model corresponding to a constant zenith angle and high eddy diffusion coefficient profile.

loss rate, the effects of diffusion do not show up in a time-dependent calculation where the simulation is carried out over a few days only. Any changes in the height distributions in this region, therefore, occur due to changes in the photochemical loss and production rates, rather than due to diffusive processes. In both sets of calculations discussed above, the photochemical production and loss rates in the stratosphere are more or less the same. This explains the similarity in the two sets of results which appear below 55 km.

On the other hand, near the mesopause the time constants against eddy diffusion are of the order of a day. Hence eddy diffusion controls the distribution of the species whose chemical loss rates have long time constants. This becomes apparent in the case of $O(^3P)$, where the two sets of results show marked differences in the mesosphere and above. The $[O(^3P)]$ profile reaches a peak between 90 and 95 km. Above this peak, the distribution is determined by eddy diffusion and the upward flux across the boundary. This upward flux causes the concentration in this altitude range to deplete below the values given by the photochemical model. Below the peak, both the photochemical and diffusive models show a sharp drop, the drop being more prominent in the latter than in the former. This is a consequence of the fact that the diffusive model is also time dependent while the photochemical values are obtained on the assumption of quasi-equilibrium conditions. When the oxygen species $O(^3P)$ and O_3 are allowed to remain with the hydrogen species H and OH, the resulting reactions cause the net conversion

$$O(^3P) + O_3 \longrightarrow 2\ O_2$$

Unless the eddy diffusion values are very high, the above conversion proceeds with time, resulting in the sharp drop of $O(^3P)$ concentration. This drop, however, is arrested below about 75 km when the H concentration drops causing one of the conversion reactions,

$$H + O_3 \longrightarrow OH + O_2$$

to slow down. Further, in the initial set of calculations only this hydrogen reaction was included, and the rest of the reactions involving both OH and HO_2 were left out in obtaining the $O(^3P)$ and O_3 values.

The above reaction between H and O_3 is also important as a loss process for O_3 in the mesosphere. During the daytime, ozone is lost mainly through photodissociation which has a high rate of about 10^{-2} sec^{-1} down to the stratosphere. However, over a small height interval corresponding to the region where the peak in the [H] profile exists, the loss through this reaction becomes comparable to or even dominate the loss through photodissociation depending on the peak [H] value. This causes a cyclic chain of reactions to take place among the constituents $O(^3P)$, O_3, H and OH. The depletion of odd oxygen species $O(^3P)$, and O_3 caused by these chain reactions is responsible for the irregularities present in both $[O(^3P)]$ and $[O_3]$ profiles around this height range. When the eddy diffusion coefficients used are too low, this mechanism can even produce a sharp valley in the $[O(^3P)]$ profile.

In the stratosphere, the production of odd oxygen species is controlled mainly by the Herzberg band dissociation of O_2. Because of the high efficiency of the three-body reaction

$$O + O_2 + M \longrightarrow O_3 + M$$

in the stratosphere, the oxygen atoms will get converted to O_3 molecules. Between O and O_3, therefore, the dominant species is O_3 at these altitudes. The time constants for the chemical loss of both $O(^3P)$ and O_3 are very short, and the vertical diffusive processes have no significant effects on their concentrations. As such, both the photochemical and the diffusive models give more or less the same values for the $[O(^3P)]$ and $[O_3]$ profiles in the stratosphere.

The distribution of the two metastable species $O(^1D)$ and $O_2(^1\Delta_g)$ are closely related to the distributions of the other oxygen species. The changes in the profiles of these two species can therefore be attributed to the changes taking place in the $[O(^3P)]$ and $[O_3]$ profiles.

In Figure 3.7, the height distributions of the hydrogen species, H, H_2, H_2O, OH, HO_2, and H_2O_2 are shown. The initial values of these constituents were determined first by calculating the distribution of H_2O using a steady-state continuity equation having the transport term, and then using the photochemical equations to determine the distribution of the rest of the constituents. In these calculations, the reformation of H_2O through reactions occurring among other species was not considered. This, however, was accounted for in the new set of calculations. However, the two H_2O profiles do not show any significant changes except that in the diffusive model, the values are slightly higher towards the upper end.

Among the other O-H species, the constituents that were affected most as a result of diffusive processes are H and H_2. Both of these have long

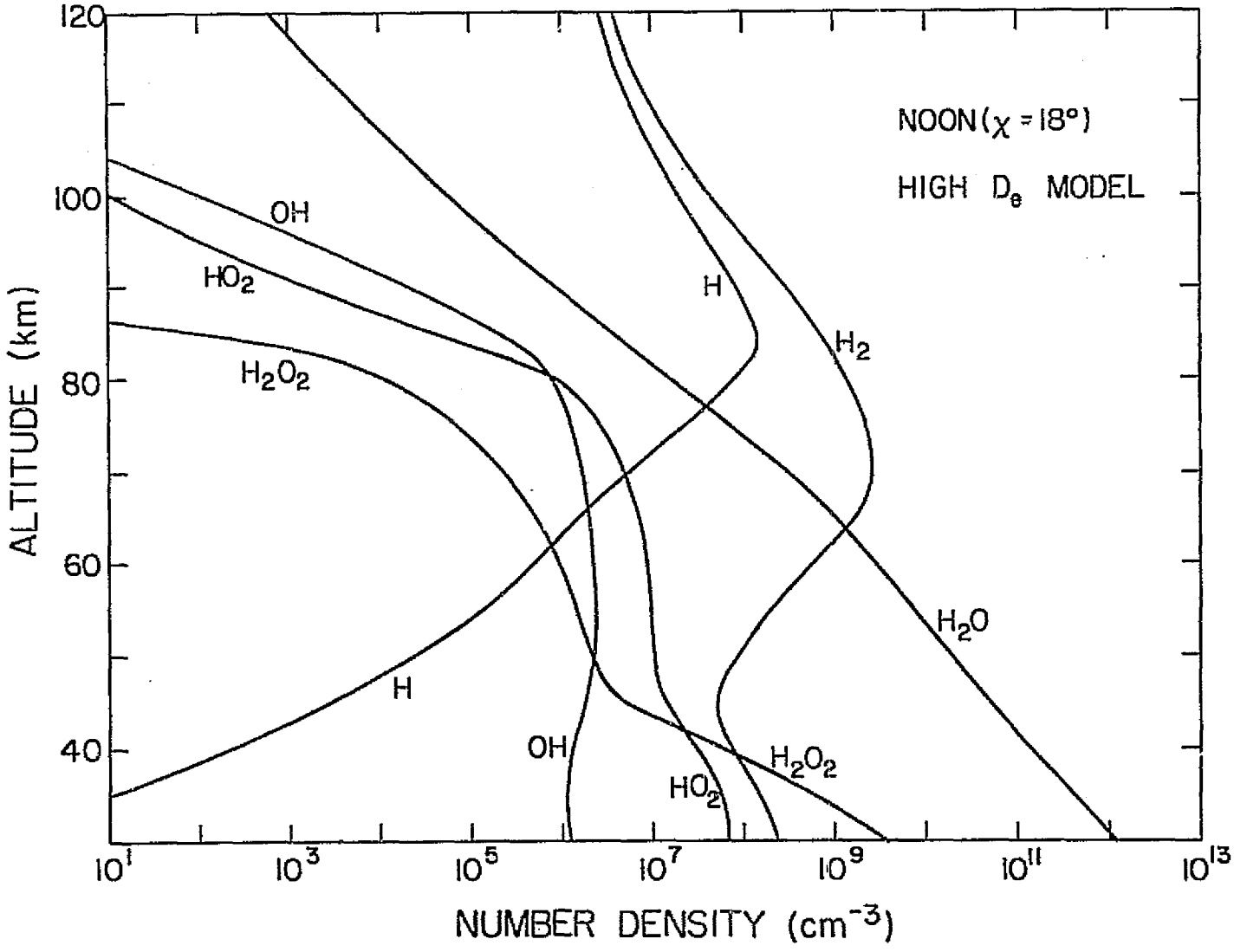

Figure 3.7 The height distributions of hydrogen and oxygen-hydrogen constituents at noon, calculated using the transport model corresponding to a constant zenith angle and high eddy diffusion coefficient profile.

time constants against chemical losses, particularly in the lower thermosphere. Atomic hydrogen, in a manner similar to the atomic oxygen profile, exhibits a peak abundance near 85 km. Above this peak, the profile resembles one given by diffusive equilibrium. Below the peak level, the photochemical and the diffusive profiles are generally of the same shape, though the absolute values differ by about a factor of 10 or more in the stratosphere. In view of the approximations made in calculating the initial values such a difference could be expected.

For the molecular hydrogen too, values are mostly affected in the lower thermosphere where the diffusive processes cause an increase in its concentration. Around 70 km, the profile has a broad peak, and below this the $[H_2]$ values are only slightly changed in the new profile.

The remaining O-H species, OH, HO_2, and H_2O_2 all have short time constants at all heights during the daytime. Hence their concentrations could be determined by photochemical equations. Their chemistry is closely linked with that of $O(^3P)$ and H. As mentioned before, both of these constituents have their concentrations reduced in the lower thermosphere due to the action of diffusive processes. As a consequence, the concentration of the species OH, HO_2, and H_2O_2 also drop at a faster rate above 80 km in the diffusive model. Below this height the three profiles have almost the same features as those found in the photochemical model. The differences in the absolute values that are present in these profiles could be attributed to changes in the $[O(^3P)]$ and $[O_3]$ profiles.

3.5.2 *Nitrogen and oxygen-nitrogen constituents.* This series of calculations was done first by determining the height profile of N_2O. In both the initial and the new set of calculations, continuity equations

with the diffusion term were used. Hence the profile of N_2O appearing in Figure 3.8 is similar to that shown in Figure 3.4. There is no significant production and its abundance there is due to the particles carried upwards from the troposphere.

The atomic species $N(^4S)$ and $N(^2D)$ are calculated in a manner similar to that discussed in the previous section. The branching ratios used for the reactions producing $N(^2D)$ were both 0.75. It is seen that while the profiles of $N(^2D)$ in the two sets of calculations are similar, the profiles of $N(^4S)$ differ widely, particularly in the mesosphere. This difference can easily be attributed to the difference in the profiles of NO. This constituent has a time constant of the order of several days in the mesosphere and therefore the photochemical equations, as used in the initial set of calculations, do not yield correct values. Consequently, the [NO] profile shows increased values with a peak near 75 km. In the transport model, however, diffusion causes the profile peak to move downwards as the NO, which is produced in the thermosphere, is allowed to diffuse downwards. This causes a minimum near 85 km in the new NO profile, and above this height the profile remains almost constant at a concentration about 3×10^7 cm^{-3}. Its broad maximum now lies around 40 km with a value nearly 2×10^9 cm^{-3}. The reduced NO concentration in the mesosphere causes the corresponding $N(^4S)$ concentration to increase, as the loss of $N(^4S)$ is mainly due to its reaction with NO.

The changes occurring in the [NO] profile as a result of introducing the diffusive transport term into its continuity equation are also reflected in the distribution of NO_2. This constituent and NO are strongly coupled to each other, as discussed in the previous chapter. During daytime, NO_2 is lost mainly through its reaction with $O(^3P)$ down to about 50 km,

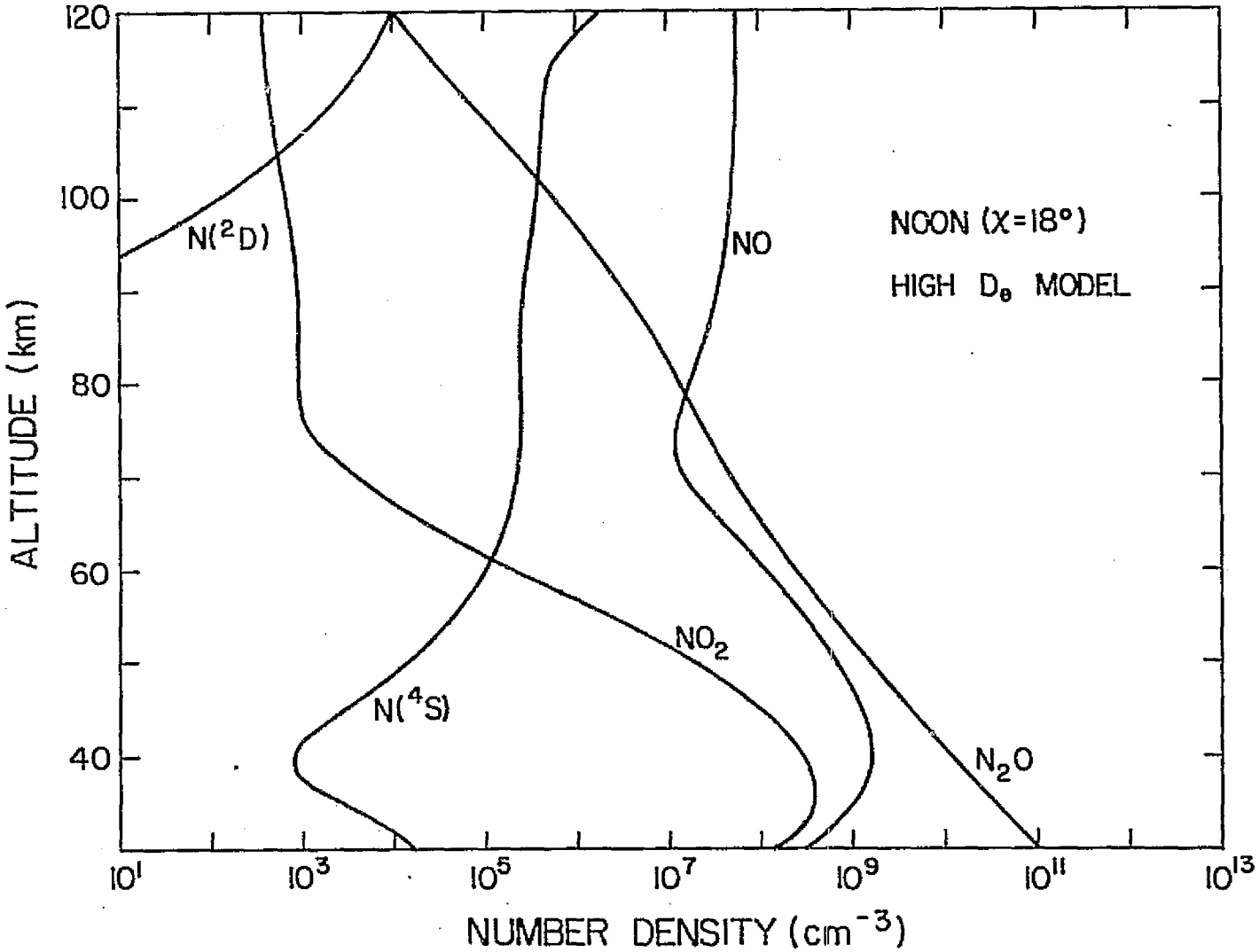

Figure 3.8 The height distributions of nitrogen and oxygen-nitrogen constituents at noon, calculated using the transport model corresponding to a constant zenith angle and high eddy diffusion coefficient profile.

and through photodissociation below 50 km. The time constants vary from about one second in the lower thermosphere to about a few minutes in the stratosphere. Hence, in this new set of calculations too, photochemical equations were made use of for the determination of the NO_2 profile. The production of NO_2, however, depends on the concentration of NO. For this reason, the values of NO_2 were also reduced several orders of magnitude below the levels obtained previously. Near 75 km, this value is about 1×10^3 cm^{-3}, while above this height, it remains constant corresponding to the constant values of NO. In the stratospheric height range 40-55 km, the NO_2 concentration is of the order of 10^8 cm^{-3}. The $[NO_2]/[NO]$ ratio given by these profiles is about 0.5 below 35 km, and drops through several orders of magnitude in the mesosphere. In the photochemical model, however, NO_2 has a value of 1×10^6 cm^{-3} at 75 km, a factor of 1000 more than the corresponding transport model value. For values towards the two boundaries, such as at 40 km and 100 km, the two models give similar results.

The above results show that eddy diffusion affects not only the constituents having long time constants, but also the constituents having short life times as well. This is a consequence of the dependence of the short lived constituents on the long lived types, whose height distributions are determined by the transport processes.

3.6 *Diurnal Variation of Neutral Species*

The simulation of the diurnal variation of the constituent concentrations was next carried out using the results obtained in the previous section as initial values. The zenith angle was varied in steps of 10° between 20° and 70°, and in steps of 5° between 70° and 100°. Between noon and sunset, and between sunrise and noon, the time increments required

for the solution of the partial differential equations were obtained from the above χ increments. Beyond 100° of the zenith angle, time steps of one hour were used. Since the scope of this work is to study the changes of the *D* region taking place during the daytime, the detailed variations occurring at sunrise and sunset were not included. In all the calculations, the height increment was maintained at 1 km.

During daytime the photodissociation rates were determined at each time step using the O_2 concentrations required for the calculation of the optical depth factor obtained from the previous time step. For χ angles greater than 100°, the photodissociation rates were all made equal to zero. At the upper boundary, constituents such as O_2, H_2O, and N_2O were subject to a flux boundary condition expressed in terms of their dissociation rates. Since the dissociation rates at night were zero, the fluxes of these constituents across the upper boundary during nighttime were automatically made to vanish. In reality this may not be true. However, the errors introduced by using this method are not expected to affect the values below about 100 km.

The calculation of the diurnal variation was done for two eddy diffusion models, discussed in Section 3.1.1. The simulation was continued until 24-hour reproducibility in values were obtained for most of the constituents. For certain constituents such as NO and H this condition was not reached within a reasonable period. Since this variation was small, the computation was, however, terminated after 10 days of simulation. On the final day of simulation, the concentration values of all the neutral constituents were written onto a magnetic tape at every time step between sunrise and sunset, for use with the ionic species calculations.

3.6.1 *Oxygen constituents.* The noon distributions of the oxygen species O_3, $O(^3P)$, $O(^1D)$, and $O_2(^1\Delta_g)$ obtained on the 10th day of simulation are shown in Figures 3.9 and 3.10, which correspond to the high and low eddy-diffusion models, respectively. Comparing the $O(^3P)$ profile in Figure 3.9 with that in Figure 3.6, which was given for a fixed sun, it appears that the two profiles differ only above 70 km. The main feature in the new profile is the reduced gradient between 70 and 85 km and the reduced peak value, which is now about 1×10^{11} cm^{-3}. In view of the shorter duration over which photodissociation production of $O(^3P)$ is allowed to take place, this reduction in the amount of $O(^3P)$ in the region where diffusion occurs can be understood. With the low eddy diffusion model (Figure 3.10), however, the rate of removal of the $O(^3P)$ into the thermosphere is reduced and consequently the peak concentrations occurring near 90 km increases to a new value of 3.2×10^{11} cm^{-3}. When the transport effects becomes reduced, the coupling between the reactions involving $O(^3P)$, OH, O_3, and H become stronger, and as a result, irregularities in the profiles of these constituents can occur in the regions where such coupling dominates. This is shown in the low eddy diffusion profile of $O(^3P)$ which has a minimum and a maximum near 80 km.

The diurnal variation of $O(^3P)$ under both high and low eddy diffusion values are shown in Figures 3.11 and 3.12, respectively. The high eddy profile shows a significant variation between noon and predawn in the lower thermosphere, whereas the corresponding variation in the low eddy profile is not very significant. The behavior of the two profiles in the mesosphere at $\chi = 60°$, both in the morning and evening, is similar though the absolute values differ slightly. In both of these sets of curves, the higher values in the thermosphere are given by the afternoon profile while the morning profile shows lower values.

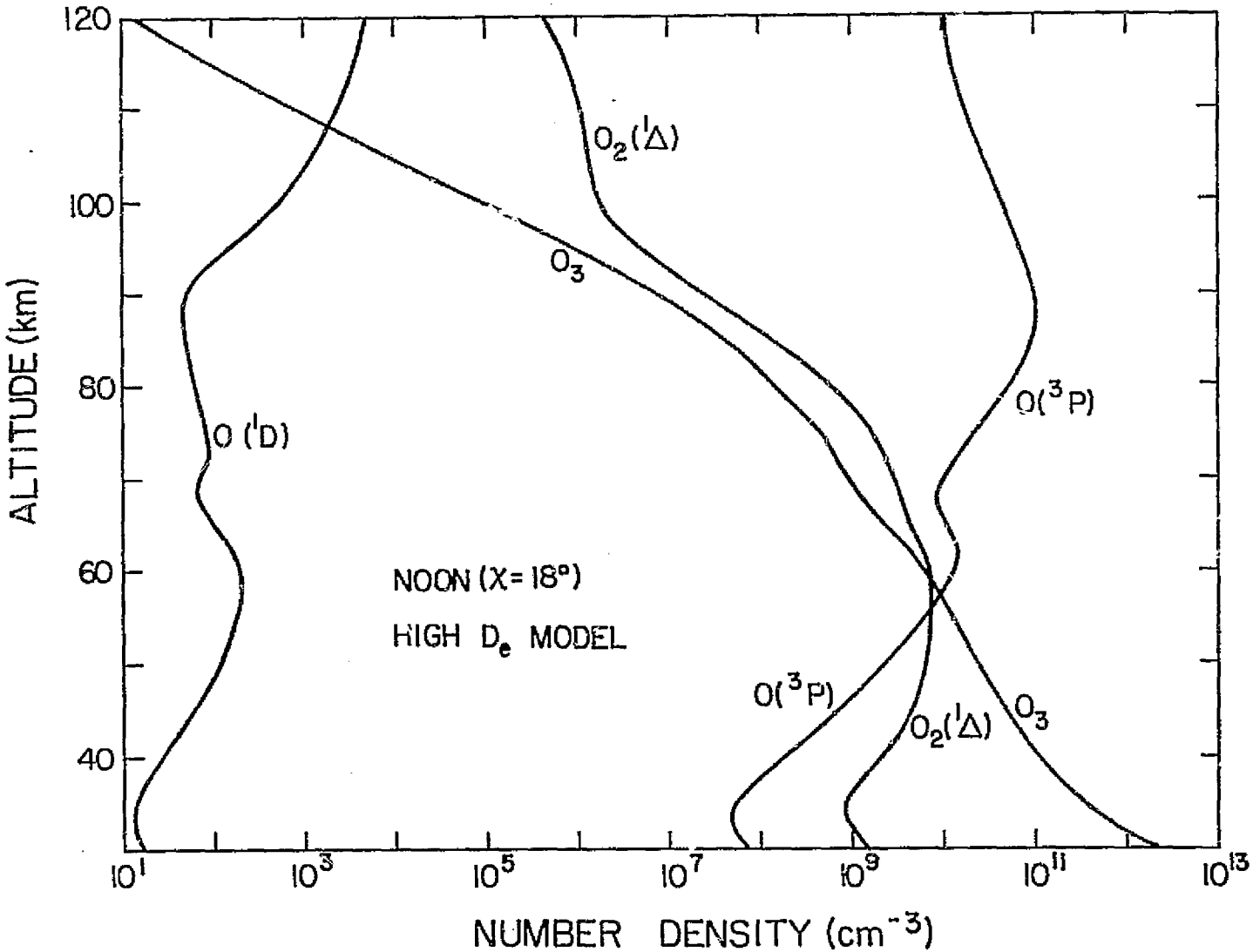

Figure 3.9 The height distribution of oxygen constituents at noon, calculated using the diurnal model with high eddy diffusion coefficient profile.

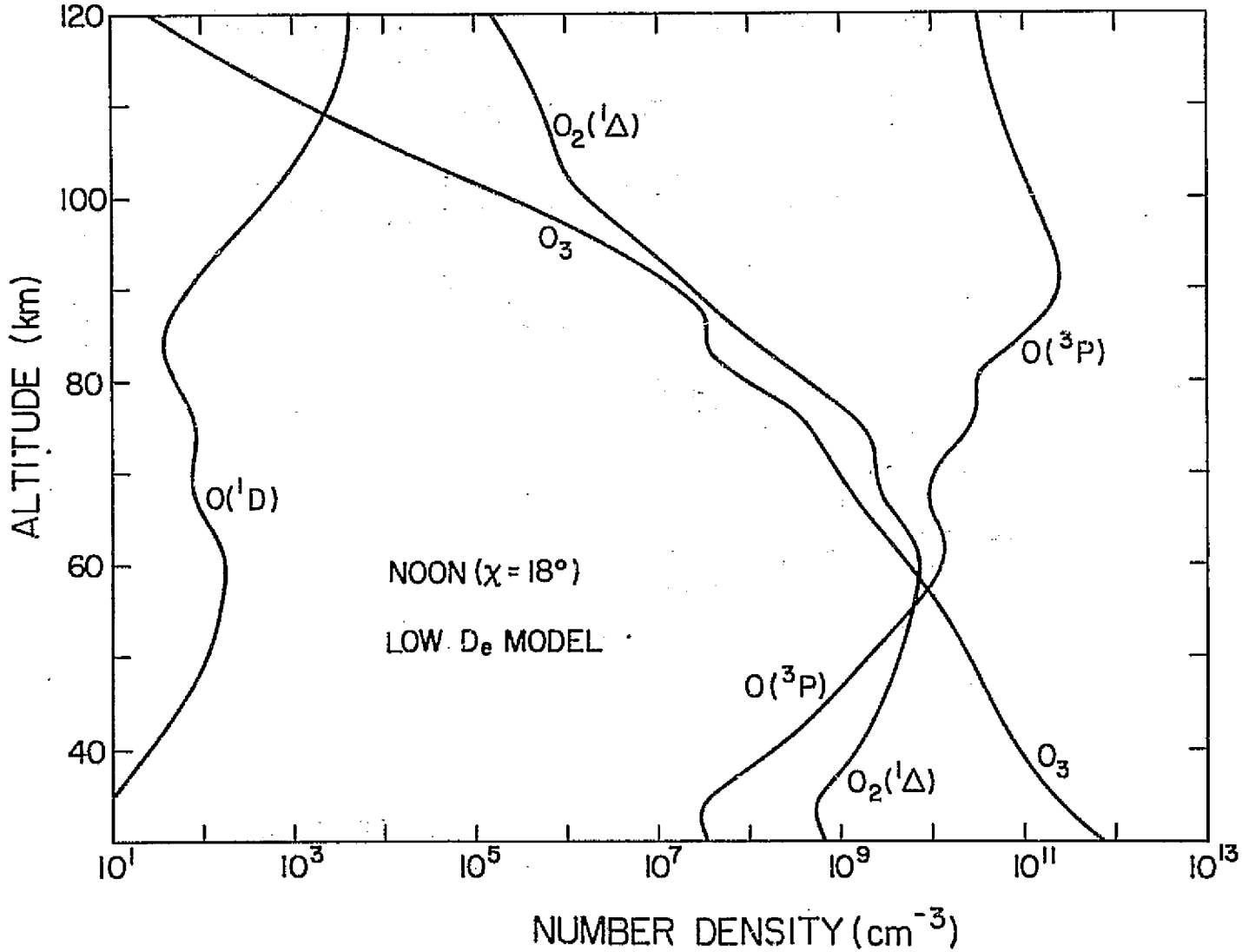

Figure 3.10 The height distribution of oxygen constituents at noon, calculated using the diurnal model with low eddy diffusion coefficient profile.

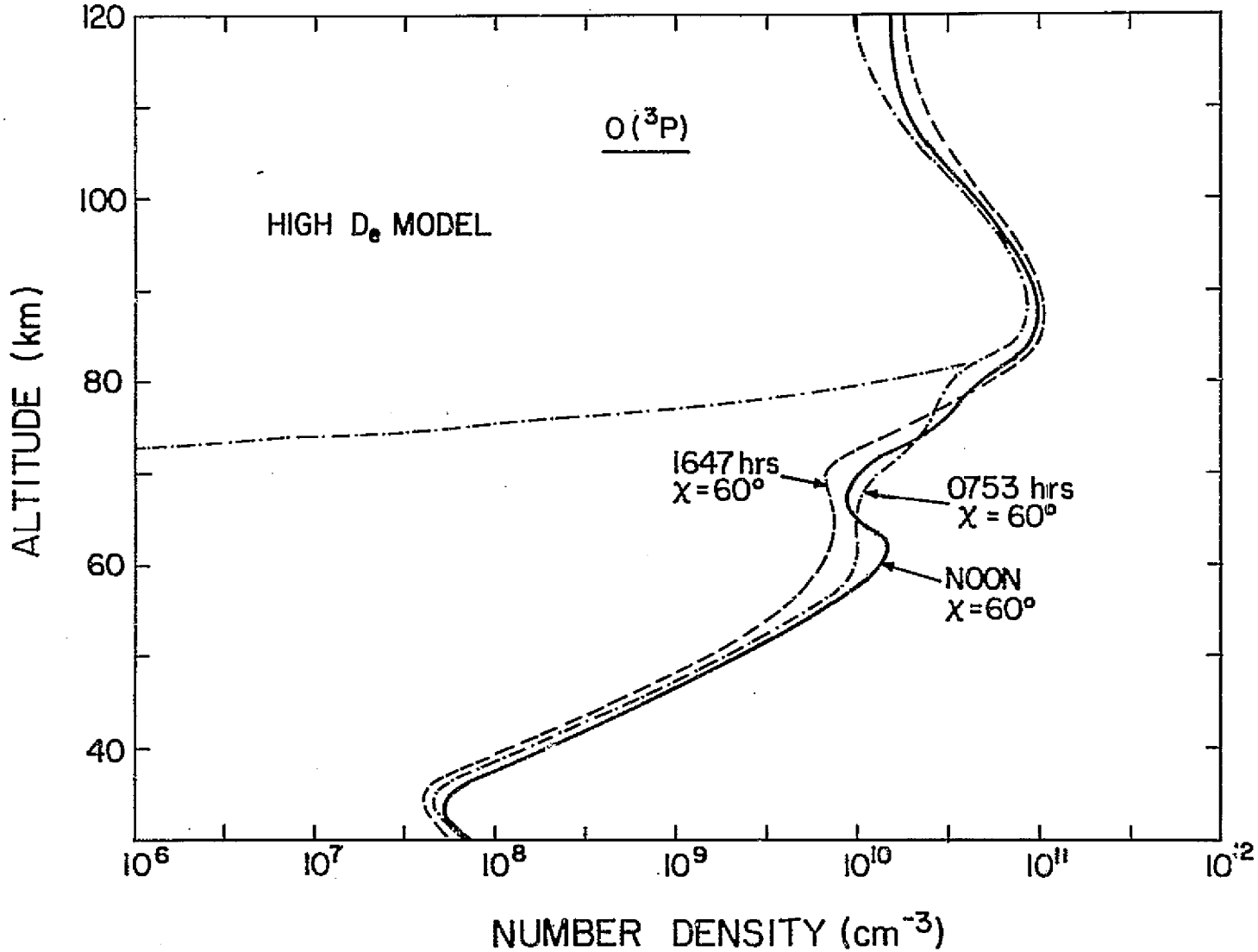

Figure 3.11 The height distribtuions of O(^{3}P) at noon, 60° zenith angles and pre-dawn, calculated using the diurnal model with high eddy diffusion coefficient profile.

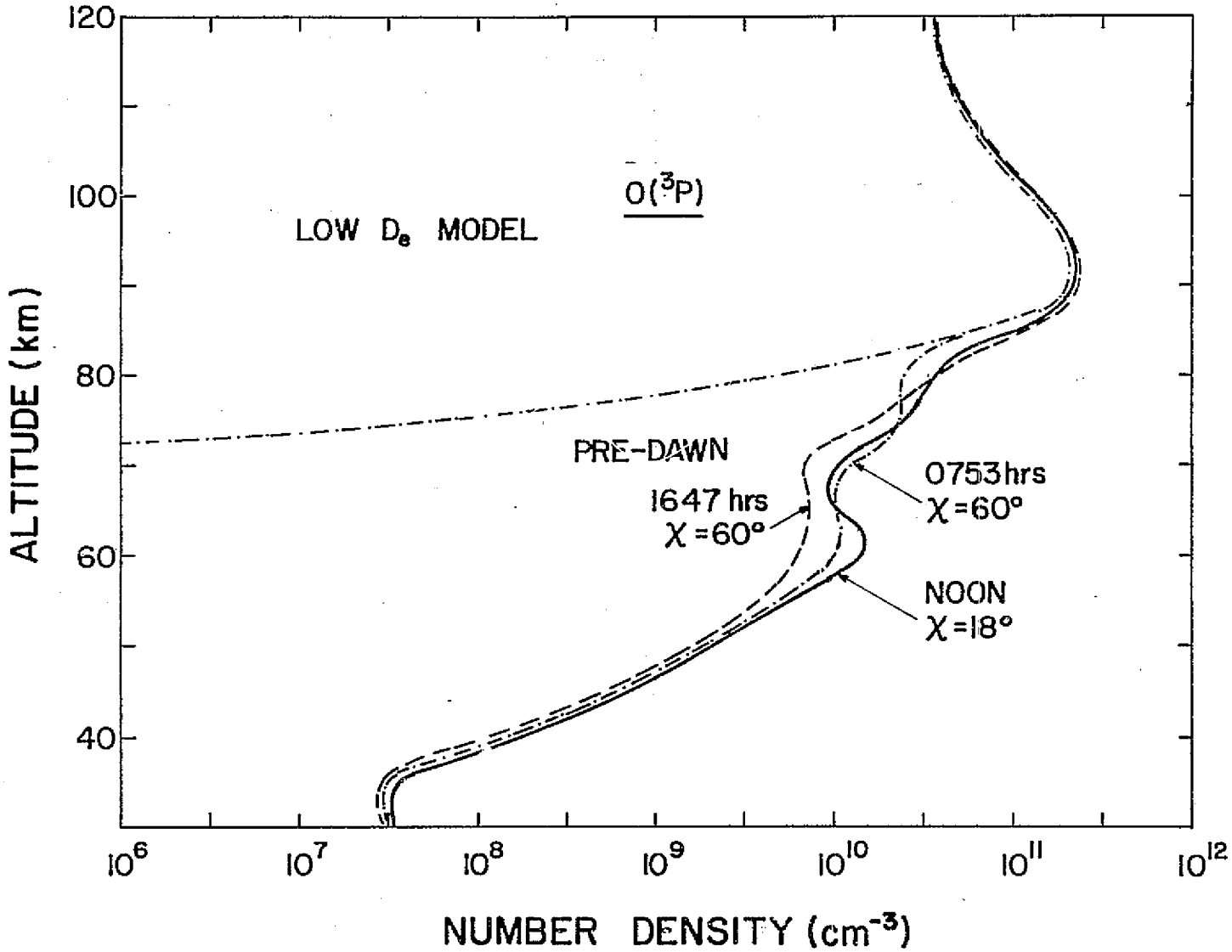

Figure 3.12 The height distributions of $O(^3P)$ at noon, 60° zenith angles and pre-dawn, calculated using the diurnal model with low eddy diffusion coefficient profile.

An interesting feature in these profiles is the increase in the morning values over the noon and evening values between 65 and 75 km. This could probably be due to the higher contribution to $O(^3P)$ production due to O_3 dissociation which has higher values over this height range in the morning than during noon or evening. The secondary peak appearing around 60 km in both the noon profiles is also absent in the two $\chi = 60°$ profiles. At this height, the difference in the concentration between the noon and the evening $\chi = 60°$ concentration is about a factor of 4. In the stratosphere, all three profiles have the same slopes though the actual values are lower by about a factor of 2 in the afternoon than in the noon. The predawn profiles, in both sets of profiles, vanish below about 80 km.

The two ozone profiles shown in Figure 3.9 and 3.10 corresponding to high and low eddy diffusion models have more or less the same values below about 75 km. The low diffusion profile shows a small irregularity around 85 km as mentioned before, so that around this height the profile corresponding to the low eddy diffusion has higher values. Between 85 and 75 km, however, it has lower values than the profile corresponding to the high eddy diffusion model. This behavior of O_3 is directly governed by that of $O(^3P)$, whose profiles are influenced greatly by the transport effects.

The variations occurring in the O_3 profiles are also reflected in the profiles of $O_2(^1\Delta_g)$ shown in Figures 3.13 and 3.14, for the two cases of high and low eddy diffusion coefficients, respectively. Below about 65 km, the photodissociation of O_3 is mostly responsible for the production of $O_2(^1\Delta_g)$, and therefore its concentration follows closely that of O_3. Consequently, both the high diffusion profile (Figure 3.13) and the low diffusion profile (Figure 3.14) show similar values below 65 km.

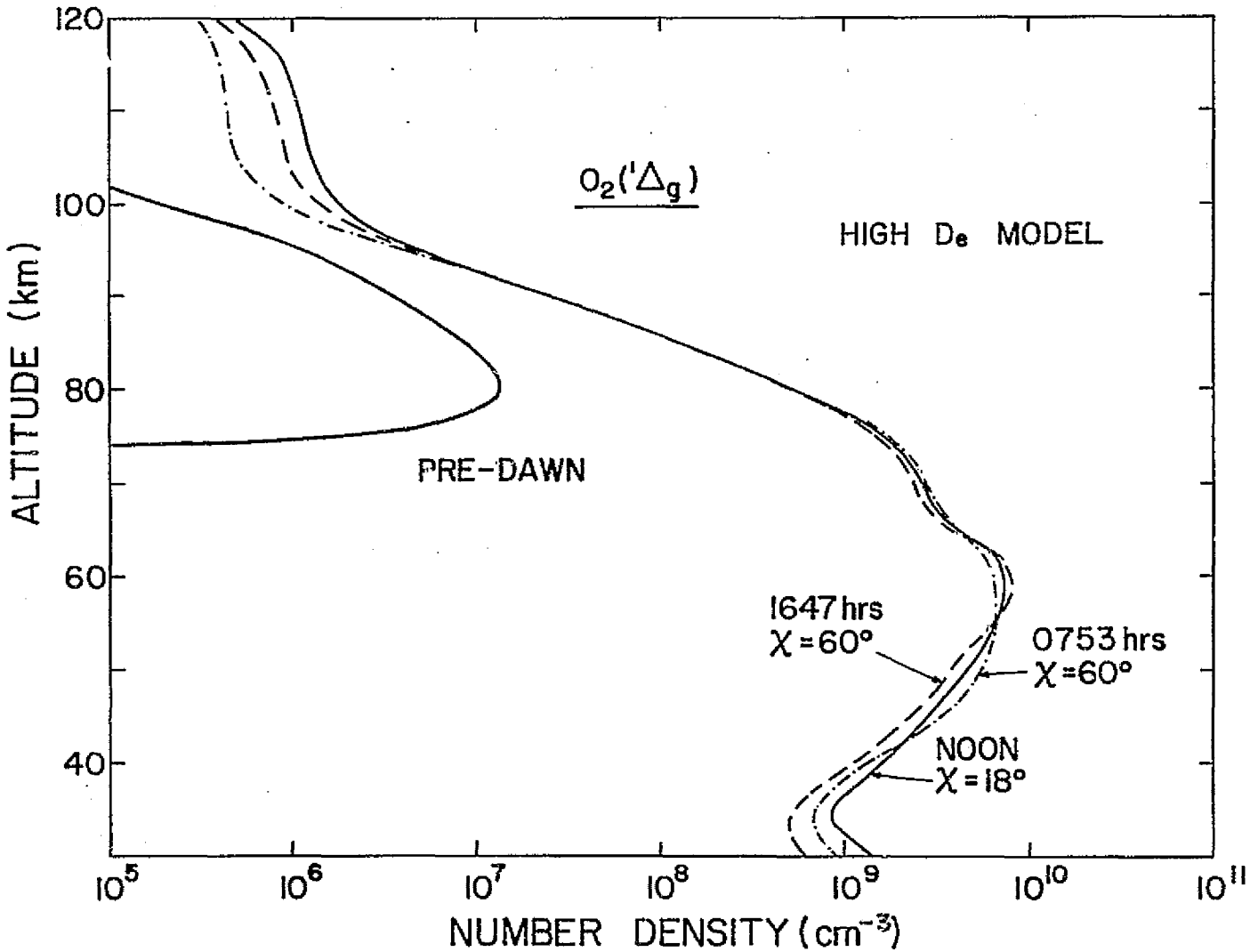

Figure 3.13 The height distributions of $O_2(^1\Delta_g)$ at noon, 60° zenith angles and pre-dawn, calculated using the diurnal model with high eddy diffusion coefficient profile.

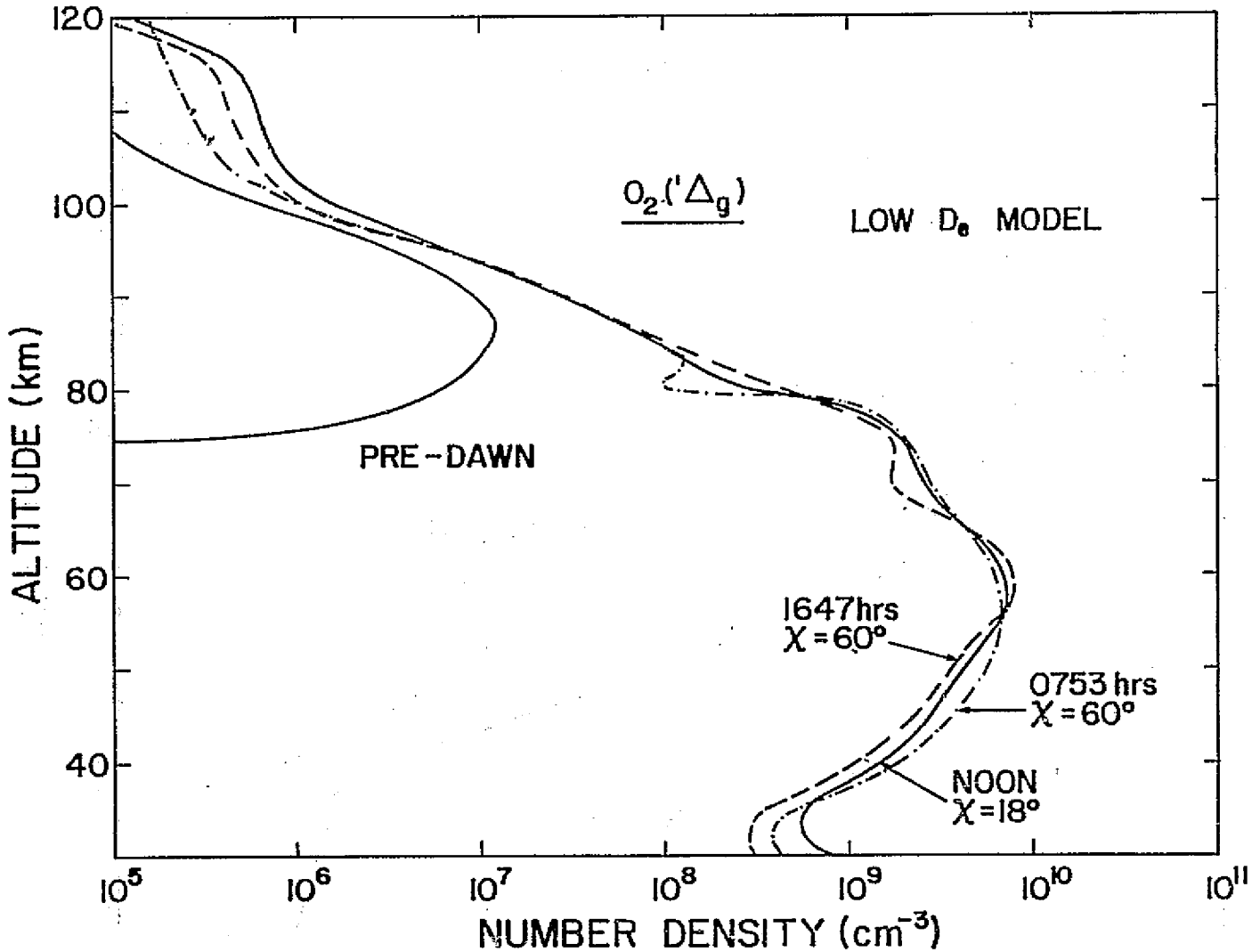

Figure 3.14 The height distributions of $O_2(^1\Delta_g)$ at noon, 60° zenith angles and pre-dawn, calculated using the diurnal model with low eddy diffusion coefficient profile.

In these profiles, the evening values exceed the morning values between 55 and 65 km, while immediately below and above, the opposite takes place. The exact height limits depend on the eddy diffusion coefficient used in each case. The morning profile with the low D_e also shows an irregularity at 80 km not shown in the other profiles, and this could be directly related to the behavior of the O_3 profile in the morning. Between 80 and 95 km, both sets of profiles do not show any variation with the zenith angle. Above this height again, however, there is marked diurnal variation taking place, caused by the dependence of $O_2(^1\Delta_g)$ production on the $O(^3P)$ concentrations.

The diurnal variation of the oxygen constituents has been studied recently by *Shimazaki and Laird* [1970, 1972], *Thomas and Bowman* [1972] and *Hunt* [1971b; 1973]. Direct comparison of the results of the present study with the results of these workers is rather difficult in view of the different parameters used by them. Nevertheless, the general features found in the results of these studies are present in the profiles of the present study.

Both the solar flux in the 1300 - 2000 Å band and the eddy diffusion coefficient used in this study agree closest with those used by Thomas and Bowman and by Hunt. Hence, a meaningful comparison of the results obtained here could be made with their results.

The $O(^3P)$ peak concentration at noon at 90 km obtained by Thomas and Bowman is about 1.6×10^{11} cm^{-3} while the corresponding value obtained by Hunt is 3×10^{11} cm^{-3}. These agree well with the results obtained with the low diffusion model which has a peak value of 2.5×10^{11} cm^{-3} at 91 km. The minimum present near 70 km which has a value of 1×10^{10} cm^{-3}

also agrees well with the results of these workers. The nighttime values in all these models vanish below about 80 km, while above this height the profiles do not show any significant diurnal variation, as found in the present study. The slight discrepancies present in these height distributions are probably due to the different values adopted for various parameters such as the eddy diffusion coefficients, recombination rate constants and solar flux.

In recent times experimental determination of the $O(^3P)$ distribution in the lower thermosphere has been carried out using rocket-borne instruments. *Henderson* [1971] obtained values between 1×10^{11} and 8×10^{11} cm^{-3} in the height range 89-94 km. The presence of the peak in the $O(^3P)$ profile near 100 km was demonstrated by *Scholz and Offerman* [1974], who obtained peak values of 2.5×10^{11} and 6×10^{11} cm^{-3} in two flights using mass spectrometric measurements incorporating cryoion sources. *Good and Golomb* [1973], using NO/O chemiluminescence measurements obtained peak values lying in the range 4×10^{11} and 8×10^{11} cm^{-3} under different solar conditions, with the average peak height near 99 km. It appears that generally, both the theoretical and experimental peak values lie in the same range, while the experimental peak heights are a little higher than the corresponding theoretical values. In view of the present uncertainties in the various parameters mentioned earlier the agreement between the model calculations and the measured values of $O(^3P)$ can be considered as satisfactory.

The ozone profiles obtained in these model calculations all show the irregularity around 75-85 km, which is obtained with the low diffusion model in the present study. In Hunt's profile this has a value

around 1 x 10^8 cm^{-3}, while in Thomas and Bowman's profile the flat portion has a value near 3 x 10^7 cm^{-3}. The value of 3 x 10^7 cm^{-3} obtained in the present study agrees with this latter value. These results are however slightly less than the values deduced by *Evans and Llewellyn* [1970] who obtained peak concentrations of (1-3) x 10^8 cm^{-3} in the height range 85-90 km. The noon concentrations obtained near 60 km in all their profiles have more or less the same value of 1 x 10^{10} cm^{-3}, in agreement with the experimental values [*Hilsenrath*, 1971].

The observations by *Evans and Llewellyn* [1970] of the 1.27 μ emissions gave $O_2(^1\Delta_g)$ distributions having peak values of 2.5 x 10^{10} cm^{-3} between 50 and 60 km during the daytime. These values are about a factor of 3 higher than the calculated values. Such a discrepancy could easily arise in view of the many uncertainties in the production rate of $O_2(^1\Delta_g)$, such as the reaction rate constants and solar flux intensities responsible for the photolysis of O_3. The calculated values, however, are in closer agreement with the profiles obtained by *Thomas and Bowman* [1972].

3.6.2 *Oxygen-hydrogen constituents*. The noon profiles of the hydrogen species, obtained after diurnal simulation are shown in Figures 3.15 and 3.16, corresponding to the high and low values of D_e, respectively. The two sets of curves are almost identical below about 60 km while above this height the effects of using different eddy diffusion values become evident.

The $[H_2O]$ profile, under high eddy diffusion gives values higher by nearly an order of magnitude in the thermosphere than under low eddy diffusion. The loss of H_2O in the mesosphere and above due to photodissociation is replenished by the upward flux generated in the troposphere.

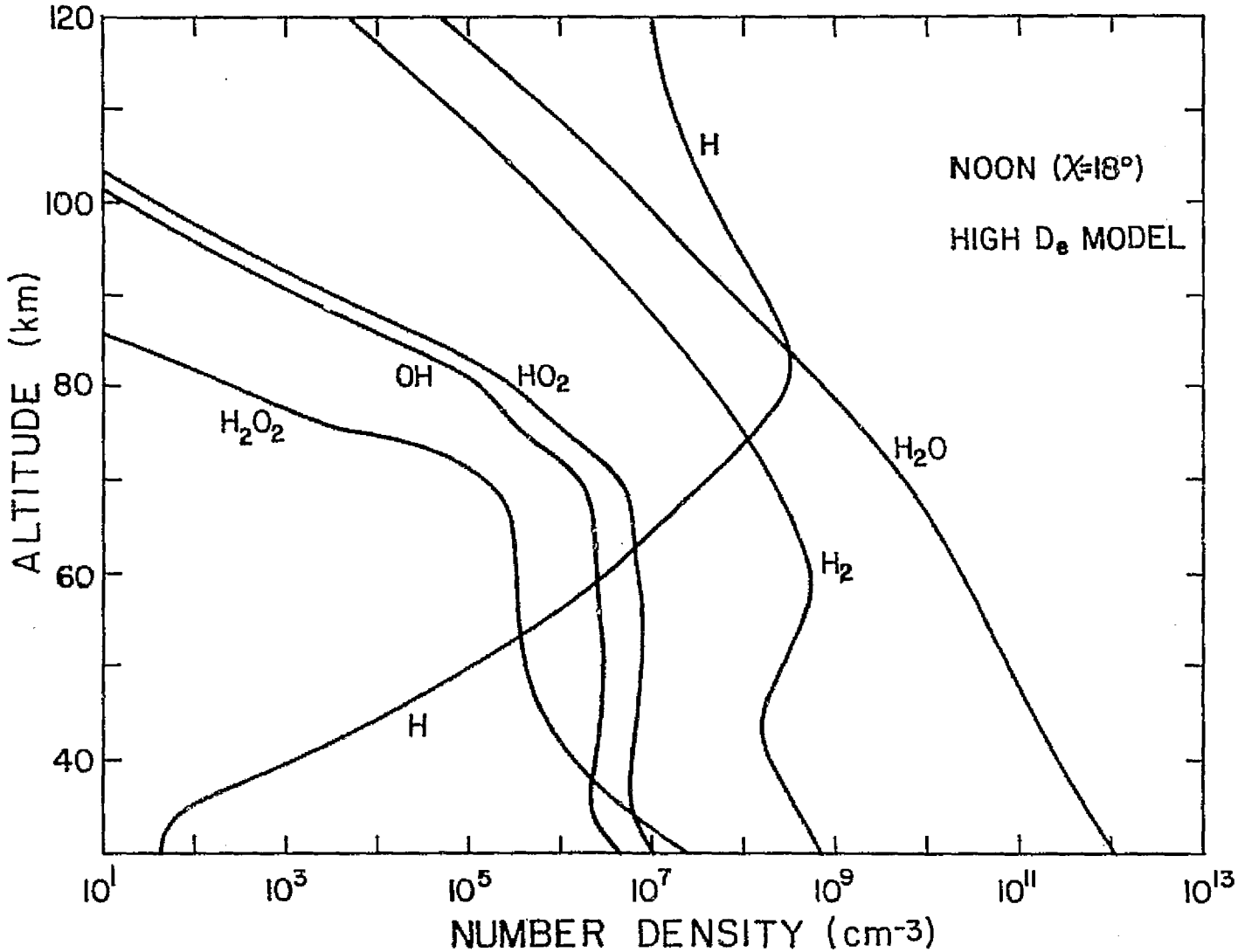

Figure 3.15 The height distributions of hydrogen and oxygen-hydrogen constituents at noon, calculated using the diurnal model with high eddy diffusion coefficient profile.

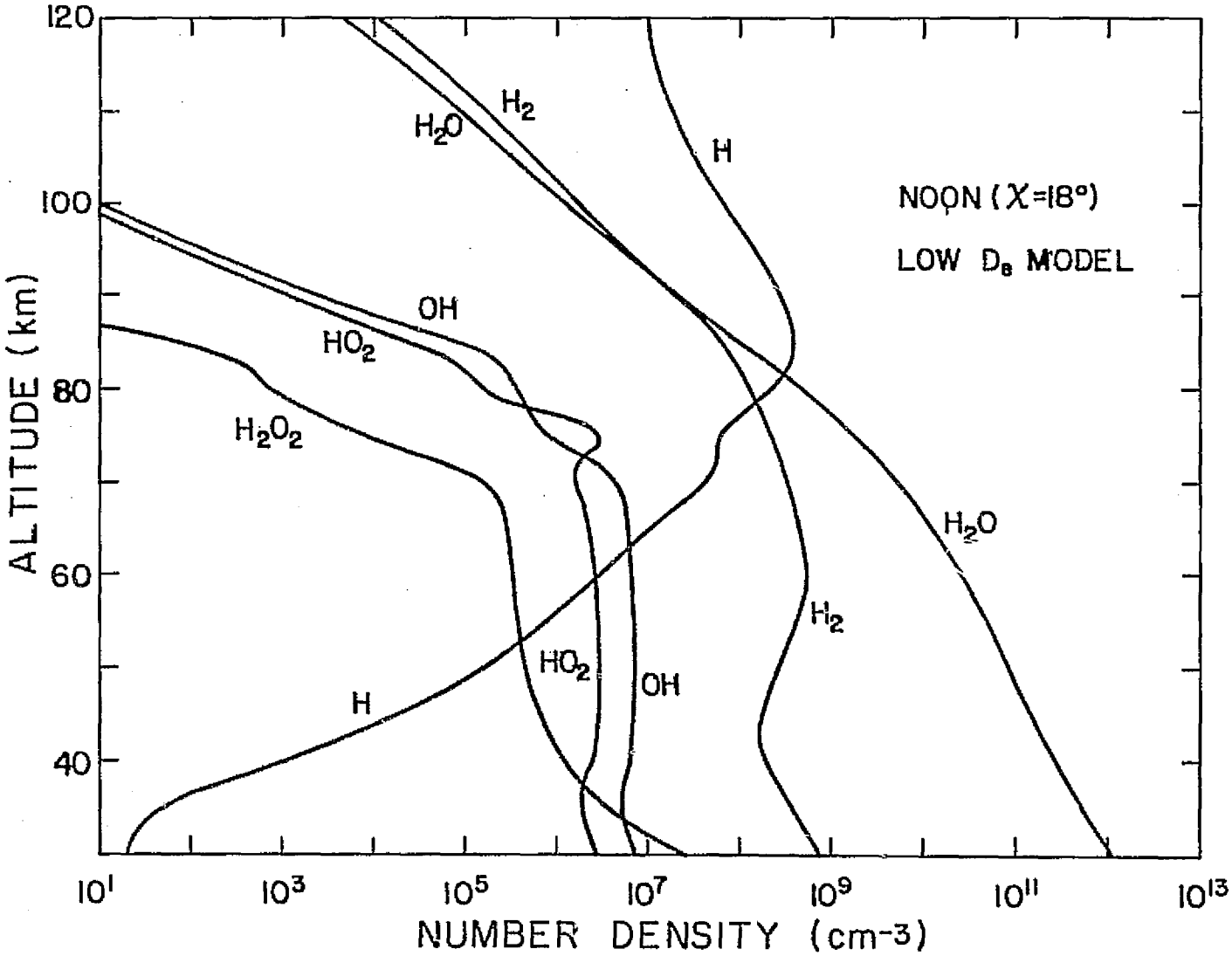

Figure 3.16 The height distributions of hydrogen and oxygen-hydrogen constituents at noon, calculated using the diurnal model with low eddy diffusion coefficient profile.

As such, the higher the eddy diffusion coefficient, the greater the concentration of H_2O at high altitudes, subject to the limiting values given by complete mixing ratios. Because of the large time constants involved in the loss of H_2O, it has no significant diurnal variation.

The low D_e atomic-hydrogen profile, while showing reduced values between 70 and 80 km, has increased values above this height range. At heights below, the values remain unchanged. The increase of values above the peak for this low D_e profile is somewhat similar to the behavior of atomic oxygen in this height range. The values at 120 km are the same for both curves, as constrained by the boundary condition. The profile of molecular hydrogen corresponding to the low D_e model also shows increased values above 65 km.

The more active constituents, OH and HO_2 exhibit only a little change, with the variation of the eddy diffusion coefficients, and even this was evident above 70 km only. Since both OH and HO_2 have short time constants in this part of the atmosphere, their concentrations are not directly affected by eddy diffusion. However, the variations in both [O] and [O_3], or [H], easily produce significant changes in [OH] and [HO_2]. Both sets of curves show near constant values below 70 km, while a sudden drop in their concentrations become a characteristic feature above this height. The [OH] profile shows an irregularity near 75 km, which is caused by the corresponding variations in both [O] and [H] at 75 km. This irregularity causes [OH] to have higher values than [HO_2] over the height range 73 and 78 km in the low diffusion model. In the high diffusion model there is no such cross-over. Further, the latter set of curves have slightly higher gradients than the low diffusion curves above 80 km. The H_2O_2

profile for both low and high diffusion profiles give the same values except over the region around 83 km where the low D_e values are slightly higher than the high D_e values.

The diurnal behavior of H is shown in Figures 3.17 and 3.18 for the high and low eddy models, respectively. As in the case of $O(^3P)$, the [H] profile reaches a peak at 85 km and vanishes in the nighttime below this height. The evening $\chi = 60°$ curve and the noon curve do not differ very much, except that the values cross over near 70 km. In both sets of curves near the peak, the evening values are slightly higher than the noon values, while below the peak, the noon values dominate. The morning values in both cases, however, exhibit a large swing between 60 and 80 km. The enhancements of H between 60 and 70 km can be regarded as a consequence of the photodissociation processes. The photodissociation of H_2O at these heights produce sufficient amounts of H causing the ledge to appear in the morning. Subsequent losses due to various chemical reactions later in the day bring down its concentration to the calculated value. The rate of production of H by photodissociation of H_2O near 75 km is not adequate to yield concentrations as given by the noon profile, and hence the presence of the minimum in the profiles at these altitudes. The valley, however, is later filled in by the transport processes.

These results are generally in agreement with the results of *Thomas and Bowman* [1972] and *Hunt* [1971b; 1973]. The [H] peak in Thomas and Bowman's profile occurs near 83 km with a value of about 5×10^8 cm^{-3}, while in Hunt's profile, it occurs near 82 km with a value about 2×10^8 cm^{-3}. In the present calculations with the low D_e model, the peak abundance of H obtained is 4×10^8 cm^{-3} near 85 km, showing good agreement

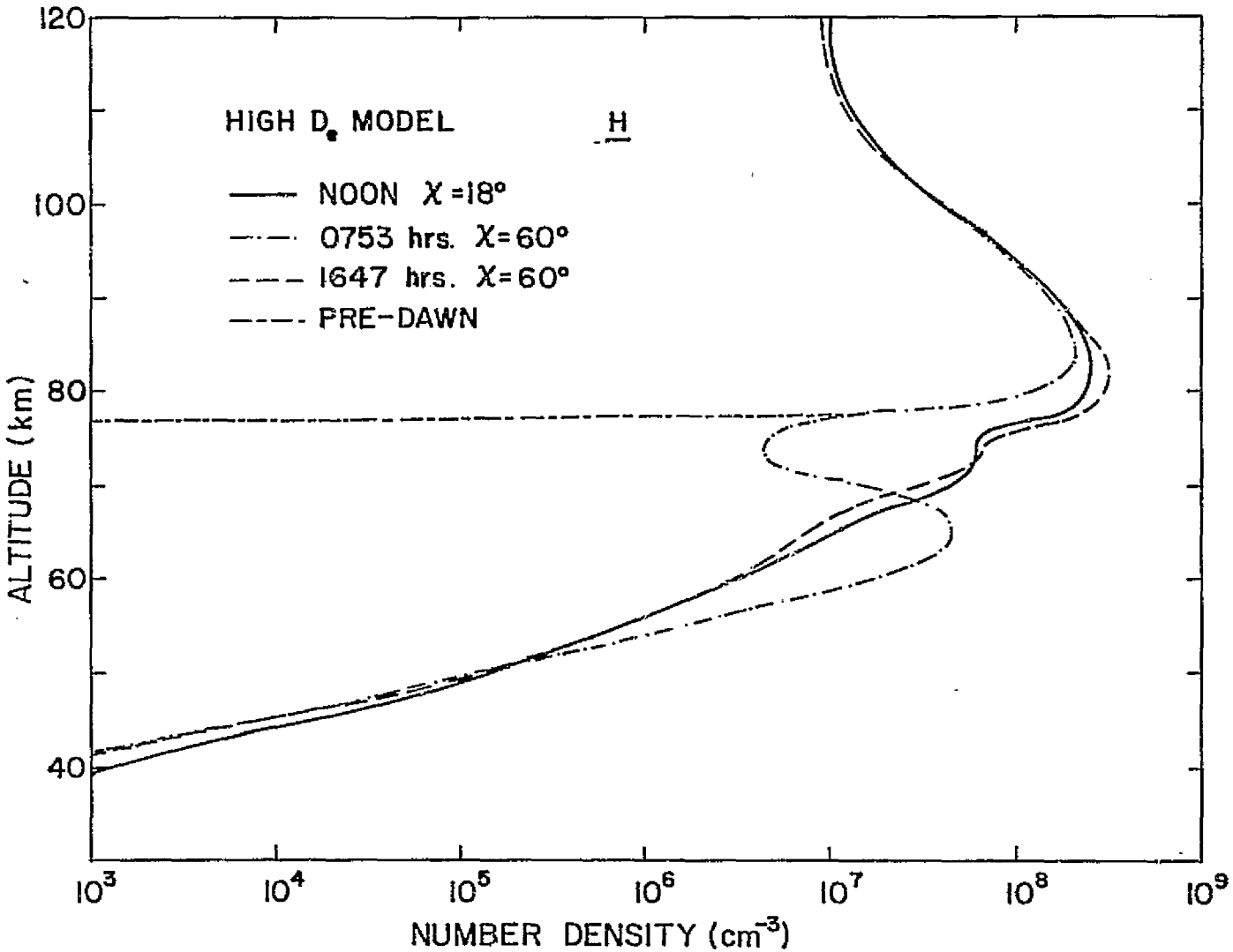

Figure 3.17 The height distributions of H at noon, 60° zenith angles and pre-dawn, calculated using the diurnal model with high eddy diffusion coefficient profile.

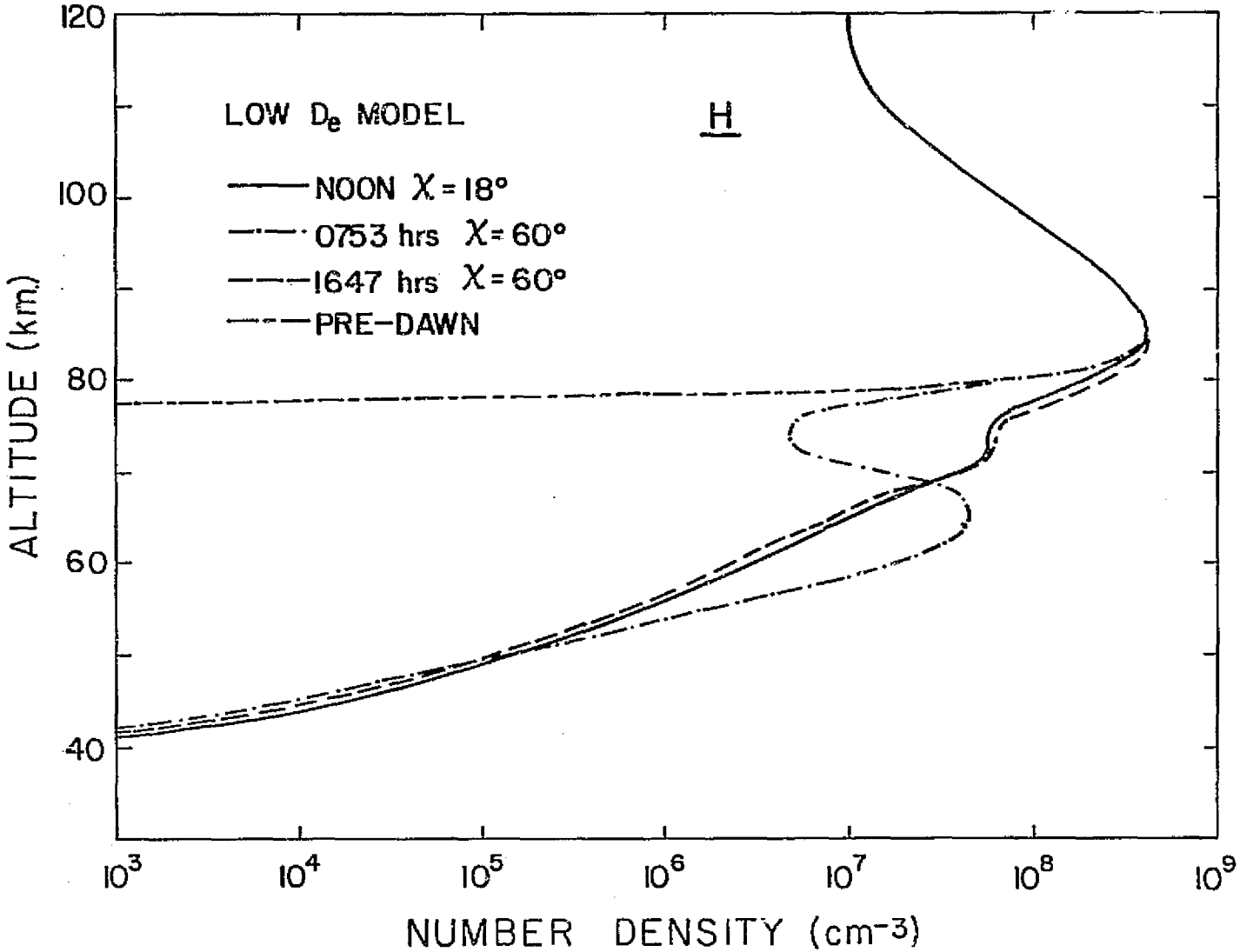

Figure 3.18 The height distributions of H at noon, 60° zenith angles and pre-dawn, calculated using the diurnal model with low eddy diffusion coefficient profile.

with the results of the previous workers. However, the only experimental estimate of the H concentration in the mesosphere carried out using OH airglow data give values about 3×10^7 cm^{-3} in the height range 80 and 90 km [*Evans and Llewellyn*, 1973]. This is about an order of magnitude lower than the corresponding theoretical values discussed above.

The diurnal variations of OH and HO_2 are shown in Figures 3.19 and 3.20, respectively, for the low D_e model only. The nature of the diurnal variation for the high diffusion model is also similar, and hence it is not shown separately. For OH in the region below 70 km, the variation between the two $\chi = 60°$ profiles is not appreciable, at the most a factor of 1.5 except below 35 km. Above 70 km, up to about 80 km, where the OH curve has a moderate slope, the evening values exceed the morning values by a factor of about 4. Above 80 km, the diurnal variation is negligible.

The more prominent feature here is the behavior of the pre-dawn profile of OH. The almost negligible loss rate in the night causes the OH concentration to build up by pre-dawn, below about 70 km. The reaction between OH and O_3, when taken into consideration is the major loss process of OH in the night. However, in this study, this reaction was not included, because of the lack of experimental evidence in favor of this reaction [*Schiff*, 1972]. The reaction between OH and HO_2 and that between two OH molecules do not contribute significantly to the loss of OH in the night, in view of the long time constants of these reactions.

A similar diurnal variation is also observed in the case of HO_2 (Figure 3.20). In the two $\chi = 60°$ profiles, the difference occurring below 68 km is rather small, while the noon profile gives the largest set of values. Between 68 and 80 km, the evening values dominate while the

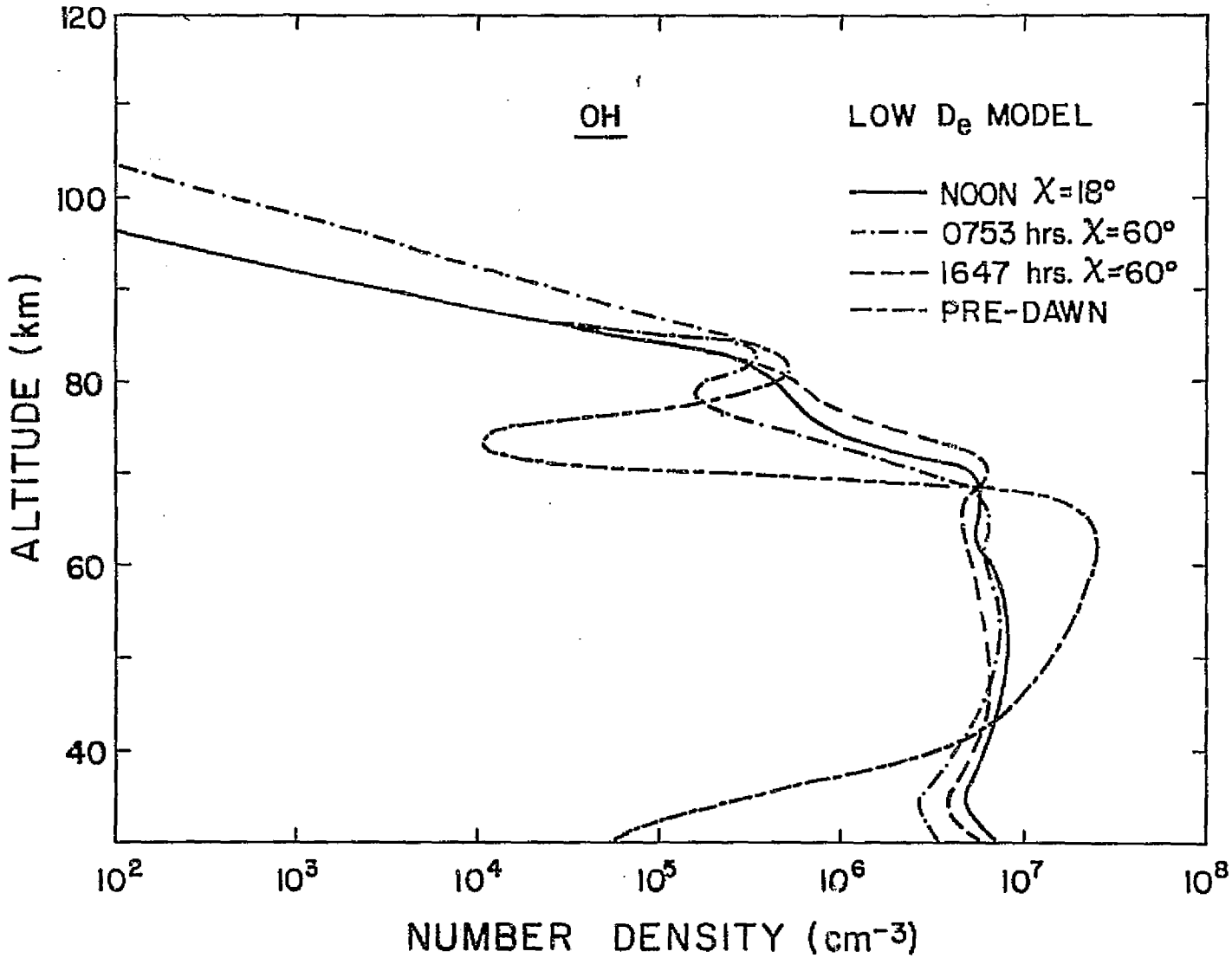

Figure 3.19 The height distributions of OH at noon, 60° zenith angles and pre-dawn, calculated using the diurnal model with low eddy diffusion coefficient profile.

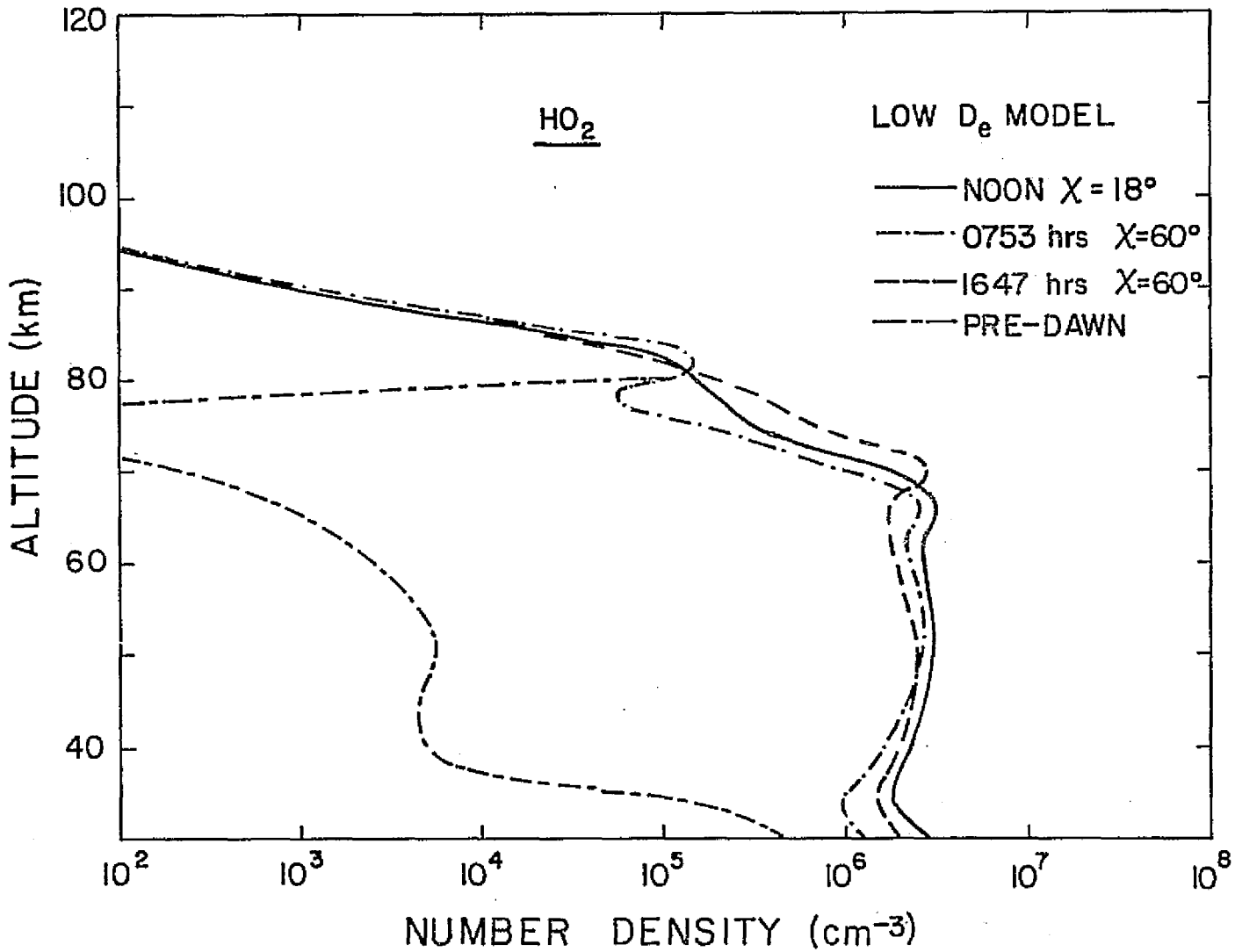

Figure 3.20 The height distributions of HO_2 at noon, 60° zenith angles and pre-dawn, calculated using the diurnal model with low eddy difussior coefficient profile.

morning values get reduced below the noon values. In this region, the morning and evening values again differ by a factor of 4. Around 80 km, the morning values display an irregularity caused by similar variations found in $O(^3P)$ and O_3 profiles. Above 85 km, there is no significant diurnal variation. The pre-dawn profile displays a much larger variation. However, unlike in the case of OH, the stratospheric values of HO_2 at nighttime do not exceed the noon values. In the upper stratosphere HO_2 has a nighttime concentration of about 5×10^3 cm^{-3}. It has a deep valley near 75 km, and reaches the daytime values above 80 km.

In the previous calculations of O-H species concentrations by other workers, the inadequate knowledge of some of the rate constants (R_{27} and R_{30}) gave rise to a certian degree of uncertainty in their height distributions. However, recent determinations of more exact values for these rate constants have enabled the calculation of more accurate height distributions, in particular for OH and HO_2. Further, the assumption of zero-rate constants for the reactions of OH and HO_2 with O_3 causes enhancement of these constituents in the stratosphere during nighttime.

Generally, the daytime profiles of both OH and HO_2 agree with those of the previous workers. The more or less constant values up to about 75 km, and the rapid drop thereafter are some noted features present in these profiles. The calculated values of OH are also in agreement with the measured values of stratospheric OH by *Anderson* [1971a, 1971b]. No direct measurements are available for any of the other O-H species at mesospheric heights.

3.6.3 *Nitrogen and oxygen-nitrogen constituents.* The results of the previous set of calculations of the O-N products were employed as initial values in the calculations of the diurnal distribution of these

species. The values obtained for the 10th day noon are given in Figures 3.21 and 3.22 corresponding to the high D_e and low D_e values, respectively.

As expected, the new values of $[N_2O]$ in the mesosphere, are higher than the corresponding values obtained in the previous calculations. During nighttime, N_2O is not subject to any losses due to photodissociation and hence the mixing ratio tends to reach the limiting values determined by the lower boundary conditions. The concentrations in the mesosphere and the lower thermosphere are controlled by eddy diffusion, and as a result, the profile under low diffusion gives values at 120 km which are higher by an order of magnitude compared to those given by the high D_e model.

In the previous calculations, it was seen that eddy diffusion plays an important role in the determination of the height distribution of NO in the mesosphere. This is because of the long time constant NO has against chemical losses, which is over two days between 70 and 90 km. Below 70 km, it comes down due to the increasing concentration of O_3, which oxidizes NO into NO_2. The two [NO] curves in Figures 3.21 and 3.22 demonstrate this. The two curves are identical below about 65 km, while above this height, the high diffusion model gives higher values than the low diffusion model values. The difference in the concentrations is within a factor of 3. The apparent coalescing of the values near the upper boundary is due to the fixed boundary value, and does not represent the real situation.

The production of NO in the thermosphere depends on the branching ratios of the NO^+ recombination reaction and the reaction between NO^+ and O_2. Different values between 0.5 and 1.0 were tried for these parameters

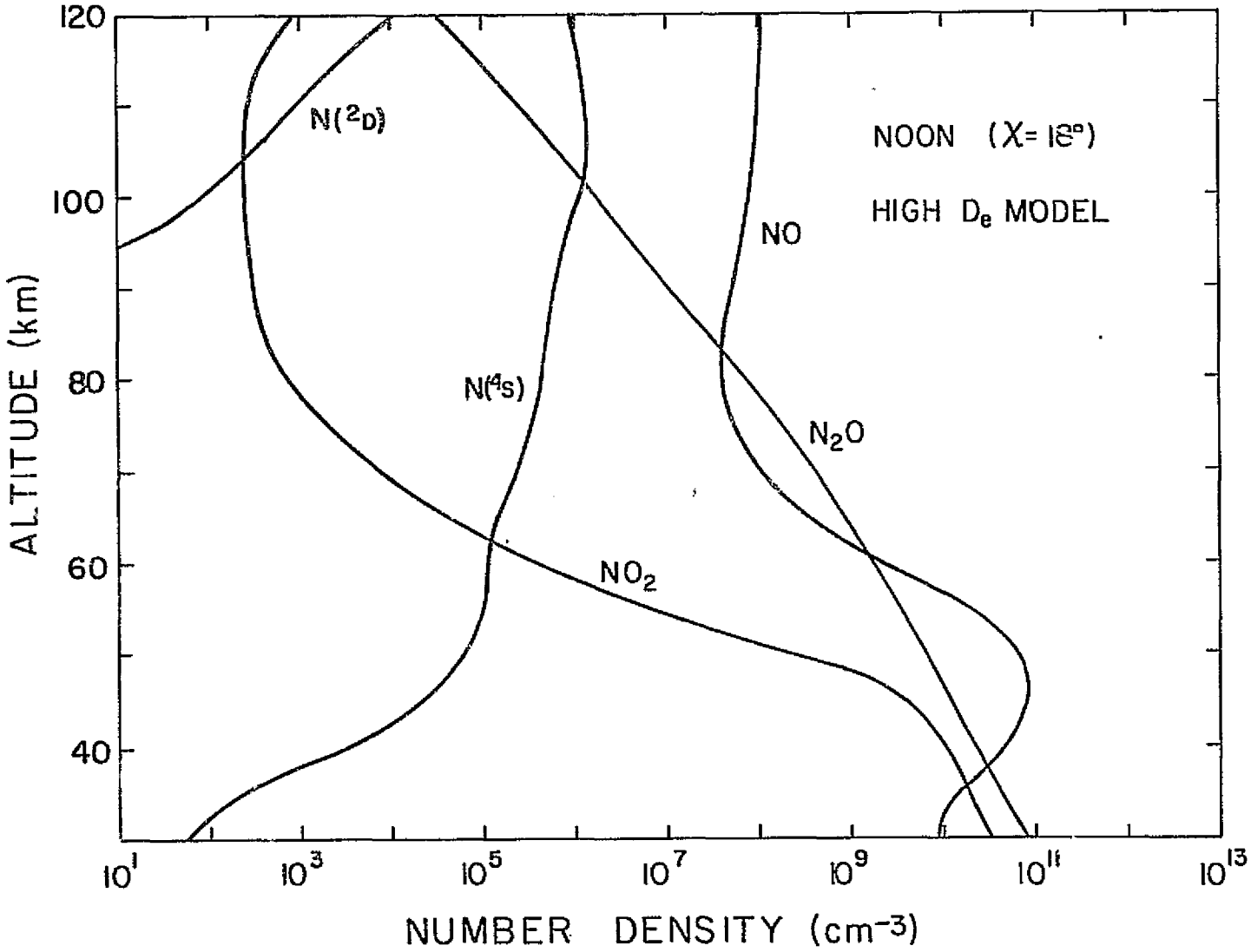

Figure 3.21 The height distributions of nitrogen and oxygen-nitrogen constituents at noon, calculated using the diurnal model with high eddy diffusion coefficient profile.

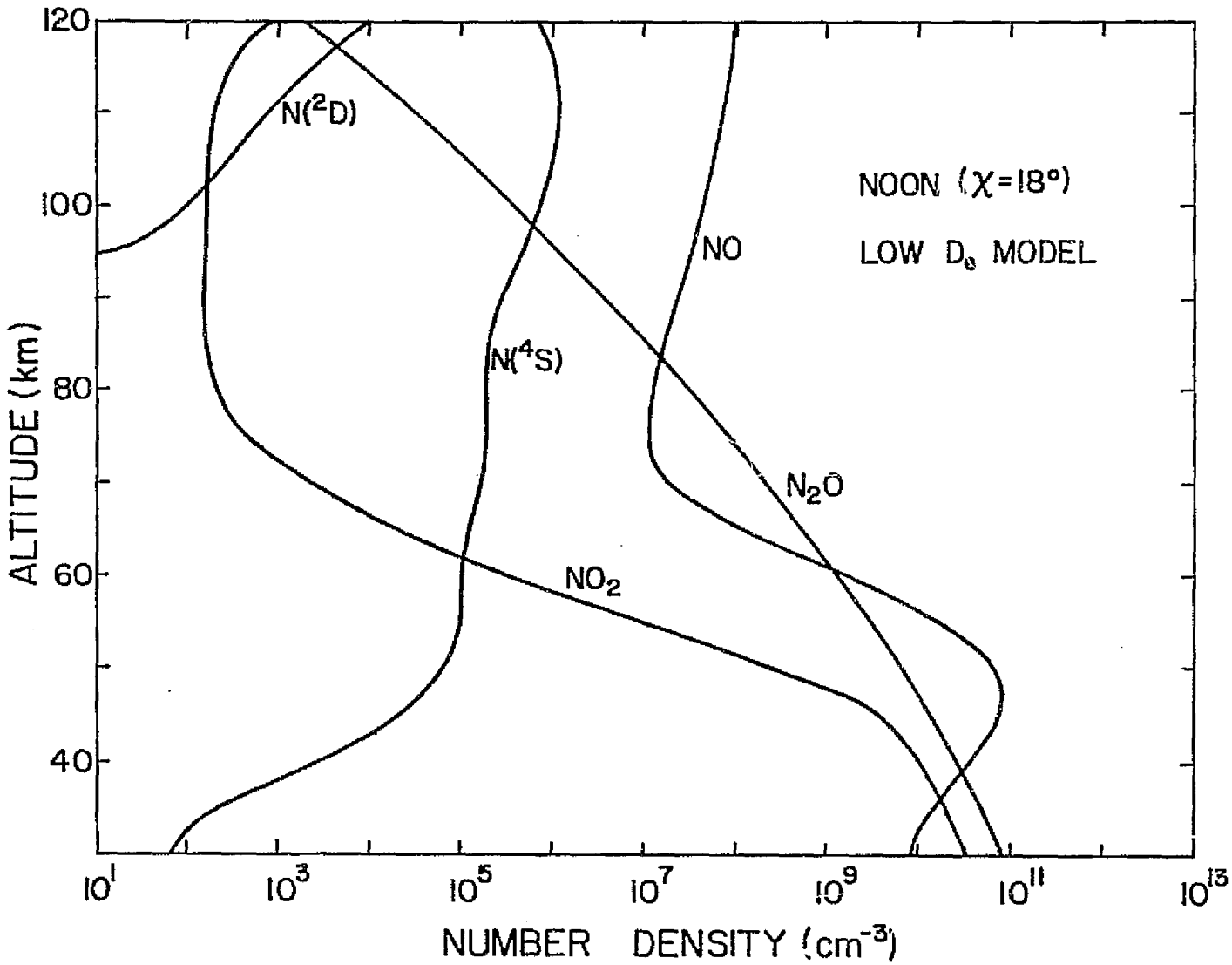

Figure 3.22 The height distributions of nitrogen and oxygen-nitrogen constituents at noon, calculated using the diurnal model with low eddy diffusion coefficient profile.

and their effect was noticeable only in the height range between 95 and 105 km. The differences obtained with these values of the branching ratios appear to be within a factor of 2 at 100 km. The profiles shown correspond to $\gamma = 0.75$.

As mentioned in Section 2.5 of the last chapter, NO and NO_2 are strongly coupled through the reactions

$$R_{38} \qquad NO + O_3 \longrightarrow NO_2 + O_2$$

$$R_{41} \qquad NO_2 + O \longrightarrow NO + O_2 \quad ,$$

which are actually effective as a catalytic process for the conversion of ozone and atomic oxygen into molecular oxygen. The reaction R_{38} acts as the main loss process for NO, and also as the main production process for NO_2 below 70 km. The other reaction R_{41} is the main loss process for NO_2 over the entire height range during the daytime. This reaction also acts as the main production process for NO below about 95 km. In view of this strong coupling, when the individual time-dependent equations are solved for NO and NO_2 in sequence, any small errors introduced at the beginning could get magnified leading to an instability in their solution. This is particularly important in the height range below 70 km.

During the daytime, NO_2 is in photochemical equilibrium with NO and, therefore, its continuity equation can be used to eliminate terms involving [O] and $[O_3]$ which appear in the continuity equation for NO. This procedure results in removing the instability mentioned above. The profiles shown in Figures 3.21 and 3.22 have been obtained after incorporating the above procedure in the height range below 70 km. This

simplification, however, was not introduced in the nighttime calculations as during this period the condition of equilibrium for NO_2 becomes invalid.

Strobel [1971b, 1972a] who studied the NO at *D*-region heights showed that its concentration in this height range is sensitive to the eddy diffusion coefficients used, and to the lower boundary conditions. Under high eddy diffusion he found the profiles to have broad minima between 65 and 70 km with values over 10^7 cm^{-3}, while the low eddy diffusion models gave minimum values in the range (2-4) x 10^6 cm^{-3}. More recently, *Brasseur and Nicolet* [1973] showed that the NO profiles have minima between 70 and 80 km with the values extending from 10^5 up to 5 x 10^6 cm^{-3} under different values of eddy diffusion coefficients and nitrogen atom production rates. In the [NO] profile obtained by *Hunt* [1973], however, no such minimum is observed in the mesosphere.

In the present study, the minima in the two noontime profiles of [NO] have values 1.4 x 10^7 and 4 x 10^7 cm^{-3}, both lying at 80 km. These profiles, which show identical values below 65 km, have broad maxima between 45 and 50 km, with values 8 x 10^{10} cm^{-3}. However, in view of the uncertain lower boundary conditions, these latter values cannot be relied upon as representing the real situation.

Though these profiles differ slightly from the theoretical profiles of the other workers, they are in good agreement with the available experimental profiles. *Meira's* [1971] profiles of [NO] show minima around 1.5 x 10^7 cm^{-3} at 84 km. The more recent measurement by *Tisone* [1973] shows a height distribution having a broad maximum of 5.5 x 10^7 cm^{-3} between 80 and 100 km. In view of the inherent weaknesses of the techniques employed in these measurements they are not, however, considered to be reliable for determining *D*-region NO concentrations [*Thomas*, 1974].

Figure 3.23 shows the diurnal variation of [NO] for the low diffusion case. Above 70 km, the variation is negligible. This is expected because of the effect of the transport processes in this height range. Between the two $\chi = 60°$ curves, the morning profile is nearly a factor of 10 below the noon profile at the stratopause, while the drop in the afternoon profile is only very small. At pre-dawn, the [NO] profile vanishes below 40 km.

These results show that the diurnal variation of the NO concentration appears only below the region where the Ly-α ionization of NO is important. Therefore, the variation of the [NO] does not contribute much to the diurnal variation of the ion-pair production rates in the *D* region.

The values of $[NO_2]$ obtained in the new set of profiles show marked changes from the constant χ profile above 80 km as well as below about 50 km. The changes taking place in the higher altitude range are due to the changes in the $[O(^3P)]$ and $[O_3]$ values, whereas in the stratosphere the diurnal cycle causes enhancements in the NO_2 concentrations. This is because at nighttime both loss processes of NO_2 in the stratosphere, *viz.* reaction with $O(^3P)$ and the photodissociation, are absent. In the height range between 60 and 75 km, where NO_2 plays an important role in the *D*-region negative-ion chemistry, the diurnal cycle does not introduce any significant changes in the noon profiles.

Unlike in the case of oxygen only or oxygen-hydrogen species, the calculation of nitrogen and oxygen-nitrogen species concentrations poses some additional problems. The odd nitrogen species, N and NO are produced in the thermosphere, where the ionic chemistry plays a significant

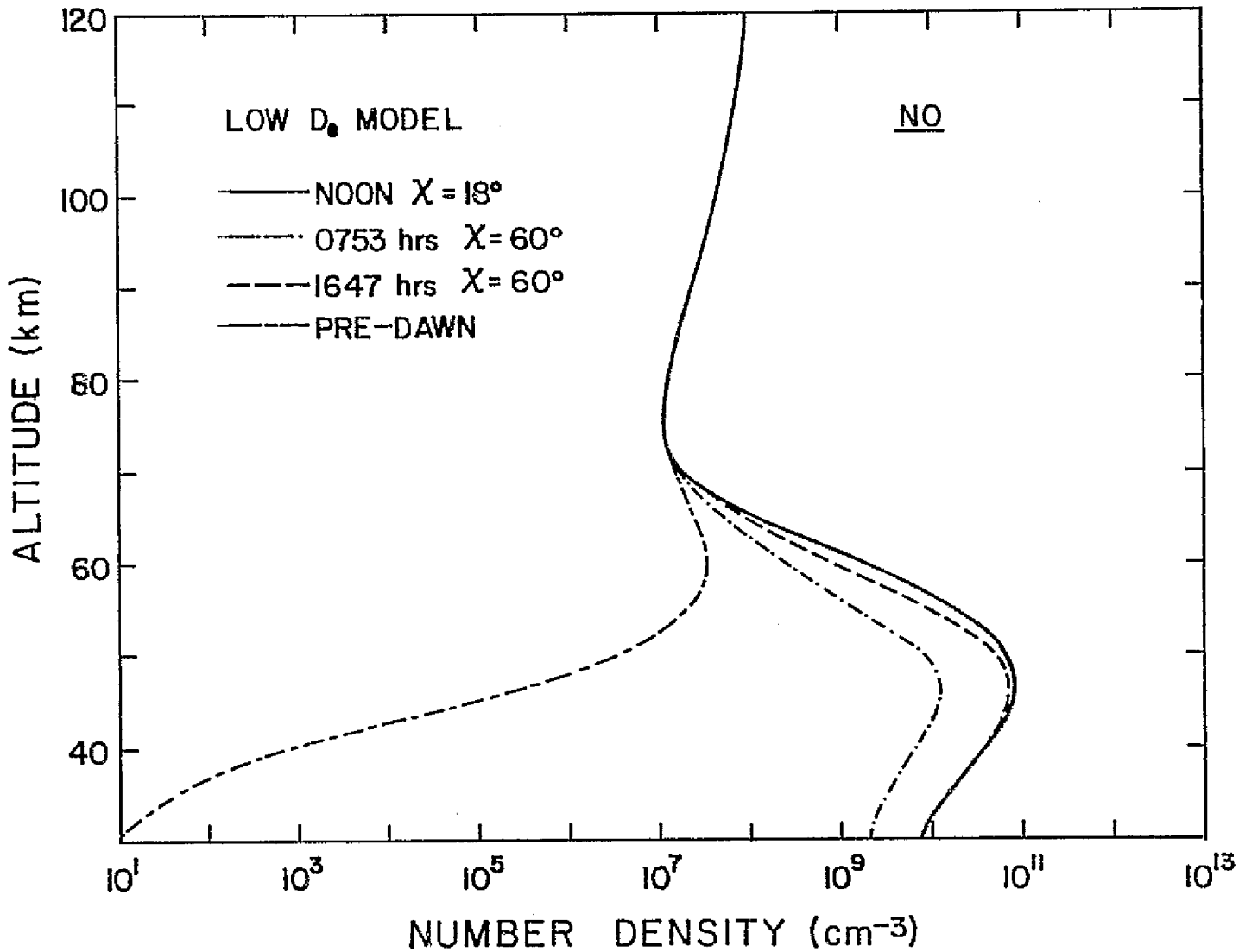

Figure 3.23 The height distributions of NO at noon, 60° zenith angles, and pre-dawn, calculated using the diurnal model with low eddy diffusion coefficient profile.

role. In view of the many uncertainties present in the ionic chemistry, the rate of production of these species cannot be determined accurately. Secondly, the sinks for the odd nitrogen species in the stratosphere have not been correctly estimated so far. Finally, the wide range in the time constants involved in the loss rates of odd nitrogen species makes the computer simulation of the diurnal behavior of this quantity a little more difficult task than in the case of the other constituents.

4. ION-PAIR PRODUCTION RATES

Several sources contribute to the ion-pair production in the *D* region. These sources include radiations of solar origin as well as others such as galactic cosmic rays and precipitating electrons which come from the outer radiation belts. The solar radiations that are capable of ionizing any atmospheric gas and penetrating down to 100 km have wavelengths below 100 Å, and also between 1000 and 1300 Å. However, as mentioned in the last chapter, wavelengths outside of these limits have also been included in order to extend the region of ionization up to 120 km for use in the calculation of neutral ntirogen species concentration.

The solar radiations get attenuated in the atmosphere mainly due to absorption by oxygen. Molecular nitrogen also plays a significant role in the attenuation of incoming radiation, particularly the X-rays below 100 Å, in view of its high abundance in the atmosphere. The intensity of these solar photon radiations at *D*-region altitudes drops with the increase of solar zenith angle, as the thickness of the atmosphere traversed by these radiations increases.

The calculation of the ion-pair production rates due to these solar EUV and X-rays and their variations with the zenith angle are presented in the next two sections.

Section 3 presents the ionization rates due to sources of non-solar origin, *viz.* galactic cosmic rays and precipitating electrons. Unlike in the case of solar radiation, these do not have a solar zenith angle variation. In the last section, a discussion of the resulting ion-pair production rates is given.

4.1 *Solar EUV Radiations*

The ionization thresholds of most of the gases present in the earth's atmosphere correspond to wavelengths below about 1330 Å. Table 4.1 lists these ionization potentials and their threshold wavelengths. Only O_2, $O_2(^1\Delta_g)$, NO_2, and NO have sufficiently low ionization potentials so as to be ionizable by wavelengths greater than 1000 Å. The most significant contribution for the O_2 ionization in this region comes from the solar Ly-β line at 1025.7 Å. The several spectral windows appearing between 1050 and 1300 Å in the oxygen absorption spectrum (Figure 2.4) makes the remaining three constituents potential sources of *D*-region ionization. Of these, NO_2 has a very low abundance at *D*-region heights and therefore does not make a significant contribution as an ionization source. Of the other remaining two constituents, NO has been long recognized as the major source of *D*-region ionization, while $O_2(^1\Delta_g)$ is considered important as an O_2^+ source in the mid-*D* region. The contributions from these as well as from O_2 are discussed in the next section.

4.1.1 NO *ionization*. Even though NO is only a minor constituent at *D*-region heights having only an abundance of a few parts per million or less, the combination of the high intensity of the solar Ly-α line at 1215.7 Å and the low absorption of this line by atmospheric O_2 makes this a major source of ionization in the *D* region. As discussed in Section 2.2.1, the intensity of this line at the top of the atmosphere corresponding to July 24, 1968 is 3.7×10^{11} photons cm^{-2} sec^{-1} or 6.0 ergs cm^{-2} sec^{-1}. According to rocket measurements [*Goldberg and Aikin*, 1971], the unit optical depth of this line lies near 77 km for low zenith angles, and its intensity is completely attenuated by the time it reaches 70 km.

Table 4.1

Ionization potential and threshold wavelengths of ionization for atmospheric gases.

Constituent	Ionization potential (eV)	Threshold wavelength (Å)
N_2	15.6	790
H_2	15.4	803
N	14.5	852
CO	14.0	882
CO_2	13.8	895
O	13.6	910
H	13.6	910
OH	13.3	930
N_2O	12.9	960
O_3	12.8	970
H_2O	12.6	980
O_2	12.0	1030
$O_2(^1\Delta_g)$	11.1	1118
NO_2	9.76	1270
NO	9.27	1330

The ion-pair production rate due to this line is given by

$$q(1216\text{Å}) = [NO]\sigma_i(NO)\ I_o(1216\ \text{Å})\ \exp(-\tau(\chi,z)) \tag{4.1}$$

where

$\sigma_i(NO)$ is the ionization cross section of NO at 1216 Å, and

$I_o(1216\ \text{Å})$ is the unattenuated intensity of the solar Ly-α line.

Since this line is absorbed mainly by molecular oxygen in the atmosphere, the optical depth factor is given by

$$\tau(\chi,z) = \sigma_a(O_2)\ \sec\chi \int_z^\infty [O_2](z)\ dz \tag{4.2}$$

where

$\sigma_a(O_2)$ is the absorption cross section of O_2 at 1216 Å.

As discussed in Section 2.2.2, $\sigma_a(O_2)$ is taken to be 1.0×10^{-20} cm^2. The value of $\sigma_i(NO)$ at 1216 Å adopted is 2.0×10^{-18} cm^2.

The required $[O_2]$ and [NO] values are taken from the diurnal model of the neutral atmosphere presented in the last chapter. Above about 70 km, transport effects control the [NO] profile and therefore its variation with χ in this region is negligible. Hence, the variation of $q(1216\ \text{Å})$ with χ is mainly due to the variation of the value of sec χ appearing in the optical depth factor.

The production rates obtained using the previously calculated [NO] profiles are shown in Figure 4.1 for different χ angles. These curves show that the zenith angle variation becomes significant for heights below about 90 km only. Above this height the optical depth factor is very

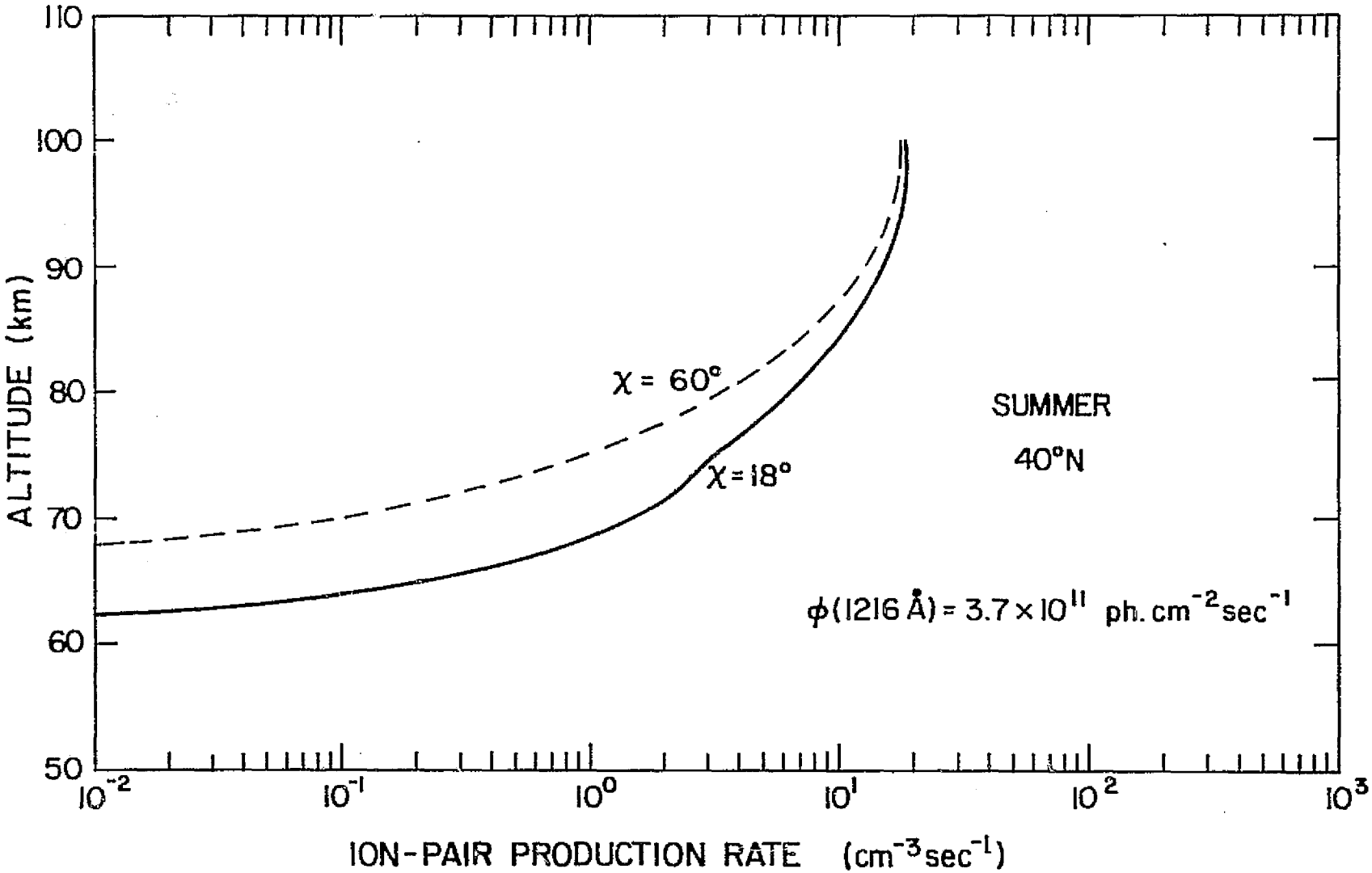

Figure 4.1 The ion-pair production rates due to Lyman-α (1216 Å) ionization of NO at zenith angles 18° (noon) and 60°.

small and the variation of the sec χ factor has no influence on the intensity of the downcoming radiation. As the optical depth factor begins to grow the variations become very prominent, and even exceed an order of magnitude between $\chi = 18°$ and $\chi = 60°$ below 72 km.

4.1.2 $O_2(^1\Delta_g)$ *ionization.* The metastable $O_2(^1\Delta_g)$ was suggested as an important source of *D*-region ionization by *Hunten and McElroy* [1968]. Its importance is in the production of O_2^+ in the mid-*D* region rather than in the total ion-pair production. The formation of water cluster ions in the mesosphere requires the presence of an O_2^+ source, according to the original theories put forward to account for the presence of these cluster ions [*Fehsenfeld and Ferguson,* 1969]. Even with the current theories on the production of these cluster ions, it is easier to explain the presence of ions such as H_3O^+ and $H_3O^+ \cdot H_2O$ if the O_2^+ production rate becomes enhanced as in the case of a PCA event [*Narcisi et al.,* 1972b].

The original values of O_2^+ production rates due to $O_2(^1\Delta_g)$ ionization were of the correct magnitude to account for the presence of the cluster ions around 80 km. However, a re-evaluation of this production rate by *Huffman et al.* [1971], taking into account the CO_2 absorption of solar radiation between 1027 and 1118 Å responsible for $O_2(^1\Delta_g)$ ionization, showed that the O_2^+ production rates are reduced significantly from the previously calculated values. This modified ionization rate is calculated here using the formula given by *Paulsen et al.* [1972]

$$q(O_2(^1\Delta_g)) = O_2(^1\Delta_g) \left\{0.549 \times 10^{-9} \exp(-2.406 \times 10^{-20} N(O_2)) + 2.614 \times 10^{-9} \exp(-8.508 \times 10^{-20} N(O_2))\right\} \quad (4.3)$$

where

$N(O_2)$ is the column density of O_2 molecules along the solar ray path.

According to Paulsen et al, the combined uncertaintly due to any uncertainty in the $[O_2]$ and $[CO_2]$ profiles is at most 15%. Larger uncertainties, however, occur in the solar flux values and in the O_2 and CO_2 absorption cross sections used to derive this formula. The rms error due to all these data has been estimated to be less than 10% with a maximum error less than 33%.

In the above formula, values obtained from the diurnal model calculations are used for $O_2(^1\Delta_g)$. These calculations have shown that $O_2(^1\Delta_g)$ has a significant diurnal variation, with the values at 80 km increasing by as much as an order of magnitude from post-sunrise (χ = 85°) to noon (χ = 18°). As a source of O_2^+ in the mid-*D* region, $O_2(^1\Delta_g)$ has to compete with 1-8 Å X-rays and precipitating electrons. Of these, the X-ray ionization rates have a solar zenith angle variation caused by the optical depth variation only, while $O_2(^1\Delta_g)$ ionization rates have a solar zenith angle variation caused by both optical depth variation and $[O_2(^1\Delta_g)]$ variation. On the other hand, ionization rates due to precipitating electrons do not have any solar variation at all. Hence, the contributions made by each of these sources vary at different rates during the day. Figure 4.2 illustrates the calculated O_2^+ production rates due to $O_2(^1\Delta_g)$ ionization at different solar zenith angles.

4.1.3 O_2 *ionization*. In the spectral region below 1030 Å, the threshold wavelength for O_2 ionization, there are some wavelength bands, particularly in the Lyman continuum, for which N_2 offers only a small absorption cross-section. Consequently, these wavelengths penetrate to

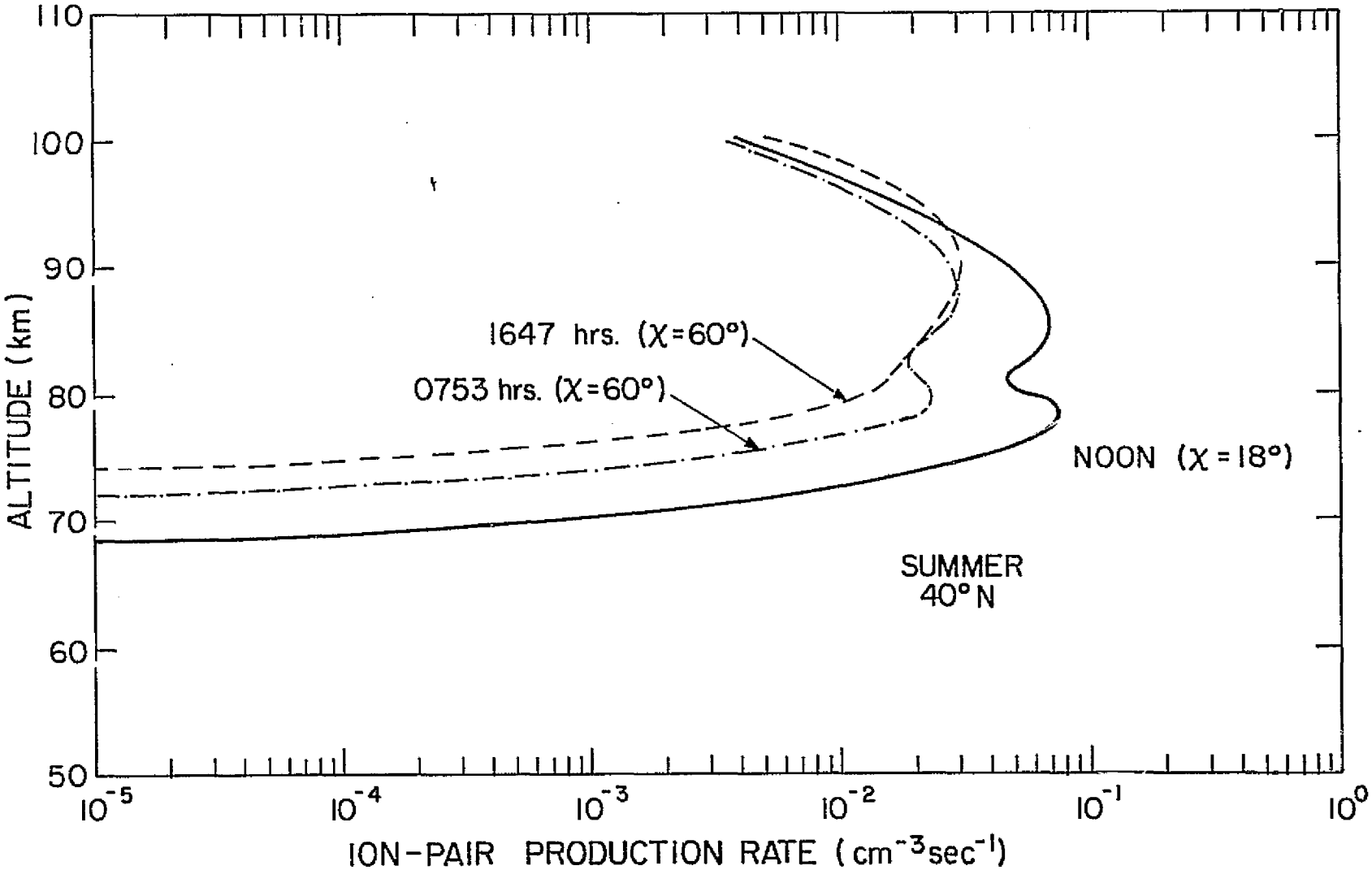

Figure 4.2 The ion-pair production rates due to EUV (1027-1118 Å) ionization of $O_2(^1\Delta_g)$ at zenith angles 18° (noon) and 60°.

heights below 100 km and contribute to lower *E* region ion-pair production. The biggest contribution comes from the Ly-β line at 1025.7 Å, and to a lesser extent from the C III line at 977 Å. The unattenuated intensity of this Ly-β line has been measured over a long period of time and was found to vary by about a factor of 1.5 during a solar cycle [*Hall et al.*, 1969]. However, no measurements are available for this line on July 24, 1968. The closest day on which a Ly-β measurement has been reported is for November 21, 1968, the flux on this day being 3.7×10^9 photons cm^{-2} sec^{-1} [*Hall et al.*, 1969]. The Ly-α flux reported for this day by *Timothy and Timothy* [1970] is 3.5×10^{11} photons cm^{-2} sec^{-1}. Assuming the two lines, Ly-α and Ly-β undergo similar variations maintaining the same flux ratios, one can deduce the Ly-β flux if Ly-α flux is available for that day. Since the value adopted for the Ly-α flux for July 24, 1968 is 3.7×10^{11} photons cm^{-2} sec^{-1}, it follows that Ly-β flux is 3.9×10^9 photons cm^{-2} sec^{-1}. This is within the range of values given by *Hall et al.* [1969] for the Ly-β flux.

For the 977 Å line and others in the Lyman continuum, fluxes reported by *Hinteregger* [1970] have been adopted. The absorption cross sections and ionization yields employed here are those given by *Ohshio et al.* [1966]. The optical depths are controlled by O_2 absorption, and hence its variations are due to changes of sec χ only. The ion-pair production rates are calculated using equations similar to equations (4.1) and (4.2) for solar zenith angles 18° and 60°. These results, illustrated in Figure 4.3, show that between 95 and 110 km, EUV ionization of O_2 is the main source of ion-pair production.

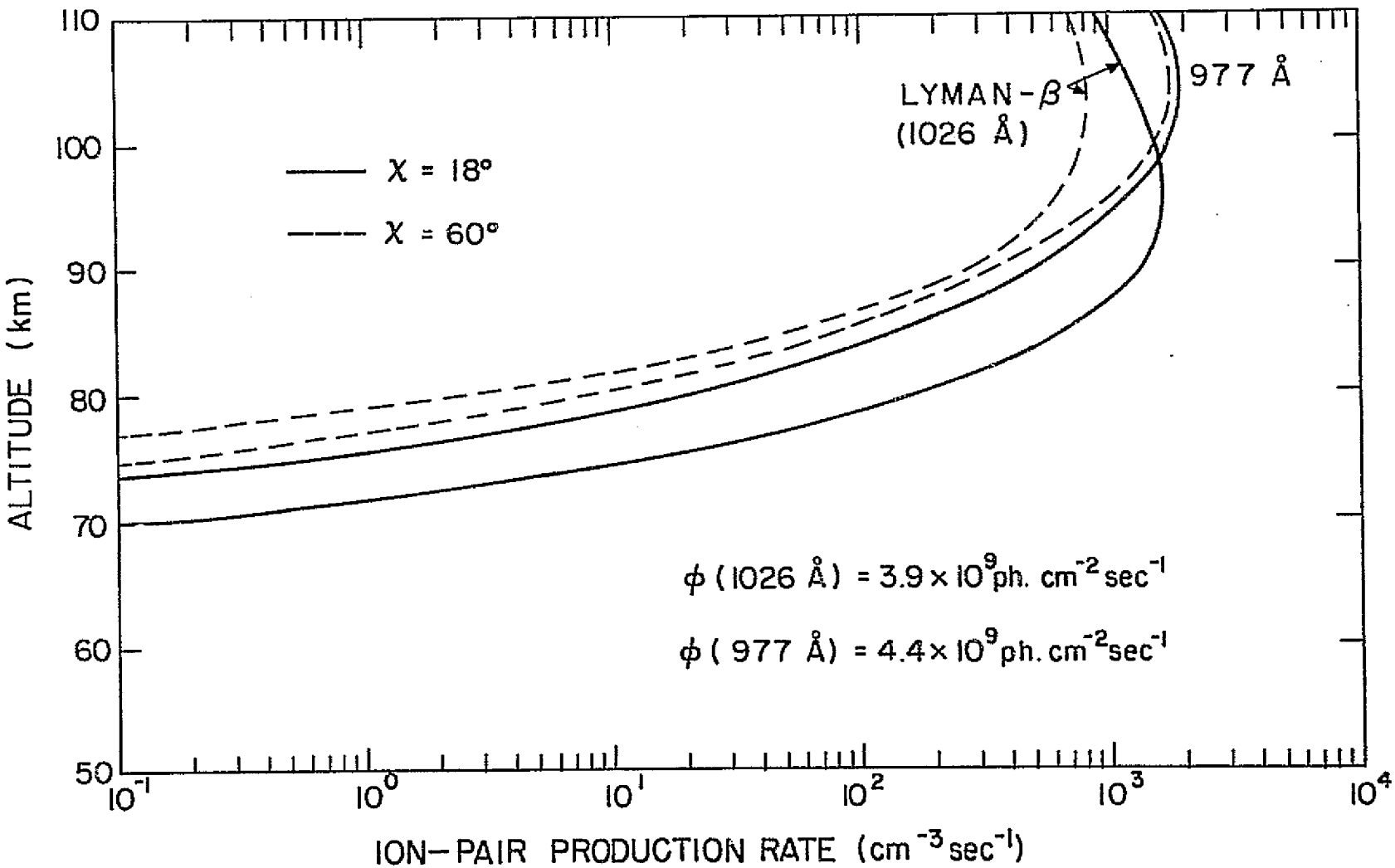

Figure 4.3 The ion-pair production rates due to Lyman-β (1027 Å) and C III (977 Å) ionization of O_2 at zenith angles 18° (noon) and 60°.

4.2 *Solar X-Rays*

The penetration of solar X-rays into the atmosphere depends mainly on the absorption cross sections offered by the major constituents O_2 and N_2 to X-rays. The absorption cross sections for these gases are obtained from experimentally determined mass absorption coefficients, μ/ρ. The values of this quantity measured by several workers were assessed and the weighted means were tabulated by *Henke and Elgin* [1970]. The absorption cross sections for O_2 and N_2 deduced from these tabulations are shown in Figure 4.4. An important feature of these plots is the existence of a sharp discontinuity at 23.3 Å in the case of O_2, and at 30.9 Å in the case of N_2. This critical wavelength, λ_K is associated with the ejection of a *K* electron from the atom, and sometimes referred to as the *K* absorption edge. These absorption cross sections are represented by the following empirical formulas in each of the three given wavelength intervals.

$\underline{\lambda < 5 \text{ Å}}$

$$\sigma(O_2) = 1.67 \times 10^{-22} \quad \lambda^3 \tag{4.4a}$$

$$\sigma(N_2) = 9.69 \times 10^{-23} \quad \lambda^3 \tag{4.4b}$$

$\underline{5 \text{ Å} < \lambda < \lambda_K}$

$$\sigma(O_2) = 1.70 \times 10^{-22} \quad \lambda^3 - 3.35 \times 10^{-24} \quad \lambda^4 \tag{4.5a}$$

$$\sigma(N_2) = 1.02 \times 10^{-22} \quad \lambda^3 - 1.72 \times 10^{-24} \quad \lambda^4 \tag{4.5b}$$

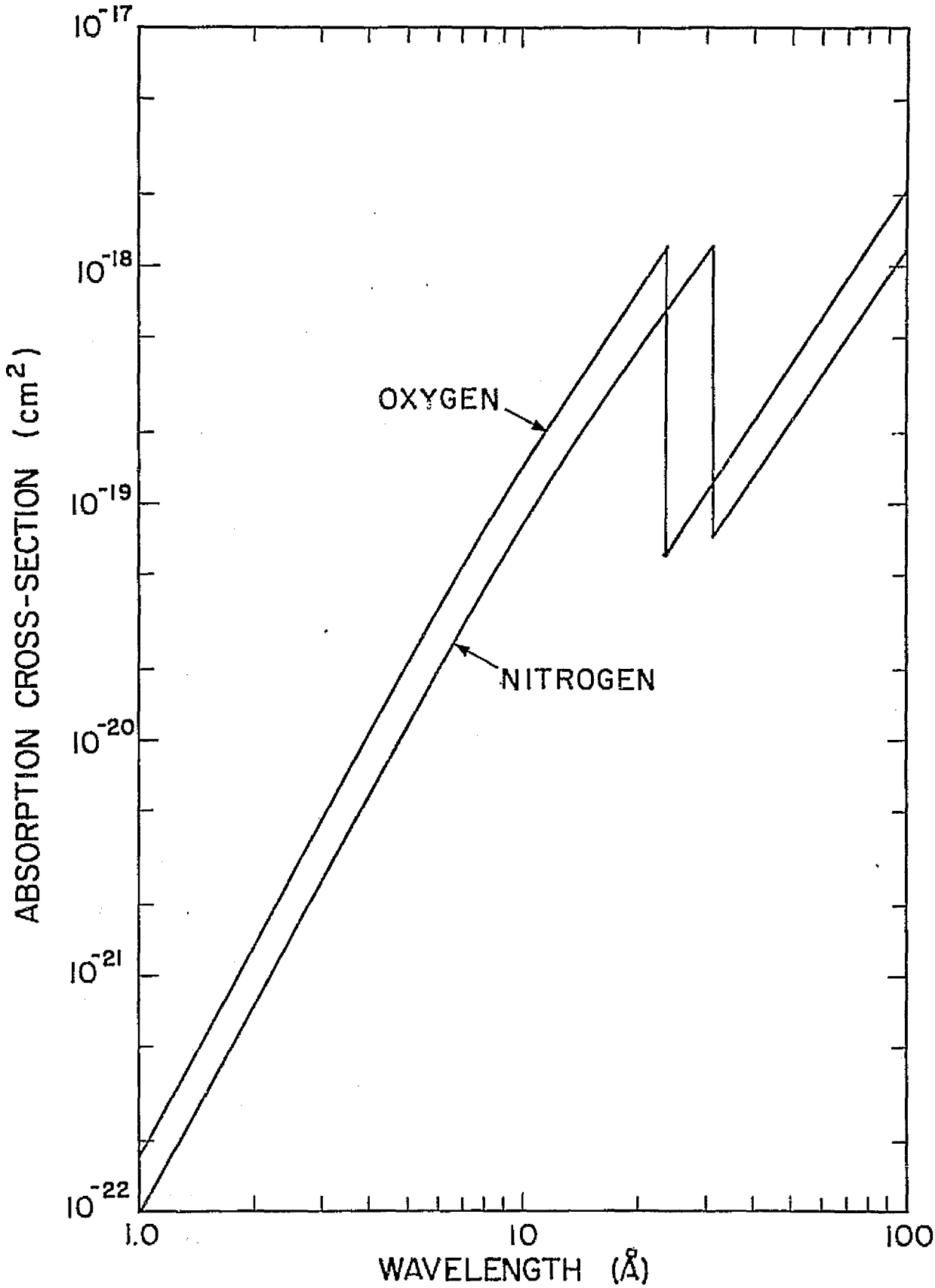

Figure 4.4 The absorption cross sections of oxygen and nitrogen at X-ray wavelengths (1-100 Å).

$\underline{\lambda_K < \lambda < 100 \text{ Å}}$

$$\sigma(O_2) = 2.65 \times 10^{-23} \ \lambda^{2.46} \tag{4.6a}$$

$$\sigma(N_2) = 1.97 \times 10^{-23} \ \lambda^{2.40} \tag{4.6b}$$

where λ is in Angstroms. The values for $\sigma(O)$ are taken as half of $\sigma(O_2)$. These expressions are similar to those reported by *Swider* [1969].

The presence of the discontinuity in the absorption spectra of O_2 and N_2 divides the spectrum below 100 Å into two groups, one group lying below λ_K and the other lying above λ_K. Referring to Figure 4.4 one sees that the cross sections just above λ_K have the same low values as the cross sections near 10 Å. This similarity in the cross sections makes it possible for both of these wavelength regions to penetrate to equal depths. The wavelengths just above λ_K and near 10 Å reach altitudes between 90 and 100 km, while the wavelengths below about 8 Å whose cross sections are much lower reach the *D*-region altitudes. The ionization effects of these two wavelength bands are therefore considered separately.

4.2.1 *X-rays below 10 Å.* X-rays in this band of the solar spectrum are produced in the solar corona which is a hot plasma with temperatures over a million degrees Kelvin. Several ionic processes take place in this region giving rise to different components of the spectrum. The free-free transitions (bremsstrahlung-type emissions) and free-bound transitions (radiative recombination emissions) cause the continuum while bound electron transitions between different energy levels in the ions give rise to the line spectrum. Both the theory [*Elwert*, 1961; *Mandel'stam*, 1965] and observations [*Rugge and Walker*, 1968; *Evans and Pounds*, 1968] show that the region below about 15 Å is mainly a continuum spectrum, except for a

few lines scattered towards the high end of the band. The relative importance between the line spectrum and the continuum spectrum depends on the coronal temperature, the line spectrum becoming more prominent at high temperatures such as those prevailing during solar flares. Under non-solar flare conditions the line spectrum below 10 Å can be easily neglected.

Photographs of the solar disc taken with rocket-borne pin-hole cameras and X-ray sensitive plates show that these X-rays are emitted from highly localized regions spread over a small fraction of the total disc area [*Friedman*, 1963]. Observations with selective spectral sensitivities have shown that the emitting regions become more localized with the decrease in the wavelength. Theoretical interpretation of the observations requires a higher coronal temperature to explain the emission of shorter wavelengths while longer wavelengths can be accounted for in terms of lower coronal temperatures.

The solar spectrum below 8 Å has been regularly monitored over the past two decades by satellite-borne detectors. These detectors respond to two wavelength bands, 0.5-3 Å and 1-8 Å [*Kreplin*, 1961, 1965]. In order to convert the detector currents to flux values it has been necessary to assume spectral distributions over the measured bands. The procedure adopted at the inception of this series of measurements is to assume a black-body distribution given by Planck's radiation formula which expresses the energy per unit wavelength interval as

$$E(\lambda) = K_1 \lambda^{-5} (e^{c_2/\lambda T} - 1)^{-1} , \qquad (4.7)$$

where

K_i is a constant,

c_2 is the second radiation constant, 1.439 cm K, and

T is the equivalent black-body temperature.

Fixed temperatures of 2×10^6 K and 10×10^6 K have been used in the conversion of 1-8 Å and 0.5-3 Å data, respectively. This assumes that the X-ray flux variations are due solely to variations of the nature of the emitting regions of the corona, rather than due to any temperature variations. However, it is believed that enhanced emissions are accompanied by hardening of the spectrum caused by an increase in the temperature [*Culhane et al.*, 1964].

This procedure of using a black-body model in the conversion of satellite data into flux values is still continued even though more realistic models for the energy distribution in the bands are presently known [*Elwert*, 1961, *Mandel'stam*, 1965]. According to these models, the emissions due to bremsstrahlung and radiative recombination could be adequately represented by [*Horan*, 1970]

$$E(\lambda) = Ke^{c_2/\lambda T_e} \tag{4.8}$$

where T_e is the electron temperature in the corona, and K is a function of the emission measure B which is given by

$$B = \int_v N_e^2 \, dv \tag{4.9}$$

where N_e is the electron concentration and the integration is performed

over the respective emitting regions. The value of K also depends to a smaller extent on λ and T_e. Better agreement has been found with spectra measured during enhancements with the above distribution than with a black-body type spectrum.

In order to compute the ion-pair production rates due to these X-rays, one has to construct the spectral distributions from the measured broad-band fluxes. The main difficulty here is the estimation of the correct coronal temperature and the emission measures corresponding to the relevant bands. *Horan* [1970], however, has developed a method to work out these quantities in terms of satellite-measured fluxes using a numerical technique which is somewhat tedious.

Using a more simple procedure, it is also possible to construct the spectral distribution over the entire range 0-10 Å in terms of the measured fluxes in the 0.5-3 Å and 1-8 Å bands. Here, the energy distribution per unit wavelength interval is given by an empirical formula [*Rowe et al.*, 1970]

$$E(\lambda) = A\lambda^n \tag{4.10}$$

where A and n are constants. n determines the shape of the spectrum while A determines the absolute flux. n is obtained from the ratio of the measured fluxes over the two bands using the formula

$$n = \frac{\log(\phi(8\ \text{Å})/\phi(3\ \text{Å}))}{\log 2.667} - 1 \tag{4.11}$$

where $\phi(8\ \text{Å})$ and $\phi(3\ \text{Å})$ are the two measured fluxes over the bands 1-8 Å and 0.5-3 Å, respectively. The constant A is obtained using the flux value over one band,

$$A = \frac{(n+1)\ \phi(8\ \text{Å})}{8^{n+1} - 1} \tag{4.12}$$

The ratio $\phi(8\ \text{Å})/\phi(3\ \text{Å})$ is generally of the order of 100 under quiet conditions, but varies by as much as a factor of 5 under extreme conditions. In two proportional counter spectra measured under conditions of low and moderate solar activity [*Pounds*, 1970], the values corresponding to this flux ratio were found to be 1780 and 43, respectively. The (1-8 Å) flux deduced from the solar active day spectrum, smoothed and shown in Figure 4.5, has a value 1.14×10^{-3} erg cm^{-2} sec^{-1}. With this flux value and the $\phi(8\ \text{Å})/\phi(3\ \text{Å})$ ratio of 43, the spectrum was reconstructed using equation (4.10). These results are also shown in Figure 4.5. The excellent agreement between these values and the measured spectrum shows that equation (4.10) is a valid representation of the X-ray spectrum below 10 Å.

These X-rays ionize all constituents present in the atmosphere. In calculating their ion-pair production rates, the ionizing effects on N_2, O_2, and O have been considered, with the production function given by

$$q(1\text{-}10\ \text{Å}) = \sum_i [X]_i \int_{\lambda_1}^{\lambda_2} \eta_i(\lambda)\sigma_a^i(\lambda) I_o(\lambda) e^{-\tau(\chi,z)} \tag{4.13}$$

where i denotes the constituents N_2, O_2, and $O(^3P)$ • $\eta_i(\lambda)$ is the ionization yield of the ith constituent, and $I_o(\lambda)$ is the energy distribution function given by equation (4.10) expressed in photons cm^{-2} sec^{-1}.

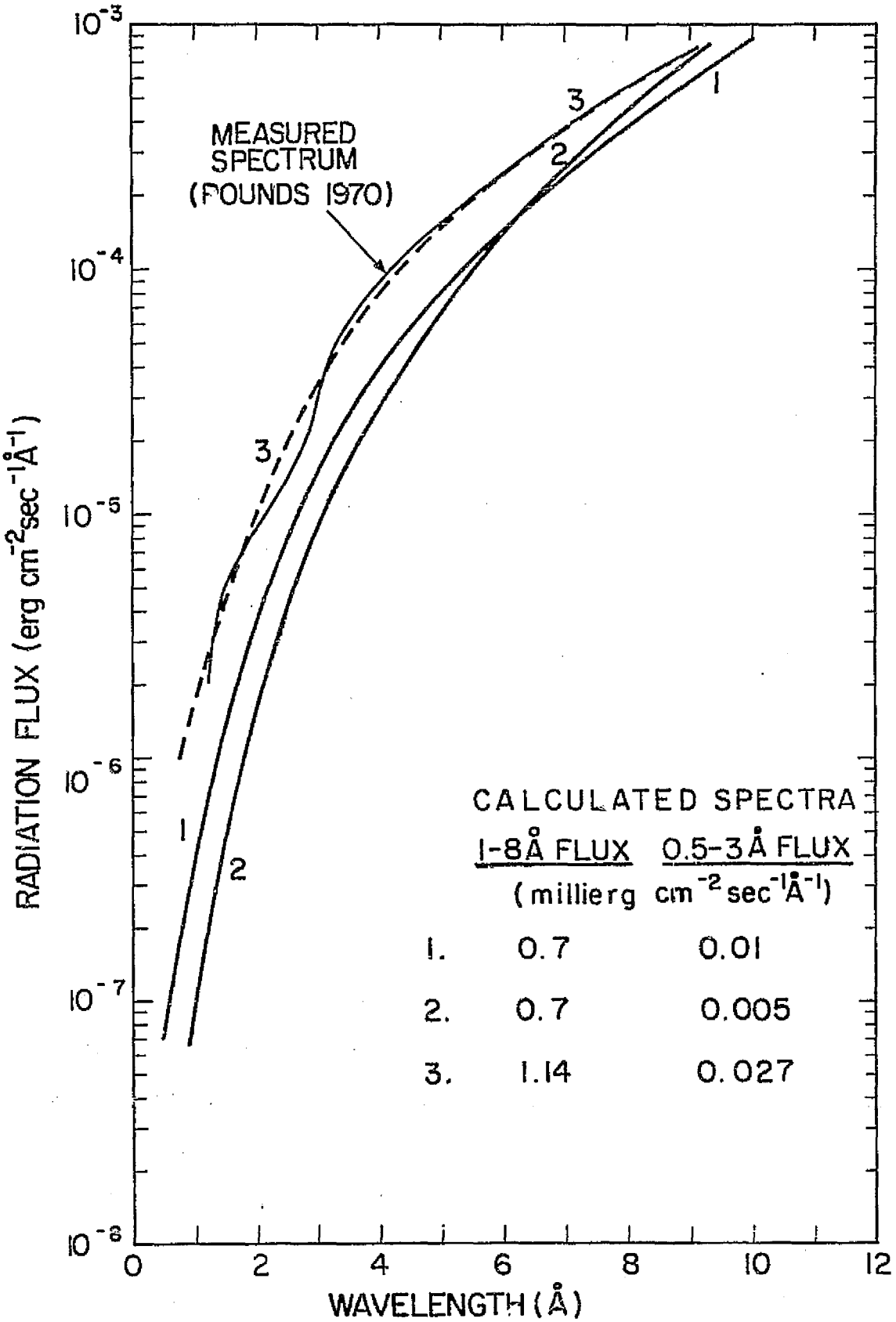

Figure 4.5 The spectral distributions of X-rays below 10 Å corresponding to different flux values in the 1-8 Å and 0.5-3 Å bands. The broken curve shows the spectrum measured by *Pounds* [1970].

Equations (4.4) and (4.5) give the values of σ_a over the wavelengths from 1 to 10 Å.

The optical depth factor is governed by absorption due to all constituents, and is given by

$$\tau(\chi,z) = \sec\chi \sum_i \sigma_a^i(\lambda) \int_z^\infty [X]_i(z)\, dz \quad . \tag{4.14}$$

The energies of the incident photons in the 1-10 Å X-ray band vary from 12.4 keV to 1.24 keV, which are far in excess of the energy required to produce one ion-pair in air. Therefore, each photon is capable of producing more than one ion-pair. The first ion-pair is produced by the incident photon while the rest are produced by the secondary electrons through impact ionization. Photons in the soft X-ray bands were found to spend, on an average, about 35 eV in producing one high energetic photon, or the ionization yield, can be expressed as [*Swider*, 1969]

$$\eta = \frac{12400}{35\ \lambda(\text{Å})} = \frac{354}{\lambda(\text{Å})} \quad . \tag{4.15}$$

This formula, however, does not take into account the efficiency of different species in producing secondary electrons through impact ionization, which depends on the impact ionization cross section of each species.

Ionization yields have also been tabulated by *Ohshio et al.* [1966] over the entire range of X-ray and EUV wavelengths, using values adopted from the results of several workers. In the X-ray wavelengths these values show the $\eta(N_2)/\eta(O_2)$ ratio is about 1.13, indicating that N_2 is more efficient in producing secondary electrons than O_2.

More recently, *Schlegel* [1971] has calculated the ionization yields of N_2, O_2, and O in the upper atmosphere using a Monte Carlo simulation of a model ionosphere. According to his results η is a function of both the altitude and the solar flux. The height averaged ionization yields for the range 130-300 km, when compared with values reported by *Ohshio et al.* [1966], show that the two sets of values are in good agreement in the case of N_2 and O. However, a wide discrepancy exists with the O_2 values, the Monte Carlo values being lower by a factor nearly 10 for a photon of wavelength 10 Å. Schlegel attributes this discrepancy as due to the wide difference in the O_2 and O densities in the height range considered. However, even at 120 km, where the O_2 and O densities do not differ very much, Monte Carlo values for O_2 are about a factor of two less than the corresponding values given by Ohshio et al. for the wavelength interval 10-15 Å. The implications of this study on the ionization rates near 100 km have not been assessed so far. Since the contribution by X-rays is only a fraction of the total ionization at altitudes of interest it is expected that a reduction in the O_2^+ yield will not cause any serious error in the present calculations. In view of this, and also for ease in computations, ionization yields tabulated by *Ohshio et al.* [1966] have been adopted in this study.

In the present study, X-ray fluxes as measured on July 24, 1968 were used, so that the results could be compared with the electron density profiles measured on that day. Figure 4.6 shows the fluxes in the bands 0.5-3 Å, 1-8 Å, and 8-20 Å as measured with instruments on board the SOLRAD 9 satellite. The two rocket measurements at $\chi = 18°$ and $\chi = 60°$ were taken at 1700 UT and 2136 UT, respectively. It is seen from the recordings

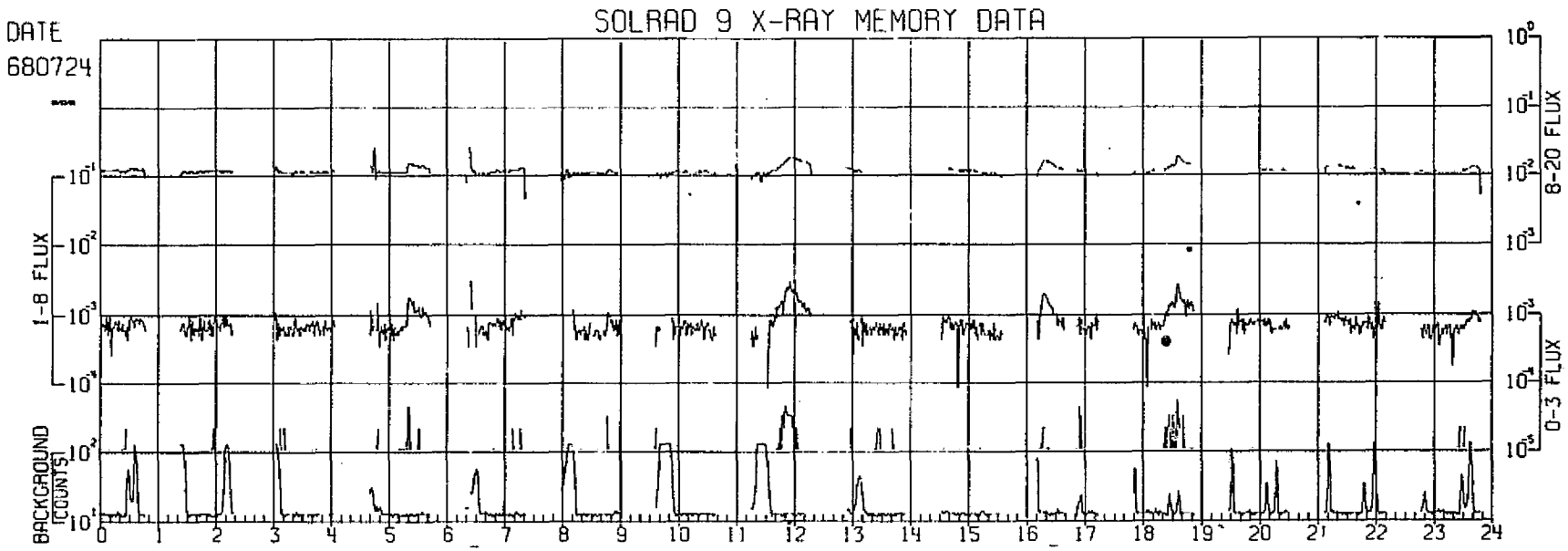

Figure 4.6 X-ray fluxes in the bands 0.5-3 Å, 1-8 Å, and 8-20 Å as measured on July 24, 1968 with instruments on board SOLRAD 9 satellite (courtesy NOAA Environmental Data Service).

that these times are free of any solar flares or any other enhancements. Further, the X-ray flux in the 1-8 Å band appears to be identical at both instances, being equal to 0.7 millierg cm^{-2} sec^{-1}. The flux in the 0.5-3 Å band on this day, however, is below the threshold value for detection by the instruments, i.e., below 0.01 millierg cm^{-2} sec^{-1}. Hence, the calculations were done using two values for this quantity; an upper limit of 1×10^{-5} erg cm^{-2} sec^{-1} and a lower limit of 0.5×10^{-5} erg cm^{-2} sec^{-1}. These two values correspond to flux ratios of 70 and 140, respectively. The spectra corresponding to these flux ratios and 1-8 Å flux of 0.7 millierg cm^{-2} sec^{-1} are also shown in Figure 4.5.

It should also be noted here that the above satellite measured fluxes could be in error to a considerable extent. One source of such error is the assumption of a gray-body spectrum for the solar spectrum in the data processing procedure. According to *Kreplin* [1970], the published fluxes deduced on the basis of this assumption are unlikely to differ by more than a factor of 10 from the absolute flux values for wavelengths below 20 Å. The other source of error is due to the uncertainty in the effective passband of the detector windows. Recently, *Wende* [1971] investigated the consistency between data from several experiments measuring X-ray fluxes below 20 Å and found that both the passbands and the conversion factors of the relevant bands have to be modified in order to bring agreement among different sets of results. Unfortunately, these corrections have been carried out for the early experiments only, and the extent of this error as applicable to SOLARD 9 data cannot be assessed.

The production rates q(1-10 Å) calculated using the above mentioned spectral distributions for solar zenith angles 18° and 60° are illustrated in Figure 4.7.

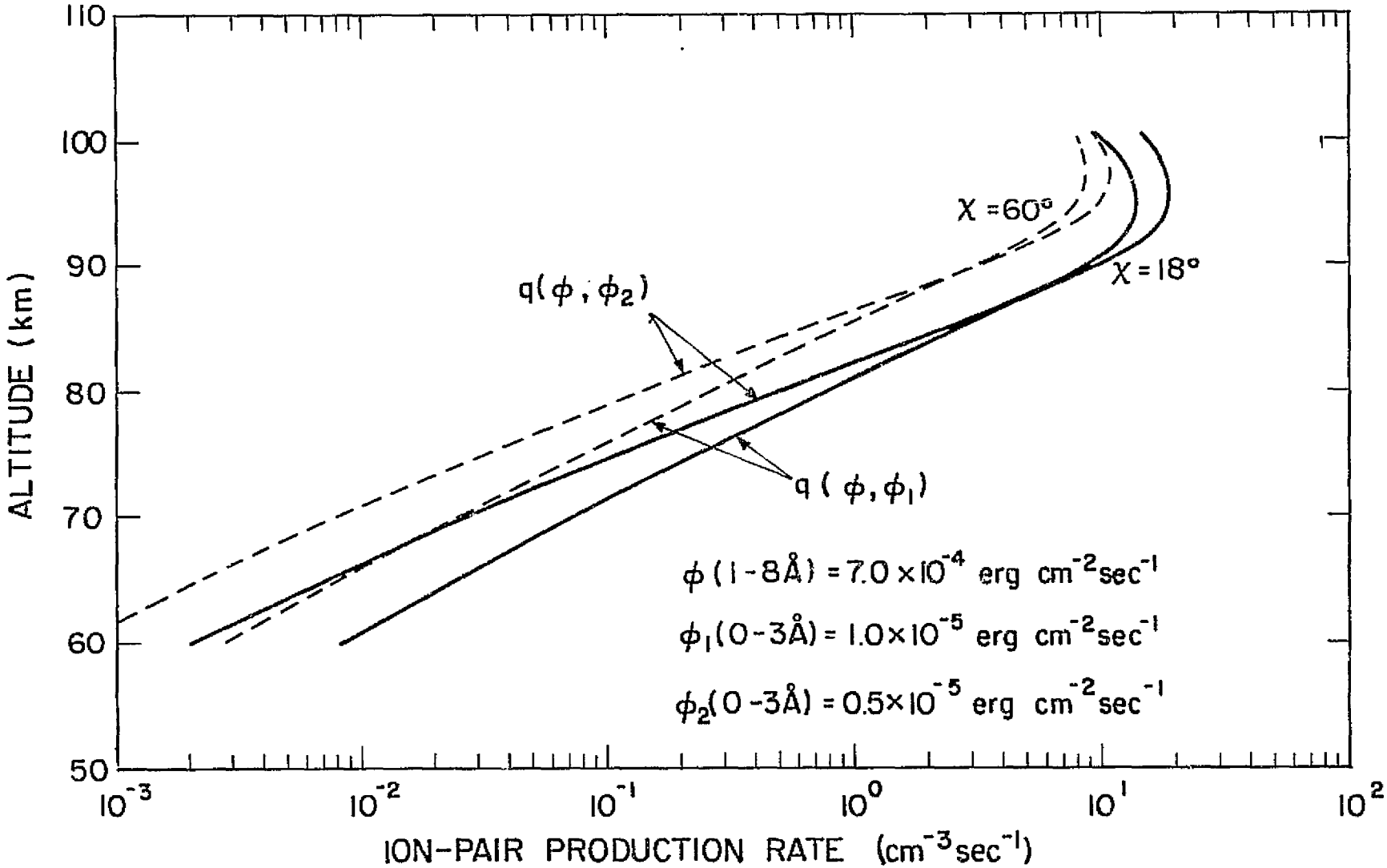

Figure 4.7 The ion-pair production rates due to X-rays below 10 Å at zenith angles 18° (noon) and 60°, calculated for the two 1-10 Å spectra shown in Figure 4.5 (curves 1 and 2).

4.2.2 *30 - 100 Å X-rays.* This region of the spectrum, unlike the shorter wavelength region, is composed mostly of emission lines as evidenced by both theory [*Mandel'stam*, 1965] and observations [*Manson*, 1967, 1972; *Freeman and Jones*, 1970]. These wavelengths come from regions of the corona having low temperatures and are not subject to as high a variability as the shorter wavelengths. Most of the emission lines between 16 and 100 Å are due to transitions occurring in heavy elements such as oxygen, carbon, sulphur, and other heavy elements including silicon, magnesium and iron. Of these lines, a major contribution comes from the C IV line at 33.7 Å as it lies just above the critical wavelength λ_K. Since the absorption cross section of this line is low, it is capable of penetrating down to heights close to 90 km. In order to compute the ion-pair production rates due to these lines, it is necessary to find out the distribution of energy among the different lines.

Manson [1972], using a rocket-borne telemetering monochromator, obtained a highly resolved spectrum between 33 and 128 Å on August 8, 1967. The 10.7 cm flux on this day was 143 units. The 33.7 Å line intensity measured was not more than 2×10^{-3} erg cm^{-2} sec^{-1}. Using parachute-recovered photographic plates, *Freeman and Jones* [1970] obtained well resolved spectra on two days. The measurement on March 20, 1968 (10.7 cm flux = 131 units) which extended from 14 Å to about 400 Å recorded an intensity of 9 millierg cm^{-2} sec^{-1} for the 33.7 Å line. The other measurement on November 20, 1969 (10.7 cm flux = 189 units) which extended from 15 Å to 76 Å, recorded an intensity of 7 millierg cm^{-2} sec^{-1} for the 33.7 Å line. On the other hand, the flux intensities of

33.7 Å measured by *Argo et al.* [1970] using a rocket-borne spectrometer under a variety of solar conditions during the period 1964-1968 gave values lying in the range $2 \times 10^{-2} - 6 \times 10^{-2}$ erg cm^2 sec^{-1} These values are several factors larger than the values of Freeman and Jones, and more than an order of magnitude larger compared to Manson's value. Since Manson's spectrum begins only at 33 Å, one could argue that any end-errors could have affected his measurement at 33.7 Å, though he claims an accuracy of ± 25% over the entire range of measurements. These measurements also show that the variability of the other lines between these different days is much less than that of the 33.7 Å line, and that this line could be specially sensitive to changes in the solar activity [*Manson*, 1972].

Broad-band measurements in the range 44-60 Å are also made regularly by satellite-borne detectors. However, in view of the many assumptions made in the processing of data, these measurements can only be taken as an index of solar activity rather than as absolute flux values [*Kreplin*, 1970]. Further, it has been recently reported that the 44-60 Å detector is also sensitive to radiation in the 8-20 Å band, and that the published data could be in error by several factors [*Kreplin et al.*, 1973]. Unfortunately, of the days for which rocket measurements are available, 44-60 Å flux data are available only one day, *viz.* August 8, 1967. Hence a proper comparison between the rocket-measured and the satellite-measured flux cannot be made.

The 44-60 Å flux measured on August 8, 1967 is 0.306 erg cm^{-2} sec^{-1}, while that measured on July 24, 1968 is 0.28 erg cm^{-2} sec^{-1}. Considering the uncertainties involved, these two measurements show identical conditions as far as soft X-ray emissions are concerned. Hence, the resolved

spectrum obtained on August 8, 1967 by *Manson* [1972] can be assumed to be applicable on July 24, 1968 as well. Therefore, in this study Manson's data are adopted for solar flux above 30 Å except for the 33.7 Å line. For this line a flux of 7 millierg cm^{-2} sec^{-1} has been adopted, considering the variability of the measured data.

X-rays beyond about 50 Å are significant in the ionization of heights above 100 km only and not really important in *D*-region studies. Nevertheless, as mentioned in Section 4.1.3, contributions from all wavelengths have been included in order to calculate the ion-pair production rates up to 120 km. The results of these calculations are shown in Figure 4.8 for the solar zenith angles 18° and 60°.

4.3 *High-Energetic Particles*

The sources included in this section are the precipitating electrons originating from the outer radiation belts surrounding the earth, and the galactic cosmic rays. Both of these sources are considered to have flux incident on the atmosphere independent of the solar zenith angle, though observations indicate the existence of a small day/night asymmetry.

4.3.1 *Precipitating electrons*. The effect of these electrons in the earth's atmosphere is most prominent in the polar regions. The ionization produced by them in these regions has been investigated in detail by several workers [*Rees*, 1963]. It was not until satellite detectors began to monitor these particles over the earth's atmosphere that they were recognized as a potential source of ionization in the *D* region. The ion-pair production by precipitating electrons is naturally a function of their initial energies and the energy deposition rate in the atmosphere. From laboratory measurements of energy-range relationship, it is found

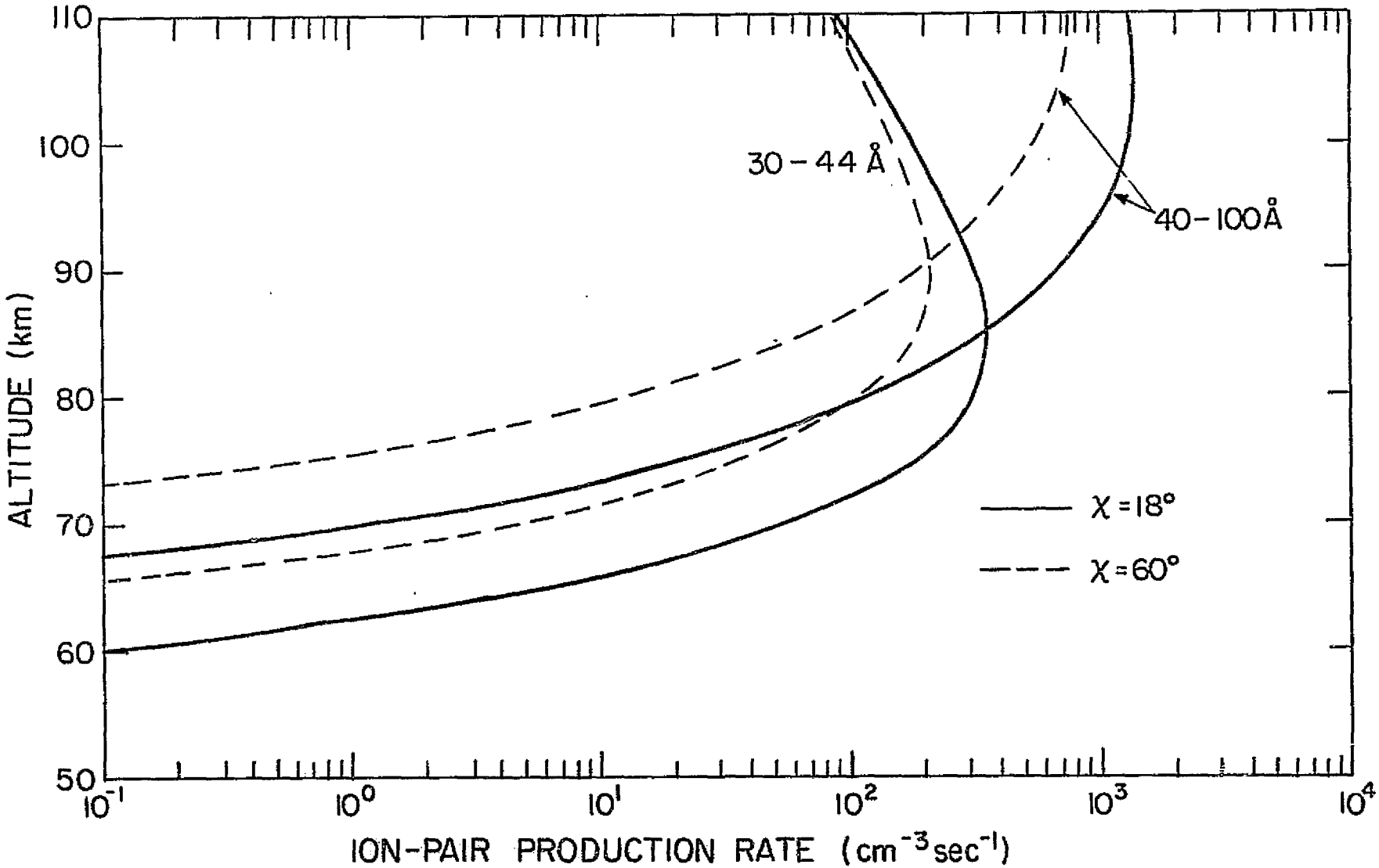

Figure 4.8 The ion-pair production rates due to X-rays in the bands 30-44 Å and 40-100 Å, calculated for zenith angles 18° (noon) and 60°.

that only the electrons with energies greater than about 40 keV could penetrate to *D*-region altitudes, and energies over 200 keV are required for penetration down to 70 km.

The energy deposition rates of these electrons have been worked out by *Rees* [1963] for different distributions of the flux over the hemisphere. Using these results, the calculation of the ion-pair production rate can be easily determined. The ion-pair production rate due to monoenergetic electrons of unit flux is given by

$$q(PE) = \frac{E_{in}}{\varepsilon} \frac{\lambda(S/R)}{r_o} \frac{\sum a_i [X]_i \ (z)}{\sum a_i [X]_i \ (R)} \quad , \tag{4.16}$$

where

E_{in} is the initial energy of the incident electron,

ε is the energy required to produce one electron-ion pair in air (35 eV),

R is the maximum penetration depth of the electron,

S is the penetration depth at an altitude z,

r_o is the maximum range of the electrons,

λ is the normalized energy deposition function, and

a_i is the ionization efficiency of the ith constituent.

Rees [1963] calculated the normalized energy deposition function for an isotropic distribution of the incident electrons over the pitch angles from 0° to 80°. His results can be expressed by the empirical formulas.

$$\begin{aligned} \lambda(S/R) &= 1.1\ (S/R)^3 - 3.3\ (S/R) + 2.2, \qquad 1 > S/R > 0.1 \\ &= 1.9 \qquad\qquad\qquad\qquad\qquad\qquad S/R < 0.1 \end{aligned} \tag{4.17}$$

The penetration depth R of an electron with initial energy E_{in} is given by the formula

$$R = 4.57 \times 10^{-6} E_{in}^{1.75} \tag{4.18}$$

where E_{in} is in keV and R is in g.cm^{-2}. When the incident electrons have a distribution of energy, the corresponding production rates are obtained by integrating over the desired energy range.

Usually, the detectors measuring the precipitating electrons respond to the total flux above a certain minimum threshold energy E_{min}. Therefore, the energy spectrum is expressed in terms of this total flux $N_o(E_{min})$. Measurements carried out in the past [*Potemra and Zmuda*, 1970] have shown that the total flux of precipitating electrons can be expressed by a power exponential form

$$N(>E) = N_o(>E_{min}) \ (E/E_{min})^{\gamma} \tag{4.19}$$

where

$N(>E)$ is the flux of electrons with energies greater than E, and

γ is a constant representing the hardness of the spectrum.

It is also sometimes possible to express $N(>E)$ by a simple exponential form

$$N(>E) = (>E_{min}) \exp(-\frac{E-E_{min}}{E_o}) \tag{4.20}$$

where E_o is the e-folding energy, a parameter representing the hardness of the spectrum.

Because of the scarcity of the observations and the wide scatter of the available data, it is difficult to determine unambiguously the correct form of a general expression for the precipitating electron spectrum that can be applied in instances such as ionospheric calculations. In general, the exponential spectrum shows smaller fluxes of electrons with higher energies. In the present calculations, a power exponential spectrum is preferred as it would give higher ionization rates at lower altitudes than a simple exponential spectrum with the same N_o. According to *O'Brien* [1964], satellite measurements of the average flux of precipitating electrons with energies greater than 40 keV were found to vary from 10^2 to 10^3 electrons cm^{-2} sec^{-1} $ster^{-1}$ at midlatitudes. On the other hand, rocket measurements of midlatitude electron precipitation show low fluxes in the range 4-7 particles cm^{-2} sec^{-1} $ster^{-1}$ for electrons with energies greater than 40 keV under magnetic quiet conditions [*O'Brien et al.*, 1965; *Gough and Collin*, 1973]. *Potemra and Zmuda* [1970] who compared the *D*-region nighttime ionization rates due to scattered Ly-α radiation and precipitating electron found that the ionization rates due to precipitating electrons with N_o(>40 keV) equal to 300 and $\gamma = 3$ just exceed those due to scattered Ly-α radiation.

In the present study, it is necessary to look for an O_2^+ source between 70 and 80 km that would partly account for the cluster ion formation. In order to investigate the precipitating electrons as a potential source of O_2^+ ions in this height range, ion-pair production rates have been calculated using total fluxes of 300 electrons cm^{-2} sec^{-1} $ster^{-1}$ and γ varying from 2 to 4. The results are shown in Figure 4.9.

4.3.2 *Galactic cosmic rays.* Cosmic rays penetrating down to *D*-region altitudes are composed mostly of protons possessing energies

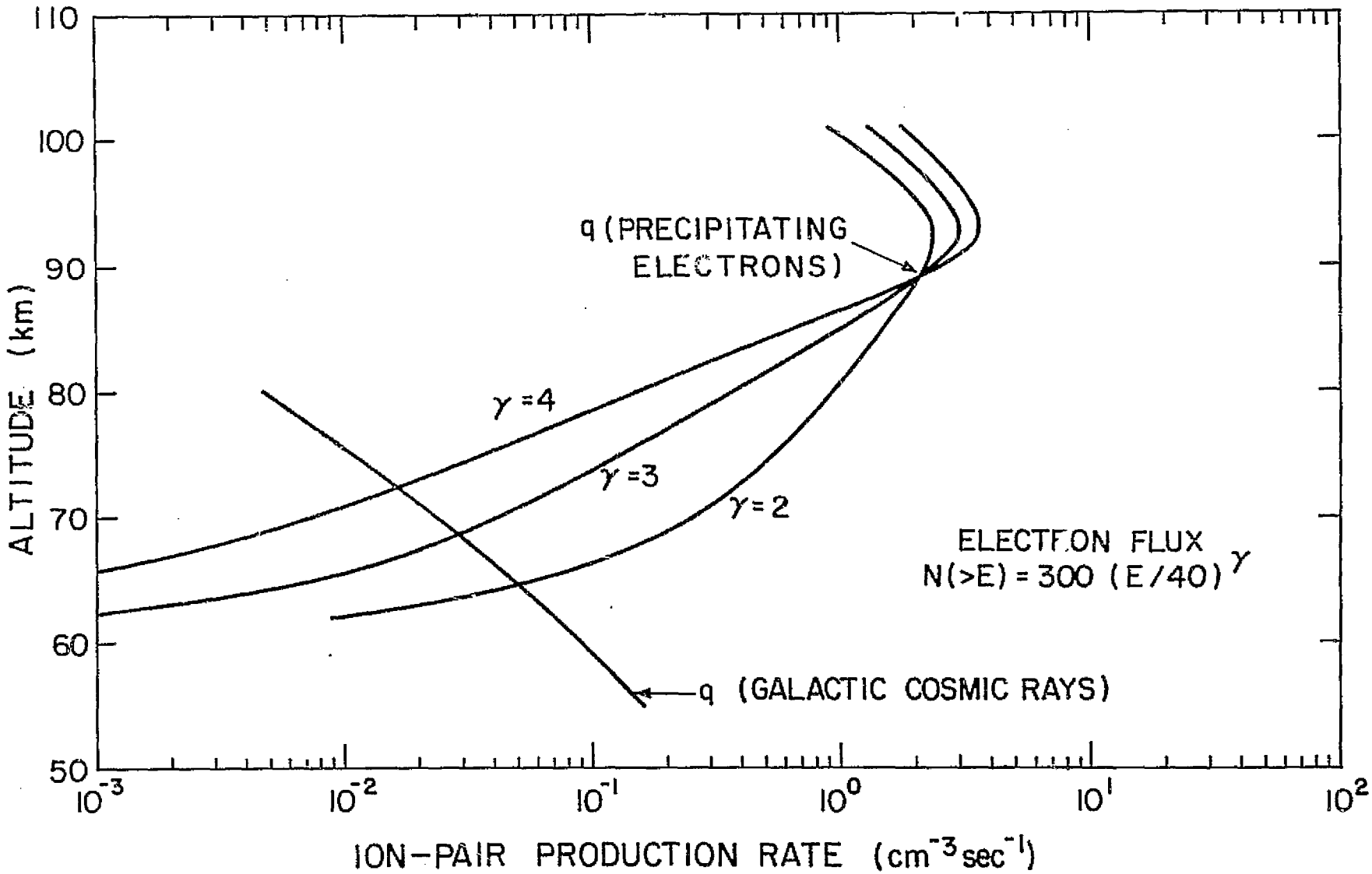

Figure 4.9 The ion-pair production rates due to galactic cosmic rays, and precipitating electrons having energies greater than 40 keV (N(> 40 keV) = 300), and hardness indices of 2, 3, and 4.

greater than about 10 MeV, and the galactic proton flux spectrum in this energy range peaks around 300 MeV. The proton spectrum for energies above this value is generally expressed in a power exponential form, similar to that given in the last section for precipitating electrons.

Velinov [1968] has worked out the ion-pair production rates due to galactic cosmic rays using laboratory derived energy deposition functions for relativistic particles, and using assumed energy distributions for the incoming particles. He showed that this ion-pair production rate has a geomagnetic latitude (λ_m) dependence of $\cos^{-6}\lambda_m$ when the rigidity spectrum is of the power exponential form with the exponent equal to 2.5, and the geomagnetic threshold of rigidity is given by $R_c = 14.9 \cos^4\lambda_m$. In order to calculate the ion-pair production rates theoretically, one has to know correctly the energy distribution functions, the composition of the incident particle flux, etc. In spite of several years monitoring of the incident cosmic ray intensities, no proper picture has emerged so far which will represent these fluxes correctly.

In view of these difficulties it has been custormary to obtain the ion-pair production rate using the semi-empirical formula

$$q(GCR) = q_o \, n(z)/n_o \tag{4.21}$$

where

q_o is the ion-pair production rate at a reference height z_o, and

n_o is the number density of air at height z_o.

The values of q_o are usually deduced from direct measurements. Using balloon observations, *Neher and Anderson* [1962] found that the

cosmic ray ionization rates at a low altitude increases by a factor of 10 between latitudes 0° and 60° during solar minimum, and by a factor of five during solar maximum. Using these data *Swider* [1969] has tabulated factors for determining $q(GCR)$ for different latitudes and solar epochs, from which a value of 1.0×10^{-17} (sec^{-1}) is chosen as appropriate for the conditions under investigation. Thus, the ion-pair production rates are given by

$$q(GCR) = 1.0 \times 10^{-17}\, n(z) \tag{4.22}$$

The height distribution of this production function is illustrated in Figure 4.9.

4.4 *Discussion*

The major sources responsible for the daytime ionization of the region below 110 km are shown in Figure 4.10. According to these curves the region between 110 and 104 km is ionized at noontime mainly by the 977 Å solar line. Ly-β line ionizes the region immediately below, between 96 and 104 km. X-rays between 30 and 40 Å, consisting mainly of the C IV line at 33.7 Å, are responsible for ionizing the next layer, between 89 and 96 km. The production function due to X-rays between 40 and 100 Å is also shown here. Though it is never a dominant source at these heights, it still makes a significant contribution between 100 and 110 km.

The ionization of nitric oxide by the solar Ly-α line becomes the major source below 89 km, extending down to about 65 km. Below this altitude, galactic cosmic rays become the major source, both at daytime

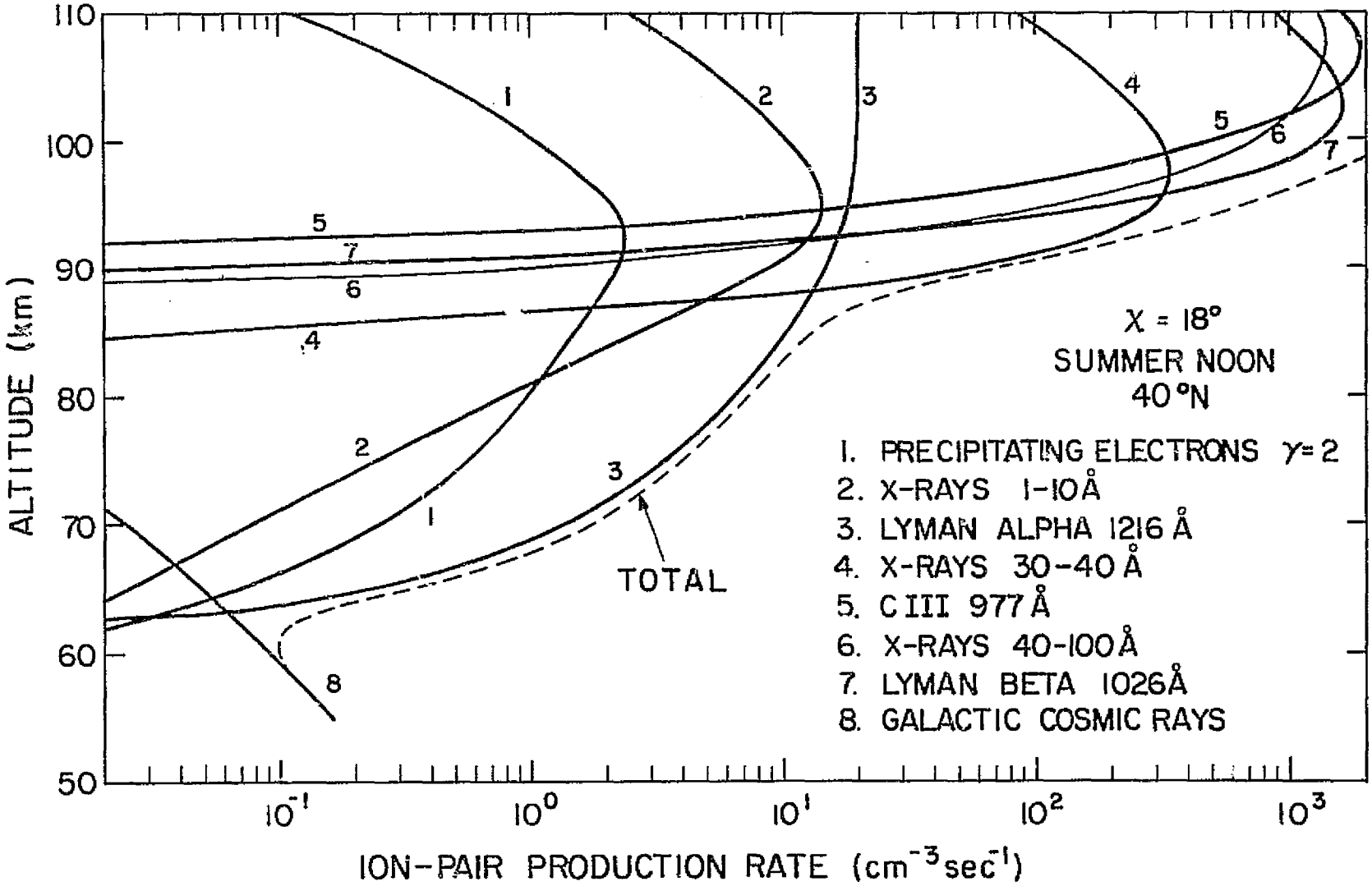

Figure 4.10 The ion-pair production rates in the *D* region due to major ionization sources at daytime (χ = 18°).

and nighttime. Ionization due to precipitating electrons also become important here, if one considers a hard spectrum for these particles.

The rest of the sources considered, *viz.* EUV ionization of $O_2(^1\Delta_g)$ and the X-rays below 10 Å, both remain as minor sources at all heights and zenith angles. For X-rays, two spectral distributions were assumed, one with a 0-3 Å flux of 1×10^{-5} erg cm^{-2} sec^{-1} $Å^{-1}$, and the other having half this value. Both of these spectral distributions give ionization rates below 90 km which vary in the range 3-4, corresponding to a variation of χ from 18° to 60°.

The solar zenith angle variation of the total ion-pair production rates in the *D* and lower *E* region are given in Figure 4.11. As mentioned above, the sources ionizing the region between 90 and 110 km consist of several components. The solar zenith angle variation of each of these sources becomes appreciable in the bottom part of the individual production curves. This is because the optical depth factor is near zero in the upper portion, and any change in χ does not affect the attenuation of the incident radiation significantly. Since each of these production curves tail off at different heights, the sum total of the variation between two χ values due to all of these components remains approximately the same. Between 18° and 60°, it is about a factor of 1/3 in the height interval 90-100 km. At 90 km, however, the contribution to this difference from the EUV ionization is only 1/10. The remainder comes from the Ly-α ionization of NO.

The decrease of the Ly-α production function with increase in χ is very small at heights above 90 km. At 90 km it is about a factor of 1.2. As the optical depth factor increases below this height, the variation of the production function also increases. At 70 km, the Ly-α

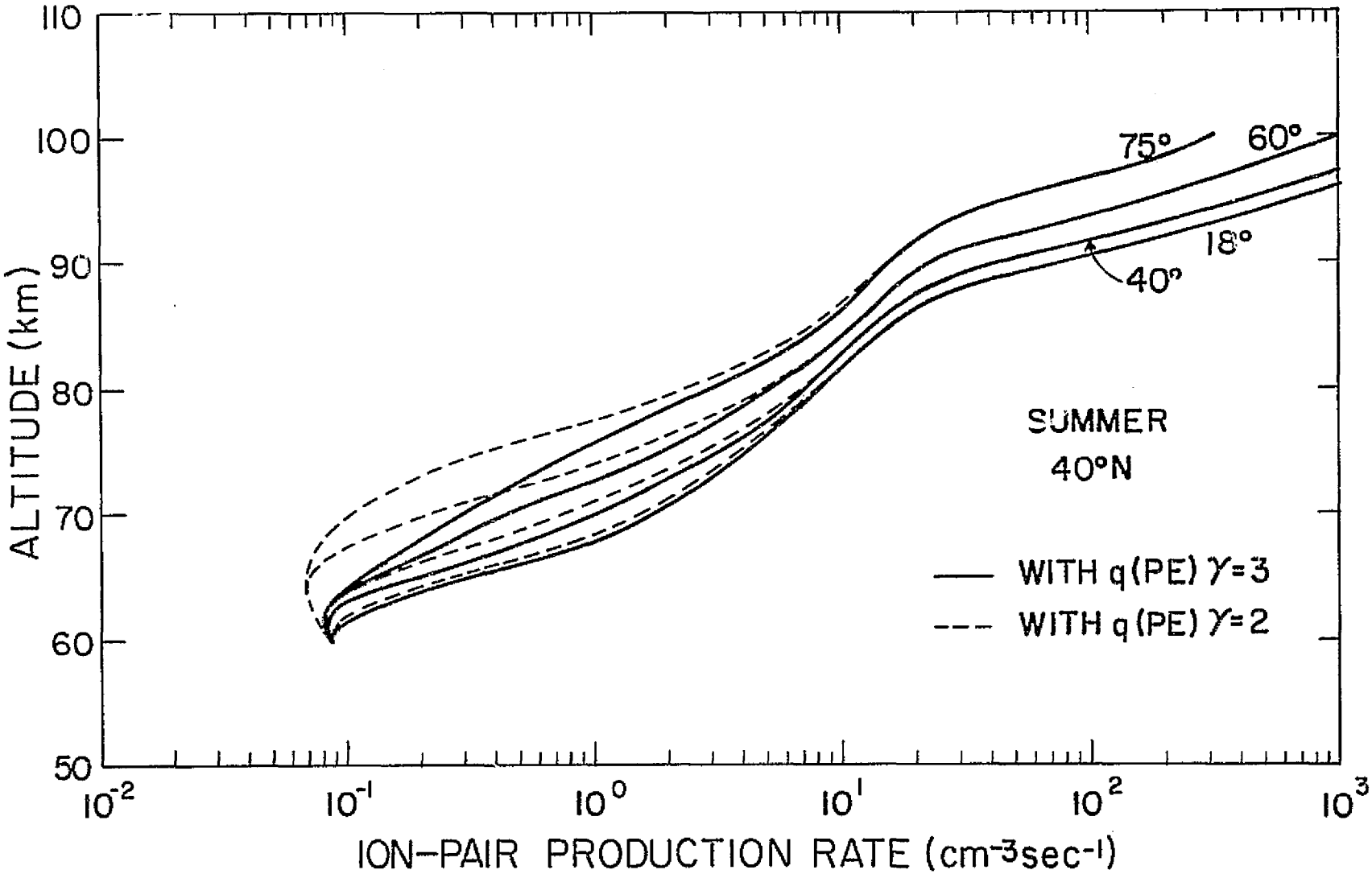

Figure 4.11 The variation of the *D* region ion-pair production function with the solar zenith angle, shown with contributions from two different precipitating electron spectra.

ionization rate drops by a factor of 1/15 between 18° and 60°. Since there is no diurnal variation in [NO] between 70 and 90 km as obtained in the diurnal calculations, this variation is due solely to the attenuation of the incident Ly-α intensity.

Below 70 km, however, the variation due to Ly-α ionization is masked by those due to precipitating electrons and galactic cosmic rays. Since both of these sources do not have a diurnal variation, their contribution becomes dominant at large χ angles when the Ly-α contribution drops rapidly. Therefore, the diurnal variation exhibited by the total ion-pair production curves at a given height in this range depends on the relative contributions from each of these sources at that height.

In the case of the precipitating electrons, the relative contributions they make at different heights depend on the spectral characteristics of the incident particle flux. In this study, two spectral distributions given by $\gamma = 2$ and $\gamma = 3$ have been used for the precipitating electron flux. In the total ion-pair production curves shown in Figure 4.11, the solid lines refer to the $\gamma = 2$ spectral distribution while the broken lines refer to the $\gamma = 3$ spectral distribution Figure 4.9. Since these production rates remain in the background as fixed values without varying with χ, they control the ionization production at large χ angles and hence the reduced variation shown by the solid curves.

The ionization due to $\gamma = 3$ precipitating electrons is much less than the Ly-α ionization, even at large χ angles, in the height interval 56-70 km. Hence, the broken lines show a much larger variation with increasing χ. At 70 km, this is nearly a factor of 7 corresponding to a 18°-60° increase in χ.

Below 65 km, the galactic cosmic ray ionization becomes dominant. Hence both sets of curves, corresponding to all values of χ, converge towards the q(GCR) values shown in Figure 4.9. Thus the total production function does not exhibit a significant diurnal variation at these altitudes.

5. *D*-REGION ION CHEMISTRY

Over the past few years, many experiments have been carried out using rocket-borne instruments to measure the *D*-region ion composition as well as the electron densities. Several attempts have been made to interpret these measurements through model calculations, but without much success.

Some of the problems encountered in explaining the *D* region ion-composition measurements have already been mentioned in Chapter 1. These occur mainly due to our poor understanding of the ion reaction schemes, and also due to lack of accurate data on various factors such as reaction rate constants and minor neutral constituent densities.

In this chapter, the *D*-region ion chemistry is discussed, with a view to develop a unified model for the *D*-region ion distribution. In Section 1, the previous measurements of the ion composition and electron-density profiles are discussed. The relevant ionic reaction schemes and the available data on reaction rate constants are described in the subsequent sections.

5.1 *Measurement of Charged Species Distribution*

5.1.1 *Positive-ion composition.* The techniques available for the *in-situ* measurement of the *D* region positive-ion composition are summarized in Chapter 1. Using a quadrupole mass spectrometer described there, *Narcisi and Bailey* [1965] carried out the first detailed measurement of the positive-ion composition in the *D* region. Contrary to the previous theories that this portion of the ionosphere should comprise O_2^+ and NO^+ [*Nicolet and Aikin*, 1960], these measurements revealed for the first time that the dominant ions below about 82 km are hydrated

clusters of the type $H^+ \cdot (H_2O)_n$ where n = 1, 2, ... (Figure 1.4). The main feature of these profiles is the sudden disappearance of these cluster ions H_3O^+ and $H^+ \cdot (H_2O)_2$ above about 82 km, and the appearance of the molecular ions O_2^+ and NO^+ above this height. Below about 75 km, ions with mass numbers greater than 45 were also observed, while some metal ions were also observed in small quantities above 85 km.

The unexpected nature of these results naturally caused much speculation regarding their validity. There was doubt that these measurements represent the ambient ion distributions in the *D* region. The possibility of rocket contaminants giving rise to hydrated cluster ions was always there. Further, in the event these cluster ions are really present, the possibility of their breaking up into small fragments during the process of collection by the probes also cause much doubt about the validity of these measurements. *Narcisi* [1966] however maintained that these clusters H_3O^+ and $H^+ \cdot (H_2O)_2$ were indeed true constituents of the *D* region rather than the products of rocket contamination. According to *Narcisi* [1966], the absolute values of these measurements are correct to within a factor of 4, while the relative values are correct to within a factor of 2. The possibility of ion fragmentation however was not ruled out.

Subsequently a large number of positive-ion measurements have been carried out as summarized by *Narcisi* [1970]. Many of these measurements correspond to special events such as eclipses, PCA events at high latitudes, sunrise and sunset, and not to the ambient daytime *D* region at mid-latitudes. Nevertheless, almost all of these profiles exhibit the same features mentioned above. In addition, some profiles reveal the presence of $NO^+ \cdot (H_2O)$ in appreciable quantities in the *D* region. These measurements are also subject to large errors, factors of two or more, particularly in the cluster ion region below 80 km.

Goldberg and Aikin [1971] measured the *D* region positive-ion composition at solar zenith angles 28° and 53° near the geomagnetic equator. They too observed similar ionic distributions with the hydrated cluster H_3O^+, $H^+\cdot(H_2O)$ and $H^+\cdot(H_2O)_2$ dominating below about 82-83 km. They estimated the errors to be within ± 20% on major species, and 100% on the minor species. However, it is their opinion that the results are mostly qualitative in nature. They noticed that the heavy cluster ions tend to break up under shock effects created by the rocket trajectory, leaving only the more stable H_3O^+ and $H^+\cdot(H_2O)$ behind.

Another feature noticed in these ion-composition profiles is the presence of O_2^+ down to 65 km in appreciable quantities. On the upleg, concentrations around 100 cm^{-3} were detected between 65 and 85 km while on the downleg somewhat reduced values were detected. The computed profiles however showed steady decline of O_2^+ concentrations with values less than 1 ion cm^{-3} below 75 km.

Positive-ion composition measurements at high latitudes were carried out by *Johannessen and Krankowsky* [1972] during daytime (χ = 55°). They observed the cluster-molecular ion transition around 85 km. Unlike in the previous measurements, $H^+\cdot(H_2O)_3$ was found to dominate the cluster-ion region in a narrow height range around 85 km. Above and below this height range, $NO^+\cdot H_2O$ and $H^+\cdot(H_2O)_2$ were dominant among the cluster ions, respectively. They also observed high abundance of $H^+\cdot(H_2O)_4$ near 85 km. The appearance of these heavy clusters at this altitude range was attributed to the very low temperatures prevailing there during the time of measurements. These observations were made on both the upleg and downleg trajectories, and in both cases the fragmentation of the heavy clusters was considered to be small in this altitude range.

A similar set of positive-ion composition profiles was also reported by *Krankowsky et al.* [1972] who carried out measurements at high latitudes under nighttime conditions during different seasons of the year. They also observed cluster ions $H^+ \cdot (H_2O)_n$ where n = 1, 2, 3 dominating below 82-83 km, with the relative abundance of the heavier clusters increased on the downleg trajectory. This is attributed to the reduced shock effects on the downleg, resulting in less fragmentation of the heavier clusters on this trajectory. They also observed increased amounts of $NO^+ \cdot H_2O$ and $H^+ \cdot (H_2O)_4$ in a flight made on a summer night. This again is attributed to the very low temperatues which prevail in the high latitude summer nights affecting the reaction rates so as to increase the yield of these cluster ions.

More recently, *Johannessen and Krankowsky* [1974] measured the daytime positive-ion composition at a mid-latitude station during summer. Their results are also similar to those obtained by previous workers. The molecular ion to cluster ion transition was observed at 85 km. $NO^+ \cdot H_2O$ ions were detected in appreciable quantities between 85 and 95 km. A distinct feature observed is the high abundance of metal ions above 85 km.

In spite of the many positive-ion measurements that have been carried out in the recent past, only a very few have been reported as relating to ambient conditions prevailing in the mid-latitude, daytime, summer *D* region. Fortunately, when the measurements are made under quiet conditions, the positive-ion composition measurements made near the equator and at high latitudes do not differ significantly, except that the relative abundance of the heavier clusters tends to increase around the high-latitude mesopause.

5.1.2 *Negative-ion measurements.* The model calculations that have been carried out in the past to determine the negative-ion distribution in the daytime *D* region have shown that negative ions become important only below about 75 km [*Reid*, 1970; *Thomas et al.*, 1973]. However, the high ambient pressures prevailing in this region and the low ionization level, make it difficult to carry out *in-situ* measurements of the daytime negative-ion composition. On the other hand, the negative ion density above 75 km increases in the nighttime due to attachment of the free electrons to the neutral particles, making it possible to carry out rocket measurements in this altitude range.

Measurements made by *Narcisi et al.* [1971] at high latitudes during nighttime under quiescent conditions indicated the presence of molecular ions O_2^- and Cl^-, and two others which were identified as CO_3^- and NO_3^- between 78 and 80 km. Above 80 km, heavy clusters of the type $CO_3^- \cdot H_2O$ and $NO_3^- \cdot H_2O$ were also observed. A second flight made under similar conditions showed the presence of heavier ions above 80 km. No records were obtained below 75 km in both flights.

Arnold et al. [1971] also measured the nighttime negative-ion composition at a high latitude station, but under enhanced ionization during a weak aurora. Their results showed the presence of CO_3^-, Cl^-, HCO_3^- and NO_3^- between 72 and 77 km. They did not detect any hydrated clusters, though many of the other ions observed were of the same type as observed by *Narcisi et al.* [1971].

The only daytime negative-ion composition results available are those obtained during a PCA event at high latitudes, and during totality of an eclipse at mid-latitudes [*Narcisi et al.*, 1972a, 1972b]. The PCA event

measurements showed the presence of the molecular ions O_2^-, NO_3^- and hydrated clusters of the type $NO_3^- \cdot (H_2O)_n$ with n = 0-5 dominated the *D* region below 88 km.

Here again, the problem of constructing a suitable experimental *D* region negative-ion distribution representing the daytime quiet conditions at mid-latitudes is encountered. Most of the nighttime measurements give ion densities above 75 km, and are therefore not very helpful in constructing a daytime model for the mid and lower *D* regions. The two daytime measurements give values below 70 km, but these have been obtained under abnormal conditions. It is evident from these measurements that hydrated clusters $NO_3^- \cdot (H_2O)_n$ are present in the daytime *D* region.

It was noted that in many experiments the results are expressed in terms of the count rate only, rather than in terms of the ion densities. This is because the conversion of the count rate to absolute ion densities poses many problems. However, *Arnold et al.* [1971], expressed their results in terms of negative ion densities making use of the simultaneous measurements of the total positive-ion density and electron density.

5.1.3 *Electron-density measurements.* Some methods available for the measurement of *D* region electron densities are described in Chapter 1. These methods have been recently reviewed by *Sechrist* [1974], who concludes that the electron-density profiles derived from the rocket measurements of differential absorption, Faraday rotation and dc probe current have the greatest accuracy and the best height resolution. In fact, among various *in-situ* measurements of *D*-region parameters, accurate measurements are possible only in the case of electron densities [*Mechtly*, 1974].

C-3

An extensive series of *D* region electron-density profiles have been obtained using the above technique by *Mechtly et al.* [1972a] since 1967. Based on these measurements *Mechtly et al.* [1972a] have prepared two reference profiles for the mid-latitude daytime ($\chi = 60°$) *D*-region electron densities, corresponding to solar maximum and solar minimum periods.

In order to study the diurnal variation of the electron densities in the *D* region, a set of four profiles has been obtained on July 24, 1968, at solar-zenith angles 90°, 84°, 18° (noon) and 60° (Figure 1.3). As mentioned before, the present study was undertaken with a view to interpret the diurnal variation of the *D*-region ionization, as exhibited by these electron-density profiles, in particular those corresponding to 18° and 60° solar zenith angles. Some of the main features of these two profiles are summarized below.

(a) Between 90 and 100 km, the two profiles have approximately the same gradient, with the values differing by a constant factor of about 3.

(b) Between 85 and 90 km, the profiles have sharp gradients, particularly the noon profile whose number density increases from about 1.8×10^3 cm^{-3} to about 2.1×10^4 cm^{-3}, i.e. more than an order of magnitude. At 85 km, the difference is only a factor of 1.5.

(c) The profiles have a slow rise between 75 and 85 km, with the difference increasing to a factor nearly 3 at 75 km. The noon profile values increase from 1.2×10^3 cm^{-3} to about 1.8×10^3 cm^{-3} in this height interval.

(d) The difference between the two profiles decreases below 75 km, and around 66 km, they cross over. Below this level, the noon

profile has a very sharp gradient with the values dropping from about 150 cm^{-3} at 66 km to nearly 15 cm^{-3} at 65 km.

(e) Below 65 km, the drop in the afternoon profile is rather gradual, while the noon profile exhibits a slow variation. This difference in the height variations makes them to cross again just below 60 km.

The X-ray measurements taken by the SOLRAD 9 satellite on this day did not show any signs of solar flares (Figure 4.6) while the 10.7 cm flux recorded on this day was 148 units. This indicates that the measurements were taken on an undisturbed day during a high solar activity period.

5.2 *Ionic-Reaction Schemes*

5.2.1 *Positive-ion reactions.* Prior to detection of the hydrated cluster ions in the lower *D* region, the entire *D* region was thought to comprise only O_2^+ and NO^+ ions [*Nicolet and Aikin*, 1960]. As described in Chapter 4, the X-rays and EUV radiation below 1027 Å ionize O_2 while X-rays and EUV radiation below 911 Å as well as energetic particles ionize both O_2 and N_2. N_2^+ thus formed quickly undergoes a charge transfer reaction to yield O_2^+. Therefore, the abundance of N_2^+ in the *D* region during undisturbed periods becomes negligible. The O_2^+ formed in this manner yields NO^+ through direct the charge transfer reaction

$$O_2^+ + NO \rightarrow NO^+ + O_2$$

and also through the charge rearrangement reaction

$$O_2^+ + N \rightarrow NO^+ + O \quad .$$

Of course, NO^+ is also produced directly through Ly-α ionization of NO. In addition, NO^+ is produced from N_2^+ through the charge rearrangement reaction

$$N_2^+ + O \rightarrow NO^+ + N$$

and through the charge transfer reaction

$$N_2^+ + NO \rightarrow NO^+ + N_2$$

The first of these two reactions is not so important as far as NO^+ production is concerned but it plays a significant role in determining the yield of atomic nitrogen, both the ground state $N(^4S)$ and the metastable $N(^2D)$ species.

Above 100 km the production of O^+ is also important. This ion yields NO^+ and O_2^+ through reactions with N_2 and O_2, respectively. Unlike in the case of the molecular ions, O^+ does not undergo recombination with electrons. Its loss rate is determined solely by these ion-neutral reactions.

This scheme of positive-ion reactions, however, does not take into account the presence of the hydrated cluster ions in the mid and lower portions of the *D* region. The present reaction schemes which include the cluster ions are based on the scheme suggested by *Fehsenfeld and Ferguson* [1969].

According to this scheme, the clustering reaction chain starts with O_2^+ as the precursor ion with the 3-body association reaction

$$O_2^+ + O_2 + M \rightarrow O_4^+ + M \quad .$$

Though it appeared to be successful initially, it failed when the O_2^+ production rates due to $O_2(^1\Delta_g)$ ionization were reduced as shown by *Huffman et al.* [1971]. It was later shown that the yield of the hydrated cluster ion $O_2^+ \cdot H_2O$ through the reaction

$$O_4^+ + H_2O \rightarrow O_2^+ \cdot H_2O + O_2$$

is further reduced due to the reaction

$$O_4^+ + O \rightarrow O_2^+ + O_3 \quad ,$$

which reconverts O_4^+ into O_2^+.

The rate constant for this reaction measured and reported by *Fehsenfeld and Ferguson* [1972b] indicates that if the $[O]/[H_2O]$ ratio is sufficiently high, it can arrest the formation of the hydrated cluster ions. The introduction of this intercepting or short-circuiting reaction leads to the hypothesis that the sudden disappearance of the cluster ion population above the 82-85 km level could be caused by the sharp increase in the $O(^3P)$ concentration observed in this height range [*Ferguson*, 1971].

Following the work of *Lineberger and Puckett* [1969], *Ferguson* [1971] suggested a new series of reactions where the water molecules clustered to NO^+ through direct hydration

$$NO^+ \cdot (H_2O)_n + H_2O + M \rightarrow N^+ \cdot (H_2O)_{n+1} + M$$

$$n = 0, 1, 2, \ldots..$$

This direct hydration scheme, however, does not convert the NO^+ to its hydrate fast enough. An alternate path, faster than this, was found by *Dunkin et al.* [1971]. According to them, the association reaction

$$NO^+ + CO_2 + M \rightarrow NO^+ \cdot CO_2 + M$$

is followed by the fast switching reaction

$$NO^+ \cdot CO_2 + H_2O \rightarrow NO^+ \cdot H_2O + CO_2 \quad .$$

Dunkin et al. [1971] demonstrated the possibility of a similar association reaction involving N_2, but he could measure only an upper limit for the rate constant which was found to be very low. However, *Heimerl et al.* [1972] later established that its rate constant is much higher, and that it could form a faster path for the production of $NO^+ \cdot CO_2$, according to

$$NO^+ + N_2 + M \rightarrow NO^+ \cdot N_2 + M$$

$$NO^+ \cdot N_2 + CO_2 \rightarrow NO^+ \cdot CO_2 + N_2$$

The $NO^+ \cdot CO_2$ thus formed can undergo hydration to form $NO^+ \cdot H_2O$ shown above.

The reactions forming the multiple clusters of $NO^+ \cdot H_2O$ beginning from this ion were given by *Lineberger and Pucket* [1969]. However, according to Heimerl [*Thomas*, 1974] the association of $NO^+ \cdot H_2O$ with N_2 and subsequent switching with H_2O could form a more efficient mechanism to produce the multiple clusters of $NO^+ \cdot H_2O$. The reaction sequence here is

$$NO^+ \cdot H_2O + N_2 + M \rightarrow NO^+ \cdot H_2O \cdot N_2 + M$$

$$NO^+ \cdot H_2O + N_2 + H_2O \rightarrow NO^+ \cdot (H_2O)_2 + N_2 \quad .$$

Unfortunately, no reaction rate data are available for these reactions, and hence are not included in this study.

According to *Lineberger and Puckett* [1969], the multiple clusters $NO^+ \cdot (H_2O)_n$ with $n \geq 3$, can get converted to $H^+(H_2O)_n$ through the binary reactions

$$NO^+ \cdot (H_2O)_n + H_2O \rightarrow H^+ \cdot (H_2O)_n + HNO_2$$

$$n \geq 3 \quad .$$

This conversion reaction does not take place for $n < 3$ in view of reaction energetics. Therefore, the hydration of NO^+ ultimately leads to the products

$$NO^+ \rightarrow NO^+ \cdot CO_2 \rightarrow NO^+ \cdot H_2O \rightarrow NO^+ \cdot (H_2O)_2 \rightarrow H^+ \cdot (H_2O)_3$$

and the higher hydronium clusters. The absence of both H_3O^+ and $H^+ \cdot (H_2O)_2$ in this sequence creates a problem, because these are the two observed ions which dominate the middle portion of the *D* region where the primary ionization source is NO.

To avoid this difficulty, *Burke* [1970] suggested the reactions

$$NO^+ \cdot H_2O + H \rightarrow H^+ \cdot H_2O + NO$$

$$NO^+ \cdot (H_2O)_2 + H \rightarrow H^+ \cdot (H_2O)_2 + NO \quad .$$

Laboratory measurements of the rate constant of the first of these two reactions gave values less than 1×10^{-11} cm^3 sec^{-1} [*Ferguson*, 1971] which is too slow to make this path acceptable.

It was shown recently by *Heimerl et al.* [1972] that a fast path for the conversion of $NO^+ \cdot H_2O$ into the corresponding hydronium ions could be achieved thorugh the reactions.

$$NO^+ \cdot H_2O + OH \rightarrow H^+ \cdot H_2O + NO_2$$

$$NO^+ \cdot HO_2 + HO_2 \rightarrow H^+ \cdot H_2O + NO_3 \quad .$$

They showed that when established values of OH and HO_2 are used, the rate constants of these two reactions have to be about 5×10^{-9} $cm^3\ sec^{-1}$ in order to become effective in this conversion process. In this study the value adopted for the rate constants of both reactions is 1×10^{-9} $cm^3\ sec^{-1}$. Once $H^+ \cdot H_2O$ is formed *Heimerl et al.* [1972] suggested that its multiple hydrates are formed more rapidly through association with N_2 and subsequent switching with H_2O rather than through direct clustering, as mentioned earlier. With assumed data on reaction rates, this reaction path has been included in our study.

The complete positive-ion reaction scheme adopted in this study, along with the reaction rate constants used is given in Table 5.1. The more important reaction paths are shown in Figure 5.1.

5.2.2 *Negative-ion reactions.* The three-body attachment of a free electron to a neutral oxygen molecule produces a negative ion. The O_2^- ion so formed has a relatively low electron affinity. As a result a series of charge transfer and charge rearrangement reactions take place giving rise to a complex reaction scheme. The various negative ions thus formed include O_3^-, O_4^-, CO_3^-, CO_4^-, NO_2^-, NO_3^- and a large number of hydrated cluster ions. Associative detachment to

Table 5.1

Positive ion reactions.

Reaction No.	Reaction	Rate Constant $cm^n\ sec^{-1}$*
R_{101}	$O^+ + N_2 \longrightarrow NO^+ + N(^4S)$	1.0(-12)(300/T)** *Ferguson et al.* [1969]
R_{102}	$O^+ + O_2 \longrightarrow O_2^+ + O$	2.2(-11)(300/T) *Ferguson et al.* [1969]
R_{103}	$N_2^+ + O \xrightarrow{\gamma} NO^+ + N(^2D)$ $\xrightarrow{(1-\gamma)} NO^+ + N(^4S)$	1.4(-10) *Fehsenfeld et al.* [1970]
R_{104}	$N_2^+ + O_2 \longrightarrow O_2^+ + N_2$	4.7(-11)(300/T) *Ferguson et al.* [1969]
R_{105}	$N_2^+ + O_2 \longrightarrow O_2^+ + N_2$	3.3(-10) *Fehsenfeld et al.* [1970]
R_{106}	$O_2^+ + N \longrightarrow NO^+ + O$	1.8(-10) *Ferguson* [1967]
R_{107}	$O_2^+ + NO \longrightarrow NO^+ + O_2$	6.3(-10) *Fehsenfeld et al.* [1970]
R_{108}	$O_2^+ + O_2 + M \longrightarrow O_2^+O_2 + M$	$2.4(-30)(300/T)^2$ *Good et al.* [1970b]
R_{109}	$O_2^+ + H_2O + M \longrightarrow O_2^+ \cdot H_2O + M$	$2.6(-28)(300/T)^2$ *Fehsenfeld et al.* [1971a]
R_{110}	$O_2^+ \cdot O_2 + H_2O \longrightarrow O_2^+ \cdot H_2O + O_2$	2.2(-9) *Fehsenfeld et al.* [1971a]
R_{111}	$O_2^+ \cdot O_2 + O \longrightarrow O_2^+ + O_3$	3.0(-10) *Fehsenfeld and Ferguson* [1972b]
R_{112}	$O_2^+ \cdot H_2O + H_2O \longrightarrow H_3O^+ \cdot OH + O_2$	1.9(-9) *Fehsenfeld et al.* [1971a]

* n = 3 for binary reactions, and 6 for 3-body reactions.
**Read a(-n) as a x 10^{-n}.

(Table 5.1 continued)

R_{113}	$O_2^+ \cdot H_2O + H_2O \longrightarrow H_3O + OH + O_2$	0.3(-9) *Fehsenfeld et al.* [1971a]
R_{114}	$H_3O^+ \cdot OH + H_2O \longrightarrow H_3O^+ \cdot H_2O + OH$	3.2(-9) *Fehsenfeld et al.* [1971a]
R_{115}	$H_3O^+ + H_2O + M \longrightarrow H_3O^+ \cdot H_2O + M$	$3.46(-27)(300/T)^2$ *Good et al.* [1970a, 1970b]
R_{116}	$H_3O^+ + N_2 + M \longrightarrow H_3O^+ \cdot N_2 + M$	$1.4(-30)(300/T)^2$ *Heimerl et al.* [1972]
R_{117}	$H_3O^+ \cdot N_2 + H_2O \longrightarrow H_3O^+ \cdot H_2O + N_2$	1.0(-9) *Heimerl et al.* [1972]
R_{118}	$H_3O^+ \cdot H_2O + H_2O + M \longrightarrow H_3O^+ \cdot (H_2O)_2 + M$	$2.24(-27)(300/T)^2$ *Good et al.* [1970a, 1970b]
R_{119}	$H_3O^+ \cdot (H_2O)_2 + H_2O + M \longrightarrow H_3O^+ \cdot (H_2O)_3 + M$	$2.32(-29)(300/T)^2$ *Good et al.* [1970a, 1970b]
R_{120}	$H_3O^+ \cdot (H_2O)_3 + H_2O + M \longrightarrow H_3O^+ \cdot (H_2O)_4 + M$	$0.9(-27)(300/T)^2$ *Good et al.* [1970a]
R_{121}	$H_3O^+ \cdot (H_2O)_2 + M \longrightarrow H_3O^+ \cdot H_2O + H_2O + M$	7.0(-26) *Good et al.* [1970b]
R_{122}	$H_3O^+ \cdot (H_2O)_3 + M \longrightarrow H_3O^+ \cdot (H_2O)_2 + H_2O + M$	7.0(-18) *Good et al.* [1970b]
R_{123}	$NO^+ + N_2 + M \longrightarrow NO^+ \cdot N_2 + M$	$3.5(-31)(300/T)^2$ *Heimerl et al.* [1972]
R_{124}	$NO^+ + CO_2 + M \longrightarrow NO^+ \cdot CO_2 + M$	$2.4(-29)(200/T)^2$ *Dunkin et al.* [1971]
R_{125}	$NO^+ + H_2O + M \longrightarrow NO^+ \cdot H_2O + M$	$1.29(-28)(300/T)^2$ *Howard et al.* [1971]
R_{126}	$NO^+ \cdot N_2 + CO_2 \longrightarrow NO^+ \cdot CO_2 + N_2$	1.0(-9) *Heimerl et al.* [1972]
R_{127}	$NO^+ \cdot N_2 + H_2O \longrightarrow NO^+ \cdot H_2O + N_2$	1.0(-9) *Heimerl et al.* [1972]
R_{128}	$NO^+ \cdot CO_2 + H_2O \longrightarrow NO^+ \cdot H_2O + CO_2$	1.0(-9) *Dunkin et al.* [1971]
R_{129}	$NO^+ \cdot H_2O + H_2O + M \longrightarrow NO^+ \cdot (H_2O)_2 + M$	$1.12(-27)(300/T)^2$ *Howard et al.* [1971]

(Table 5.1 continued)

R_{130}	$NO^{+}\cdot(H_2O)_2 + H_2O + M \longrightarrow NO^{+}\cdot(H_2O)_3 + M$	$1.30(-27)(300/T)^2$ *Howard et al.* [1971]
R_{131}	$NO^{+}\cdot(H_2O)_2 + M \longrightarrow NO^{+}\cdot H_2O + H_2O + M$	1.5(-14) *Dunkin et al.* [1971]
R_{132}	$NO^{+}\cdot(H_2O)_3 + M \longrightarrow NO^{+}\cdot(H_2O)_2 + H_2O + M$	1.3(-12) *Dunkin et al.* [1971]
R_{133}	$NO^{+}\cdot(H_2O)_3 + H_2O \longrightarrow H_3O^{+}\cdot(H_2O)_2 + HNO_2$	7.0(-11) *Howard et al.* [1971]
R_{134}	$NO^{+}\cdot H_2O + H \longrightarrow H_3O^{+} + NO$	5.0 (-12) Estimate
R_{135}	$NO^{+}\cdot H_2O + OH \longrightarrow H_3O^{+} + NO_2$	1.0(-9) *Heimerl et al.* [1972]
R_{136}	$NO^{+}\cdot H_2O + HO_2 \longrightarrow H_3O^{+} + NO_3$	1.0(-9) *Heimerl et al.* [1972]

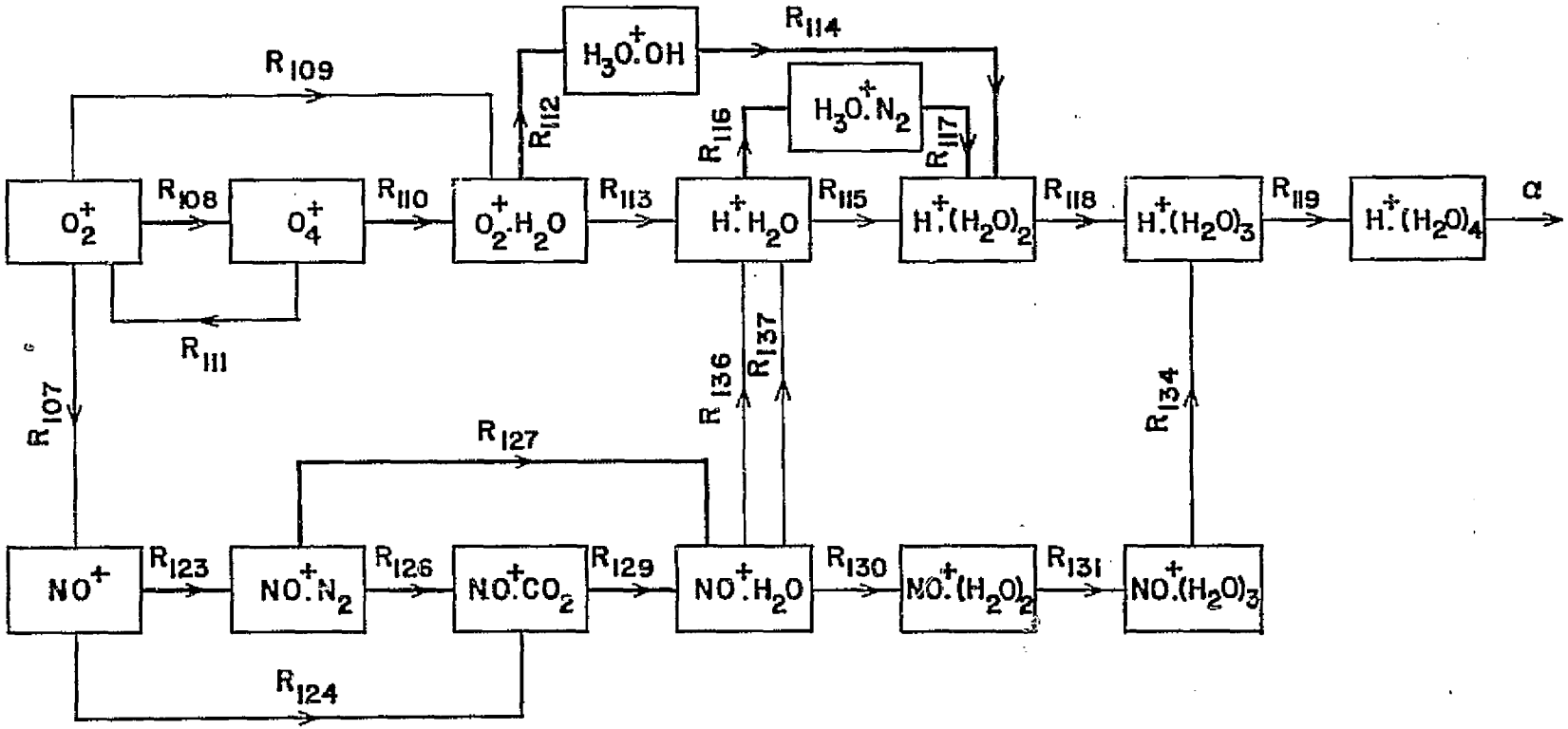

Figure 5.1 More important positive-ion reaction paths in the *D* region.

neutrals, mutual recombination with positive ions and photodetachment during the daytime are the main loss processes of these negative ions.

The development of the *D* region negative-ion chemistry has been based largely on the laboratory measurements of the reaction rate constants and model calculations, and not so much on actual ion composition measurements.

The reaction chain from O_2^- takes place in two different paths. In one, O_3^- is formed through charge transfer to O_3, and in the other, O_4^- is formed through a 3-body association reaction with O_2. In the first path, O_3^- yields CO_3^- through a charge rearrangement reaction with CO_2, which in turn yields NO_2^- through a similar reaction with NO. In the other path, charge rearrangement reactions with the same constituents yield CO_4^- and NO_3^- successively.

While the above sequences gives the main reaction paths, a large number of reactions involving atomic oxygen and other minor constituents also take place causing the negative-ion reaction scheme to be a complex one. The present reaction scheme which includes these molecular negative ions was developed by *Reid* [1970]. Among the more important secondary reactions are those involving $O(^3P)$. These cause reformation of O_2^- from O_3^- and CO_3^-, conversion of O_4^- to O_3^- and CO_4^- to CO_3^-, respectively. Hence, the negative-ion distribution depends to a large extent on the relative abundance of O_3 and O.

The complete reaction scheme used in this study is shown in Table 5.2.

Among these molecular ions, the high electron affinity of NO_3^- makes it a terminal ion. The possible mechanisms of its destruction

Table 5.2

Negative-ion reactions.

Reaction No.	Reaction	Rate Constant $cm^n\ sec^{-1*}$
R_{151}	$e + O_2 + O_2 \longrightarrow O_2^- + O_2$	$1.4(-29)(300/T)e^{-1.2/RT}$ ** *Phelps* [1969]
R_{152}	$e + O_2 + N_2 \longrightarrow O_2^- + N_2$	1.0(-31) *Phelps* [1969]
R_{153}	$O_2^- + O \longrightarrow O_3 + e$	2.5(-10) *Phelps* [1969]
R_{154}	$O_2^- + O_2(^1\Delta_g) \longrightarrow 2O_2 + e$	2.0(-10) *Phelps* [1969]
R_{155}	$O_2^- + O_3 \longrightarrow O_3^- + O_2$	3.0(-10) *Fehsenfeld et al.* [1967]
R_{156}	$O_2^- + NO_2 \longrightarrow NO_2^- + O_2$	8.0(-10) *Fehsenfeld and Ferguson* [1968]
R_{157}	$O_3^- + O \longrightarrow O_2^- + O_2$	1.0(-10) *Lelevier and Branscomb* [1968]
R_{158}	$O_3^- + CO_2 \longrightarrow CO_3^- + O_2$	4.0(-10) *Fehsenfeld et al.* [1967]
R_{159}	$O_3^- + NO \longrightarrow NO_3^- + O$	1.0(-11) *Fehsenfeld et al.* [1967]
R_{160}	$CO_3^- + O \longrightarrow O_2^- + CO_2$	8.0(-11) *Fehsenfeld et al.* [1967]
R_{161}	$CO_3^- + NO \longrightarrow NO_2^- + CO_2$	9.0(-12) *Fehsenfeld et al.* [167]
R_{162}	$CO_3^- + NO_2 \longrightarrow NO_3^- + CO_2$	8.0(-11) *Ferguson* [1969]
R_{163}	$NO_2^- + O_3 \longrightarrow NO_3^- + O_2$	1.8(-11) *Fehsenfeld and Ferguson* [1968]

* n = 3 for binary reactions.

**Read a(-n) as a x 10^{-n}.

(Table 5.2 continued)

R_{164}	$NO_2^- + H \longrightarrow OH^- + NO$	3.0(-10) *Fehsenfeld and Ferguson* [1972a]
R_{165}	$O_2^- + O_2 + M \longrightarrow O_4^- + M$	1.0(-29) Estimate
R_{166}	$O_4^- + O \longrightarrow O_2^- + O_3$	4.0(-10) *Fehsenfeld et al.* [1969]
R_{167}	$O_4^- + CO_2 \longrightarrow CO_4^- + O_2$	4.3(-10) *Fehsenfeld et al.* [1969]
R_{168}	$O_4^- + NO \longrightarrow NO_3^- + O_2$	2.5(-10) *Fehsenfeld et al.* [1969]
R_{169}	$CO_4^- + O \longrightarrow CO_3^- + O_2$	1.5(-10) *Fehsenfeld et al.* [1969]
R_{170}	$CO_4^- + NO \longrightarrow NO_3^- + CO_2$	4.8(-11) *Fehsenfeld et al.* [1969]

are the mutual neutralization through reactions with positive ions, and photodetachment during daytime. This latter process yields free electrons. Therefore, the relative abundance of the *D* region electrons and negative ions during the daytime is governed to a large extent by the photodetachment of the terminal ions [*Thomas et al.*, 1973].

Recent laboratory work and daytime negative-ion composition measurements have indicated that the *D* region negative molecular ions can undergo hydration reactions forming water cluster ions such as $O_2^- \cdot H_2O$, $O_3^- \cdot H_2O$, $CO_3^- \cdot H_2O$, $NO_2^- \cdot H_2O$ and $NO_3^- \cdot H_2O$, and their multiple hydrates.

Fortunately, the rate constants for the non-terminal ions indicate that the hydration processes are slower than the charge transfer and charge rearrangement reactions mentioned above. Even for the terminal ion NO_3^-, the losses due to hydration become important only if the photodetachment rate is less than about 10^{-3} sec^{-1} [*Thomas et al.*, 1973].

In the event the photodetachment rate of NO_3^- is indeed less than 10^{-3} sec^{-1}, the negative terminal ion will be either $NO_3^- \cdot H_2O$ or one of its multiple clusters. The abundance of this terminal ion will then be determined by its recombination rate with the positive ions and its photodetachment rate. None of these quantities is presently known. If one is to include these ions in the reaction scheme, appropriate values for these quantities have to be assumed. Since this is true for NO_3^- also, it makes little difference whether the terminal ion used is NO_3^- or $NO_3^- \cdot (H_2O)_n$ with $n > 1$.

There is, however, a difference between the two types of ions, which could affect the electron-density distribution. That is the

mutual neutralization coefficient with the positive ions. Considering the fact that the positive cluster ions have recombination coefficients of the positive molecular ions and that one could expect the mutual neutralization rates of positive cluster ions with either the negative molecular ions or the negative cluster ions, the hydrated cluster ions are totally excluded from the present negative-ion reaction scheme.

The more important reaction paths in the adopted reaction scheme are shown in Figure 5.2.

5.3 *Reaction Rate Constants*

The accuracy of model calculations depends largely on the availability of correct reaction rate constants. Unfortunately, the measurements of rate constants in laboratories are subject to various sources of error, and the best measurements are accurate only to within ± 30%. This is true for the main products, and for secondaries the errors are much larger, sometimes as much as a factor of 2.

The rate constants of the molecular ion reactions shown in Table 5.1 are those measured by *Ferguson et al.* [1969] and *Fehsenfeld et al.* [1970]. The accuracy of most of these values have been estimated to be ± 3 The only uncertainty is the ratio of the $N(^2D)/N(^4S)$ yield in the reaction between N_2^+ and O. The values used in this study are 0.75.

The rate constants for the reactions leading to $H^+(H_2O)_n$ from O_2^+ are taken from the results of *Fehsenfeld et al.* [1971a] and *Good et al.* [1970a, b]. These values are in good agreement with the original values measured by *Fehsenfeld and Ferguson* [1969].

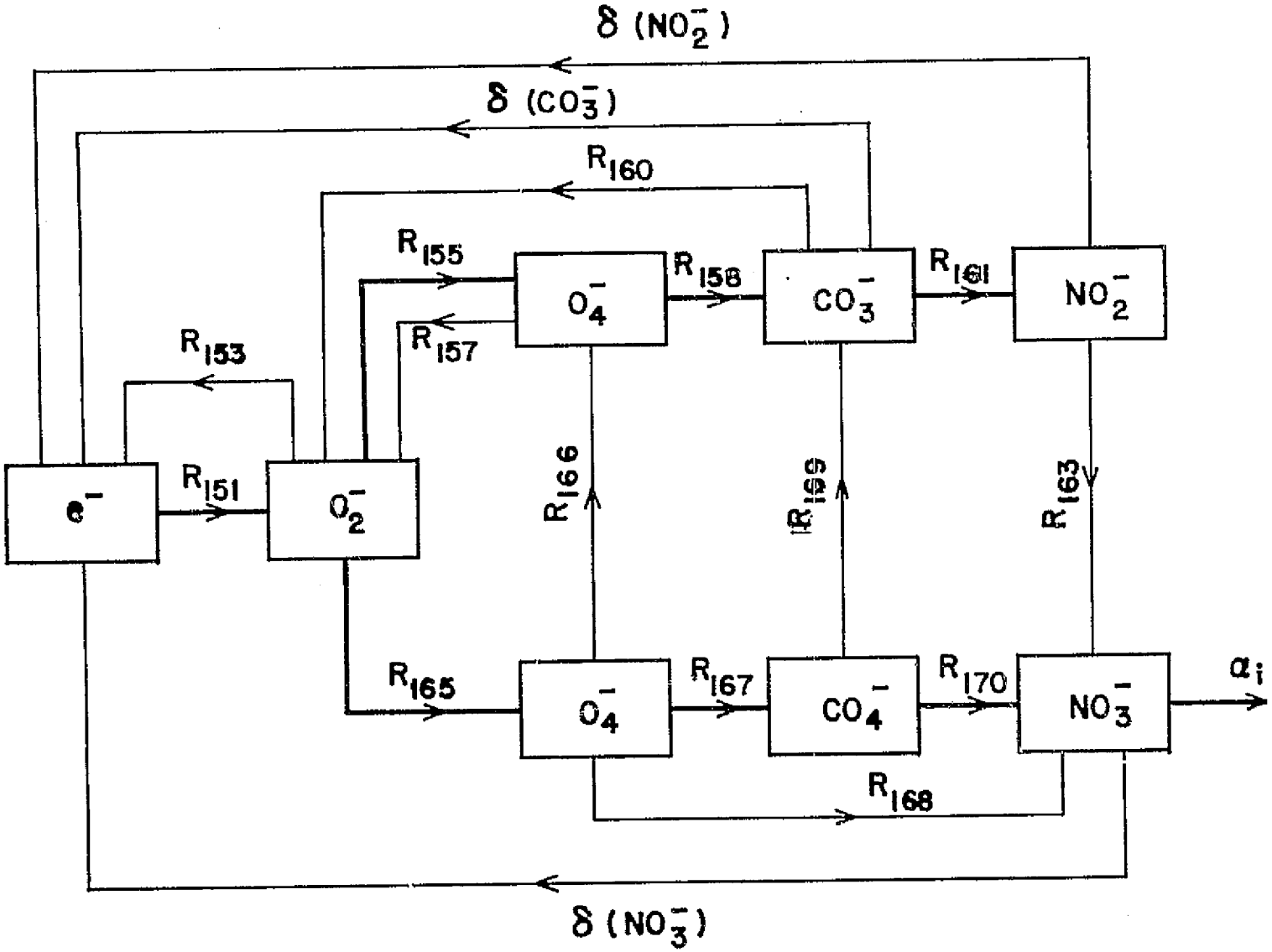

Figure 5.2 More important negative-ion reaction paths in the *D* region.

The reactions leading to the production of $NO^+ \cdot (H_2O)_n$ with n = 1, 2, 3, and the subsequent conversion to $H^+(H_2O)_3$ were investigated by *Fehsenfeld et al.* [1971b] and *Howard et al.* [1971]. The measurement of the relevant rate constants was carried out by both groups at 295 K. For the third body, both groups used He, Ar, and H_2, but the latter group used O_2 in addition. Considering the possible errors involved, the agreement between the corresponding values obtained by both groups is very good. The values used in this study are those of *Howard et al.* [1971].

The rate constants of the 3-body reactions generally vary with the type of the third body. A close examination of the results of the above workers shows that N_2 is more efficient than O_2 as a third body, the ratio of the corresponding rate constants being 3:2 [*Fehsenfeld et al.*, 1971a; *Howard et al.*, 1971]. It is also noted that the efficiency of He as a third body is rather poor, while Ar gives rate constants which are close to corresponding values obtained with O_2. Measurements with NO show that its efficiency is similar to that of N_2 in the 3-body reactions [*Howard et al.*, 1971]. In view of the wide difference in the efficiencies of N_2 and O_2 as the third body, a weighted average was taken for tabulating the values in Table 5.1, wherever values with either N_2 or O_2 are available. In other instances, the available values were adopted without any correction for the third-body efficiency.

The rate constants of the 3-body reactions are also known to depend on the temperature, with the values increasing with decrease of the temperature. *Ferguson* [1971] estimated the rate constant of the O_2^+ to $O_2^+ \cdot O_2$ clustering reaction to increase from 2.8×10^{-30} cm^3 sec^{-1}

to 1×10^{-29} cm^3 sec^{-1} between 300 K and *D* region temperatures. *Dunkin et al.* [1971] found that the rate constant of the NO^+ to $NO^+ \cdot CO_2$ clustering reaction to increase by a factor of 2.5 between the temperatures 300 K and 200 K. On the basis of these observations the temperature variation of the 3-body reactions may be expressed as $(T/300)^{-n}$ where $n > 2$. However, taking a more conservative figure, this expression is taken as $(T/300)^{-2}$ for the rates of 3-body clustering reactions.

One of the most important parameters that determine the electron densities of the ionosphere is the recombination coefficient, α, of the positive ions. In the region where the negative-ion concentrations are small, the electron losses take place solely due to recombination reactions with the positive ions.

Laboratory measurements as well as ionospheric observations have indicated the wide difference that exists between recombination coefficients of the molecular ions and those of the cluster ions. Among the molecular ions N_2^+ has a recombination coefficient of 2.6×10^{-7} cm^3 sec^{-1} which is temperature independent. The other two molecular ions, on the other hand, have temperature dependent recombination coefficients. Measurements made by *Kasner and Biondi* [1968] have shown a 1/T temperature dependence for $\alpha(O_2)$, with the values given by

$$\alpha(O_2^+) = 2.2 \times 10^{-7} \ (300/T) \ cm^3 \ sec^{-1} \quad .$$

The recombination coefficient of NO^+, $\alpha(NO^+)$, has a $1/T^{-1.5}$ temperature dependence, and the coefficients are given by [*Weller and Biondi*, 1968]

$$\alpha(NO^+) = 4.1 \times 10^{-7} \ (300/T)^{1.5} \ cm^3 \ sec^{-1} \quad .$$

The accuracies of these laboratory measurements are quite good, being of the order of ± 10%. They are also in good agreement with the results of theoretical calculations which for O_2 yields a value of 2.8×10^{-7} cm^3 sec^{-1} at 300 K [*Chan*, 1968].

Laboratory measurements of the recombination coefficients of the hydrated cluster ions have been obtained only recently. The values by *Leu et al.* [1973] indicated that α increased from about 1×10^{-6} to about 10×10^{-6} cm^3 sec^{-1}, corresponding to an increase of the cluster ion mass number from 19 to 109. They also concluded that it was unlikely that α could have a value greater than 1×10^{-5} cm^3 sec^{-1} even for heavier clusters. In normalizing the data which were obtained at different temperatures to a standard temperature of 300 K, they have assumed a temperature dependence of $T^{-1/2}$.

For many other cluster ions, no direct measurements of α generally increased with the size of ion. Assuming this relation to hold true for other ions as well, values of α were estimated on the basis of the number of clustered molecules. These, together with the values obtained for other ions, are shown in Table 5.3 with the appropriate temperature dependence.

The value for the mutual neutralization coefficient used is an average value based on the measurements done on different combinations of positive and negative ions. *Hirsh and Eisner* [1972] obtained 1.7×10^{-7} and 0.34×10^{-7} cm^3 sec^{-1} for this quantity in the reactions

Table 5.3

Recombination coefficients.

Reaction	Recombination coefficient $cm^3\ sec^{-1}$
$N_2^+ + e \longrightarrow N + N$	2.6(-7) * *Mehr and Biondi* [1969]
$O_2^+ + e \longrightarrow O + O$	2.2(-7)(300/T) *Kasner and Biondi* [1968]
$NO^+ + e \longrightarrow N + O$	$4.1(-7)(300/T)^{1.5}$ *Weller and Biondi* [1968]
$O_4^+ + e \longrightarrow O_2 + O_2$	$3.0(-6)(300/T)^{0.5}$ Estimate
$O_2^+ \cdot H_2O + e \longrightarrow O_2 + H_2O$	$3.0(-6)(300/T)^{0.5}$ Estimate
$H_3O^+ \cdot OH + e \longrightarrow$ Neutrals	$3.0(-6)(300/T)^{0.5}$ Estimate
$H_3O^+ + e \longrightarrow$ Neutrals	$1.2(-6)(300/T)^{0.5}$ *Leu et al.* [1973]
$H_3O^+ \cdot H_2O + e \longrightarrow$ Neutrals	$3.0(-6)(300/T)^{0.5}$ *Leu et al.* [1973]
$H_3O^+ \cdot (H_2O)_2 + e \longrightarrow$ Neutrals	$5.1(-6)(300/T)^{0.5}$ *Leu et al.* [1973]
$H_3O^+ \cdot (H_2O)_3 + \longrightarrow$ Neutrals	$6.1(-6)(300/T)^{0.5}$ *Leu et al.* [1973]
$H_3O^+ \cdot N_2 + e \longrightarrow$ Neutrals	$3.0(-6)(300/T)^{0.5}$ Estimate
$NO^+ \cdot N_2 + e \longrightarrow$ Neutrals	$3.0(-6)(300/T)^{0.5}$ Estimate
$NO^+ \cdot CO_2 + e \longrightarrow$ Neutrals	$3.0(-6)(300/T)^{0.5}$ Estimate
$NO^+ \cdot H_2O + e \longrightarrow$ Neutrals	$3.0(-6)(300/T)^{0.5}$ Estimate

*Read a(-*n*) as a x 10^{-n}.

(Table 5.3 continued)

$NO^+ \cdot (H_2O)_2 + e \longrightarrow$ Neutrals	$5.0(-6)(300/T)^{0.5}$ Estimate
$NO^+ \cdot (H_2O)_3 + e \longrightarrow$ Neutrals	$6.0(-6)(300/T)^{0.5}$ Estimate
$X^- + Y^+ \longrightarrow$ Neutrals	2.0(-7) Estimate

between NO^+ and NO_2^-, and NO^+ and NO_3^-, respectively. However, in the region where the effect of the negative ions becomes important, the dominant positive ions are the hydrated clusters of H_3O^+. Judging by their recombination coefficients, one could assume that the mutual neutralization coefficients of these ions are higher than those corresponding to the molecular ions. Hence, a conservative value of 2×10^{-7} cm^3 sec^{-1} is adopted for this coefficient.

The rate constants given in Table 5.2 for the negative-ion reactions are those reported by *Fehsenfeld et al.* [1967], *Fehsenfeld and Ferguson* [1968], *Phelps* [1969] and *Fehsenfeld et al.* [1969]. Most of these are fast binary reactions which are independent of the temperature. Exceptions are the three-body attachment reaction between O_2 and free electrons, and the three-body association reaction between O_2^- and O_2, which yields $O_2^- \cdot O_2$. The former has a temperature dependence given by $(1/T)e^{-1.2/RT}$ [*Phelps*, 1969], and its reaction rate is also known. On the other hand, the rate constant of the latter is not so well known. *Pack and Phelps* [1970] obtained 4×10^{-31} cm^6 sec^{-1} at 300 K for this quantity. According to *Fehsenfeld et al.* [1969], however, the rate constant for this reaction is likely to exceed 10^{-30} cm^6 sec^{-1} at *D*-region temperatures. *Thomas et al.* [1973], in their model calculations, used a value of 2×10^{-29} cm^6 sec^{-1} for this rate constant.

Rate constants for many of the clustering reactions of negative ions with water vapor have been reported in the literature during the past few years. Since these hydrated ions are not included in the negative ion reaction scheme adopted, values of these are not shown in Table 5.2.

The photodetachment rates used in the present computations are given in Table 5.4. The values corresponding to O_2^- and O_3^- are those measured experimentally and reported in the DASA Reaction Rate Handbook. The values used for CO_3^-, NO_2^- and NO_3^- are those used by *Thomas et al.* [1973]. In view of the many uncertainties in both the negative-ion chemistry and the experimental data on the daytime negative-ion composition, no effort was made to determine the effect of the photodetachment rates on the negative-ion composition and the electron density in the lower *D* region.

Table 5.4

Photodetachment rates.

Reaction	Photodetachment rate sec^{-1}
$O_2^- + h\nu \longrightarrow O_2 + e$	0.33
$O_3^- + h\nu \longrightarrow O_3 + e$	0.66
$CO_3^- + h\nu \longrightarrow CO_3 + e$	0.04
$NO_2^- + h\nu \longrightarrow NO_2 + e$	0.04
$NO_3^- + h\nu \longrightarrow NO_3 + e$	0.04

Reference: *Thomas et al.* [1973]

6. ION COMPOSITION AND ELECTRON-DENSITY PROFILES

Several photochemical calculations have been carried out in the recent past in order to interpret the behavior and the structure of the *D* region as revealed in ground-based and rocket measurements. Among those who investigated the daytime *D*-region positive ion and electron densities are *Goldberg and Aikin* [1971], *Hunt* [1971a, 1973], *Keneshea and Swider* [1972] and *Rowe et al.* [1974]. *Goldberg and Aikin* [1971] made use of neutral constituent concentrations, adopted from values obtained by others, to determine the distribution of individual positive-ion species. The model calculations carried out by *Keneshea and Swider* [1972] and *Hunt* [1973], on the other hand, are more comprehensive. They calculate the relevant neutral constituent concentrations, positive-ion densities, and the negative-ion densities in the same computer code. *Rowe et al.* [1974] developed a simplified model of the *D* region ion composition, subject to several constraints, to study the behavior of this region under different conditions.

In this chapter, a numerical model for the *D* region ion composition is developed concurrently with the minor neutral constituent model described in Chapter 3. In the next section, details of the numerical method for calculating the height distribution of several ionic species are presented. This is followed by a discussion of the computed ion composition and electron-density profiles.

6.1 *Ion-Composition Model*

The ion-composition model developed in our study incorporates 17 positive ions and 7 negative ions. The difference between the densities of positive ions and negative ions gives the electron density.

The positive ions included are:

molecular ions: N_2^+, O_2^+ and NO^+, and

cluster ions: $O_2^+ \cdot O_2$, $O_2^+ \cdot H_2O$, $H_3O^+ \cdot OH$, $H^+ \cdot H_2O$, $H^+ \cdot (H_2O)_2$,

$H^+ \cdot (H_2O)_3$, $H^+ \cdot (H_2O)_4$, $H_3O^+ \cdot N_2$, $NO^+ \cdot N_2$,

$NO^+ \cdot CO_2$, $NO^+ \cdot H_2O$, $NO^+ \cdot (H_2O)_2$ and $NO^+ \cdot (H_2O)_3$.

The metallic ions present between 80 and 90 km are not included in view of their negligible abundance under normal conditions.

The negative ions included in the study are the following:

molecular ions: O_2^-, O_3^-, CO_3^-, NO_2^-, NO_3^- and

cluster ions: $O_2^- \cdot O_2$ and $CO_2^- \cdot O_2$

For reasons mentioned before, the negative hydrated cluster ions are not incorporated into the model.

6.1.1 *Continuity equations.* The set of continuity equations for the charged species can be written in the form

$$\frac{d[X]}{dt} = Q - P[X] \tag{6.1}$$

where

Q is the production term for a given ionic species, X, and

P is the loss coefficient.

The chemical time constants of the reactions involved are generally very small. As such the transport terms are not included in the continuity equations for the ionic species.

In general, the production term for a positive ion X_m^+ can be written in the form

$$Q(X_m^+) = q_m + \sum k\ A\ [X^+]_n \quad , \qquad m \neq n \tag{6.2}$$

where

q_m is the primary ionization rate, and

$\sum k\ A\ [X^+]_n$ is the total contribution due to charge transfer or rearrangement reactions producing X_m^+ from other positive ions.

In equation (6.2), q_m appears only for the molecular ions O^+, N_2^+, O_2^+, and NO^+.

The loss coefficient for a positive ion generally appears as

$$P(X_m^+) = \sum k\ B + \alpha_m[e] + \alpha_i[N^-] \tag{6.3}$$

where

$\sum k\ B$ is the total contribution due to reactions converting X_m^+ into other positive ions,

$\alpha_m[e]$ is the term due to dissociative recombination with electrons and,

α_i is the mutual neturalization coefficient, and

$[N^-]$ is the total negative-ion density.

In the case of a negative ion X_m^- the production is generally due to charge transfer or rearrangement processes, except for O_2^- and O_4^- where they are formed by 3-body attachment processes. Therefore

$$Q(O_2^-) = \beta[e] \tag{6.4a}$$

$$Q(O_4^-) = \beta' \, O_2^- \quad , \tag{6.4b}$$

$$Q(X_m^-) = \sum k \, A[X^-]_n \qquad m \neq n \tag{6.4c}$$

where

β is the attachment rate,

$\sum k \, A[X^-]_n$ is the total contribution due to charge transfer or rearrangement reactions producing X_m^-.

The loss coefficient for X_m^- is in general,

$$P(X_m^-) = \sum k \, B + \alpha_i[N^+] + \delta \tag{6.5}$$

where

$\sum k \, B$ is the total contribution due to reactions converting X_m^- into other negative ions,

$[N^+]$ is the total positive-ion density, and

δ is the electron detachment rate.

The continuity equation for electrons is

$$\frac{d[e]}{dt} = Q_e - \sum \alpha_m[X^+]_m[e] - \beta[e] \tag{6.6}$$

where

Q_e is the total ion-pair production rate and

$[e]$ is the electron density.

It is possible to write a continuity equation for the total positive-ion density, in the form

$$\frac{d[N^+]}{dt} = Q_e - \bar{\alpha}[e][N^+] - \alpha_i[N^-][N^+] \tag{6.7}$$

where

$\bar{\alpha}$ is the average electron recombination coefficient for positive ions in the *D* region.

The charge neutrality condition yields the relation

$$[N^+] = [N^-] + [e] \tag{6.8}$$

which can be written in the form

$$[N^+] = (1+\lambda)[e] \quad , \tag{6.9}$$

where

$$\lambda = [N^-]/[e] \quad . \tag{6.10}$$

Eliminating $[N^+]$ and $[N^-]$ in equation (6.7),

$$\frac{d[N^+]}{dt} = Q_e - (\bar{\alpha}+\lambda\alpha_i)(1+\lambda)[e]^2 \tag{6.11}$$

An effective recombination coefficient for the electrons, which takes into account the presence of the negative ions, is defined by

$$\alpha_{eff} = (1+\lambda)(\bar{\alpha}+\lambda\alpha_i) \quad . \tag{6.12}$$

Equation (6.12) becomes

$$\frac{d[N^+]}{dt} = Q_e - \alpha_{eff}[e]^2 \tag{6.13}$$

Under steady-state conditions,

$$Q_e = \alpha_{eff}[e]^2 \tag{6.14}$$

The effective recombination coefficient is a convenient parameter that can be used in calculating the electron density using known values of the ion-pair production rates. Alternatively, it can be deduced from the simultaneous measurement of the electron density and the production functions.

The condition of steady-state conditions is generally valid around noon up to zenith angles of 60° at least. The time derivative factor $d[N^+]/dt$ is appreciable only at large zenith angles. However, for the sake of completeness, this factor is retained in our calculations.

6.1.2 *Methods of computation.* The set of differential equations written for each of the ionic species is converted to a set of difference equations in the form given in equation (3.25). The neutral constituent concentrations required for substitution in the production terms and loss coefficients are taken from concurrent solutions of the netural constituent model described in Chapter 3. The calculations involving the ionic concentrations were incorporated into a separate subroutine which is introduced at sunrise on the final day of the netural chemistry model run.

Initially, prior to sunrise, the values of $[X^{\pm}]$ and $[e]$ are all set to zero. The ionic concentrations were obtained at the same time

intervals as used in the neutral chemistry program. At each of these time steps, the optical depth factor was calculated separately and the corresponding flux levels were determined.

In Chapter 3, results of the neutral chemistry calculations were presented for two different models of the eddy diffusion coefficient. The high D_e model yielded NO profiles having mesospheric values larger than those given by the low D_e model. Preliminary calculations indicated that the high D_e model generally gave electron densities that are too high compared to the observed values. Therefore, the detailed calculations were carried out using the neutral chemistry results obtained with the low D_e model only.

At each time step, the solution was obtained by iterating the concentrations until the charge neutrality condition was achieved. Generally, this is achieved in a few iterations at altitudes above about 75 km, where the electron density is used as the controlling parameter. Below this height, however, where the abundance of the negative ions begins to grow, a large number of iterations was required before the charge neutrality condition was reached. At 65 km and below, computations were terminated before this condition was achieved in view of the excessive computer time taken.

The exact values of several parameters that go into the calculations are not known. Therefore, it was necessary to carry out several runs using different values for such parameters, keeping the rest of the conditions unaltered. These parameters include the branching ratios of the reactions R_{103} and the recombination reaction of NO^+, the rate constants for the reactions R_{135} and R_{136}, and the O_2^+ production rates.

In Chapter 4, ion-pair production rates were calculated corresponding to different input conditions. For X-rays below 3 Å, the exact flux intensity $\phi(3\ \text{Å})$ was not known. Therefore, two values of $\phi(3\ \text{Å})$ were used to calculate the productions functions. These are 1×10^{-5} erg cm^{-2} sec^{-1} and 0.5×10^{-5} erg cm^{-2} sec^{-1}, respectively (Figure 4.7). Also for the precipitating electrons, the exact nature of the spectral distribution was not known. Therefore, contributions due to two hardness indices, *viz.* $\gamma = 2$ and $\gamma = 3$ were used in the calculations (Figure 4.9). Of these, $\gamma = 2$ gives the higher production rate, and this was used in conjunction with the high X-ray flux (1×10^{-5} erg cm^{-2} sec^{-1}) in the program. The results obtained with this combination are described under 'high O_2^+ production'. The other two parameters, $\gamma = 3$ and $\phi(3\ \text{Å}) = 0.5 \times 10^{-5}$ erg cm^{-2} sec^{-1} were used together and the corresponding results are described under 'low O_2^+ production'.

6.2 *Positive-Ion Composition*

The computed positive-ion profiles are shown in Figures 6.1 - 6.3, corresponding to $\chi = 18°$ (noon), $\chi = 60°$ (morning) and $\chi = 60°$ (evening), respectively. Each figure has two sets of curves; one for the high O_2^+ production case (solid lines) and the other for the low O_2^+ production case (broken lines).

6.2.1 *Molecular-ion concentrations.* Among the molecular ions, only O_2^+ and NO^+ are shown in the figures. The concentrations of N_2^+ and O^+ are too low to show here. In all of these three cases, NO^+ and O_2^+ profiles cross over; the noon profiles at 93 km, and the other two at 97 km. NO^+ dominates below these height levels, and O_2^+ above.

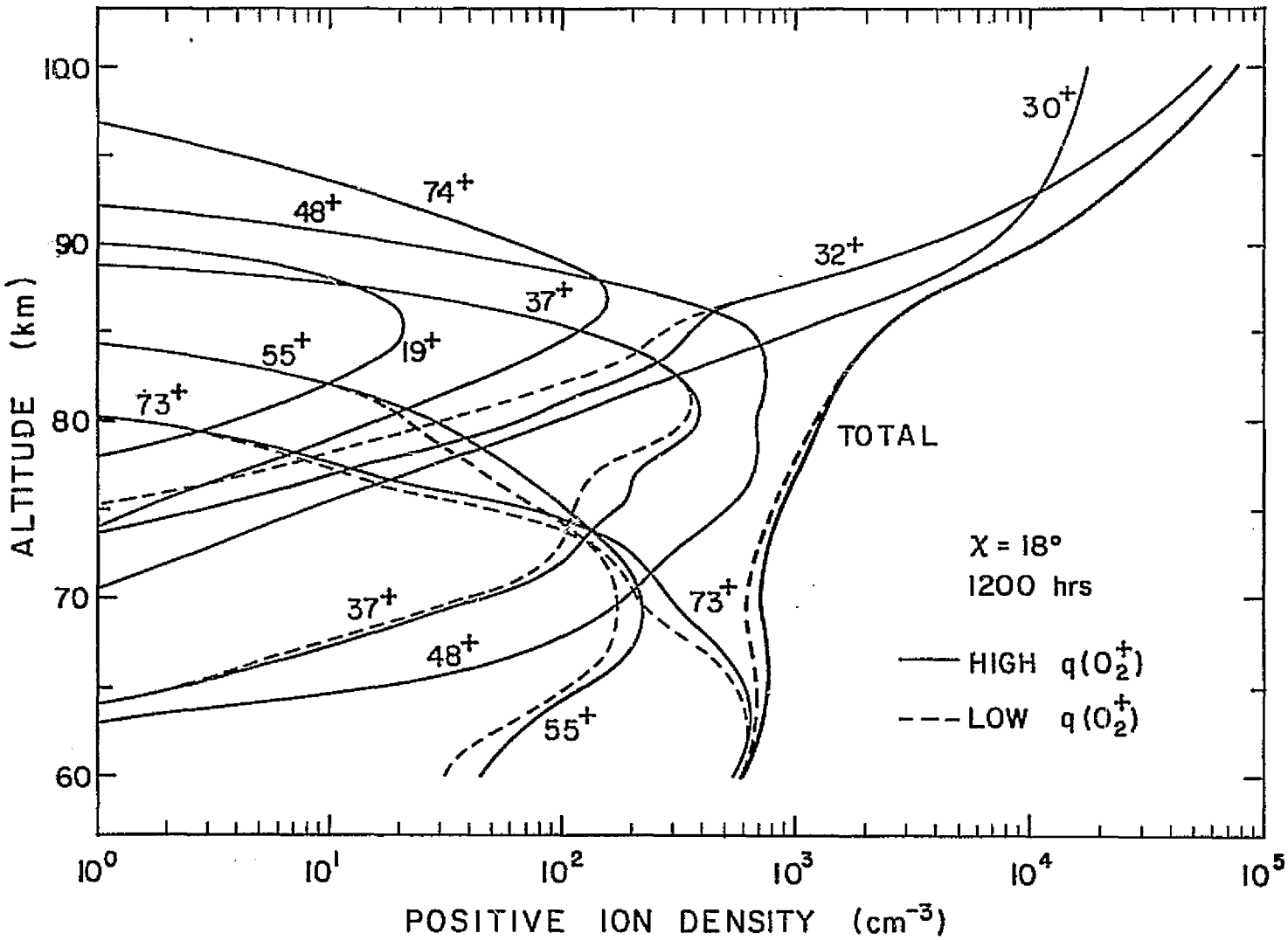

Figure 6.1 The height distributions of positive-ion species. These results correspond to low eddy diffusion and summer noon (χ = 60°) conditions.

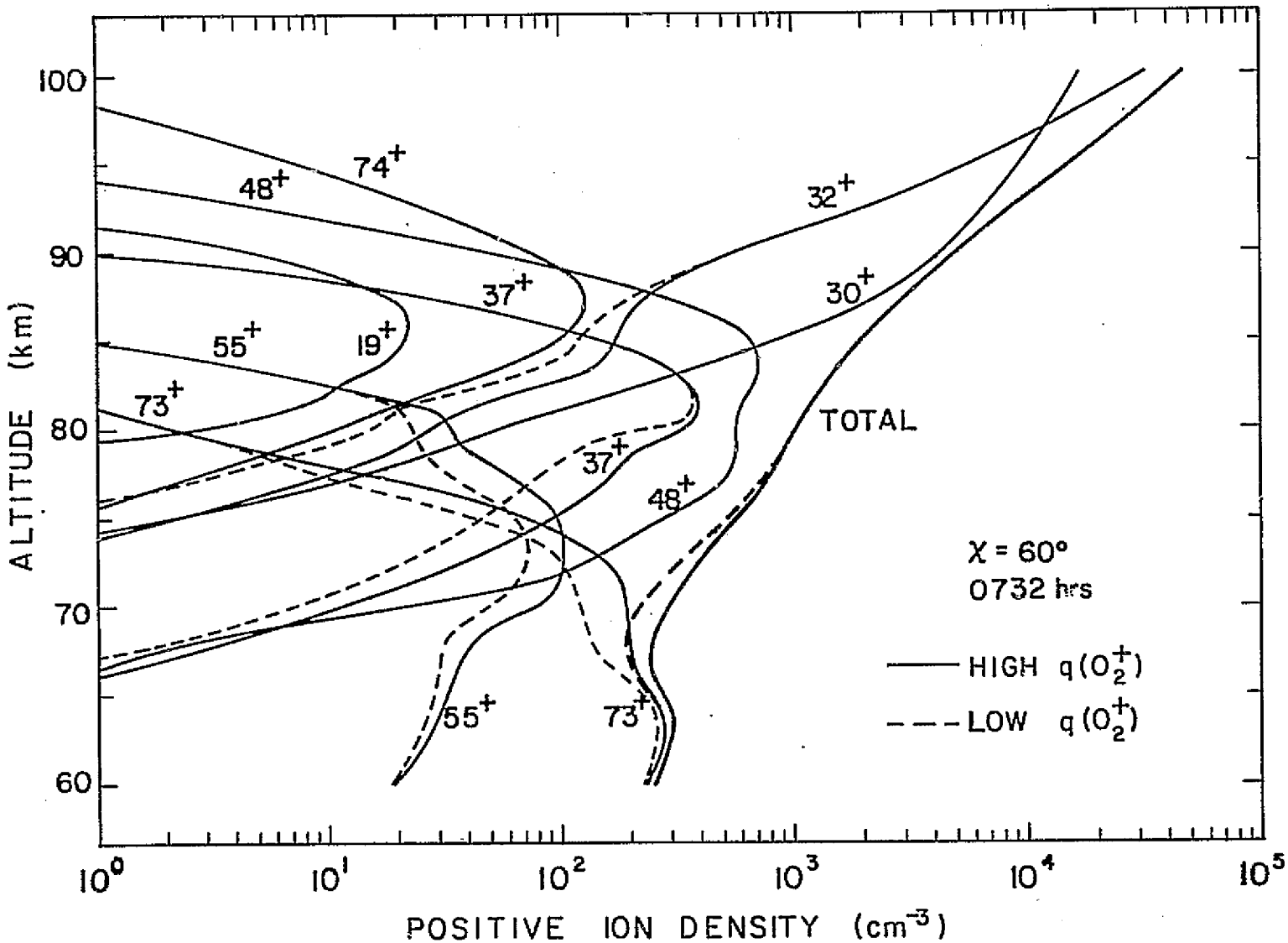

Figure 6.2 The height distributions of positive-ion species. These results correspond to low eddy diffusion and summer morning (χ = 60°) conditions.

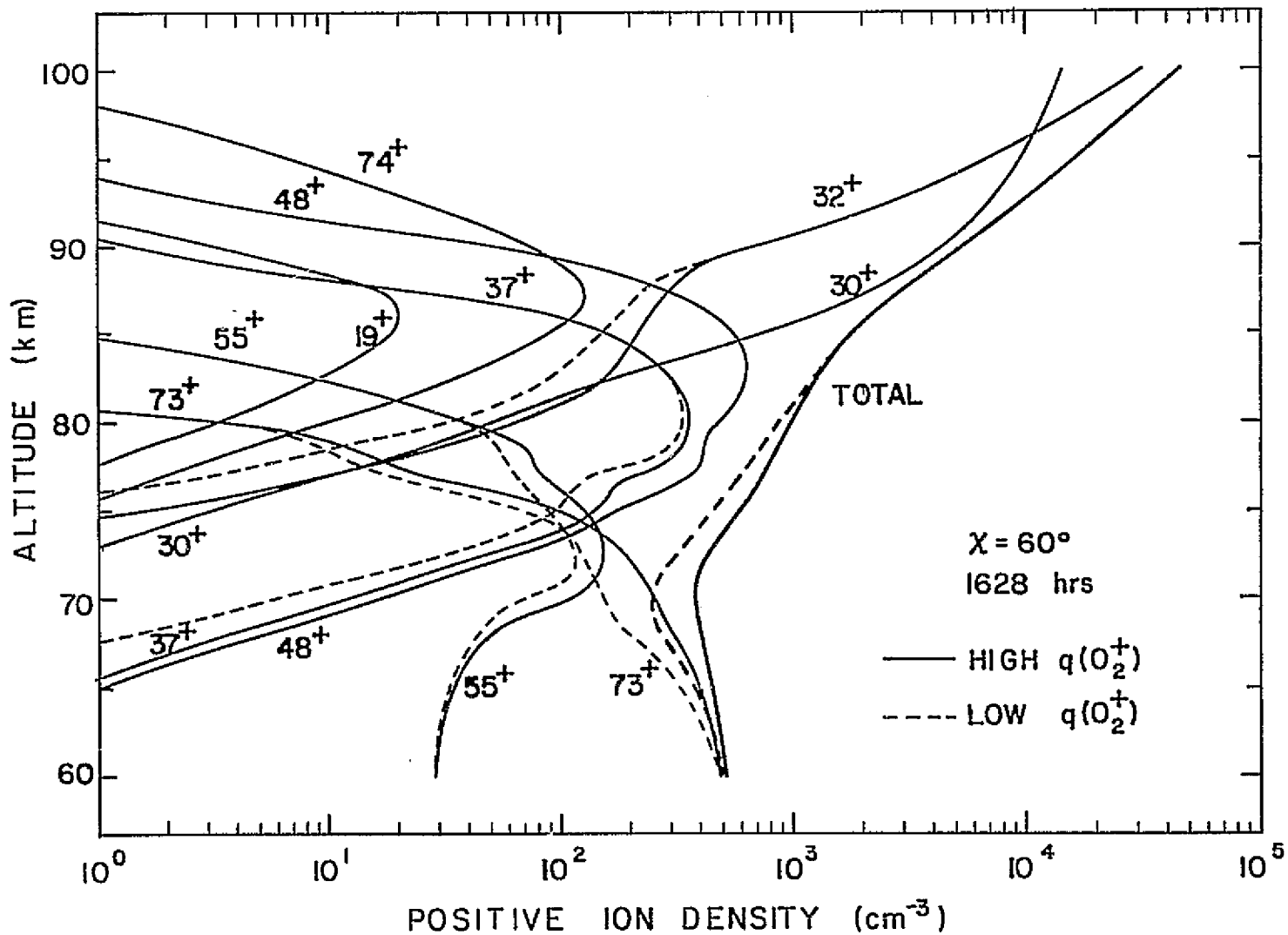

Figure 6.3 The height distributions of positive-ion species. These results correspond to low eddy diffusion and summer evening (χ = 60°) conditions.

The relative densities of these two ions appear to depend on the zenith angle.

The behavior of NO^+ and O_2^+ is generally described in terms of the ratio of their number densities, i.e. $[NO^+]/[O_2^+]$. This parameter can be easily measured because it does not require absolute calibration of the equipment. Further, this ratio can be used to calculate the average electron recombination rate in the height range where NO^+ and O_2^+ dominate.

In all three sets of profiles, NO^+ and O_2^+ dominate above about 85 km. Below this height, the hydrated cluster ions dominate. In the noon profiles, the ratio $[NO^+]/[O_2^+]$ has a maximum value of 4.4 at 87 km, which drops down to unity at 93 km. Above this height the ratio drops through unity to 0.3 at 100 km. At $\chi = 60°$ this ratio is a factor about 8 at 88 km, reduces to unity at 97 km, and above this height reduces to about 0.2 at 100 km. These results indicate that the point of unity ratio gets lifted as the zenith angle increases. Under the same conditions, the difference between the NO^+ and O_2^+ profiles widen near the mesopause.

Similar results have been obtained in model calculations done by Keneshea and reported by *Narcisi* [1970]. According to these calculations, the $[NO^+]/[O_2]$ ratio has values around 10 at 60° zenith angle and at heights between 85 and 90 km. It approaches unity at heights near 100 km. For smaller zenith angles, the ratio approaches unity at lower heights. These results are similar to the observations made by *Narcisi* [1970].

The O_2^+ concentration at these altitudes is due to direct ionization of O_2 by X-rays and EUV radiation, as well as due to conversion of

O^+ and N_2^+ into O_2^+ through reactions R_{102} and R_{104}. Part of the O_2^+ thus produced is converted into NO^+ through reaction R_{107}. The contribution made by reactions R_{101}, R_{103}, R_{105}, and R_{106} in converting O^+ and N_2^+ directly into NO^+ is not significant below 100 km. Above about 90 km, the ionization caused by X-rays and EUV radiation results in the O_2^+ production, and the NO^+ production due to Ly-α ionization of NO is rather negligible. The formation of NO^+ in this altitude range is mainly due to conversion of this O_2^+ through reaction R_{107}. Hence, the ratio $[NO^+]/[O_2^+]$ represents the relative amounts of NO available in this region.

At altitudes below about 85 km, both NO^+ and O_2^+ drop rapidly causing the hydrated cluster ions to dominate. The effect of high and low O_2^+ production due to variation in the X-ray flux below 3 Å and the precipitating electron flux appears in this region. Under noon conditions, this variation is only a factor of 1.5 - 3.5, the values increasing as the height decreases. The decrease of both O_2^+ and NO^+ in the *D* region is really an exponential variation, being approximately linear on the semi-logarithmic scale. The O_2^+ profile follows closely the O_2^+ production curve. However, in the case of the NO^+ profile, the values drop faster than the decrease in the NO^+ production rate, particularly above 70 km. This is caused by the conversion of NO^+ into its hydrated cluster ions.

The NO^+ and O_2^+ profiles obtained are generally in agreement with the profiles measured by *Narcisi* [1970] and *Johannessen and Krankowsky* [1972].

In certain observations [*Goldberg and Aikin*, 1971], it was noted that the O_2^+ profile remained more or less constant at a fixed value below

about 75 km, instead of decreasing rapidly. One reason for assuming a high O_2^+ production rate, effective in this height range, is to verify whether this increase in the O_2^+ concentration is caused by an increase in the O_2^+ production rate. The computations show that in spite of an increase in the O_2^+ production rate, O_2^+ continues to drop. This indicates that one has to look for a decrease in the loss coefficient of O_2^+ in order to explain such a constant value of O_2^+. However, it has to be noted that O_2^+ is only a minor ion at these altitudes, and therefore, its measurement cannot be considered as very reliable.

6.2.2 *Cluster-ion concentrations.* The noon profile as well as the two $\chi = 60°$ profiles of the positive-ion composition shows that the hydrated cluster ions dominate the region below about 86 km. However, contrary to the observations, the major cluster ion according to these profiles is $NO^+ \cdot H_2O$ rather than $H^+ \cdot (H_2O)_2$ or $H^+ \cdot (H_2O)_3$. The height range from about 88-89 km to about 72-74 km is dominated by this NO^+ hydrated cluster ion with a peak value of 860 cm^{-3} near 83 km.

According to the given reaction scheme the formation of $NO^+ \cdot H_2O$ from NO^+ ions takes place with a time constant of about 13 secs at 80 km. This is achieved through the formation of the intermediate cluster $NO^+ \cdot N_2$ and subsequent switching to $NO^+ \cdot H_2O$. Its fastest loss path is due to electron recombination, which has a time constant of about 300 secs at 80 km. The other loss reactions have time constants much greater than this value. However, one possibility for achieving a faster loss rate is through the formation of the cluster $NO^+ \cdot H_2O \cdot N_2$ or $NO^+ \cdot H_2O \cdot O_2$ and subsequent switching with H_2O to yield $NO^+ \cdot (H_2O)_2$. This ion in turn can produce $NO^+ \cdot (H_2O)_3$ in a similar association -

switching process [*Arnold and Krankowsky*, 1974]. However, these reactions are not included in our calculations because of the lack of evidence as to their existence and rate constants of the reactions involved.

The two paths suggested by *Heimerl et al.* [1972] which involve OH and HO_2 have time constants about 3000-6000 sec. These high values are due to low concentrations of OH and HO_2 obtained in the low D_e model calculations. If the concentrations of these two constituents were sufficiently high, they would have resulted in the formation of H_3O^+ through reactions R_{135} and R_{136}, which could subsequently yield $H^+\cdot(H_2O)_2$. The reaction involving H atoms also has a time constant greater than 1000 sec, corresponding to a rate constant of 5×10^{-12} cm^3 sec^{-1} (Reaction R_{112}).

The multiple hydrated cluster of NO^+, i.e. $NO^+\cdot(H_2O)_2$ and $NO^+\cdot(H_2O)_3$ have negligible concentrations according to the computations. This is mainly because of the low production rates for these ions. The faster path of producing $H^+\cdot(H_2O)_2$ is given by reactions R_{108}, R_{110}, R_{112}, and R_{114}, which proceeds according to

$$O_2^+ \longrightarrow O_2^+\cdot O_2 \longrightarrow O_2^+\cdot H_2O \longrightarrow H_3O^+\cdot OH \longrightarrow H^+\cdot(H_2O)_2$$

The alternate path of producing $H^+\cdot(H_2O)_2$ from $O_2^+\cdot H_2O$ is through the formation of H_3O^+. However, the conversion of H_3O^+ into $H^+\cdot(H_2O)_2$ through the conventional 3-body reaction is found to have a time constant of about 600 sec. On the other hand, the association/switching reactions involving the major neutral particles can convert H_3O^+ into $H^+\cdot(H_2O)_2$ within about 5 secs.

The third path of producing this cluster ion is through the formation of $NO^+ \cdot H_2O$:

$$NO^+ \cdot H_2O \xrightarrow{OH,\ HO_2} H^+ \cdot (H_2O) \xrightarrow{H_2O,\ M} H^+ \cdot (H_2O)_2$$

This path is again limited by the conversion rate of $NO^+ \cdot H_2O$ into $H^+ \cdot (H_2O)$, which is over 1000 sec., as mentioned before.

The existing reaction schemes, therefore, give time constants which are too long for converting NO^+ into $H^+ \cdot (H_2O)_2$. As a result, the concentration of $H^+ \cdot (H_2O)_2$ reaches only a low value. It reaches a peak value of 390 ions cm^{-3} at 81 km. It remains as the second major cluster ion between about 74 and 85 km in the noon profile. This height range is little affected by the zenith angle variation.

Above 88 km, $H^+ \cdot (H_2O)$ concentration drops rapidly, becoming less important than $NO^+ \cdot CO_2$ and H_3O^+. One reason for this rapid drop is the increase in $O(^3P)$ concentration which occurs towards the high altitudes.

Towards the lower heights, particularly below 72.5 km, its abundance becomes less than that of $H^+ \cdot (H_2O)_3$ and $H^+ \cdot (H_2O)_4$. The effect of O_2^+ production rates become more prominent in the $\chi = 60°$ profiles than in the noon profile.

The higher clusters $H^+ \cdot (H_2O)_3$ and $H^+ \cdot (H_2O)_4$ dominate below about 71 km in the noon profiles. The conversion of $H^+ \cdot (H_2O)_2$ into $H^+ \cdot (H_2O)_3$ and $H^+ \cdot (H_2O)_4$ becomes more efficient with decrease in the altitude due to corresponding increase in the $[H_2O]$ and neutral particle density. Since the electron density decreases rapidly below

about 75 km, the loss of these heavy ions due to electron recombination also gets reduced. At the same time, the negative-ion concentrations increase below about 70 km. These ions undergo mutual neutralization with the positive ions. Therefore, the negative ions become increasingly important in controlling the positive ions at these altitudes.

The next higher hydronium cluster $H^+ \cdot (H_2O)_3$ appears below 82 km, reaches a peak value of about 200 cm^{-3} at 69 km, and then drops to about 35 at 60 km. It also has two profiles corresponding to high and low O_2^+ production rates, between about 63 and 81 km. Its abundance becomes equal to that of $H^+ \cdot (H_2O)_2$ near 72.5 km in the noon profile and near 72.5 km in the $\chi = 60°$ profiles.

The cluster ion $H^+ \cdot (H_2O)_5$ appears to be the dominant *D* region ion below 72 km. Its variation with O_2^+ production varies in the height range from 72 to 74 km only. Its peak value is 7.2 cm^{-3} which occurs at 65 km. This is the terminal positive ion in the hydronium cluster series. The ion density in this region is determined by the ion-pair production rate which is due to cosmic rays and hence the profiles do not show much variation towards the lower heights.

Another cluster ion that is present in significant amounts is $NO^+ \cdot CO_2$. It has a peak value of 260 cm^{-3} around 88 km, which reduces to 230 cm^{-3} at $\chi = 60°$. This ion is an intermediate one in the formation of $NO^+ \cdot H_2O$ from NO^+. At higher altitudes, H_2O concentration drops, and hence the conversion of this ion into $NO^+ \cdot H_2O$ becomes less efficient which results in increasing the concentration of $NO^+ \cdot CO_2$.

The distribution of the heavy cluster ions $H^+ \cdot (H_2O)_3$ and $H^+ \cdot (H_2O)_4$ agree well with the measured profiles discussed in

Section 5.1.1. These are the ions dominating the lower *D* region. However, as mentioned earlier, a major discrepancy occurs regarding the dominant ion in the mid-*D* region. The observations indicate the presence of $H^+\cdot(H_2O)_2$ and $H^+\cdot(H_2O)_3$ in large quantities in this height interval, while $NO^+\cdot H_2O$ has been found to be only a minor ion. The computed distributions, however, show the opposite. $NO^+\cdot H_2O$ is the dominant ion while $H^+\cdot(H_2O)_n$ with n = 1, 2, 3 are only minor ions in the height range 72-85 km. This demonstrates a serious weakness in the existing theories concerning the *D* region positive-ion chemistry. Some clues as to a possible circumvention of this situation have been suggested by *Arnold et al.* [1974]. According to them the rapid formation of heavy hydrated clusters could be made possible through (N_2+O_2) and CO_2 association/switching reactions. The inclusion of such a reaction scheme into the current computer codes is not however feasible due to the absence of data on the rate constants of these reactions.

6.3 *Negative-Ion Composition*

The ion composition model yields the density profiles of the negative ions O_2^-, O_3^-, CO_3^-, NO_2^-, NO_3^-, O_4^- and CO_4^-. All of these ions except O_3^- reach density levels greater than 0.1 ions cm^{-3} during the daytime. Figures 6.4 - 6.6 show the density profiles of these ions corresponding to χ = 18° (noon), χ = 60° (morning) and χ = 60° (evening), respectively. The difference in the values obtained for the two cases, high $Q(O_2^+)$ and low $q(O_2^+)$, is insignificant for the negative-ion densities. Therefore, only the results corresponding to the high O_2^+ production case are given here. Also shown in these figures are the corresponding electron-density profiles.

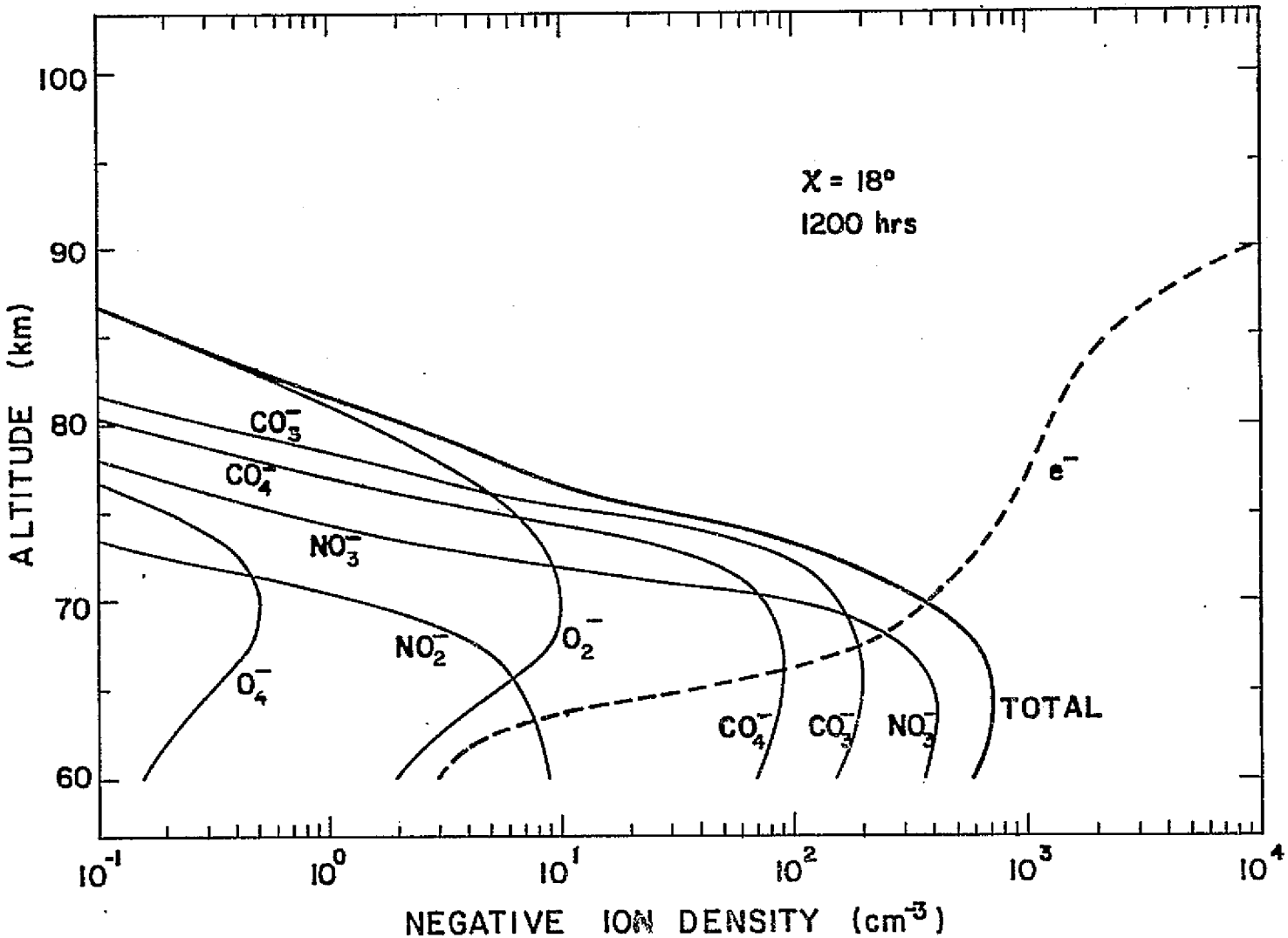

Figure 6.4 The computed height distributions of negative-ion species. These results correspond to low eddy diffusion and summer noon (χ = 18°) conditions.

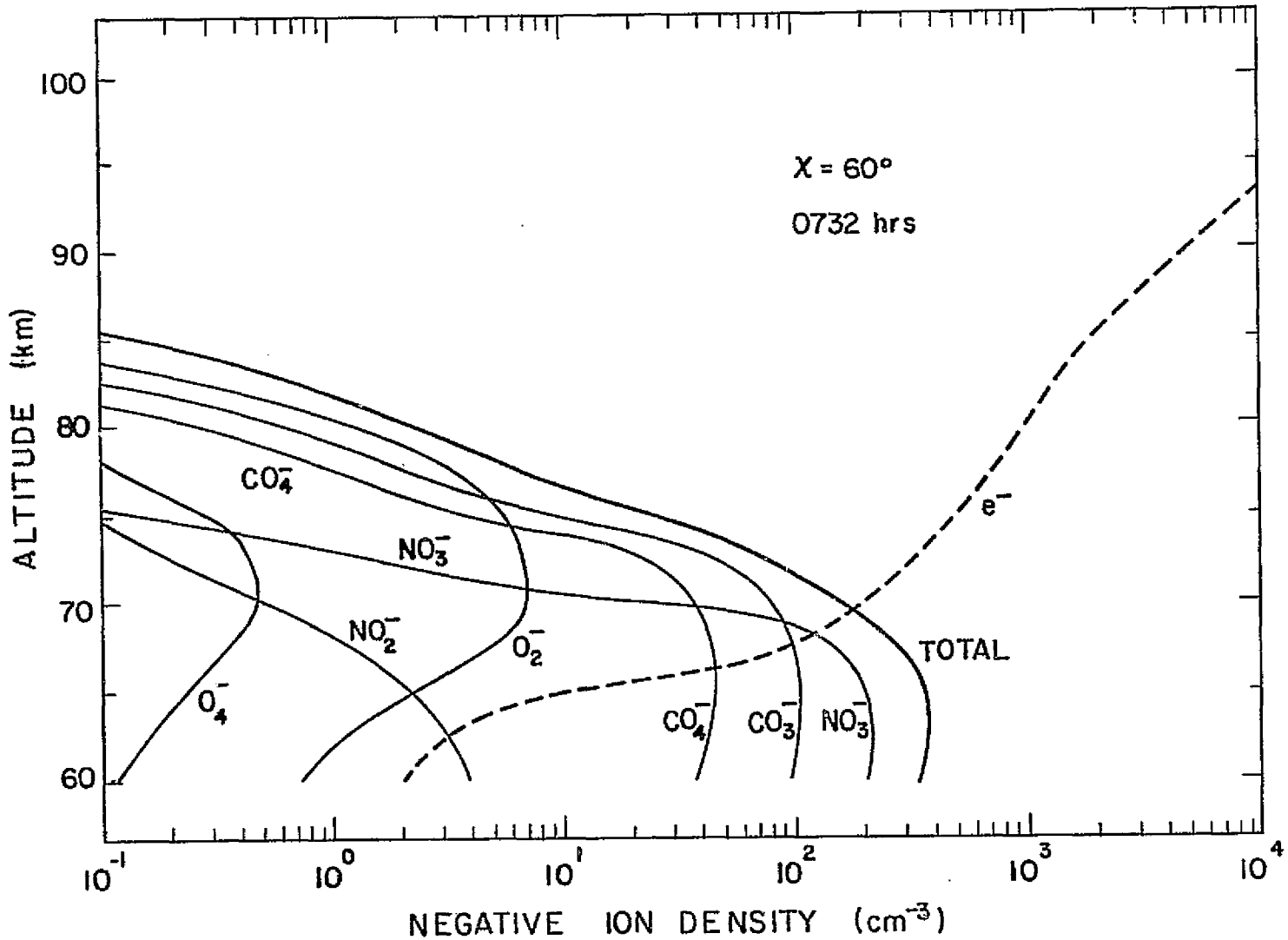

Figure 6.5 The computed height distributions of positive-ion species. These results correspond to low eddy diffusion and summer morning (χ = 60°) conditions.

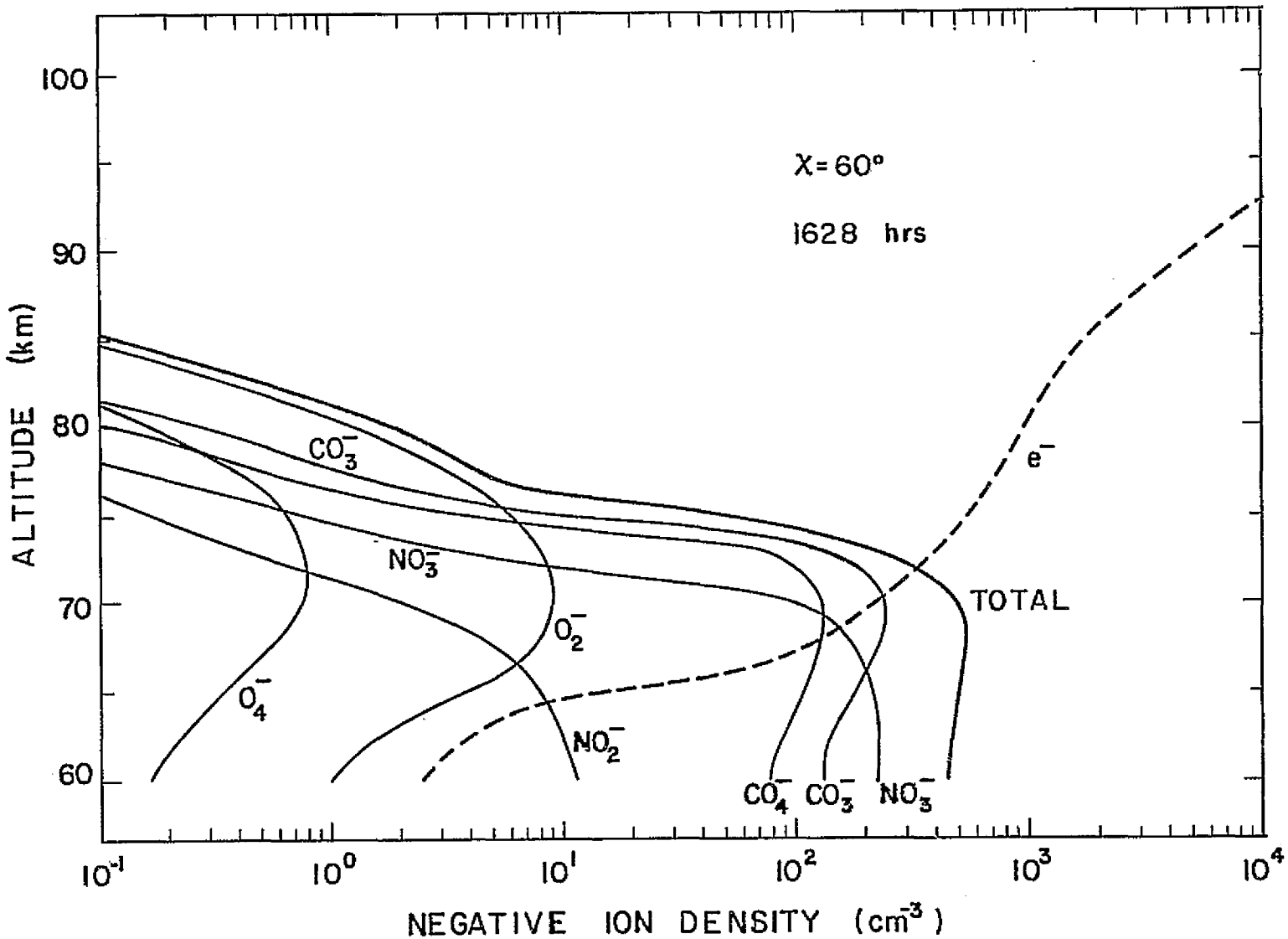

Figure 6.6 The computed height distributions of negative-ion species. These results correspond to low eddy diffusion and summer evening (χ = 60°) conditions.

As mentioned before, the negative-ion model adopted in our study is a very approximate one. In reality, it is believed that these ions exist clustered to water molecules or possibly other neutral molecules as well. However, for the purpose of computing the electron-density profiles below 75 km, the present model seems to be adequate.

In the noon profile (Figure 6.4), the total negative-ion density and the electron density become equal at 70 km, i.e. $\lambda = 1$. Above 70 km, the negative-ion density drops rapidly so that at 75 km, it reduces to 1/27, and at 80 km, it is even below 1/600. The negative-ion density is an order of magnitude less than the electron density at 74 km. Therefore, the negative ions could be completely neglected in *D* region studies above this height.

Below 70 km, however, the negative ions dominate over the electrons. Between 65 and 66 km, the negative-ion density reaches values 10 times the electron density. At 63 km, λ is nearly 100, and at 60 km, it is about 100.

In the other two negative-ion profiles (Figures 6.5 and 6.6) λ behaves somewhat similarly. In the morning profile, $\lambda = 1$ just below 70 km, while in the evening profile this is close to 72 km. λ becomes 1/10 and 10 near 74 km and 66 km, respectively, in the morning profile. In the evening profile this happens near 75 and 66 km, respectively. Therefore, the overall behavior of the negative ions relative to the electron densities is almost identical in the three profiles.

The absolute values of the negative-ion density, on the other hand, appears to vary with the zenith angle. In the noon profile, $\lambda = 1$ when the negative-ion density is about 360 ions cm^{-3}, while in the morning and evening profiles this occurs when the ion density is 170 and 320 ions

cm^{-3}, respectively. Further, the peak density of negative ions is 700 ions cm^{-3} at $\chi = 18°$, 360 ions cm^{-3} at $\chi = 60°$ (morning) and 540 ions cm^{-3} at $\chi = 60°$ (evening), respectively.

One should, however, remember that these values are subject to several uncertainties. Among these are: firstly, the production function; secondly, the photodetachment rates, and finally the mutual recombination coefficient of the major negative ions.

The ion-composition profiles show that NO_3^-, CO_3^-, and CO_4^- are the major negative ions below 75 km. In the noon profile, NO_3^- dominates below 66 km, while CO_3^- dominates above this height. CO_4^- is a secondary ion with values about a factor 2 - 3 below the major ion species. The next set of ions includes O_2^- and NO_2^-. These have concentrations which are about a factor 20 - 30 below the major ion concentrations. Between these two ions NO_2^- dominates below about 67 km, while above this height, O_2^- dominates.

In the negative-ion chemistry, the primary ion produced is O_2^-, and the rest are all produced subsequently through charge exchange or rearrangement reactions. The species that have low loss rates can attain high concentration levels. In the case of NO_3^-, the loss mechanisms are only photodetachment and mutual neutralization with the positive ions. Hence it is considered a terminal ion, though in reaiity, further reactions to form hydrated cluster ions may be possible. Thus NO_3^- could attain a high concentration.

In the case of CO_3^- and CO_4^-, however, large concentrations are possible because of the relatively high abundance of CO_2 present in this region. As discussed in Section 5.2.2, the negative-ion reactions proceed in two paths, one via O_3^- and the other via O_4^-. Both of these react with

CO_2 to yield CO_3^- and CO_4^-, respectively. The time constants of these reactions are much shorter than those of the other reactions. This results in these ions attaining a high abundance in the lower *D* region.

The $\chi = 60°$ profiles also show a similar distribution of the negative ions. However, the relative abundance of the different ions appears to have changed. In the morning profiles, the absolute concentrations of the three major ions have gone down by a factor of about 1.5 - 2 below 70 km, while maintaining the relative distribution somewhat identical. Such a reduction in the overall negative-ion density can be understood because of a similar reduction in the total ion-pair production between noon and $\chi = 60°$.

In addition to the photodetachment, collisional detachment processes also control the relative abundance of the negative ions and electrons. Of such processes, the reaction R_{153} where $O(^3P)$ reacts with O_2^- plays an important role in controlling the O_2^- level. Between $\chi = 60°$ in the morning and noon, $[O(^3P)]$ in the height range from 60 to 70 km does not change very much (Figure 3.12). However, between noon and $\chi = 60°$ in the afternoon $[O(^3P)]$ drops through a factor about 1.5 in the same height interval. Such a drop in $[O(^3P)]$ can result in enhanced negative-ion concentrations. This is what is shown in the evening set of profiles. In addition to changes in $[O(^3P)]$, changes in [NO] and $[NO_2]$ also contribute towards the disimilarity in the negative-ion concentrations in the morning and afternoon profiles.

As discussed in Section 5.1.2, no proper measurements of the absolute negative-ion densities carried out under quiet daytime conditions are available for comparison purposes. Nevertheless, the available

measurements indicate the presence of CO_3^-, NO_3^- and their hydrated clusters as the major negative ions, in agreement with the computed results.

6.4 *Electron Density*

The computed electron-density profiles are shown separately in Figure 6.7. These correspond to 18° and 60° zenith angles, the solid lines corresponding to the high O_2^+ production and the broken lines corresponding to the low O_2^+ production. The electron-density profiles measured at these zenith angles at Wallops Island on July 24, 1968 are also shown here for comparison.

6.4.1 *Comparison with measured profiles.* In discussing the positive-ion composition in Section 6.2, it was noted that there is a discrepancy between the type of hydrated cluster ion that is dominant in the *D* region as computed and as observed. Fortunately, the dissociative recombination coefficient of both these ions has the same value, and therefore the electron densities obtained is independent of the actual type of the positive ion. As such, the comparison of the computed profiles with those measured will still be valid here.

The general agreement between the two sets of profiles is good. However, certain discrepancies do occur. In the noon profile, the computed values are significantly less than the measured values above 88 km. This difference is about a factor of 2.5 above 90 km. The two profiles have equal values at 88 km. In this region of the ionosphere, the dominant positive ions are O_2^+ and NO^+. The metallic ion abundances are also negligible. Hence, the effective electron recombination rate can easily be determined once $\alpha(O_2^+)$ and $\alpha(NO^+)$ are known Therefore, the missing factor has to be in the production function.

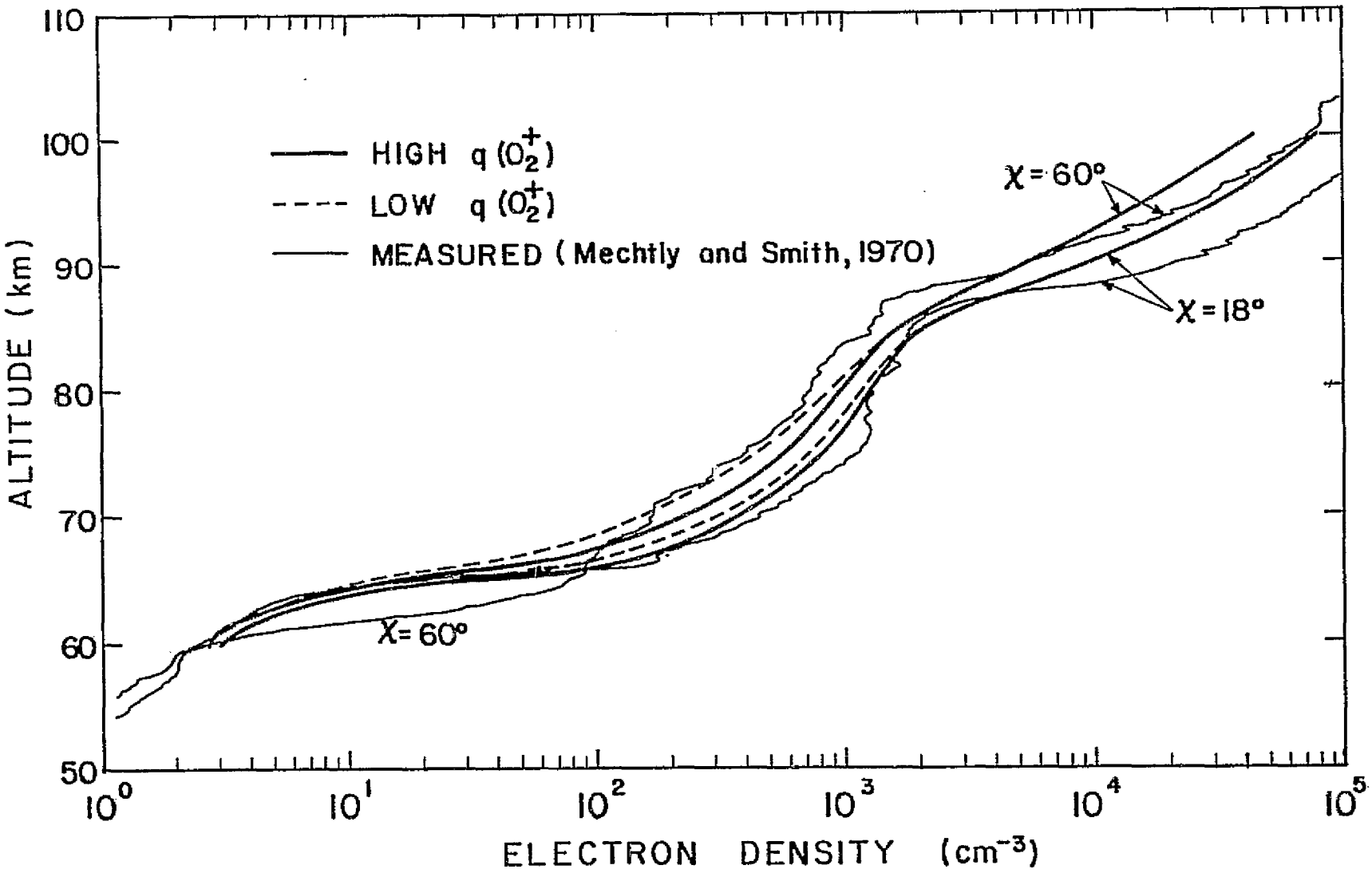

Figure 6.7 The computed electron-density profiles corresponding to 18° and 60° solar zenith angles. The measured profiles are also shown for comparison.

Above 90 km, it is mainly the O_2 molecules that contribute to the ion-pair production, which is ionized by X-rays in the 30-40 Å band (mainly by the 33.7 Å line) and Ly-β (1016 Å) radiation. Though O_2 undergoes small changes in its density, it is unlikely that the change is large enough to cause the observed discrepancy. Therefore, the only other factor left for consideration is the incident flux of the 33.7 Å and 1215 Å radiation lines. The values used in this study are those reported by *Hinterreger* [1970]. The Ly-β line intensity has been measured many times and its flux variation is fairly well known. On the other hand, the 33.7 Å line intensity is not so well known. The flux intensity used here is that measured by *Manson* [1972]. This is nearly an order of magnitude less than the measurements of *Argo et al.* [1970]. However, measurements of Argo et al. cover only a few lines. Manson's data covers the entire spectrum between 30 and 100 Å. Naturally, one would prefer to use Manson's data. However, being on the extreme edge of the spectrum measured, the 33.7 Å line may have been subject to a greater error than the rest of the spectrum in his measurements, which could have resulted in getting a too low value. An increase in the 33.7 Å intensity can easily increase the electron densities between 90 and 95 km considerably. Such an increase can also make the $\chi = 60°$ profile agree better with the measured profile above 90 km. However, this has to wait until more accurate measurements of this line is made available.

In the height range between 80 and 88 km, the agreement between the noon profile and the measured profile is very good. The electron-density profile has values between 1300 and 2000 cm^{-3} in this region. The dominant positive ions are the hydrated clusters. Though the computations show $NO^+ \cdot H_2O$ to be the dominant ion here, the actual one could be

$H^+ \cdot (H_2O)_n$, with $n \geq 4$. The recombination coefficient of such ions are nearly 1×10^{-5} cm^3 sec^{-1} [*Leu et al.*, 1973]. This is particularly so in view of the valley in the temperature profile which is present in this height interval.

The $\chi = 60°$ profile, however, shows a significant deviation from the measured profile. Between 80 and 88 km, the computed electron densities are about 1.3 - 1.4 times greater than the observed values. This implies that either the loss coefficient has increased or the production function has decreased over the interval of time corresponding to $\chi = 18°$ and 60°.

The loss coefficient depends on the actual domination present at these heights, and the effective recombination coefficient. The formation of the dominant ion is controlled by the concentrations of several minor neutral constituents such as H_2O and $O(^3P)$. These have long time constants around 80 - 85 km, and it is very unlikely that their concentrations would vary significantly over this interval of time.

The effective recombination coefficient depends to a large extent on the recombination coefficient of the dominant cluster ions in this region. To bring about an increase of a factor of 1.4 in the electron density, the effective recombination coefficient (α_{eff}) has to increase by a factor of 2. The value of α_{eff} can change for two reasons. Firstly, it can change due to a change in the composition of the positive ions, when the dominant ion changes from one having a low recombination coefficient to one having a large recombination coefficient. Alternatively, the dominant ion could remain unchanged, but its α may change due to a change in the ambient temperature.

According to *Leu et al.* [1973], in a simulated environment, the dominant hydrated cluster ion could be made to vary from one having a low mass to one having a high mass, by changing the ambient temperature. They found that between 300 K and 200 K, the dominant ions changed from $H^+ \cdot (H_2O)_3$ and $H^+ \cdot (H_2O)_4$ to $H^+ \cdot (H_2O)_5$ and $H^+ \cdot (H_2O)_6$, respectively. This means that α_{eff} changed from about 4×10^{-5} cm^3 sec^{-1} to about 8×10^{-5} cm^3 sec^{-1}, corresponding to this 100° C drop in temperature. On the other hand, the change in α with temperature for a given ion was found to be rather small, given by $T^{-0.5}$ only. For a temperature change from 300 to 200 K, this gives a difference of only 25%, which is much smaller than the required factor of 2.

During the summer days, the mesopause temperatures are considered to reach very low values. THe measurements of the mesosphere temperatures by *Smith et al.* [1970] during the summer of 1968 have shown that the mesopause temperature could vary generally between 160 and 200 K. They also have observed that on a given summer day, the mesopause temperature had changed through 20° C within a time interval of about 10 hours. Further, near the mesopause, the gradient in the temperature was observed to be quite high. Temperature variations of about 20° C within a distance of 2 km are not uncommon in the mesosphere. Generally, much larger variations are observed in the winter months than in the summer months.

Therefore, it is conceivable that the low temperatures prevailing at the mesopause could have given rise to heavier clusters over a narrow height range. As discussed earlier, the formation of the heavier clusters take place through 3-body association reactions. These reactions have rate constants which are strongly temperature dependent. In our study,

a T^{-2} temperature dependence is assumed for these rate constants. In reality it is quite possible that the temperature dependence is even stronger than this. Thus, it is apparent that the sharp valley in the temperature profile around 85 km could give rise to firstly, an enhancement in the heavier clusters having large values for α, and secondly, an increase in α of each cluster ion around the mesopause. The possibility of such a scheme was demonstrated in the *D* region positive-ion measurements made recently by *Krankowsky et al.* [1972] who observed high concentrations of heavy clusters such as $H^+ \cdot (H_2O)_4$ around 85 km on a summer night.

Next, one could consider the possibility of reducing the production function within the short period of time concerned. Below 88 km, it is the NO ionization due to Ly-α radiation that is most important. Therefore, either the [NO] or the intensity of Ly-α has to decrease by a factor of nearly 2. However, NO at this altitude has a life time against chemical and diffusion losses over a day. Thus, the expected change to occur in a few hours appears unlikely. In the case of the Ly-α line, *Timothy and Timothy* [1970] observed only a maximum of 10-12% variation in the intensity of this line over short term periods, i.e., periods less than a day. Hence the necessary 100% variation again seems unlikely. The other means by which the production rate could change is through a variation of the optical depth. Such a variation could be brought about by changing the O_2 density. Below 88 km, however, this again appears to be difficult to realize.

The missing factor of 1.4 in the electron-density profile corresponding to $\chi = 60°$ and 80-88 km range could therefore be attributed most probably

to the change in α_{eff} caused by a sharp temperature variation at the mesopause.

The most striking feature in the 70-80 km range of the computed profiles is the relatively low dependence of their values on the solar zenith angle. Throughout the height interval of 70-75 km, the measured profiles maintain a number density ratio of 3, while the corresponding ratio in the computed profiles is about 1.5 - 1.7.

It is also noted that all four computed profiles, including the profiles corresponding to high and low O_2^+ production rates, lie enveloped by the two measured profiles; i.e., at $\chi = 18°$ the measured values are greater than the computed values whereas at $\chi = 60°$ the measured values are smaller than the computed values. Therefore, any adjustment that is to be made to the computed profiles to bring them into agreement with the measurements has to be selective regarding the solar zenith angle.

Based on the same arguments presented earlier, any possibility of the minor neutral constituents such as NO and H_2O varying through the required extent may be ruled out. Being away from the mesopause any abrupt change in the temperature profile also may be considered unlikely.

Towards the lower end of this height interval, of course, the presence of the negative ions become important. A relative increase in the negative ion density makes α_{eff} increase causing a reduction in the electron density. Such an increase in N^- is indeed possible through the collisional detachment of O_2^- in its reaction with $O(^3P)$. The present computations show that $O(^3P)$ below 75 km drops markedly from the noon values. This drop could get further enhanced if lower values for the eddy diffusion coefficient are used. However, above 70 km this mechanism is only marginal in reducing the electron densities.

Referring to Figure 6.7, it is also noted that the difference between the computed and the measured profiles is not so great when the low $q(O_2^+)$ results are employed. However, with these results, the values in the computed noon profile fall short of the measured electron densities which is worse with the low $q(O_2^+)$ case than with the high $q(O_2^+)$ case. An explanation for this behavior could be sought in terms of the production mechanisms.

Below 75 km, Ly-α is still the dominant ionization source. However, the X-rays in the band 2 - 10 Å and precipitating electrons also make significant contributions, particularly towards the lower region. The precipitating electron flux has no diurnal variation. The agreement between the measured and computed profiles is obtained when low flux ($\gamma = 3$) for this source is used. In fact making it zero would make the agreement at $\chi = 60°$ still better.

The X-ray wavelengths less than 3 Å cause ionization below 75 km. An enhancement in the 0-3 Å band flux at noon, with its contribution exceeding that of Ly-α, can cause a corresponding increase in the noon electron density below 75 km. In Chapter 4 when the appropriate fluxes were selected from the available data, 0-(3 Å) was taken as 1×10^{-5} erg cm^{-2} sec^{-1} for the high O_2^+ production case. However, Figure 4.6 shows that shortly before 1200 hours on the day the measurements were made, a sudden enhancement in the 0-3 Å flux had indeed taken place. Such an increase in the X-ray flux in the 0-3 Å band occurring near noon and absent at $\chi = 60°$ could account for the differences appearing below 75 km in the computed and measured profiles. In order to obtain quantitative values for this increase, however, more detailed recordings of the 0-3 Å band flux

are required. As discussed in Section 4.2.1, many uncertainties exist in both the measurements and interpretation of the solar X-ray fluxes below 3 Å. Nevertheless, this mechanism provides a satisfactory explanation because of the selective manner in which this enhancement affects the electron-density profiles, i.e., affecting only the noon values lying below 75 km.

The region below 70 km is controlled mostly by the negative ions. The overall agreement between the computed electron densities and the measured values could be considered satisfactory in view of the many uncertainties present in the negative-ion chemistry. However, the computed profiles fail to reproduce a characteristic feature revealed in the measured profiles. That is the cross-over of the noon and the $\chi = 60°$ profiles near 65 km. The production function does not show such a cross-over at these heights. Hence, this could be safely attributed to changes taking place in the negative-ion chemistry. As mentioned in the last section, many of the parameters such as the photodetachment rates and the mutual neutralization coefficients are not properly known. Hence, at this stage, attempts to interpret the detailed behavior of the electron-density profiles below 70 km would seem futile.

6.4.2 *Solar zenith angle variation.* The computed electron density profiles do not exhibit a marked solar zenith angle variation, as revealed in Figure 6.8. Here, the computed electron densities are plotted against the solar zenith angle, for heights of 75, 80 and 85 km. The solar zenith angle variations as observed in partial reflection, and cross-modulation experiments are also shown in this figure [*Thrane*, 1969]. These show larger variations, particularly for 85 km. One could also compare the diurnal variation of absorption measurements. However, these are mostly

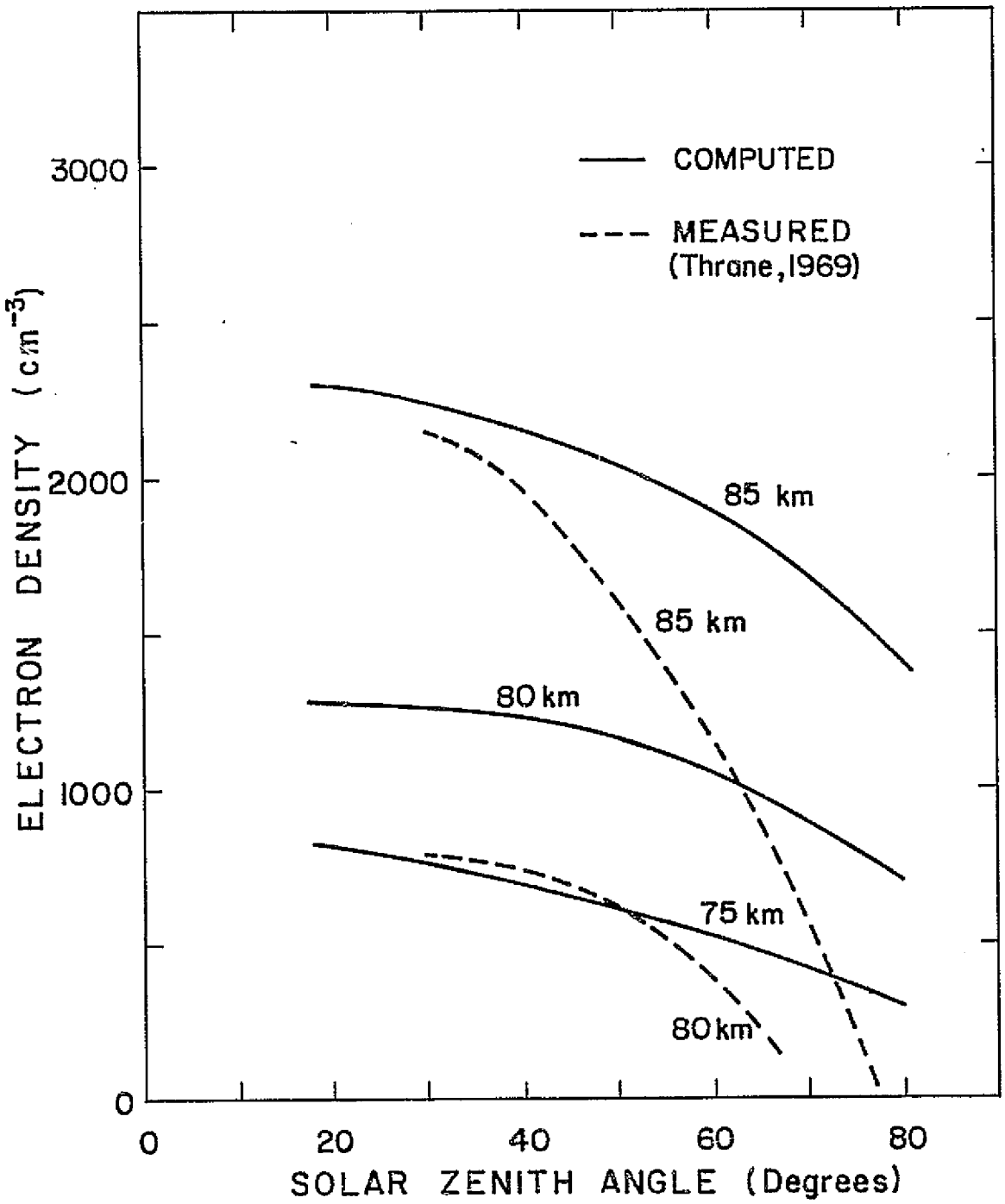

Figure 6.8 The solar zenith angle variation of the computed electron densities, shown for heights 75, 80 and 85 km.

sensitive to heights above 85 km, and hence not related to the computed variations.

Figure 6.9 shows the effective recombination coefficient deduced from the computed electron density values and the production functions. As shown in this figure, there is no significant variation in the α_{eff} values deduced for $\chi = 18°$ and $\chi = 60°$.

The effective recombination coefficient shown here also exhibits the regions where different loss mechanisms occur. Above 88 km, α_{eff} is less than 1×10^{-6} cm^3 sec^{-1}. The molecular ions, NO^+ and O_2^+ dominate this region. Between 70 and 85 km, α_{eff} has values lying in the range 3×10^{-6} - 1×10^{-5} cm^3 sec^{-1}. This region is associated with the hydrated cluster ions. In the intermediate region, i.e. 85-88 km, electron loss mechanism changes from cluster-ion recombination to molecular-ion recombination.

Below 70 km, α_{eff} increases rapidly. In the 10 km range from 70 km to 60 km, α_{eff} increases by a factor of nearly 1000. This factor would undergo a solar zenith angle variation only if the dominant ion in a particular height range varied systematically from one having a low α_i to another having a high α_i, or vice versa. In these computations, however, it is found that no such variation occurs.

In the 75-85 km region, the minor constituents, particularly NO and H_2O, have long time constants and, therefore, their chemistry does not reveal a detectable solar zenith angle variation. Hence, in the production function, the solar zenith angle dependence appears through the variation in the incident flux. This takes place due to changes in the sec χ factor in the optical depth. At higher altitudes, of course, the O_2 density could

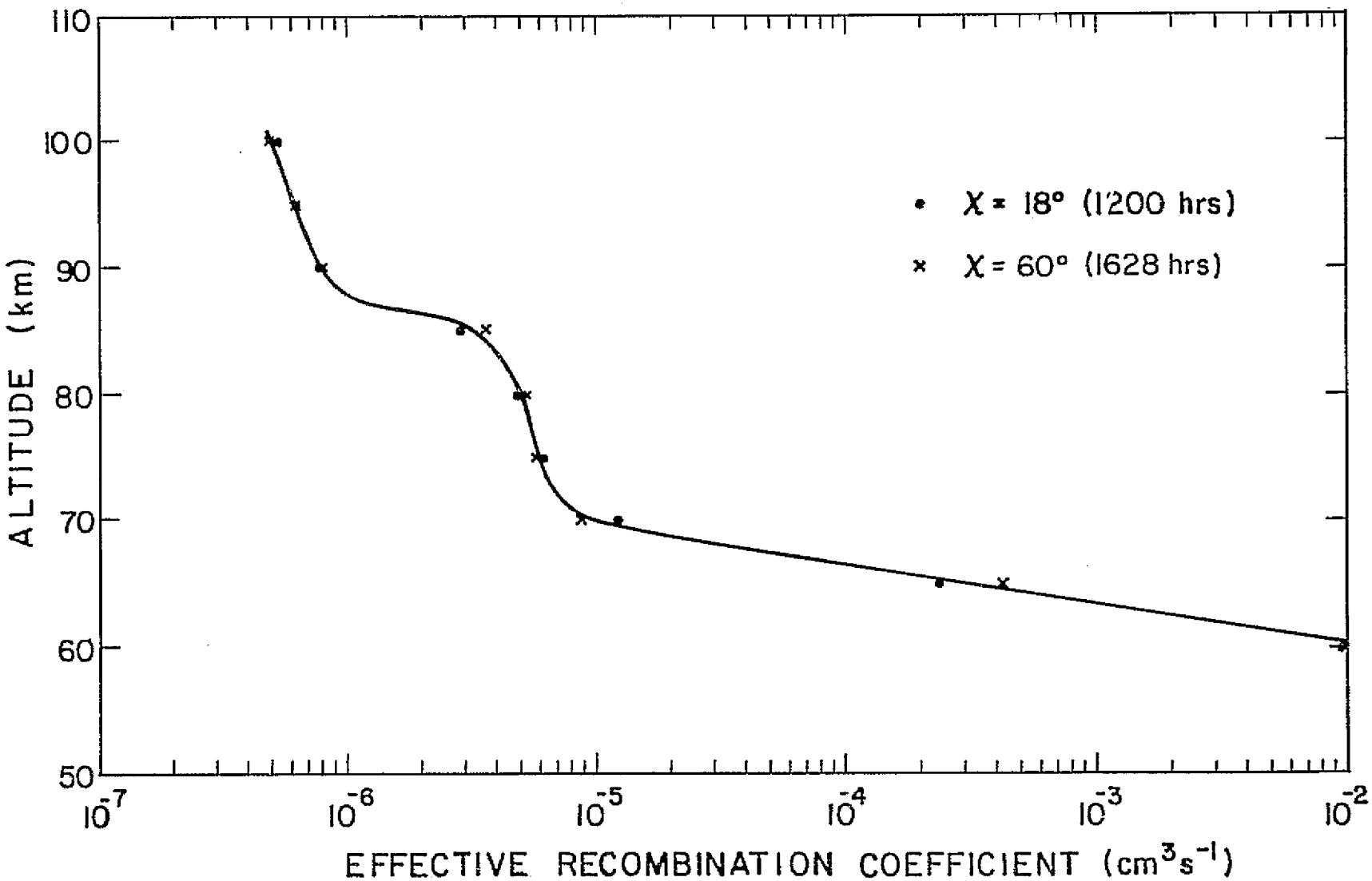

Figure 6.9 The effective recombination coefficient of the electrons, obtained from the electron densities computed at 18° and 60°.

have a diurnal variation which could change the optical depth and hence the attenuation of the downcoming radiation. However, the results of the neutral chemistry model show that this is not important below 100 km.

Therefore, it appears that above 70 km, the only systematic solar zenith angle variation of the electron densities occurs through changes in the sec χ term in the optical depth factor. The concentrations of the major ionizable constituents such as NO and O_2 remain unchanged. Further, there is no systematic change in the effective recombination coefficient. For heights below 70 km, systematic changes in the negative-ion chemistry which take place during the daytime could cause corresponding variations in the electron densities. However, in the absence of proper data on the negative-ion chemistry, the behavior of the electron densities in this region is only a matter of conjecture.

It has now become apparent that the systematic variations of the computed electron densities fail to account completely for the behavior of the measured profiles. Hence it was found necessary to invoke additional sources that would cause short term variations in the *D*-region electron density. These include the temperature variations around the mesopause and enhancements in the solar X-ray flux in the 0-3 Å band. Variations of such quantities cannot be predicted in advance, and could only be detected through continuous monitoring related parameters. Therefore, any predication of the solar zenith angle variation of the *D* region ionization will generally fall short of the actual measured variations.

7. SUMMARY AND CONCLUSIONS

An attempt has been made in this study to investigate the solar zenith angle variation of the *D*-region ionization. In particular, the variation occurring between 60° zenith angles corresponding to a summer, quiet-sun day during the high solar epoch has been the main interest. One objective in this study is to interpret the measured electron-density profiles available at two zenith angles 18° and 60°, on July 24, 1968. These two profiles are among a series of electron-density profiles measured using *in situ* rocket experiments which are capable of yielding accurate electron densities in the *D* region.

The ionization parameters studied include the positive-ion density, negative-ion density and the electron density. Prior to constructing a model for the *D* region ion chemistry, it was found necessary to construct a model for the neutral constituent chemistry encompassing the *D*-region altitudes. In order to minimize the effects of boundary conditions, the neutral chemistry model was extended from 30 km to 120 km.

Model calculations were carried out to study the diurnal behavior of 14 minor constituents which include oxygen only, oxygen-hydrogen, and oxygen-nitrogen species. Initially, the carbon compounds were also included, but these were later removed from the model as they were found to contribute only a little to the ion chemistry of the *D* region. As far as the behavior of this region is concerned, the most important minor neutral constituents are $O(^3P)$, O_3, H_2O, NO, NO_2 and perhaps OH and HO_2.

The neutral chemistry model includes both the photochemistry of the neutral species and the transport terms to account for the eddy diffusion of long-lived constituents. In both of these areas many of the parameters

used are quite uncertain. The solar-radiation intensity over certain bands, the absorption cross section of O_2 in the S-R band and the rate constants of several reactions are some of the lesser known photochemical parameters used in the model. In addition to these, the parameters such as the eddy diffusion coefficient a the boundary conditions of the constituents under diffusion are also subject to much uncertainty.

Based on the observations of several workers, as well as on the previous work of a similar nature, two models for the eddy diffusion coefficient were adopted, which are designated high and low D_e models. Using the photochemical production and loss terms, continuity equations were written which turned out to be simple first-order differential equations for the short-lived constituents, and second-order partial-differential equations for the long-lived constituents. These include $O(^3P)$, H, H_2, H_2O, NO, and H_2O.

This set of coupled differential equations was solved numerically by computer simulation. The computer solution was carried out in three parts. First, the initial values were obtained by solving the steady-state equations. Next, the time-dependent equations were solved keeping the solar angle fixed at noon. Finally, the diurnal variation was simulated by running the program with the solar zenith angle varying through day and night. It was found necessary to carry out the diurnal simulation through a minimum of ten days to achieve convergence.

The results of the diurnal study show that most of the neutral constituents undergo diurnal variation at some height interval. The $O(^3P)$ concentrations have a diurnal variation throughout the 30-120 km height range with the concentrations vanishing below 80 km at night. In $O_2(^1\Delta_g)$,

the variations during the daytime appear below 75 km. Corresponding to these variations, O_3 also undergoes significant changes below about 80 km.

Among the O-H species, both H_2O and H_2 do not show any diurnal variation. On the other hand, H, OH and HO_2 exhibit large diurnal variations. The concentration of H vanishes below 77 km in the night, and during the daytime, shows a strong diurnal asymmetry, mostly between 50 and 85 km. Both OH and HO_2 show somewhat similar variations during the daytime. However, at night the depletion of HO_2 is much greater than that of OH.

In the O-N species, NO_2 has a strong diurnal variation while NO has a diurnal variation only below 70 km. N_2O on the other hand has no diurnal variation.

The ion-pair production rates were calculated using the neutral constituent concentrations obtained in Chapter 3. The results of these calculations indicate that the ion-pair production due to $O_2(^1\Delta_g)$ is small compared to other sources although it is a significant source of O_2^+ ions. The major contributions were found to be due to Ly-α in the mid-*D* region In the upper *D* region, Ly-β and 33.7 Å radiation lines were found to be important, while in the lower region, galactic cosmic rays were found to be the major source of ionization.

The diurnal variation in these major production functions was solely due to the sec χ term in the optical depth factor. The concentrations of the ionizable constituents NO and O_2 remain unaltered. The small variation of NO below 70 km does not contribute much because of the rapid attentuation of Ly-α radiation below 70 km.

To investigate the variation of the *D*-region ionization with the solar zenith angle, a model for the charged species comprising positive

ions, negative ions and the electrons was developed. This model was run concurrently with the neutral chemistry model on the last day of its diurnal simulation.

The positive-ion composition results of these computations agreed generally with the observed distributions, except for the discrepancy observed in the major ion in the mid-*D* region. The computations show $NO^+ \cdot H_2O$ to be the major ion whereas direct measurements indicate hydrated clusters of the type $H^+ \cdot (H_2O)_n$ with $n = 3$. The negative-ion composition results are generally in agreement with the results of the previous workers. Comparisons with the observations also show some similarity in the results, though such a direct comparison with the observations is not really valid because of the several approximations made in the negative ion reaction scheme.

A comparison of the electron densities show good agreement with the observations. However, there are regions where small discrepancies appear. Further, the systematic variation of the electron density with the solar zenith angle as computed is only a fraction of the observed variation. This is because the only term that can be included in any model calculation which contributes to the solar zenith angle variation is the sec χ term in the optical depth factor. However, in reality short term variations such as temperature changes near the mesopause, X-ray flux changes in the 0-3 Å band could cause variation in the electron densities within the same day. Such variations, unfortunately, do not follow a given pattern to be included even empirically in a computer code.

Therefore, in conclusion, it might be mentioned that the observed solar zenith angle variation in the *D*-region electron densities may be

considered as due to two components. Firstly, a regular variation caused by the sec χ term in the optical depth factor, and secondly, an irregular variation caused by such effects as temperature variations and X-ray flux variations.

A large number of input parameters go into the numerical modeling of the *D* region, as demonstrated in this work. Unfortunately, many of these remain uncertain. In the neutral chemistry model, more reliable data on such quantities as the solar fluxes above 1000 Å, absorption cross sections of the constituent gases, rate constants of fast neutral reactions, eddy diffusion coefficient and its height distribution are urgently required. Further, actual measurements of the distribution, of minor neutral species such as NO, $O(^3P)$ and H_2O are required to verify the validity of the model calculation results.

The ion chemistry model also requires data with better reliability for satisfactory interpretation of the measured ion composition and electron-density profiles. Among these are X-ray fluxes, energetic particle fluxes, ionization yield of O_2 and N_2 due to these high energy sources, and rate constants, particularly the electron recombination coefficients.

Also, one need not emphasize the importance of conducting coordinated experiments to measure the ion composition and electron-density profiles of the *D* region. Such measurements are necessary on quiet days in addition to those on special occasions so that a clear picture of the normal *D*-region ionization could be obtained. It is hoped that in the near future these data will become available to *D*-region investigators.

APPENDIX I. NUMERICAL SOLUTION OF PARTIAL DIFFERENTIAL EQUATIONS

The finite difference scheme adopted in the conversion of the set of partial differential equations (equation (3.16)) into the corresponding difference equations (equation (3.21)), and the method of solution of the resultant equations are given in this appendix.

Using the spatial and time divisions given in equations (3.19) and (3.20), the spatial derivatives can be expressed in the form

$$\frac{\partial Y_n^m}{\partial z} \cong \frac{Y_{n+1}^m - Y_{n-1}^m}{2\Delta z} \quad , \tag{A.1}$$

$$\frac{\partial^2 Y_n^m}{\partial z^2} \cong \frac{Y_{n+1}^m - 2Y_n^m + Y_{n-1}^m}{(\Delta z)^2} \quad , \tag{A.2}$$

where Y_n^m is the constituent concentration at altitude z_n and time t_m.

The time derivative is written in the semi-implicit form

$$\frac{\partial Y_n^m}{\partial t} \cong \frac{Y_n^m - Y_n^{m-1}}{\Delta t} \tag{A.3}$$

When equations (A.1) - (A.3) are substituted in equation (3.16), it becomes

$$\frac{Y_n^m - Y_n^{m-1}}{\Delta t} = a\,\frac{(Y_{n+1}^m - 2Y_n^m + Y_{n-1}^m)}{(\Delta z)^2} + b\,\frac{(Y_{n+1}^m - Y_{n-1}^m)}{2\Delta z} + c\,Y_n^m + d \tag{A.4}$$

In this equation, the coefficients a and b are functions of z only, while the coefficients c and d are functions of both z and t. The coefficient c includes the loss coefficient and therefore its value at time

t_m is evaluated using the concentrations $\left\{Y_n^{m-1}\right\}$. Similarly, d, which is the production term is also evaluated using concentrations obtained at time t_{m-1}.

Rearranging, equation (A.4) becomes

$$\left\{\frac{a_n}{\Delta z^2} + \frac{b_n}{2\Delta z}\right\} \Delta t\, Y_{n+1}^m + \left\{\left(c_n^{m-1} - \frac{2a_n}{\Delta z^2}\right) \Delta t - 1\right\} Y_n^m$$

$$+ \left\{\frac{a_n}{\Delta z^2} - \frac{b_n}{2\Delta z}\right\} \Delta t\, Y_{n-1}^m = - \left\{Y_n^{m-1} + d_n^{m-1}\, \Delta t\right\} \tag{A.5}$$

This simplifies to

$$\alpha_n\, Y_{n+1}^m + \beta_n^{m-1}\, Y_n^m + \gamma_n\, Y_{n-1}^m = \delta_n^{m-1} \quad , \tag{A.6}$$

which is the same as equation (3.21).

At the beginning of the computations, the coefficients β and δ are evaluated using the initial values of $\{Y_n\}$.

For the N height intervals, and corresponding to a given instant, $(N-2)$ equation of the above type can be written. The resulting system of equations could therefore be solved using the two boundary conditions.

In general, a boundary condition can be written in the form

$$u\,\frac{dY}{dz} + \nabla Y = w \quad , \tag{A.7}$$

where u, v and w are evaluated at the two boundaries.

When written in the difference form and rearranged, this becomes

$$\frac{u_o}{\Delta z} Y_1^m + (v_o - \frac{u_o}{\Delta z}) Y_o^m = w_o \quad , \tag{A.8}$$

$$(v_N + \frac{U_N}{z}) Y_N^m - \frac{u_N}{z} Y_{N-1}^m = w_N \quad , \tag{A.9}$$

for the lower and upper boundaries, respectively.

Following the method given by *Richtmyer* [1957], a recurrence formula is written for the variable Y_n^m in terms of two view variables, r and s, so that

$$Y_n^m = r_n Y_{n+1}^m + s_n \quad . \tag{A.10}$$

Eliminating terms including Y_{n+1}^m and Y_{n-1}^m from the equation (A.6) using the above formula, one gets

$$(\frac{\alpha}{r_n} + \beta \gamma r_{n-1}) Y_n^m + (\gamma s_{n-1} - \frac{\alpha}{r_n} s_n - \delta) = 0 \quad , \tag{A.11}$$

(In writing this equation, the suffix in the coefficients are left out for simplicity.)

This expression is true for all values of Y_n^m, so that one may write

$$\frac{\alpha}{r_n} + \beta + \delta r_{n-1} = 0 \quad , \tag{A.12}$$

$$\gamma s_{n-1} - \frac{\alpha}{r_n} s_n - \delta = 0 \quad . \tag{A.13}$$

This yeilds

$$r_n = - \frac{\alpha}{\beta + \gamma\, r_{n-1}} \quad , \tag{A.14}$$

and

$$s_n = \frac{\delta - \gamma\, s_{n-1}}{\beta + \gamma\, r_{n-1}} \quad . \tag{A.15}$$

The starting values of r_n and s_n are determined using the lower boundary conditions,

$$r_o = \frac{u_o}{u_o - v_o\, \Delta z} \quad , \tag{A.16}$$

$$s_o = - \frac{w_o\, \Delta z}{u_o - v_o\, \Delta z} \quad , \tag{A.17}$$

Thus, starting from r_o and s_o, all the values of r_n and s_n could be readily evaluated.

Next, using the upper boundary condition (equation (A.9)), one gets

$$Y_N = \frac{w_N\, \Delta z + s_{N-1}\, u_N}{v_N\, \Delta z + (1-r_{N-1})\, u_N} \tag{A.18}$$

Therefore, once Y_N is known, the other values of Y_n could be obtained using the above equation, in the descending order of n.

REFERENCES

Ackerman, M., F. Biaume and M. Nicolet (1969), Absorption in the spectral range of the Schumann-Runge bands, *Can. J. Chem. 47*, 1834-1840.

Anderson, J. G. (1971a), Rocket-borne ultraviolet spectrometer measurements of OH resonance fluorescence with a diffusive transport model for mesospheric photochemistry, *J. Geophys. Res. 76*, 4634-4652.

Anderson, J. G. (1971b), Rocket measurements of OH in the mesosphere, *J. Geophys. Res. 76*, 7820-7824.

Appleton, E. and W. R. Piggott (1954), Ionospheric absorption measurements during a sunspot cycle, *J. Atmos. Terr. Phys. 5*, 141-172.

Argo, H. V., J. A. Bergey and W. D. Evans (1970), Measurement of the solar X-ray flux in selected emission lines, *Astrophys. J. 160*, 283-292.

Armistead, G. W., J. V. Evans and W. A. Reid (1972), Measurements of *D*- and *E*-region electron densities by the incoherent scatter technique at Millstone Hill, *Radio Sci. 7*, 153-162.

Arnold, F. and D. Krankowsky (1974), New aspects of *D*-region positive cluster ion composition inferred from an improved mass spectrometer measurement, submitted to *J. Geophys. Res.*

Arnold, F., J. Kissel, D. Krankowsky, H. Wieder and J. Zahringer (1971), Negative ions in the lower ionosphere: a mass-spectrometer measurement, *J. Atmos. Terr. Phys. 33*, 1169-1175.

Arnold, F., K. H. Marien and D. Krankowsky (1974), New aspects in lower ionosphere positive cluster ion composition: Results from an improved mass spectrometer probe experiment, in *Proceedings of the COSPAR Symposium* on, 'Direct measurements in the lower ionosphere', Konstanz, F.R.G.

Badger, R. A., A. C. Wright and R. F. Whitlock (1965), Absolute intensities of the discrete and continuous absorption bands of oxygen gas at 1.26 and 1.065 μ and the radiative lifetime of the $^1\Delta_g$ state of oxygen, *J. Chem. Phys. 43*, 4345-4350.

Bainbridge, A. E. and L. F. Heidt (1966), Measurement of methane in the troposphere and lower stratosphere, *Tellus 18*, 221-225.

Bates, D. R. and M. Nicolet (1950), The photochemistry of atmospheric water vapor, *J. Geophys. Res. 55*, 301-327.

Bates, D. R. and P. B. Hays (1967), Atmospheric nitrous oxide, *Planet. Space Sci. 15*, 189-197.

Belrose, J. (1963), *The oblique reflection of low-frequency radio waves at frequencies below 300 Kc/s*, edited by W. T. Blackband, Pergamon Press, Oxford, 149-165.

Beynon, W. J. G. and K. Davies (1955), A study of vertical incidence ionospheric absorption at 2 Mc/s, *The physics of the ionosphere*, Physical Society, London, 40-52.

Blamont, J. E. and C. de Jager (1961), Upper atmospheric turbulence near the 100 km level, *Ann. Geophys. 17*, 134-144.

Bonnet, R. M. (1968), Stigmatic spectra of the sun between 1800 Å and 2800 Å, *Space Res. VIII*, edited by A. P. Mitra, L. G. Jacchia and W. S. Newman, North Holland, Amsterdam, 458-472.

Bowles, K. L. (1958), Observations of vertical incidence scatter from the ionosphere at 41 Mc/Sec, *Phys. Rev. Letter 1*, 454-455.

Bracewell, R. N., K. G. Budden, J. A. Ratcliffe, T. W. Straker and K. Weekes (1951), The ionospheric propagation of low and very-low-frequency radio waves over distances less than 1000 km, *Proc. Inst. Elect. Engrs. 98 III*, 221-236.

Brasseur, G. and M. Nicolet (1973), Chemospheric processes of nitric oxide in the mesosphere and stratosphere, *Planet. Space Sci. 21*, 939-961.

Burke, R. R. (1970), Hydrogen atom participation in *D* region ion chemistry, *J. Geophys. Res. 75*, 1345-1347.

Campbell, I. M. and B. A. Thrush (1967), The association of oxygen atoms and their combination with nitrogen atoms, *Proc. Roy. Soc. London A296*, 222-232.

Chan, F. T. (1968), Electron-ion and ion-ion dissociative recombination of oxygen. 1. Electron-ion recombination, *J. Chem. Phys. 49*, 2533-2540.

Chapman, S. and T. Cowling (1952), *The mathematical theory of non-uniform gases*, Cambridge University Press, New York.

Christie, M. (1958), Elementary reactions in the photochemical oxidation of methyl iodide, *Proc. Roy. Soc. A 244*, 411-423.

Clark, I. D. and R. P. Wayne (1969), The reaction of $O_2(^1\Delta_g)$ with atomic nitrogen and with atomic oxygen, *Chem. Phys. Letters 3*, 405-407.

Colegrove, F. D., W. B. Hanson and F. S. Johnson (1965), Eddy diffusion and oxygen transport in the lower thermosphere, *J. Geophys. Res. 70*, 4931-4941.

Coltharp, R. N., S. D. Worley and A. E. Potter (1971), Reaction rate of vibrationally excited hydroxyl with ozone, *Applied Optics 10*, 1786-1789.

Coyne, T. N. R. and J. S. Belrose (1972), The diurnal and seasonal variation of electron densities in the midlatitude *D* region under quiet conditions, *Radio Sci. 7*, 163-174.

Coyne, T. N. R. and J. S. Belrose (1973), An investigation into the effects of limited height resolution in the differential absorption partial reflection experiment, *J. Geophys. Res. 78*, 8276-8288.

Crutzen, P. J. (1971), Ozone production rates in an oxygen-hydrogen-nitrogen oxide atmosphere, *J. Geophys. Res. 76*, 7311-7326.

Culhane, J. L., A. P. Willmore, K. A. Pounds and P. W. Sanford (1964), Variability of the solar X-ray spectrum below 15 Å, *Space Res. IV*, edited by P. Muller, North Holland, Amsterdam, 741-758.

Davis, D. D., J. T. Herron and R. E. Huie (1973), Absolute rate constants for the reaction $O(^3P) + NO_2 = NO + O_2$ over the temperature range 230-339 °K, *J. Chem. Phys. 58*, 530-535.

de More, W. B. (1967), Reaction of $O(^1D)$ with H_2 and the reactions of H and OH with ozone, *J. Chem. Phys. 47*, 2777-2783.

de More, W. B. and O. F. Raper (1967), Reaction of $O(^1D)$ with methane, *J. Chem. Phys. 46*, 2500-2505.

Detwiler, C. R., D. L. Garrett, J. D. Purcell and R. Tousey (1961), The intensity distribution in the ultraviolet solar spectrum, *Ann. Geophys. 17*, 263-272.

Donahue, T. M. (1972), Positive ion chemistry of the *D* and *E* regions, *Radio Sci. 7*, 73-80.

Dunkin, D. B., F. C. Fehsenfeld, A. L. Schmeltekopf and E. E. Ferguson (1971), Three-body reactions of NO^+ with O_2, N_2 and CO_2, *J. Chem. Phys. 54*, 3817-3822.

Elwert, G. (1961), Theory of X-ray emission of the sun, *J. Geophys. Res. 66*, 391-401.

Evans, K. and K. A. Pounds (1968), The X-ray emission spectrum of a solar active region, *Astrophys. J. 152*, 310-335.

Evans, W. F. J. and E. J. Llewellyn (1970), Molecular oxygen emissions in the airglow, *Ann. Geophys. 26*, 167-177

Evans, W. F. J. and E. J. Llewyllen (1973), Atomic hydrogen concentrations in the mesosphere and the hydroxyl emissions, *J. Geophys. Res. 78*, 323-326.

Fehsenfeld, F. C. and E. E. Ferguson (1968), Further laboratory measurements of negative reactions of atomspheric interest, *Planet. Space Sci. 16*, 701-702.

Fehsenfeld, F. C. and E. E. Ferguson (1969), Origin of water cluster ions in the *D*-region, *J. Geophys. Res. 74*, 2217-2225.

Fehsenfeld, F. C. and E. E. Ferguson (1972a), The reaction $NO_2^- + H \longrightarrow OH^- + NO$, *Planet. Space Sci. 20*, 295-296.

Fehsenfeld, F. C. and E. E. Ferguson (1972b), Recent laboratory measurements of *D*- and *E*-region ion-neutral reactions, *Radio Sci. 7*, 113-115.

Fehsenfeld, F. C., A. L. Schmeltekopf, H. I. Schiff and E. E. Ferguson (1967), Laboratory measurements of negative ion reactions of atmospheric interest, *Planet. Space Sci. 15*, 373-379.

Fehsenfeld, F. C., E. E. Ferguson and D. K. Bohme (1969), Additional flowing afterglow measurements of negative ion reactions of *D*-region interest, *Planet. Space Sci. 17*, 1759-1762.

Fehsenfeld, F. C., D. B. Dunkin and E. E. Ferguson (1970), Rate constants for the reaction of CO_2^{-+} with O, O_2 and NO; N_2^+ with O and NO; and O_2^+ with NO, *Planet. Space Sci. 18*, 1267-1269.

Fehsenfeld, F. C., M. Mosesman and E. E. Ferguson (1971a), Ion-molecule reaction in an $O_2^+ - H_2O$ system, *J. Chem. Phys. 55*, 2115-2120.

Fehsenfeld, F. C., M. Mosesman and E. E. Ferguson (1971b), Ion-molecule reactions in NO^+ - H_2O system, *J. Chem. Phys. 55*, 2120-2125.

Fejer, J. A. (1955), The interaction of pulses radio waves in the ionosphere, *J. Atmos. Terr. Phys. 7*, 322-323.

Ferguson, E. E. (1967), Ionospheric ion-molecule reaction rates, *Rev. Geophys. 5*, 305-327.

Ferguson, E. E. (1969), Negative ion-molecule reactions, *Can. J. Chem. 47*, 1805-1820.

Ferguson, E. E. (1971), Laboratory measurements of *D*-region ion-molecule reactions, *Mesospheric models and related experiments*, Reidel Publishing Co., Dordrecht-Holland, 188-197.

Ferguson, E. E., D. K. Bohme, F. C. Fehsenfeld and D. B. Dunkin (1969), Temperature dependence of slow ion-atom interchange reactions, *J. Chem. Phys. 50*, 5039-5040.

Findlay, F. D. and D. R. Snelling (1971), Collisional deactivation of $O_2(^1\Delta_g)$, *J. Chem. Phys. 55*, 545-551.

Foner, S. N. and R. L. Hudson (1962), Mass spectrometry of the HO_2 free radical, *J. Chem. Phys. 36*, 2681-2690.

Fontijin, A., C. B. Meyer and H. I. Schiff (1964), Absolute quantum yield measurements of the NO-O reactions and its use as a standard for chemiluminiscent reactions, *J. Chem. Phys. 40*, 64-70.

Freeman, F. F. and B. B. Jones (1970), Grazing incidence spectra of the sun, *Solar Phys. 15*, 288-308.

Friedman, H. (1963), Solar X-ray emission, *The Solar Corona*, edited by J. W. Evans, Academic Press, New York, 45-58.

Gardner, F. F. and J. L. Pawsey (1953), Study of the ionospheric *D*-region using partial reflections, *J. Atmos. Terr. Phys. 3*, 321-344.

Geisler, J. E. and R. E. Dickinson (1968), Vertical motions and nitric oxide in the upper mesosphere, *J. Atmos. Terr. Phys. 30*, 1505-1521.

Gnanalingan, S. (1974), Equatorial ionospheric absorption during half a solar cycle (1964-1970), *J. Atmos. Terr. Phys. 36*, 1334-1354.

Goldberg R. A. and A. C. Aikin (1971), Studies of positive-ion composition in the equatorial *D* region ionosphere, *J. Geophys. Res. 76*, 8352-8364.

Golomb, D. and M. A. MacLeod (1966), Diffusion coefficients in the upper atmosphere from chemiluminous trails, *J. Geophys. Res. 71*, 2299-2306.

Good, A., D. A. Durden and P. Kebarle (1970a), Mechanism and rate constants of ion-molecule reactions leading to the formation of $H^+ \cdot (H_2O)_n$ in moist oxygen and air, *J. Chem. Phys. 52*, 222-229.

Good, A., D. A. Durden and P. Kebarle (1970b), Ion-molecule reactions in pure nitrogen and nitrogen containing traces of water at total pressures 0.5-4 torr. Kinetics of clustering reactions forming $H^+ \cdot (H_2O)_n$, *J. Chem. Phys. 52*, 212-221.

Good, R. E. and D. Golomb (1973), Atomic oxygen profiles in the lower thermosphere, *Space Res. XIII*, edited by M. J. Rycroft and S. K. Runcorn, Akademie-Verlag, Berlin, 249-253.

Gough, M. P. and H. L. Collin (1973), Energetic electron precipitation as a source of ionization in the nighttime *D*-region over the mid-latitude rocket range, South Uist, *J. Atmos. Terr. Phys. 35*, 835-850.

Gudiksen, P. H., A. W. Fairhall and R. J. Reed (1968), Roles of mean meridional circulation and eddy diffusion in the transport of trace substances in the lower stratosphere, *J. Geophys. Res. 73*, 4461-4473.

Gutnick, M. (1961), How dry is the sky?, *J. Geophys. Res. 66*, 2867-2871.

Hall, T. C. and R. E. Blacet (1952), Separation of the absorption spectra of NO_2 and N_2O_4 in range of 2400-5000 Å, *J. Chem. Phys. 20*, 1745-1749.

Hall, L. A., J. E. Higgins, C. W. Chaynon and H. E. Hinteregger (1969), Solar cycle variation of extreme ultraviolet radiation, *J. Geophys. Res. 74*, 4181-4183.

Harries, J. E. (1973), Measurement of some hydrogen-oxygen-nitrogen compounds in the stratosphere from Concorde 002, *Nature 241*, 515-518.

Haug, A. and B. Landmark (1970), A two-ion model of electron-ion recombination in the *D* region, *J. Atmos. Terr. Phys. 32*, 405-407.

Haug, A. and E. V. Thrane (1970), The diurnal variation in the mid-latitude *D*-region, *J. Atmos. Terr. Phys. 32*, 1641-1647.

Hays, P. B. and J. J. Olivero (1970), Carbon dioxide and monoxide above the troposphere, *Planet. Space Sci. 18*, 1729-1733.

Heimerl, J. M., J. A. Vanderhoff, L. J. Puckett and F. E. Niles (1972), Fast path between NO^+ and $H_3O^+ \cdot H_2O$ in the *D* region, *Report No. 7570*, Ballistic Research Laboratories, Aberdeen Proving Ground, Maryland.

Henderson, W. R. (1971), *D*-region atomic oxygen measurement, *J. Geophys. Res. 76*, 3166-3167.

Henke, B. L. and R. L. Elgin (1970), X-ray absorption tables for the 2-2000 Å region, *Advances in X-ray analysis*, edited by B. L. Henke, J. B. Newkick and G. R. Mallet, Plenum Press, New York, 639-665.

Herron, J. T. (1969), An evaluation of rate data for the reactions at atomic oxygen $O(^3P)$ with methane and theane, *Int. J. Chem. Kinetics 1*, 527-539.

Herron, J. T. and R. Penzhorn (1969), Mass spectrometric study of the reactions of atomic oxygen with ethylene and formaldehyde, *J. Phys. Chem. 73*, 191-196.

Hesstvedt, E. (1968), On the effect of vertical eddy transport on atmospheric composition in the mesosphere and lower thermosphere, *Geophys. Norvegica 27*, 1-35.

Hilsenrath, E. (1971), Ozone measurements in themesosphere and stratosphere during two significant geophysical events, *J. Atmos. Sci. 28*, 295-297.

Hines, C. O. (1963), The upper atmosphere in motion, *Quart. J. R. Met. Soc. 89*, 1-42.

Hinteregger, H. E. (1970), The extreme ultraviolet solar spectrum and its variation during a solar cycle, *Ann. Geophys. 26*, 547-554.

Hirsh, M. N. and P. N. Eisner (1972), Laboratory measurements of ion chemistry in a simulated disturbed ionosphere, *Radio Sci. 7*, 125-131.

Hoare, D. E. and A. D. Walsh (1957), The reaction of methyl radicals with oxygen and comparison with other third-order reactions, *Trans. Faraday Soc. 53*, 1102-1110.

Hoare, D. E. and G. S. Pearson (1964), Gaseous photooxidation reaction, *Adv. Photochem. 3*, 83-156.

Hochanadel, C. J., J. A. Ghormley and P. T. Ogren (1972), Absorption spectra and reaction kinetics of the HO_2 radical in the gas phase, *J. Chem. Phys. 56*, 4426-4432.

Hodges, Jr., R. R. (1969), Eddy diffusion coefficients due to instabilities in internal gravity waves, *J. Geophys. Res. 74*, 4087-4090.

Horan, D. M. (1970), Coronal electron temperature associated with solar flares, Ph.D. Dissertation, The Catholic University of America, Washington, D. C.

Howard, C. J., H. W. Rundle and F. Kaufman (1971), Water cluster formation rates of NO^+ in He, Ar, N_2 and O_2 at 296° K, *J. Chem. Phys. 55*, 4472-4776.

Hudson, R. D. and V. L. Carter (1969), Atmospheric implications of predissociation in N_2, *J. Geophys. Res. 74*, 393-395.

Hudson, R. D., V. L. Carter and E. L. Breig (1969), Predissociation in the Schumann-Runge band system of O_2: Laboratory measurements and atmospheric effects, *J. Geophys. Res. 74*, 4079-4086.

Huffman, R. E., D. E. Paulsen, J. C. Larrabee and R. B. Cairns (1971), Decrease in *D*-region $O_2(^1\Delta_g)$ photo-ionization rates resulting from CO_2 absorption, *J. Geophys. Res. 76*, 1028-1038.

Huie, R. E., J. T. Herron and D. D. Davis (1972), Absolute rate constants for the reaction $O + O_2 + M \rightarrow O_3 + M$ over the temperature range 200-346 K, *J. Chem. Phys. 76*, 2653-2658.

Hunt, B. G. (1966), Ozone photochemistry in a moist atmosphere, *J. Geophys. Res. 71*, 1385-1398.

Hunt, B. G. (1971a), Cluster ions and nitric oxide in the *D* region, *J. Atmos. Terr. Phys. 33*, 929-942.

Hunt, B. G. (1971b), A diffusive-photochemical study of the mesosphere and lower thermosphere and the associated conservation mechanisms, *J. Atmos. Terr. Phys. 33*, 1869-1892.

Hunt, B. G. (1973), A generalized aeronomic model of themesosphere and lower thermosphere including ionospheric processes, *J. Atmos. Terr. Phys. 35*, 1755-1798.

Hunten, D. M. and M. B. McElroy (1968), Metastable $O_2(^1\Delta_g)$ as a major source of ions in the *D* region, *J. Geophys. Res. 73*, 2421-2431.

Inn, E. C. Y. and Y. Tanaka (1959), Ozone absorption coefficients in the visible and ultraviolet regions, *Adv. Chem. Ser. 21*, 263-268.

Jacchia, L. G. (1971), Revised static models of the thermosphere and exosphere with empirical temperature profiles, *Special Report 332*, Smithsonian Astrophysical Observatory, Cambridge, Mass.

Johannessen, A. and D. Krankowsky (1972), Positive-ion composition measurement in the upper mesosphere and lower thermosphere at a high latitude during summer, *J. Geophys. Res. 77*, 2888-2901.

Johannessen, A. and D. Krankowsky (1974), Daytime positive-ion composition measurements in the altitude range 73-137 km above Sardinia, *J. Atmos. Terr. Phys. 36*, 1233-1247.

Johnson, F. S. and B. Gottlieb (1971), Eddy mixing and circulation at ionospheric levels, *Planet. Space Sci. 18*, 1707-1718.

Johnston, H. and R. Graham (1973), Gas-phase ultraviolet absorption spectrum of nitric acid vapor, *J. Phys. Chem. 77*, 62-63.

Justus, C. G. (1969), Dissipation and diffusion by turbulence and irregular winds near 100 km, *J. Atmos. Sci. 26*, 1137-1141.

Kane, J. A. (1972), Evidence for the existence of negative ions in the *D*- and lower *E*-regions at twilight, *Preprint X-625-72-18*, Goddard Space Flight Center, Greenbelt, Maryland.

Karol, I. L. (1966), Quantitative investigation of stratospheric mixing processes by means of long lived radon decay products, *Tellus 28*, 337-344.

Kasner, W. H. and M. A. Biondi (1968), Temperature dependence of the electron-O_2^+ ion recombination coefficient, *Phys. Rev. 174*, 139-174.

Kaufman, F. (1964), Aeronomic reactions involving hydrogen, a review of recent laboratory studies, *Ann. Geophys. 20*, 106-114.

Kaufman, F. (1969), Neutral reactions involving hydrogen and other minor constituents, *Can. J. Chem. 47*, 1917-1924.

Keneshea, T. J. and S. P. Zimmerman (1970), The effect of mixing upon atomic and molecular oxygen in the 70-170 km region of the atmosphere, *J. Atmos. Sci. 27*, 831-840.

Keneshea, T. J. and W. Swider (1972), Formulation of diurnal *D*-region models using a photochemical computer code and current reaction rates, *J. Atmos. Sci. 27*, 831-840.

Kijewski, H. and J. Troe (1971), Study of the photolysis of H_2O_2 in the presence of H_2 and CO by means of UV absorption of HO_2, *Int. J. Chem. Kinetics 3*, 223-235.

Krankowsky, D., F. Arnold, H. Wieder, J. Kissel and J. Zahringer (1972), Positive-ion chemistry in the lower ionosphere, *Radio Sci. 7*, 93-98.

Kranzenski, D. C., R. Simonalitis and J. Heicklen (1971), The reaction of $O(^3P)$ with ozone and carbonyl sulphide, *Int. J. Chem. Kinetics 3*, 467-482.

Kreplin, R. W. (1965), NRL solar radiation monitoring satellite description of instrumentation and preliminary results, *Space Res. V*, edited by D. G. King-Hele, P. Muller and G. Righini, North-Holland Publishing Co., Amsterdam, 951-965.

Kreplin, R. W. (1970), The solar cycle variation of soft X-ray emission, *Ann. Geophys. 26*, 567-574.

Kreplin, R. W. (1971), Solar X-rays, *Ann. Geophys 17*, 151-161.

Kreplin, R. W., D. M. Haran and K. P. Dere (1973), Reduction of solar X-ray flux measurements for use in ionospheric research, *Space Res. XIII*, edited by M. J. Rycroft and S. K. Runcorn, Akademie-Verlag, Berlin, 469-470.

Kyle, T. G., D. G. Murcray, F. H. Murcray and W. O. Williams (1969), Abundance of methane in the atmosphere above 20 kilometers, *J. Geophys. Res. 74*, 3421-3425.

Lee, H. S. and A. J. Ferraro (1969), Winter *D*-region electron concentration and collision frequency features obtained with high-power interaction measurements, *J. Geophys. Res. 74*, 1184-1194.

LeLevier, R. E. and L. M. Branscomb (1968), Ion chemistry governing mesospheric electron concentrations, *J. Geophys. Res. 73*, 27-41.

Lettau, H. (1951), Diffusion in the upper atmosphere, *Compendium of Meteorology*, edited by T. F. Malone, American Meteorological Society, New York, 320-333.

Leu, M. T., M. A. Biondi and R. Johnson (1973), Measurements of the recombination of electrons with $H_3O^+ \cdot (H_3O)_n$ series ions, *Phys. Rev. A7*, 292-298.

Lin, C. L. and F. Kaufman (1971), Reactions of metastable nitrogen atoms, *J. Chem. Phys. 55*, 3760-3769.

Lineberger, W. C. and L. J. Puckett (1969), Hydrated positive ions in nitric oxide-water afterglows, *Phys. Rev. 187*, 286-291.

Mandel'stam, S. L. (1965), X-ray emission of the sun, *Space Sci. Rev. 4*, 587-665.

Manson, J. E. (1967), The spectrum of the quiet sun between 30 and 128 Å for November, 1965, *Astrophys. J. 147*, 703-710.

Manson, J. E. (1972), Measurement of the solar spectrum between 30 and 128 Å, *Solar Phys. 27*, 107-131.

Masterbrook, H. J., (1968), Water vapor distributions in the stratosphere and high troposphere, *J. Atoms. Sci. 28*, 1495-1501.

Masterbrook, H. J. (1971), The variability of water vapor in the stratosphere, *J. Atmos. Sci. 28*, 1495-1501.

McConnell, J. C., M. B. McElroy and S. C. Wofsy (1971), Natural sources of atmospheric CO, *Nature 233*, 187-188.

McCrumb, J. L. and F. Kaufman (1972), Kinetics of O + O_3 reaction, *J. Chem. Phys. 57*, 1270-1276.

McKinnon, D. and H. W. Marewood (1970), Water vapor distribution in the lower stratosphere over North and South America, *J. Atmos. Sci. 27*, 483-493.

Mechtly, E. A. (1974), Accuracy of rocket measurements of lower ionosphere electron concentrations, *Radio Sci. 9*, 373-378.

Mechtly, E. A. and L. G. Smith (1970), Changes of lower ionosphere electron densities with solar zenith angle, *Radio Sci. 5*, 1407-1412.

Mechtly, E. A., S. A. Bowhill, L. G. Smith and H. W. Knoebel (1967), Lower ionosphere electron concentration and collision frequency from rocket measurements of Faraday rotation, differential absorption, and probe current, *J. Geophys. 72*, 5239-5245.

Mechtly, E. A., S. A. Bowhill and L. G. Smith (1972a), Changes of lower ionospheric electron concentrations with solar activity, *J. Atmos. Terr. Phys. 34*, 1899-1907.

Mechtly, E. A., C. F. Sechrist, Jr. and L. G. Smith (1972b), Electron loss coefficients for the *D*-region of the ionosphere from rocket measurements during the eclipse of March 1970 and November 1966, *J. Atmos. Terr. Phys. 34*, 641-646.

Mehr, F. J. and M. A. Biondi (1969), Electron temperature dependence of recombination of O_2^+ and N_2^+ ions with electrons, *Phys. Rev. 181*, 264-271.

Meier, R. R. and P. Mange (1970), Geocoronal hydrogen: An analysis of the Lyman-alpha airglow observed from OGO-4, *Planet. Space Sci. 18*, 803-821.

Meier, R. R. and D. K. Prinz (1970), Absorption of the solar Lyman-alpha line by geocoronal atomic hydrogen, *J. Geophys. Res. 75*, 6969-6979.

Meira, L. G., Jr. (1971), Rocket measurements of upper atmospheric nitric oxide and their consequences to the lower ionosphere, *J. Geophys. Res. 76*, 202-212.

Morris, Jr., E. D. and H. Niki (1971), Mass spectrometric study of the reactions of nitric acid with O atoms and H atoms, *J. Chem. Phys. 75*, 3193-3194.

Murcray, D. G., T. G. Kyle, F. H. Murcray and W. J. Williams (1969), Presence of HNO_3 in the upper atmosphere, *J. Opt. Soc. American 59*, 1131-1134.

Nakata, R. S., K. Watanabe and F. M. Matsunge (1965), Absorption and photoionization coefficients of CO_2 in the region 580-1670 Å, *Sci. Light 14*, 54-71.

Nakayame, T., M. Y. Kitamura and K. Watanabe (1959), Ionization potential and absorption coefficients of nitrogen dioxide, *J. Chem. Phys. 30*, 1180-1186.

Narcisi, R. S. (1966), Ion composition measurements and related ionospheric processes in the *D* and lower *E* regions, *Ann. Geophys. 22*, 224-234.

Narcisi, R. S. (1970), Composition studies of the lower ionosphere, based on four lectures presented at the International School of Atmospheric Physics, Erice, Sicily.

Narcisi, R. S. and A. D. Bailey (1965), Mass spectrometric measurements of positive ions at altitudes from 64 to 112 kilometers, *J. Geophys. Res. 70*, 3687-3700.

Narcisi, R. S., A. D. Bailey, L. Della Lucca, C. Sherman and D. M. Thomas (1971), Mass spectrometric measurements of negative ions in the *D*- and lower *E*-regions, *J. Atmos. Terr. Phys. 33*, 1147-1159.

Narcisi, R. S., A. D. Bailey, L. E. Wlodyka and C. R. Philbrick (1972a), Ion composition measurements in the lower ionosphere during the November 1966 and March 1970 solar eclipse, *J. Atmos. Terr. Phys. 34*, 647-658.

Narcisi, R. S., C. R. Philbrick, D. M. Thomas, A. D. Bailey, L. Wlodyka, D. Baker, G. Federico, R. Wlodyka and M. E. Gardner (1972b), Positive ion composition of the *D*- and *E*-regions during a PCA, Proceedings of COSPAR Symposium on "Solar particle event of November 1969", AFCRL-72-0474, *Special Report No. 144*, Boston, Mass., 421-431.

Neher, H. V. and H. R. Anderson (1962), Cosmic rays at balloon altitudes and the solar cycle, *J. Geophys. Res. 67*, 1309-1316.

Nicolet, M. (1965), Nitrogen oxide in the chemosphere, *J. Geophys. Res. 70*, 679-689.

Nicolet, M. (1970), Aeronomic reactions of hydrogen and ozone, *Aeronomica Acta A, 79*, Brussels, 1-[illegible]0.

Nicolet, M. and A. C. Aikin (1960), The formation of the *D* region of the ionosphere, *J. Geophys. Res. 65*, 1469-1483.

Nicolet, M. and P. Mange (1954), The dissociation of oxygen in the high atmosphere, *J. Geophys. Res. 59*, 15-45.

Nicolet, M. and W. Peetermans (1972), The production of nitric oxide in the stratosphere by oxidation of nitrous oxide, *Ann. Geophys. 28*, 751-761.

Niki, H., E. E. Daby and B. Weinstock (1968), Reaction of atomic oxygen with methyl radicals, *J. Chem. Phys. 48*, 5729-5730.

Norton, R. B. and C. A. Barth (1970), Theory of nitric oxide in the earth's upper atmosphere, *J. Geophys. Res. 75*, 3903-3909.

Norton, R. B. and G. C. Reid (1972), Energetic metastable molecular oxygen as a source of ionization in the *D* region, *J. Geophys. Res. 77*, 6287-6290.

O'Brien, B. J. (1964), High-latitude geophysical studies with satellite Injun 3:3, Precipitating of electrons into the atmosphere, *J. Geophys. Res. 69*, 13-43.

O'Brien, B. J., F. R. Allum and H. C. Goldwire (1965), Rocket measurements of midlatitude airglow and particle precipitation, *J. Geophys. Res. 70*, 161-175.

Ogawa, M. (1968), Absorption coefficients of O_2 at the Lyman-alpha line and its vicinity, *J. Geophys. Res. 73*, 6759-6763.

Ogawa, M. (1971), Absorption cross-section of O_2 and CO_2 continued in the Schumann and favor regions, *J. Chem. Phys. 54*, 2550-2556.

Ohshio, M., R. Maeda and H. Sakagami (1966), Height distribution of local Photoionization efficiency, *J. Radio Res. Labs. 13*, 245-264.

Okabe, H. and D. A. Becker (1963), Vacuum ultraviolet photochemistry VII-Photoanalysis of butane, *J. Chem. Phys. 39*, 2549-2555.

Olivero, Jr., J. J. (1970), A study of the thermal structure of the mesosphere and lower thermosphere, *Aeron. Program Rep. 5*, College of Engrg., The University of Michigan, Ann Arbor, Michigan.

Pack, J. L. and A. V. Phelps (1970), Rates of hydration of O^-, O_2^-, O_3^- and O_4^- ions in H_2O-O_2 mixtures, paper presented at the Symposium on Physics and Chemistry of the Upper Atmosphere, Philadelphia, Penn.

Parkinson, W. H. and E. M. Reeves (1969), Measurements in the solar spectrum between 1400 and 1875 Å with a rocket-borne spectrometer, *Solar Phys. 10*, 342-347.

Paukert, T. T. and H. S. Johnston (1972), Spectra and kinetics of the Hydroperoxyl free radical in the gas phase, *J. Chem. Phys. 56*, 2824-2838.

Paulsen, D. E., R. E. Huffman and J. C. Larrabee (1972), Improved photoionization rates of $O_2(^1\Delta_g)$ in the *D* region, *Radio Sci. 7*, 51-55.

Phelps, A. V. (1969), Laboratory studies of electron attachment and detachment processes of aeronomic interest, *Can. J. Chem. 47*, 1783-1793.

Phillips, L. F. and H. I. Schiff (1962), Mass spectrometric studies of atom reactions. I. Reactions in the atomic nitrogen-ozone system, *J. Chem. Phys. 36*, 1509-1517.

Potemra, T. A. and A. J. Zmuda (1970), Precipitating energetic electrons as an ionization source in the mid-latitude nighttime *D* region, *J. Geophys. Res. 75*, 7161-7167.

Pounds, K. A. (1970), X-radiation below 25 Å, *Ann. Geophys. 26*, 555-565.

Preston, K. F. and R. F. Barr (1971), Primary processes in the photolysis of nitrous oxide, *J. Chem. Phys. 54*, 3347-3348.

Ratnasiri, P. A. J. and C. F. Sechrist, Jr. (1971), Effect of CO and CH_4 on the distribution of O-H products in the upper atmosphere, *EOS, Trans. Am. Geophys. Union 52*, 870.

Reed, R. J. and K. E. German (1965), A contribution to the problem of stratospheric diffusion by large-scale mixing, *Monthly Weather Review 93*, 314-321.

Rees, M. H. (1963), Auroral ionization and excitation by incident energetic electrons, *Planet. Space Sci. 11*, 1209-1218.

Reid, G. C. (1970), Auroral ionization and excitation by incident energetic electrons, *Planet. Space Sci. 11*, 1209-1218.

Reid, G. C. (1971) The role of water vapor and nitric oxide in determining electron densities in the *D*-region, *Mesospheric models and related experiments*, Reidel Publishing Co., Dordrecht-Holland, 198-209.

Richtmyer, R. D. (1957), *Difference methods for initial-value problems*, Interscience, New York.

Rowe, J. N., A. J. Ferraro, H. S. Lee, R. W. Kreplin and A. P. Mitra (1970), Observations of electron density during a solar flare, *J. Atmos. Terr. Phys. 32*, 1609-1614.

Rowe, J. N., A. P. Mitra, A. J. Ferraro and H. S. Lee (1974), An experimental and theoretical study of the *D*-region-II. A semi-empirical model for mid-latitude *D*-region, *J. Atmos. Terr. Phys. 86*, 755-785.

Rugge, H. R. and A. B. C. Walker, Jr. (1968), Solar X-ray spectrum below 25 Å, *Space Res. VIII*, edited by A. P. Mitra, L. G. Jacchia and W. S. Newman, North-Holland Publishing Co., Amsterdam, 439-449.

Sagalyn, R. C. and M. Smiddy (1964), Rocket investigations of the electrical structure of the lower ionosphere, *Space Res. IV*, edited by P. Muller, North Holland, Amsterdam, 371-387.

Sayers, J. (1970), *In-situ* probes for ionospheric investigations, *J. Atmos. Terr. Phys. 32*, 663-691.

Schiff, H. I. (1969), Neutral reactions involving oxygen and nitrogen, *Can. J. Chem. 47*, 1903-1916.

Schiff, H. I. (1972), Laboratory measurements of reactions related to ozone photochemistry, *Ann. Geophys. 28*, 67-77.

Schlegel, K. (1971), Photoionization yields of O, O_2, and N_2 for high and low solar activity, *J. Atmos. Terr. Phys. 33*, 1923-1931.

Schofield, K. (1967), An evaluation of kinetic rate data for reactions of neturals of atmospheric interest, *Planet. Space Sci. 15*, 643-655.

Scholz, T. G. and D. Offerman (1974), Measurement of neutral atmospheric composition at 85-115 km by mass spectrometer with Cryoion source, *J. Geophys. Res. 79*, 307-310.

Scholz, T. G., D. H. Elihalt, L. E. Heidt and E. A. Martell (1970), Water vapor, molecular hydrogen, methane, and tritium concentrations near stratopause, *J. Geophys. Res. 75*, 3049-3054.

Schutz, K., C. E. Junge, R. Beck and B. Albrecht (1970), Studies of atmospheric N_2O, *J. Geophys. Res. 75*, 2230-2246.

Schwentek, H. (1966), The determination of absorption in the ionosphere by recording the field strength of a distant transmitter, *Ann. Geophys. 22*, 276-289.

Scott, P. M., K. F. Preston, R. J. Anderson and L. M. Quick (1971), The reaction of the electronically excited oxygen atom $O(^1D_2)$ with nitrous oxide, *Can. J. Chem. 49*, 1808.

Sechrist, Jr., C. F. (1970), Interpretation of *D*-region electron densities, *Radio Sci. 5*, 663-671.

Sechrist, Jr., C. F. (1972), Theoretical models of the *D* region, *J. Atmos. Terr. Phys. 34*, 1656-1589.

Sechrist, Jr., C. F. (1974), Comparisons of techniques for measurement of *D*-region electron densities, *Radio Sci. 9*, 137-149.

Seiler, W. and C. E. Junge (1970), Carbon monoxide in the atmosphere, *J. Geophys. Res. 75*, 2217-2226.

Sheppard, P. A. (1959), Dynamics of the upper atmosphere, *J. Geophys.* *64*, 2116-2121.

Shimazaki, T. (1967), Dynamic effects on atomic and molecular oxygen density distributions in the upper atmosphere: A numerical solution to equations of motion and continuity, *J. Atmos. Terr. Phys.* *29*, 723-747.

Shimazaki, T. (1971), Effective eddy-diffusion coefficient and atmospheric composition in the lower thermosphere, *J. Atmos. Terr. Phys.* *33*, 1383-1401.

Shimazaki, T. and A. R. Laird (1970), A model calculation of the diurnal variation in minor neutral constituents in the mesosphere and lower thermosphere including transport effects, *J. Geophys. Res.* *75*, 3221-3235.

Shimazaki, T. and A. R. Laird (1972), Correction to 'A model calculation of the diurnal variation in minor neutral constituents in the mesosphere and lower thermosphere including transport effects', *J. Geophys. Res.* *77*, 276-277.

Slanger, T. G. and G. Black (1970), Reaction rate measurements of $O(^3P)$ atoms by resonance and fluorescence, I. $O(^3P) + O_2 + M = O_3 + M$ and $O(^3P) + NO + M$, *J. Chem. Phys.* *53*, 3717-3721.

Slanger, T. G., B. G. Wood and G. Black (1972), Kinetics of $O(^3P) + CO + M$ recombination, *J. Chem. Phys.* *57*, 233-238.

Smith, L. G. (1964), Langmuir probes for measurements in the ionosphere, *COSPAR Information Bulletin 17*, edited by K. Maeda, 37-81.

Smith, W. S., J. S. Theon, J. F. Casey and J. J. Horvath (1970), Temperature, pressure, density and wind measurements in the stratosphere

and mesosphere, 1968, *NASA Technical Peport NASA TR R-340*, Washington, D. C.

Strobel, D. F. (1971a), The diurnal variation of nitric oxide in the upper atmosphere, *J. Geophys. Res. 76*, 2441-2452.

Strobel, D. F. (1971b), Odd nitrogen in the mesosphere, *J. Geophys. Res. 76*, 8384-8393.

Strobel, D. F. (1972a), Minor neutral constituents in the mesosphere and lower thermosphere, *Radio Sci. 7*, 1-21.

Strobel, D. F. (1972b), Nitric oxide in the *D* region, *J. Geophys. Res. 77*, 1337-1339.

Strobel, D. F., D. M. Hunten and M. B. McElroy (1970), Production and diffusion of nitric oxide, *J. Geophys. Res. 75*, 4307-4321.

Swider, Jr., W. (1969), Ionization rates due to the attenuation of 1-100 Å nonflare solar X-rays in the terrestrial atmosphere, *Rev. Geophys. 7*, 573-394.

Tanaka, Y., E. C. Y. Inn and K. Watanabe (-1953), Absorption coefficients of gases in the vacuum ultraviolet; 4. Ozone, *J. Chem. Phys. 21*, 1651-1653.

Thomas, L. (1974), Recent developments and outstanding problems in the theory of the *D* region, *Radio Sci. 9*, 121-135.

Thomas, L. and M. R. Bowman (1972), The diurnal variations of hydrogen and oxygen constituents in the mesosphere and lower thermosphere, *J. Atmos. Terr. Phys. 34*, 1843-1858.

Thomas, L., P. M. Godhalekar and M. R. Bowman (1973), The negative-ion composition of the daytime *D*-region, *J. Atmos. Terr. Phys. 35*, 397-404.

Thompson, B. A., P. Harteck and R. R. Reeves, Jr. (1963), Ultraviolet absorption coefficients of CO_2, CO, O_2, H_2O, N_2O, NH_3, NO, SO_2 and CH_4 between 1850 and 4000 Å, *J. Geophys. Res. 68*, 6431-6436.

Thrane, E. V. (1969), Diurnal variation of electron production rates in the *D* region, *J. Geophys. Res. 74*, 1311-1316.

Thrane, E. V., A. Haug, B. Bjelland, M. Anastassiades and E. Tsagakis (1968), Measurements of *D*-region electron densities during the International Quiet Sun Years, *J. Atmos. Terr. Phys. 30*, 135-150.

Timothy, A. F. and J. G. Timothy (1970), Long-term intensity variations in the solar helium 2 Lyman-alpha line, *J. Geophys. Res. 75*, 6950-6958.

Tisone, G. C. (1973), Measurements of NO densities during sunrise at Kuaui, *J. Geophys. Res. 78*, 746-750.

Tousey, R. (1963), The extreme ultraviolet spectrum of the sun, *Space Sci. Rev. 2*, 3-69.

Vallance Jones, A. and R. L. Gattinger (1963), The seasonal variation and excitation mechanism 1.58 μ $^1\Delta_g$ - $^3\Sigma_g$ - twilight airglow band, *Planet. Space Sci. 11*, 961-974.

Velinov, P. (1968), On ionization in the ionospheric *D*-region by galactic and solar cosmic rays, *J. Atmos. Terr. Phys. 30*, 1891-1905.

Vidal-Madjar, A., J. E. Blamont and B. Phissamay (1973), Solar Lyman alpha changes and related hydrogen density distribution at the earth's exobase (1969-1970), *J. Geophys. Res. 78*, 1115-1144.

Watanabe, K. and M. Zelikoff (1953), Absorption coefficients of water vapor in the vacuum UV, *J. Opt. Soc. America 43*, 753-755.

Watanabe, K., E. C. Y. Inn and M. Zelikoff (1953), Absorption coefficients of oxygen in the vacuum ultraviolet, *J. Chem. Phys. 21*, 1026-1030.

Weeks, L. H. (1967), Lyman-alpha emission from the sun near solar minimum, *Astrophys. J. (letters)* *147*, 1203-1205.

Weill, G. M. (1969), NO(^4S-^2D) radiation in the night airglow and low latitude aurora, *Atmospheric Emissions*, edited by B. M. McCormac and A. Omholt, Van Nostrand Reinhold, New York, 449.

Weller, C. S. and M. A. Biondi (1968), Recombination, attachment, and ambipolar diffusion of electrons in photo-ionized NO afterglows, *Phys. Rev.* *172*, 198-206.

Wende, C. D. (1971), The normalization of solar X-ray data from many experiments, *NASA Report No. X-601-71-166*, NASA Goddard Space Flight Center, Greenbelt, Maryland.

Westenberg, A. A. and N. De Hass (1972), Rate measurements on OH + NO + M and OH + NO_2 + M, *J. Chem. Phys.* *57*, 5375-5378.

Wofsy, S. G., J. C. McConnell and M. B. McElroy (1972), Atmospheric CH_4, CO and CO_2, *J. Geophys. Res.* *77*, 4477-4493.

Zelikoff, M., K. Watanabe and E. C. Y. Inn (1953), Absorption coefficients of gases in the vacuum ultraviolet, Part II, Nitrous oxide, *J. Chem. Phys.* *21*, 1643-1647.

Zimmerman, S. P. and K. S. W. Champion (1963), Transport process in the upper atmosphere, *J. Geophys. Res.* *68*, 3049-3056.

Zipf, E. C. (1969), Collisional deactivation of metastable atoms and molecules in the upper atmosphere, *Can. J. Chem.* *47*, 1863-1870.